2008

Influence of variable thrust parameters on swirl injector fluid mechanics

Robert J. Kenny

INFLUENCE OF VARIABLE THRUST PARAMETERS ON SWIRL INJECTOR FLUID MECHANICS

by

ROBERT J. KENNY

A DISSERTATION

Submitted in partial fulfillment of the requirements
for the degree of Doctor of Philosophy
in
The Department of Mechanical and Aerospace Engineering
to
The School of Graduate Studies
of
The University of Alabama in Huntsville

HUNTSVILLE, ALABAMA
2008

In presenting this dissertation in partial fulfillment of the requirements for a doctoral degree from The University of Alabama in Huntsville, I agree that the Library of this University shall make it freely available for inspection. I further agree that permission for extensive copying for scholarly purposes may be granted by my advisor or, in his/her absence, by the Chair of the Department or the Dean of the School of Graduate Studies. It is also understood that due recognition shall be given to me and to The University of Alabama in Huntsville in any scholarly use which may be made of any material in this dissertation.

_____ _____

Robert J. Kenny date

DISSERTATION APPROVAL FORM

Submitted by Robert J. Kenny in partial fulfillment of the requirements for the degree of Doctor of Philosophy in Mechanical Engineering and accepted on behalf of the Faculty of the School of Graduate Studies by the dissertation committee.

We, the undersigned members of the Graduate Faculty of The University of Alabama in Huntsville, certify that we have advised and/or supervised the candidate on the work described in this dissertation. We further certify that we have reviewed the dissertation manuscript and approve it in partial fulfillment of the requirements for the degree of Doctor of Philosophy in Mechanical Engineering.

_____ Committee Chair
Dr. Marlow D. Moser (Date)

_____ Advisor
Dr. Noah O. Rhys

_____
Dr. Valdimir G. Bazarov

_____
Dr. Kader Frendi

_____
Dr. Ramon L. Cerro

_____ Department Chair
Dr. Kader Frendi

_____ College Dean
Dr. Phillip A. Farrington

_____ Graduate Dean
Dr. Debra M. Moriarity

ABSTRACT
The School of Graduate Studies
The University of Alabama in Huntsville

Degree Doctor of Philosophy College/Dept. Engineering/Mechanical and Aerospace Engineering

Name of Candidate Robert J. Kenny
Title Influence of Variable Thrust Parameter on Swirl Injector Fluid Mechanics

Current swirl injector design methodologies do not consider elevated chamber pressure and less than design mass flow rate operation found in variable thrust liquid rocket engines. The objective of this work is to study the effects of elevated chamber pressure and off-design mass flow rate operation on swirl injector fluid mechanics. Using a high pressure chamber, water flowed through a swirl injector at various combinations of elevated chamber pressure and reduced mass flow rate. The optically-accessible swirl injector allowed for determination of the film thickness profile down the swirl injector nozzle section. High speed video and digital stills showed significant increases in the film thickness profile at high chamber pressure and low mass flow rate operation. At prescribed combinations of chamber pressure and mass flow rate, a jump was noted in the film thickness profile. This jump was assumed related to a vortex breakdown phenomenon. Measured injector discharge coefficient values showed different trends with increasing chamber pressure at low mass flow rate operation as opposed to near-design mass flow rate operation. Downstream spray angles showed classic changes in morphology as the mass flow rate was decreased below the design value. Increasing chamber pressure worked to decrease the spray angle at any injection mass flow rate. A new set of fundamental relations linking swirl injector design parameters to injector geometry and flow conditions were derived. Impacts of the research findings to the swirl injector design process were assessed.

Abstract Approval:

Committee Chair _____
Dr. Marlow D. Moser

Department Chair _____
Dr. Kader Frendi

Graduate Dean _____
Dr. Debra M. Moriarity

ACKNOWLEDGMENTS

Successful completion of this work came from the support of many people. To begin, Dr. Clark Hawk was instrumental in sponsoring my program. He offered excellent council when asked and taught me a great deal about the field of rocket propulsion. I am grateful to have known him prior to his passing.

Nathan Walker, David Eddleman, and Kevin Pedersen were all key players in building the experimental facility used in this work. Experimental facility maintenance was reliably provided by the NASA – Marshall Space Flight Center's Test Area services. During testing, both Michelle Christensen and Nick Hensley helped me run the facility, swap hardware, and fix equipment. Their support led to viable data reported in this work.

Gregg Jones and Jim Hulka both provided valuable guidance in forming my research plan. In particular, Jim Hulka deserves credit for publication oversight and many fruitful discussions with me on the experimental results.

My committee supported my research through experimental insight and technical discussions. I would like to specifically thank Drs. Marlow Moser, Vladimir Bazarov, and Noah Rhys. Their expertise helped me solve many problems and explain much of the phenomena seen.

Most important, the support of my family is what consistently motivated me through this degree. My wife deserves the most acclaim, since she stood by my side as I began, struggled through, and completed this journey. I am blessed to have her in my life.

TABLE OF CONTENTS

Page

LIST OF FIGURES

Figure **Page**

LIST OF TABLES

Table **Page**

LIST OF SYMBOLS

A	geometric constant defined by Equation (1.9)
A_{eff}	effective cross-sectional liquid flow area
A_n	nozzle cross-sectional area
A_o	tangential orifice cross-sectional area
C	flow coefficient
C_D	injector discharge coefficient
C_{Do}	intercept of Equation (3.28)
$C_{D,o}$	orifice discharge coefficient
D_s	tangential orifice diameter
D_{vc}	vortex chamber diameter
ΔP	injector pressure drop
Fr	Froude number
k	tangential loss factor
l_s	tangential orifice length
L_{vc}	vortex chamber length
L_n	nozzle length
M_b	axial flux of velocity momentum component b
$\dot{m}_l$	liquid mass flow rate
N_s	number of tangential orifices
P_c	chamber pressure
P_f	supply pressure into injector
r	radius
R_n	nozzle radius
R_s	swirl arm, = $R_n - 0.5D_s$
r_{mn}	gas core radius

Re	Reynolds number
Re_o	Tangential orifice Reynolds number
S	swirl number, or slope of Equation (3.28)
S_θ	slope of Equation (4.4)
t	nozzle average film thickness
$t_{n,j}$	local film thickness along profile side j
U_b	liquid velocity component b
$2U_i$	total uncertainty of measurement i based on 95% confidence levels
U_a	axial liquid velocity component within injector, Bazarov notation
U_{an}	axial liquid velocity component at injector exit, Bazarov notation
U_r	radial liquid velocity component within injector, Bazarov notation
U_u	tangential liquid velocity component within injector, Bazarov notation
U_{un}	tangential liquid velocity component at injector exit, Bazarov notation
V_Σ	total liquid velocity magnitude
We	Weber number
We_o	Tangential orifice Weber number
x	axial distance
X	ratio of gas core cross-sectional area to nozzle cross-sectional area
$X_{j,i}$	horizontal location of spray boundary at profile side j
$X_{j,o}$	horizontal location of nozzle exit edge at profile side j
$Y_{j,i}$	vertical location of spray boundary at profile side j
$Y_{j,o}$	vertical location of nozzle exit edge at profile side j

Greek

α	area fullness coefficient, or momentum angle defined by Figure 1.8
ϕ	spray angle defined by Figure 1.8
Γ	circulation

μ	viscosity
Ω	rotational velocity
ω	angular velocity
Φ_j	local spray angle along profile side j
ρ	density
σ	surface tension coefficient
θ	free cone spray angle
θ_o	intercept of Equation (4.4)

Subscripts

a	axial component
g	gas
l	liquid
u	tangential component

CHAPTER 1

INTRODUCTION

1.1 Liquid Rocket Engine Injectors

The mobility of every liquid rocket is tantamount to the design and operation of one component: the engine. Liquid rocket engines utilize the reacting force of exhausting propellants to create thrust, which is used to propel the rocket's mass. The engine itself has many components, generally grouped into two main sections: the propellant delivery system and the thrust chamber assembly [1]. Of these two sections, the thrust chamber is the most influential to the engine performance [1]. Thrust chamber assemblies are divided into three main sections: the injector, the combustion chamber, and the exhaust nozzle. Figure 1.1 shows a general thrust chamber schematic with the three main sections labeled [2].

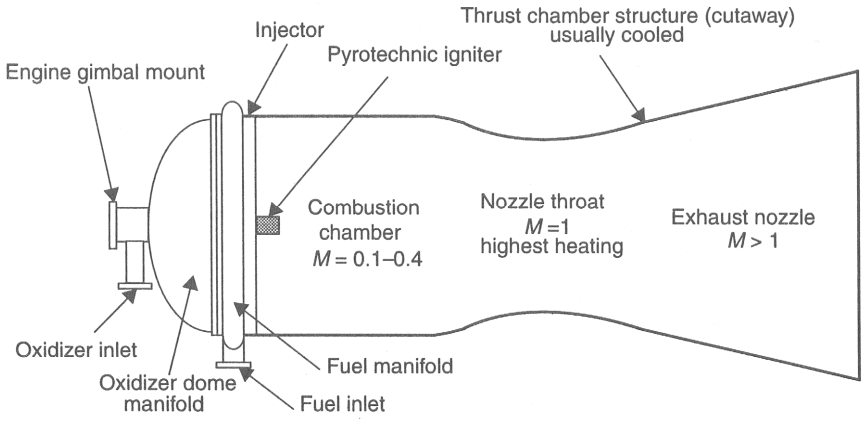

Figure 1.1 Thrust chamber components for a bipropellant engine [2]

Following Figure 1.1, the propellants are delivered to the injector manifold system via the oxidizer and fuel inlets. Next, the propellants are introduced into the thrust chamber by the injector. Depending on whether the propellant states are liquid or gas, the propellants are atomized, vaporized, and mixed in preparation for combustion within the combustion chamber. After the propellant mixture is ignited and burned, the combustion products are accelerated to supersonic speeds through a converging – diverging nozzle. Each process of injection, combustion, and expansion are interrelated in design and performance. However, the injection process, inclusive of propellant introduction and preparation, has the largest effect on the thrust chamber performance. Propellant injection can influence combustion efficiency, chamber wall heat transfer, and supersonic gas expansion [3]. Because injection quality is so important to engine performance, emphasis is given within rocket development programs to proper injector hardware design, characterization, and testing.

1.1.1 Injector Hardware and Development

According to Gill and Nurick [4], a liquid rocket engine injector "atomizes and mixes the fuel with the oxidizer to produce efficient and stable combustion that will provide the required thrust without endangering hardware durability." Essentially, the injection device is responsible for preparing the propellant combination to provide a high quality combustible mixture within the chamber. The injection device also works to preclude any harmful effects on the chamber caused by the high pressure and temperature based combustion. Different types of injectors and methods for their development are reviewed in this section.

1.1.1.1 Injector Configurations

Rocket injectors vary in geometry and layout since not all rocket engines are the same size and shape. However, the typical liquid rocket injector consists of a faceplate that is attached to one end of the thrust chamber. This faceplate is embedded with multiple injection elements which are fluid circuits that deliver propellants. The size and number of injector elements is indicative of the amount of thrust produced by the engine. Faceplate design features such as number of elements, inter-element spacing, and particular element type are all chosen to meet the desired combustion behavior.

As an example of the multi-element injector configuration, the Space Shuttle Main Engine (SSME) injector is shown in Figure 1.2 below. The SSME is a bipropellant

engine, using liquid oxygen (LOX) as the oxidizer and gaseous hydrogen (GH2) as the fuel.

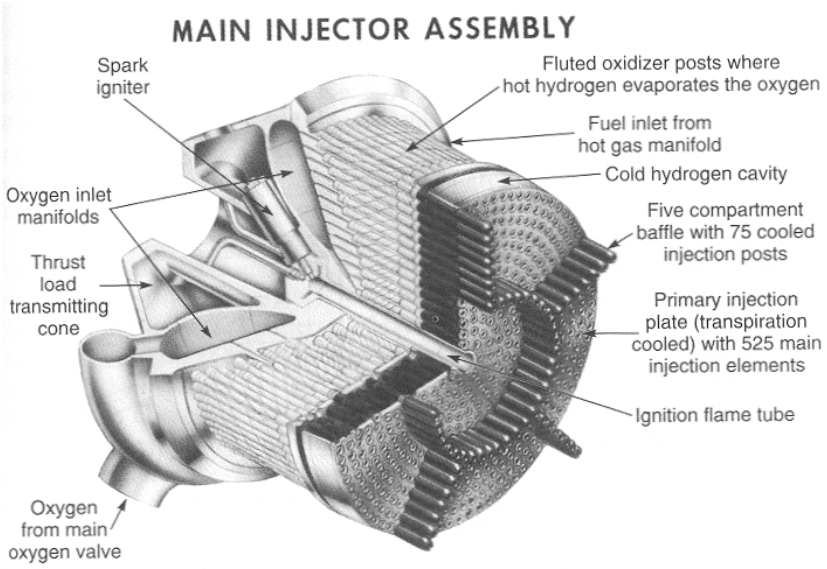

Figure 1.2 SSME multi-element injector [1]

Figure 1.2 shows how the main injector assembly receives propellants from the manifolds, and delivers the propellant combination into the combustion chamber via several hundred elements. The design features of this injector were influenced by previous engine work which helped mitigate problems with combustion stability and efficiency [5]. In combination with design heritage, a large amount of performance testing was used to help make decisions for injector geometry and element layout. The testing methodology used followed a general scheme often found within multi-element injector development programs, as described in the next section.

1.1.1.2 Testing Strategies for Injector Development

The design, testing, and acceptance process for multi-element liquid rocket injectors comprises several steps, with each step having its own set of development considerations. Initially, the overall engine operating parameters are decided, including the engine thrust, propellant combination, and mass flow rate [1]. Next, the global thrust chamber dimensions are chosen. Assuming a cylindrical chamber design, these dimensions consist of an average chamber length and diameter. This chamber diameter is also the maximum diameter of the injector faceplate assembly. Selection of engine cycle type is made, which can determine the fluid state of the propellants upon injection into the chamber [3]. Once the propellant fluid state is decided, injector element types are chosen for consideration. At this point in the design process, the specific features of the injector faceplate are still unknown. Parameters such as total number of elements, element configuration across the faceplate, and type of element used are unknown. Because the influence of single element behavior is so critical to overall injector performance and size, extensive testing and development is typically done on a single element level prior to multi-element injector construction.

After an element design has been selected, the number of elements needed to provide the total thrust is determined. However, some programs have tested 'subscale' multi-element injectors prior to building the full-scale, multi-element injector. In such a case, a small number of elements, much less than the total number anticipated for the full-scale injector design, are mounted within a smaller diameter injector faceplate. The intention of this subscale injector is to optimize element-to-element spacing and

orientation within the injector face. Numerous programs have used subscale injector testing to troubleshoot problems such as combustion stability, wall heat transfer, and inter-element flow disruptions. Satisfactory subscale injector tests lead to full-scale injector design and fabrication. The full-scale injector is tested, any desired changes are made, and the final injector design is accepted [2].

Examples of this general injector development process are readily seen within previous injector testing programs. The use of the steps listed above is dependent on the testing program rationale itself. Table 1.1 below gives some general information about the injector development process used by a select number of historical programs. The engine design parameters desired, injector elements studied, and the development processes used are all listed for comparison. Instead of targeting a few examples for discussion, the reader is encouraged to review the citations in their entirety, since more information is contained in the project summary reports than can be discussed within this introduction.

An important feature of each program is the use of subscale hardware as an intermediate step in the full-scale injector development process. Generally, the programs reviewed in Table 1.1 used subscale and/or full scale chambers. Subscale testing allows for lower costs, higher operational safety margins, and higher accessibility for diagnostic instrumentation [6], [7], [8]. These benefits continue to become even more attractive with growing demands for economical, yet comprehensive, liquid rocket component research. Implementation of subscale testing can be done in a laboratory-sized testing environment where design parameters are easier to change and study.

Table 1.1 Past LRE injector development programs

Program Period	Organizations	Engine/Rocket Designations	Full-scale Operating Parameters	Propellant Combinations / Injector Type	Scaling Hardware Used	Research Focus	References
1963 - 1967	• Aerojet • NASA-LeRC	M-1 Engine	• 5.3 MN thrust • 6.8 MPa chamber pressure • 428 sec specific impulse (vac)	• LOX/H2 • shear coaxial element	• 7.41:1 subscale combustor • Matched chamber pressure at 6.8 MPa • Used 51 full-scale injection elements compared to full-scale number of 3248 elements	• Engine stability mapping - tested fuel temperature ramping and baffle optimization • Compared C* efficiencies between sub and full-scale tests	[9]
1970 - 2000	• Rocketdyne • NASA • Air Force	Linear Aerospike Engine (X-33)	• 1.9 MN thrust • 1.4 MPa chamber pressure • 450 sec specific impulse	• LOX/H2, LOX/HC • element type unavailable	• Subscale engine testing used 20 smaller combustion chambers for each engine block, as opposed to the full-scale design with 14 large chambers	• Engine performance studies • Focused on propellant performance and ignition characteristics	[10]
1972 - 1974	• Rocketdyne • NASA-JSC	Shuttle Orbital Maneuvering Engines (OMS)	• 26.7 kN thrust • 0.7-0.9 MPa chamber pressure • 300-340 sec specific impulse (vac)	• NTO/50-50 • NTO/MMH • O2/MMH • O2/50-50 • O2/HC • doublet/triplet impinging jets	• Single element hardware sized at full-scale geometry	• Engine performance studies - optimized element design in subscale tests • Looked at sensitivity of engine operating parameters on chamber pressure, mixture ratio, injection temperatures, and chamber length	[11]
1972 - 1975	• Aerojet • NASA-JSC	Shuttle Orbital Maneuvering Engines (OMS)	• 26.7 kN thrust • 0.9 MPa chamber pressure • 315 sec specific impulse (vac)	• N2O4/MMH • splash plate • X-doublet impinging jets	• Full-scale unielement injector tests used to evaluate mixing and combustion performance • Subscale injector tests used 1/10th of full-scale element number compared to full-scale design	• Comprehensive program to study the optimum performance, wall heat transfer, and combustion stability of platelet-based OMS engines • Varied injection parameters, injector designs, and overall chamber geometry	[12]
1990 - 1993	• Pratt-Whitney • NASA-MSFC	STME Main Injector	• 2.6 MN thrust • 15.5 MPa chamber pressure • 345 sec specific impulse (vac)	• LOX/H2 • LOX/CH4 • swirl-coaxial element	• 0.2 MN subscale combustor tested with 62 full-scale elements	• Study to assess injector unielement and multielement performance for heat transfer and stability • Full-scale phase never initiated	[13]
1993 - Current	• EADS-ST • KBKhA	TEHORA (i.e., Arianne 5)	• 2.0 – 4.0 kN thrust • 2.1 – 4.1 MPa chamber pressure	• LOX/H2 • LOX/HC • swirl-coaxial • impinging jets • advanced throttling elements	• Subscale injector tests using 19 - 37 elements, reduced in size • Also used full-scale unielement studies	• Targeting development of lesser-used propellant combinations with various injector types and geometries • Focus on performance and heat transfer	[14] [15] [16]

Upon acceptance of subscale design parameters, the full-scale hardware design is extrapolated and built by various means. Ultimately, this process can allow for optimization of full-scale design features and performance at a fraction of the cost compared to full-scale iteration and design.

There are many venues of scaling techniques defined within literature, leading to ambiguity in defining what 'subscale' actually means. Table 1.2 was compiled in order to classify what kind of subscale testing was used for each program listed in Table 1.1. After choosing the chamber scale, the next level is based on whether or not tests run were with single element or multi-element injectors. Lastly, if the program had a cold flow characterization step, it is listed in conjunction with the hot fire component.

Table 1.2 Subscale testing classification

Program	Subscale Chamber				Full Scale Chamber	
	Single Element		Multi-Element		Multi-Element	
	Cold Flow	Hot Fire	Cold Flow	Hot Fire	Cold Flow	Hot Fire
M-1				X		X
X-33				X	X	X
Rocketdyne OMS		X				X
Aerojet OMS	X	X	X	X		X
STME	X		X	X		
TEHORA	X		X	X		

Most programs in Table 1.2 start with single element testing. Single element performance evaluations are crucial inputs to decide the multi-element design, since there

is no accepted set of criteria used to directly design a multi-element injector [17]. Single element evaluation involves characterization using experimental techniques. Referencing Huzel and Huang [17], there are three types of injector evaluation tests:

1. *Hydrostatic:* Hydrostatic pressure evaluation uses a series of water flow tests that subject the injector hardware, single or multi-element, to pressure drops and internal stresses representative of those felt during normal operation. The intention is to check out the injector's structural integrity and fluid-mechanical sealing.
2. *Non-reacting:* Cold flow characterization refers to the quantification of injector spray fluid features, without the influence of reacting flow processes. The injector features studied in cold flow include hydraulic resistance, intact spray features, and spray atomization behavior.
3. *Reacting:* Hot firing tests evaluate the injector's influence on the combustion processes. This type of test is considered the best way to evaluate the injector's performance, since all thermo-fluid processes are captured.

The use of cold flow characterization is an important step, since most element design methods are based on strictly fluid mechanic considerations. This step is becoming more important with the advent of liquid rocket injector numerical simulations. Usually, numerical simulations are first proven with just the injection fluid mechanics, and then move onto the reacting flow simulation. Correspondingly, there is a need for

cold flow spray measurements to compare against numerical results. The process and examples of injector element cold flow characterization are reviewed in the next section.

1.1.1.3 Injector Element Cold Flow Characterization

The cold flow simulants are chosen to match the actual propellants' fluid properties under given operating conditions. Generally, important fluid properties to match are fluid densities, surface tension, and viscosities. The water/air combination is typically used to simulate liquid oxygen (LOX) / gaseous fuel propellants, respectively. The LOX / gaseous hydrogen (GH2) propellant combination is specifically important to many engine programs, including those of current interest to NASA [18]. While the surface tension and viscosity of water does not match that of LOX, water density is very close to LOX density. Assuming a LOX injection temperature range of 90 – 120K, the corresponding density is 0.8 – 1.2 times that of the density of water [1]. Recent works have identified viscosity and surface tension importance on spray fluid mechanics [19], [20]. However, rocket injection conditions are such that high element Reynolds numbers are reached, approximating inviscid flow behavior. The assumption of inviscid flow is the basis for most historical injector elements designs [20], [21], [22].

This range of mass flow rate and chamber pressure, along with the propellant properties, defines a general working space that a cold flow test should strive to match. For LOX/GH2 elements, mass flow rate of LOX and GH2 are on the order of 0.5 kg/s and 0.1 kg/s, respectively. Chamber pressure varies more according to the engine design. LOX/GH2 engine pressures range from approximately 2 MPa (RL-10A-3) [10] to

21 MPa (SSME) [5]. Previous cold flow research has not always been able to match all of the operating conditions absolutely, but instead have matched appropriate non-dimensional groupings of propellant momentum ratios, mixture ratios, and fluid property ratios.

Work performed by Cox is an example of basic rocket injector cold flow characterization [23]. The objective of the work was to characterize SSME rocket injector elements. To best match the properties of LOX at elevated pressures, several liquid simulants were used, including water, solvents, and chlorodifluoromethane. Air was used to simulate GH2. Tests were run at SSME operational mass flow rates and at 3.8 MPa chamber pressure. Measurements were taken to ascertain the elements' hydraulic resistance, liquid/gas spray distribution, and droplet atomization behavior. The work showed how manufacturing tolerances within the element hardware can lead to spray maldistribution and off-design performance. The use of simulants instead of actual propellants did not reduce the effectiveness of the study, since it was assumed that the data taken could be analyzed and extrapolated to high-pressure conditions found in hot fire tests. The important thing to note from this work is the extensive use of cold flow characterization to size and rate element types investigated prior to hot fire testing. The use of cold flow testing aided design improvements and gave insight into how changes in element hardware can affect the hot fire performance.

Another example of high-pressure cold flow characterization is work done by Cohn et al. [24], [25]. This research, jointly run between the Air Force Research Laboratory and Sierra Engineering, has been working to develop a methodology to interpret results from single element cold flow characterization to hot fire performance.

The technique uses a mechanical patternator to define mass flux distributions for a given injection spray. A mechanical patternator uses multiple tubes to capture liquid spray, and then the volume of liquid in each tube is compared by volume fraction, giving a general spatial distribution of liquid over a cross-section. Gaseous nitrogen and water were used to test a number of various LOX / gaseous fuel element designs. The testing environment consists of a 3.5 MPa, optically accessible chamber. Cold flow tests have been run at elevated pressures to match selected nonreacting and reacting operating conditions. The mass flux distributions were converted to mixing efficiencies, which were correlated to the associated hot fire combustion efficiency of the propellants. Results showed that the cold flow mixing efficiency is related to the combustion efficiency, and that cold flow characterization can help predict hot fire performance of the propellants.

Cohn's work acknowledged that cold flow simulants typically operate within subcritical conditions, while the actual hot fire environment is supercritical. Other programs, such as those led by Mayer, have used liquid nitrogen (LN2) in place of water as a LOX simulant [19]. LN2 has similar surface tension and viscosity values like those of LOX, simulating the supercritical fluid mechanics more accurately. Results by Mayer have shown much more accurate predictions of LOX spray behavior, particularly in spray breakup. The effects of surface tension and viscosity are less apparent in the upstream spray area closer to the element tip. In this zone, the fluid density is the most important property to match between cold flow and hot fire. As stated earlier, the fluid densities of water and LOX are approximately the same. Thus, it is fair to say that using water as a cold flow simulant is acceptable, as long as one is careful about which propellant spray features are being studied.

Cold flow injector measurement interpretation to predict hot-fire injector performance is still unresolved. The non-reacting spray features themselves still need increased levels of understanding, especially for conditions indicative of liquid rocket engine operation. Current research programs are studying these features, but are focused more on effects of changing injector geometry and not operating conditions [26], [27]. As reviewed by Hulka and Kenny [28], upcoming engine programs like those in current NASA architecture [18] will need to understand the spray fluid mechanics to better size and rate a desired injection scheme for a liquid rocket engine.

1.2 Coaxial Injection Elements for Liquid/Gas Propellants

Historical LOX/GH2 engines include the J-2, the RL-10A, the RL-10A-3, and the SSME [1]. This propellant combination has traditionally been injected into the thrust chamber by coaxial element injectors. A coaxial element has a center tube, or 'post', which LOX flows through and an outer tube surrounding the inner post that flows GH2 through an annular area. Figure 1.3 shows the general features of a coaxial injector element.

The coaxial spray has four main zones: (1) turbulent liquid core, (2) primary breakup and atomization, (3) secondary atomization, and (4) droplet flow as seen in Figure 1.3. Combustion chamber performance is linked through spray mixing and droplet characteristics within these zones. Efficient mixing is related to the propellant interface behavior and to the vaporization of the liquid core, captured within zones (1) and (2).

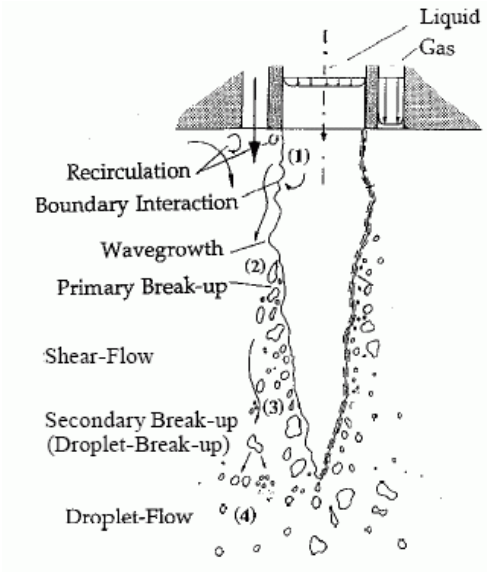

Figure 1.3 Liquid/gas coaxial spray features [29]

The better the mixing of the two propellants is, the better the combustion process. The droplet size and distribution, contained within zones (3) and (4), also plays a large role in creating efficient combustion. Spray features, such as core breakup lengths and droplet behavior, are implemented through the design of the coaxial element itself. Two traditional types of coaxial element designs are used for LOX/GH2 injectors: shear – coaxial and swirl – coaxial.

1.2.1 Shear – Coaxial Element Design

Shear – coaxial element design is mainly focused towards delivering both the LOX jet and the co-flowing GH2 gas with large axial velocity components. The faster

GH2 shears the surface of the liquid jet creating ligaments and droplets as the propellants flow downstream. In addition to the gas shearing, the liquid jet is breaking up due to its own internal turbulence and hydrodynamic instabilities [22]. The liquid is completely disintegrated into droplets in the secondary atomization zone and the liquid jet core is nonexistent. The spray spreads out from the element tip creating a spray angle.

As discussed by Heister [30], the spray angle and liquid jet breakup length are important features influencing combustion processes and subsequent engine efficiency. The combustion zone, or flame front, exists along and downstream of the LOX jet core for shear – coaxial sprays in reacting environments. Work performed by Mayer et al. [19] reported that this flame front generally holds the same shape and length as defined by the nonreacting liquid jet spray angle and breakup length. Conclusions from Mayer's work show that good understanding and control of the shear – coaxial element's nonreacting design features leads to good combustion process and engine efficiency.

Shear – coaxial elements are simple to design and analyze [4], [20]. The heritage of this element type has produced a large database of design references. The injected jet core is highly directional causing the spray to mix and combust at a safe distance from the thrust chamber wall. The working pressure drop needed is relatively low, and the shearing gas – liquid core interface provides high quality propellant mixing and good atomization characteristics.

Fabrication tolerance and element response to unsteady flow perturbations are disadvantages of using shear – coaxial elements [20]. Tailoring the liquid post's and surrounding gas annulus' exit dimensions is important to achieve high atomization. Any manufacturing deviations can lead to changes in the propellant mixing and atomization

behavior; usually for the worst. Flow fluctuations are introduced when combustion processes cause chamber pressure pulsations. Transverse flow fluctuations in the secondary atomization zone can modify the injected spray angle, causing intraelement and interelement behavior that can lead to combustion instabilities. Unsteady flow fluctuations can also 'penetrate' into the element itself, causing upstream mass flow rate fluctuations during injection. These mass flow rate fluctuations can disrupt the design mixture ratio and atomization quality of the shear – coaxial element, lowering combustion performance. The liquid post dimensions can be designed with a metering orifice to damp out these fluctuations, but there is an associated penalty in higher orifice pressure drop. According to Hutt [31], this increase in pressure drop can be considered wasted energy that could have been direct towards providing better mixing and atomization.

1.2.2 Swirl – Coaxial Element Design

Much like the shear – coaxial element, the swirl – coaxial element flows liquid oxidizer through a central post, and then subjects the exiting liquid to shearing annular gas flow. However, instead of the liquid being injected axially into one end of the post, the fluid is introduced by a series of short orifices tangent to the post's centerline. Figure 1.4 shows the general fluid circuits of a swirl – coaxial element.

Liquid enters tangential orifices at the post's end, and has a tangential velocity component (V_{tang}) as well as an axial component (V_{ax}). The tangential velocity imparts a

swirling motion upon the liquid, causing a finite thickness of swirling liquid film to form inside the post.

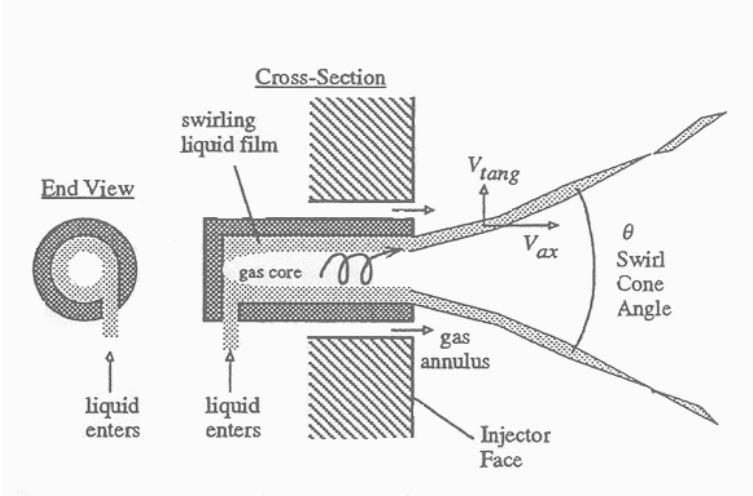

Figure 1.4 Swirl – coaxial element spray features [32]

A gas core is formed in the center to fill the vacuum left by the thinning film. The swirling liquid film moves axially down the post and exits at the injector as a thin conical sheet with a free cone spray angle, θ. The liquid cone's sheet thickness continues to thin as the flow moves downstream of the element tip, until finally the sheet begins to break up into liquid ligaments and droplets. This distance downstream of the element tip is known as the primary breakup length, and has a cone angle different from the free cone spray angle. This angle is called the chamber spray angle and is a function of chamber pressure and upstream spray conditions [33].

Advantages of swirl – coaxial elements are numerous, especially when compared to an equivalent shear – coaxial element [20]. The thinning sheet of the swirling liquid provides increased liquid surface thus increasing mixing efficiency over the shear –

coaxial jet. The thinning conical sheet self-atomizes more readily than a liquid jet and has increased atomization quality and subsequent combustion efficiency. The gas core within the liquid post can act as an acoustic damper to control combustion instabilities potentially occurring within the thrust chamber itself. Fabrication tolerance can be less strict than shear – coaxial element tolerances, and still have good mixing and atomization characteristics.

Swirl – coaxial elements are not without their shortcomings. The tangential orifices require added pressure drop from the propellant delivery system. Improperly designed swirl elements can lead to flow intensity and mixture ratio non-uniformity around the spray's circumference. These non-uniformities contribute to poor combustion efficiency within the thrust chamber. Wide spray angles give the possibility of spray-to-wall impingement, reducing chamber life from erosive burning of the chamber wall. Finally, none of the swirl element design methods published have been verified to work with changing mass flow rate and chamber pressure operation.

Compared to the shear-coaxial database, swirl injector development heritage is considerably smaller. In the United States, only the RL-10A-3 engine has used a swirl-coaxial injector [5]. Inside the element, the LOX flow is swirled by a solid ribbon placed inside the post. The ribbon swirl injector did not operate as effectively as the tangential slot design used by current injector designers. A large amount of swirl injector research and development has occurred in the former Soviet Union, but much of this work is focused on hot-fire testing as opposed to swirl injector spray features. As noted by Heister [30], proper understanding of basic spray features can lead to optimal coaxial

injector design relations. The fundamentals of the liquid swirl spray features must first be understood in order for swirl – coaxial elements to be designed properly.

1.3 Swirl Injector Element Fluid Mechanics

Swirl injector fluid mechanics have been reviewed by several research groups. A comprehensive review and comparison of the various analytical frameworks has been presented by Khavkin [34]. These groups included Yule and Chinn [35], Bayvel and Orzechowski [36], Abramovich [37], and Bazarov [20]. Khavkin concluded that each swirl theory reviewed had no distinct advantage over one another, especially compared to the simplest theory given by Abramovich. Abramovich's theory uses many of the same simplifying assumptions as the other theories do, with emphasis on developing a set of relations for inviscid, ideal swirling flow. These assumptions are

1) Inviscid flow.
2) Constant angular momentum.
3) Working fluid is considered incompressible.
4) Gravity forces are deemed negligible.
5) Radial component of liquid velocity is negligible.

The Bazarov design methodology uses similar assumptions as Abramovich to theoretically describe the swirl injector fluid mechanics. In contrast to Bazarov's theoretical relations, Doumas and Laster's design method is largely grounded in

empirical data, and includes viscous flow effects. Comparisons of these two methodologies will be continually made throughout this work. The following subsections will review global swirl injector fluid mechanics theory and past empirical observations of swirl injector flow features.

1.3.1 Global Analysis

A comprehensive review of swirl theories that Khavkin presented compared analytical work done by several research groups [34]. Bazarov's theory will now be explored through a broad derivation of the relevant formulas in order to define important swirling flow features of interest. The reader is encouraged to review the detailed derivation by Bazarov [20]. The Abramovich assumptions listed earlier are made here.

Figure 1.5 below gives the general diagram as used by Bazarov for his derivations. Many of the variables in Figure 1.5 simply serve as intermediate terms such that the final equations will only be functions of a few variables. The first equation relates the total pressure drop through the swirl element to the total fluid exit velocity for incompressible flow.

$$\Delta P = P_f - P_c = \frac{1}{2}\rho_l V_\Sigma^2 \tag{1.1}$$

The total velocity consists of three components: axial (U_a), tangential (U_u), and radial (U_r). Solving Equation (1.1) for the total velocity component and neglecting the radial velocity gives Equation (1.2).

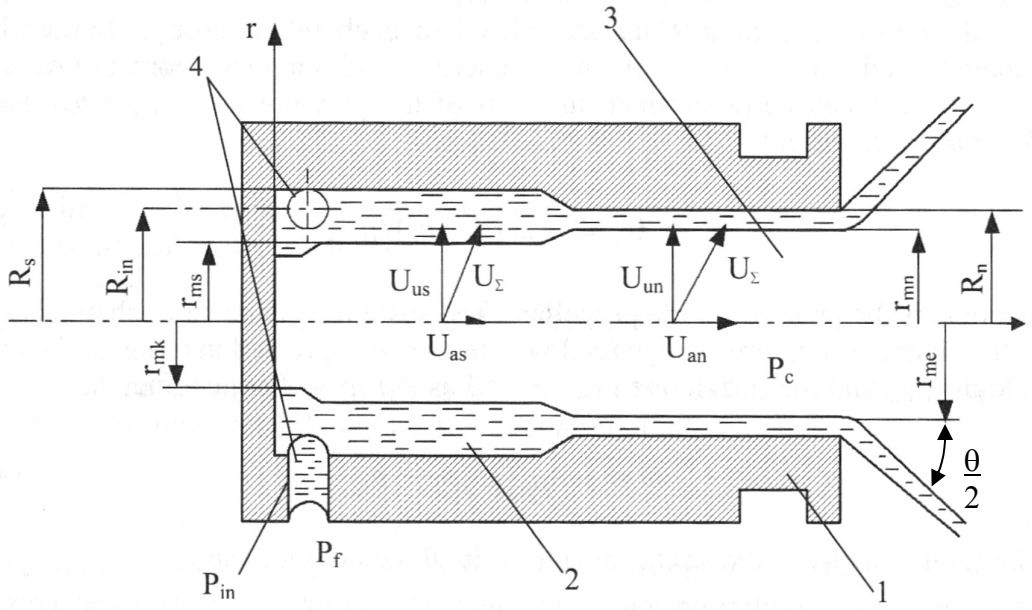

Figure 1.5 Swirling flow variables used in Bazarov analysis [20]

(1-injector casing; 2-vortex chamber; 3-nozzle passage; 4-tangential passages)

$$V_\Sigma = \sqrt{2\Delta P / \rho_l} = \sqrt{U_a^2 + U_u^2} \tag{1.2}$$

Equation (1.2) is true for any point along the swirl chamber including within the vortex chamber and in the length of the nozzle. The mass flow rate of liquid moving through the swirl element is constant, with the general form of Equation (1.3).

$$\dot{m}_l = \rho_l V_\Sigma A_{eff} \tag{1.3}$$

In Equation (1.3), A_{eff} is the effective cross-sectional area through which the liquid is moving through.

At the nozzle section of the swirler, the maximum effective area is the nozzle cross-sectional area. The ratio of the actual mass flow rate in the nozzle section to the ideal maximum mass flow rate in the nozzle section is the mass flow rate discharge coefficient, C_D.

$$C_D = \frac{\rho_l U_{an} A_{eff}}{\rho_l V_\Sigma A_n} = \frac{\rho_l U_{an} A_n \alpha}{\rho_l V_\Sigma A_n} = \frac{U_{an} \alpha}{V_\Sigma} \tag{1.4}$$

In Equation (1.4), the actual mass flow rate moving axially down the nozzle is the product of the liquid density, axial velocity component, and the effective liquid flow area. The maximum liquid flow area possible is the nozzle cross-sectional area, used in the denominator. For swirl injectors the nozzle cross-sectional area is only partly filled by liquid, so the area fullness coefficient is introduced as the ratio of liquid flow area to nozzle cross-sectional area. For a circular nozzle exit, the area fullness coefficient is be defined as Equation (1.5).

$$\alpha = \frac{A_{eff}}{A_n} = \frac{\pi(R_n^2 - r_{mn}^2)}{\pi R_n^2} = 1 - \left(\frac{r_{mn}}{R_n}\right)^2 \tag{1.5}$$

If the fluid at the exit has a film thickness t, then the film thickness is defined as

$$t = R_n - r_{mn} \tag{1.6}$$

Substituting Equation (1.6) into Equation (1.5) gives Equation (1.7).

$$\alpha = 1 - \left(\frac{R_n - t}{R_n}\right)^2 = 1 - \left(1 - \frac{t}{R_n}\right)^2 \tag{1.7}$$

The ideal free cone spray angle, θ, is defined as the vector angle between the tangential and axial velocity components at the nozzle exit.

$$\tan\left(\frac{\theta}{2}\right) = \frac{U_{un}}{U_{an}} \tag{1.8}$$

A convenient grouping of geometric parameters is the geometrical constant A defined as Equation (1.9). This grouping uses the nozzle diameter as a normalizing length, and the nozzle cross-sectional area as a normalizing area. A groups the total tangential inlet cross-sectional area, the nozzle area, the tangential inlet diameter, and the nozzle diameter. It will be shown in Chapter 5 how A is created during the analytical derivation process.

$$A = \frac{2R_s D_n}{N_s D_s^{\,2}} \tag{1.9}$$

With the use of the geometrical constant defined in Equation (1.9), the area fullness coefficient, and the definition of discharge coefficient in Equation (1.4), it can be shown that the discharge coefficient is written as Equation (1.10) [20].

$$C_D = \frac{1}{\sqrt{\frac{A^2}{1-\alpha} + \frac{1}{\alpha^2}}} \tag{1.10}$$

Common to both Bazarov's and Abramovich's theories is the principle of maximum consumption, which is now applied to Equation (1.10). In general, this principle states that the gas core in the center of the swirling flow will establish a certain diameter of $2r_{mn}$, as to maximize the liquid consumption, or mass flow rate. This maximum liquid consumption is seen by maximizing the discharge coefficient at the nozzle exit. The gas core diameter is represented through the area fullness coefficient, and the maximum value of the discharge coefficient can then be found by setting the partial derivative of Equation (1.10) equal to zero.

$$\frac{\partial C_D}{\partial \alpha} = 0 \tag{1.11}$$

Application of Equation (1.11) to Equation (1.10) gives a value of A, which then can be substituted back into Equation (1.10) to find the maximum discharge coefficient.

$$C_D = \alpha\sqrt{\frac{\alpha}{2-\alpha}} \tag{1.12}$$

Equation (1.10) is plotted in Figure 1.6 for different values of geometric constant and fullness coefficient. For each value of geometric constant, there is a subsequent global maximum value of the discharge coefficient. These maximum values are correspondingly defined in Equation (1.12), also plotted in the same figure.

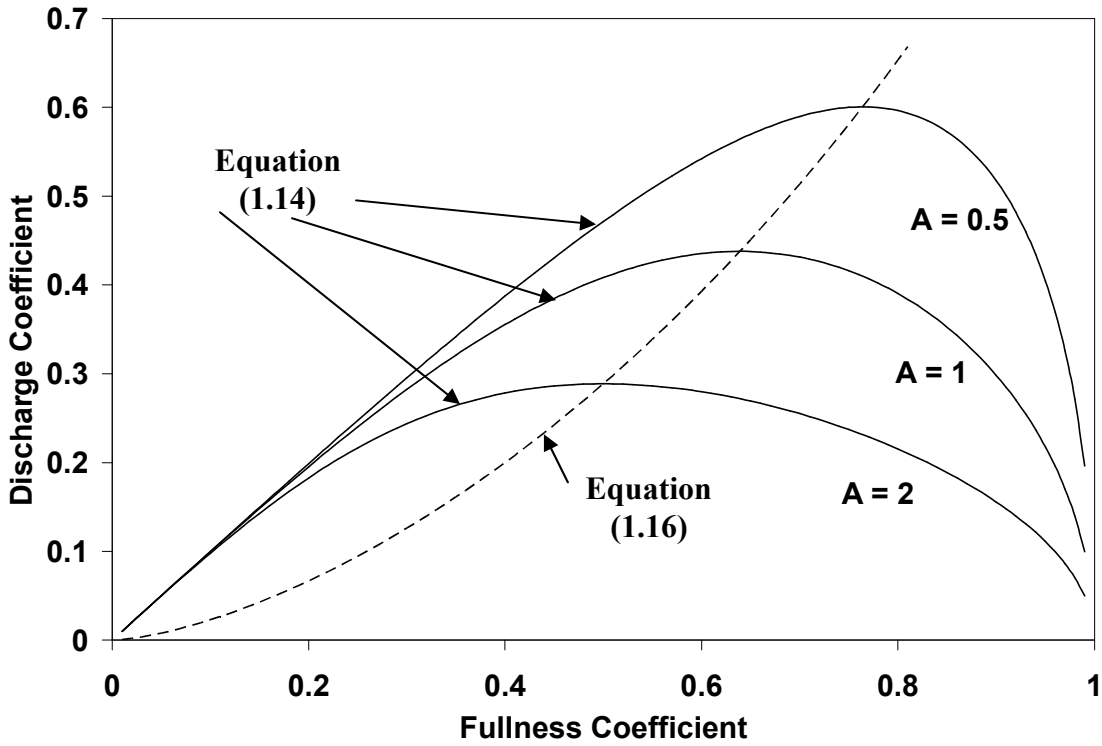

Figure 1.6 Discharge coefficient variation with fullness coefficient and geometric constant

Using Equation (1.12) and relations between the axial and tangential velocity components, Equation (1.8) can be written as Equation (1.13).

$$\tan\left(\frac{\theta_n}{2}\right) = \sqrt{2\left(\frac{1-\alpha}{\alpha}\right)} \tag{1.13}$$

This angle is actually the vector angle between the axial and tangential velocity components of the swirling flow right at the injector exit. To relate the injector exit angle to the actual free cone spray angle, Bazarov uses an additional variable, *a*, that is the ratio of the gas core cross sectional area at the top of the vortex chamber to the nozzle cross sectional area. This variable is defined as Equation (1.14) and the corresponding free cone spray angle definition is given as Equation (1.15).

$$a = \frac{2(1-\alpha)^2}{(2-\alpha)} \tag{1.14}$$

$$\tan\left(\frac{\theta}{2}\right) = \sqrt{\frac{a}{1-a}} \tag{1.15}$$

Thus, the discharge coefficient and the free cone spray angle are theoretically only functions of the area fullness coefficient, which is only a function of the average nozzle film thickness and nozzle radius.

1.3.2 Swirl Features: Observations and Correlations

Swirl features include overall spray morphology, inner film thickness, and the spray cone angle at a given point downstream of the element tip. Each of these features will be discussed individually in the following subsections.

1.3.2.1 General Morphology

The term 'general morphology' refers to the overall structure of the swirling spray as it exits the nozzle. The general form of a swirling sheet is much like that of a cone. However, this cone structure is only true for injection pressure drops in the high to mid range of swirler operation. At lower injection pressure drops, the cone structure begins to change due to surface tension forces overcoming injected liquid momentum. This change was visually investigated by Ramamurthi and Tharakan [47]. They investigated the effect of individual geometry changes and mass flow rate to the overall profile of the swirling sheet. The swirling sheet was issued into open, atmospheric air. It was seen that as the mass flow rate was increased from zero, the structure of the swirling sheet moved through several shapes, or morphologies, that influenced how the sheet atomized. These morphologies are also noted by Khavkin [34] and Lefebvre [22] and shown graphically in Figure 1.7.

Further work by Ramamurthi and Tharakan [48] defined discrete flow regimes where an injected swirling spray transitioned from Tulip stage to a cone-shaped stage.

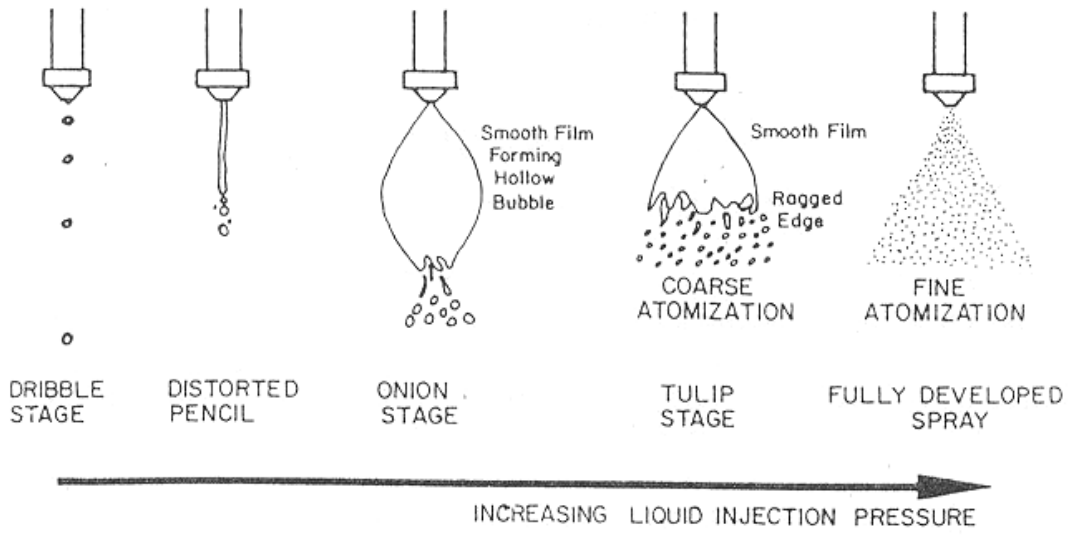

Figure 1.7 Liquid swirling spray morphologies [22]

(Reprinted with permission)

This boundary was defined in terms of Weber and Reynolds numbers based on the axial components of the injected sheet velocity and the exit film thickness of the spray. Using the previous experimental data from Ref. [47], Ramamurthi and Tharakan found that the Weber number was actually better in setting a distinct boundary between Tulip and Cone stages for the spray. In addition to the experimental work, theoretical analysis was used to evaluate the stability behavior of the swirling sheet upon injection. The general finding was that even though the swirling sheet was unstable for all mass flow rate, the growth of disturbance waves was much higher within the Cone stage region of operation, as opposed to the Tulip stage.

This finding was later confirmed by Ghorbanian using the same techniques [49]. It was shown that the free cone spray angle was a minimum in the Onion stage, and increased with increasing swirler pressure drop. This trend lasted until the Tulip stage

was reached and the free cone spray angle was deemed independent of pressure drop. These findings showed how the injected pressure drop changed the morphology and subsequent fluid mechanics (i.e., sheet breakup length). The effect of ambient gas pressure on spray morphology was not included in these studies.

Work performed by Rahman [50] looked at similarity considerations of swirling flows. Rahman looked at the droplet distribution behavior for a LOX/GH2 swirl-coaxial injection element, beginning with water/GN2 cold flow experiments at ambient conditions. Although Rahman focused extensively on droplet characterization with inert and reacting propellant, some qualitative observations of intact-length features were made for just swirling water flow.

Rahman fabricated a geometrically doubled- scaled injection element to help determine similarity relations. Rahman chose the Weber number based on the predicted film thickness to define similarity between the two element sizes. In order to maintain the same Weber number in the double scale element, the total injection velocity was lowered by way of the mass flow rate. Rahman observed that the two spray fields gave approximately the same breakup lengths when normalized by the nozzle film thickness. The issuing free cone spray angles were also deemed equal. Element testing was only conducted at design mass flow rate and atmospheric gas pressures.

1.3.2.2 Film Thickness and Free Cone Spray Angle

Swirl design methods use average film thickness and free cone spray angle as ‘cornerstone’ values in the swirl injector sizing process. These values are based on

injector operation at full flow conditions. This section will look at findings for film thickness and free cone spray angle behavior since they are commonly related to each other. A more detailed review on the inner swirling flow itself is presented in a following section.

Simmons and Harding [51] derived a semi-empirical relation for film thickness as a function of geometric and operational parameters. This relation is given as Equation (1.16), with all variables being in units (kg-m-sec-Pa).

$$t = 0.00805 \frac{\dot{m}_l}{\sqrt{\Delta P} D_n \cos(\theta/2)} \tag{1.16}$$

This relation was derived for the full flow operating point of a given swirler and neglects effects from changing injection pressure drop.

Lefebvre and Rizk investigated the film thickness and free cone spray angle changes with swirler geometry and operation [52]. Semi-empirical derivation was first used to find a relation between free cone spray angle, film thickness, and swirler parameters. This relation is given as Equation (1.17).

$$\left(\cos\left(\frac{\theta}{2}\right)\right)^2 = \frac{12\dot{m}_l \mu_l \, A/B}{\pi \rho_l D_n \Delta P t^2 (1 - X)} \tag{1.17}$$

In Equation (1.17), the empirical constant of A/B was found to be 400 for liquid sprays issuing into atmospheric environments. X is the ratio of the gas core area to the nozzle area. It is defined by Equation (1.18) for circular cross sections.

$$X = \left(\frac{D_n - 2t}{D_n} \right)^2 \tag{1.18}$$

Equation (1.19) shows that this ratio is also related to the area fullness coefficient.

$$\alpha = 1 - \left(\frac{R_n - t}{R_n} \right)^2 = 1 - X \tag{1.19}$$

Using work performed by Giffen and Muraszew [53], Rizk and Lefebvre derived Equation (1.20) as an additional expression for the free cone spray angle.

$$\left(\cos\left(\frac{\theta}{2} \right) \right)^2 = \frac{1 - X}{1 + X} \tag{1.20}$$

Equations (1.17) and (1.20) were set equal to each other and solved for the film thickness at the injector tip

$$t^2 = \frac{1560 \dot{m}_l \mu_l}{\rho_l D_n \Delta P} \frac{1 + X}{(1 - X)^2} \tag{1.21}$$

Equation (1.21) gave good agreement when compared with experimental data from a number of atmospheric tests. Since Equation (1.21) was noted as having to be implicitly solved for film thickness, the form was empirically replaced by Equation (1.22).

$$t = 3.66\left(\frac{D_n \dot{m}_l \mu_l}{\rho_l \Delta P}\right)^{0.25} \tag{1.22}$$

Equation (1.22) showed good agreement with the compared experimental results, while also having the benefit of being explicit in film thickness. The empirical constant of 3.66 was later suggested to be changed to 2.7 [54], in order to account for averaging effects of film thickness measurements.

Suyari and Lefevbre looked experimentally at the film thickness for a simple swirl injector, with emphasis on developing newer theoretical models. Using the work by Giffen and Muraszew [53], along with work discussed previously by Rizk and Lefevbre [52], Suyari and Lefevbre [54] derived the following expression for the ratio X that was defined as Equation (1.23).

$$0.09\left[\frac{N_s \pi/4 D_s^2}{D_{vc} D_n}\right]\sqrt{\frac{D_s}{D_n}} = \frac{(1-X)^3}{1+X} \tag{1.23}$$

This expression defined the ratio X, and the corresponding film thickness, as being functions solely of swirler geometry. Film thickness measurements were obtained by placing two electrodes within the swirler nozzle. The swirling flow of water made contact with the electrodes, creating a closed circuit. As the film thickness grew or shrank, the amount of voltage across the two electrodes needed to maintain a constant current was measured. The change in voltage was then calibrated to certain levels of film thickness. Using this technique, the film thickness was measured over a variety of

swirler mass flow rate (up to 2.02 gm/s) and tangential slot diameters (0.76 mm to 1.35 mm). The experimental results collected were compared to Equations (1.16) and (1.22) for prediction accuracy. Equation (1.22) showed excellent agreement to the data, while Equation (1.22) showed less satisfactory results.

1.3.2.3 Spray Angle

Figure 1.8 shows three kinds of spray angles defined by Hulka and Makel [33], also defining what variables influence these angles. The free cone spray angle represented in Figure 1.8 as the oxidizer free swirl angle, θ, has been discussed previously as being a function of internal swirl injector geometric and flow properties. These properties include internal film thickness, injector pressure drop, and nozzle diameter. The free cone spray angle is considered not a direct function of chamber pressure. The momentum angle, α, is a function of the interaction between the swirling liquid sheet and the coaxial gas. The spray angle, ϕ, is a function of the upstream free cone spray angle, chamber pressure, and the injected liquid momentum. Hulka and Makel noted that this angle is influenced by gas entrainment as the swirling spray moves downstream of the injector. This gas entrainment causes the spray to decrease in overall cone angle relative to the free cone spray angle.

DeCorso and Kemeny studied the effects of ambient gas pressure on swirling flows at fuel flow rate up to 0.11 kg/s [55]. The spray was issued into a high-pressure tank limited to ambient nitrogen gas pressures up to 0.79 MPa.

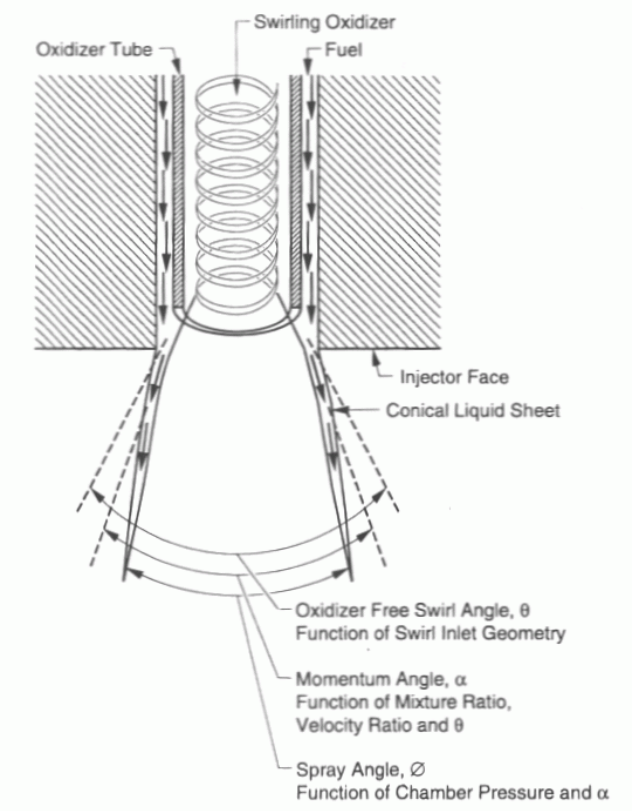

Figure 1.8 Swirling spray angles within a pressurized chamber [33]

(Reprinted with permission)

The radial spray pattern was measured with an angled mechanical patternator at 113 mm downstream of the injector tip. Measured spray angles were normalized by the spray angle values at the same flow rate and atmospheric conditions. The collapsed data showed a trend of decreasing normalized spray angle with the increase of the variable $\Delta P \rho^{1.6}$, where ΔP is the injection pressure in psi and ρ is the ambient gas density in lbm/ft^3.

Dodge and Biaglow [56] researched the influence of ambient gas temperature and pressure on a fuel swirl atomizer with a design free cone spray angle of 80 deg. The test chamber consisted of a large stainless steel pipe with quartz windows mounted on the walls for optical access. Air was the ambient gas, with the operating range of up to 1090 K and 1.62 MPa. The swirler mass flow rate was kept at a constant, full flow value for the majority of experimentation. Downstream cone angles were measured at 9.9 mm away from the nozzle exit. The data showed that the air temperature has very little effect on the chamber angle, with only the ambient gas pressure showing any real influence. The chamber angles were correlated with the ambient gas density and referenced from the measured spray angle at atmospheric conditions. This correlation is given as Equation (1.24).

$$\theta = 79.8 - 0.918\left(\frac{\rho_g}{\rho_{go}}\right) \tag{1.24}$$

ρ_g is the ambient gas density and ρ_{go} is the ambient gas density at atmospheric conditions.

Ortman and Lefebvre investigated the effects of liquid injection pressures and ambient gas pressures on the radial distribution from a liquid swirler [57]. Radial patternator studies were conducted with a number of simplex swirl atomizers that were flowed within a pressurized cold flow facility. The ambient gas pressures were ranged from atmospheric up to 0.7 MPa, and swirl injectors used ranged in liquid flow rate from 1.8 to 3.0 gm/s. The authors agreed with DeCorso and Kemeny that $\Delta P \rho^{1.6}$ normalized

chamber angle data for similar test conditions. Ortman and Lefebvre also found that as the ambient gas pressure was increased towards 0.7 MPa, the change in chamber angle diminished, implying a limit from ambient gas pressure influence. This observation was later confirmed qualitatively by Hautman for swirl-coaxial injectors at liquid flow rate up to 1.8 kg/s and ambient gas pressures up to 3.6 MPa [58].

No coaxial gas flow is considered in this work, so the momentum angle defined by Figure 1.8 is not considered. The free cone spray angle is considered the theoretical angle predicted from a given swirl injector element design method. The spray angle in Figure 1.8 is considered the measured angle in this work. Differences between the free cone spray angle and the measured spray angle will be addressed in this work.

1.3.3 Internal Flow

The internal flow structure of the swirling liquid consists of both interior tangential and axial velocity components, and the film thickness. The vector angle between the tangential and axial velocity components is defined as the helical angle. Traditional swirl design methods do not factor in any spatial changes in film thickness, velocity components, or helical angles along the swirl vortex chamber and nozzle lengths. However, experimental measurements have shown the internal structure of swirling flows do change along the swirl vortex chamber and nozzle lengths. Bazarov [20], Hutt [31], and Cooper and Yule [38], have suggested several flow effects to explain these spatial changes, discussed in the subsections below.

1.3.3.1 Flow Striations

Hutt observed that the film thickness profile exhibited spatially stationary variations along the nozzle length [31]. These variations have been also documented by Cooper and Yule, who showed a decrease in helical angle as one moved axially downstream in the vortex chamber [38]. The film thickness also exhibited changing values with vortex chamber axial station, giving a helical structure that was related to the number of tangential slots. For the swirler in Cooper and Yule's work, the number of tangential slots was either two or eight, which gave a helical structure of either two or eight striations on the liquid surface, respectively. These striations were spatially resolute, as determined by high speed video observations. Figure 1.9 gives a notional diagram of how these striations are formed from an injector with three tangential inlet slots.

1.3.3.2 Viscous Effects

Both Hutt's and Yule's work showed that viscous losses influence the flow such that inviscid theory needs correction to properly predict internal helical angles and film thickness. Increasing the swirler length, whether in the vortex chamber or nozzle, will further increase friction losses and reduce helical angles while increasing inner film thickness. Bazarov's swirling flow relations have considered the effect of wall viscosity on the liquid swirling flow as a global increase in the average film thickness value [20].

However, Bazarov's viscous effects treatment does not define the spatial change of film thickness profile due to viscosity.

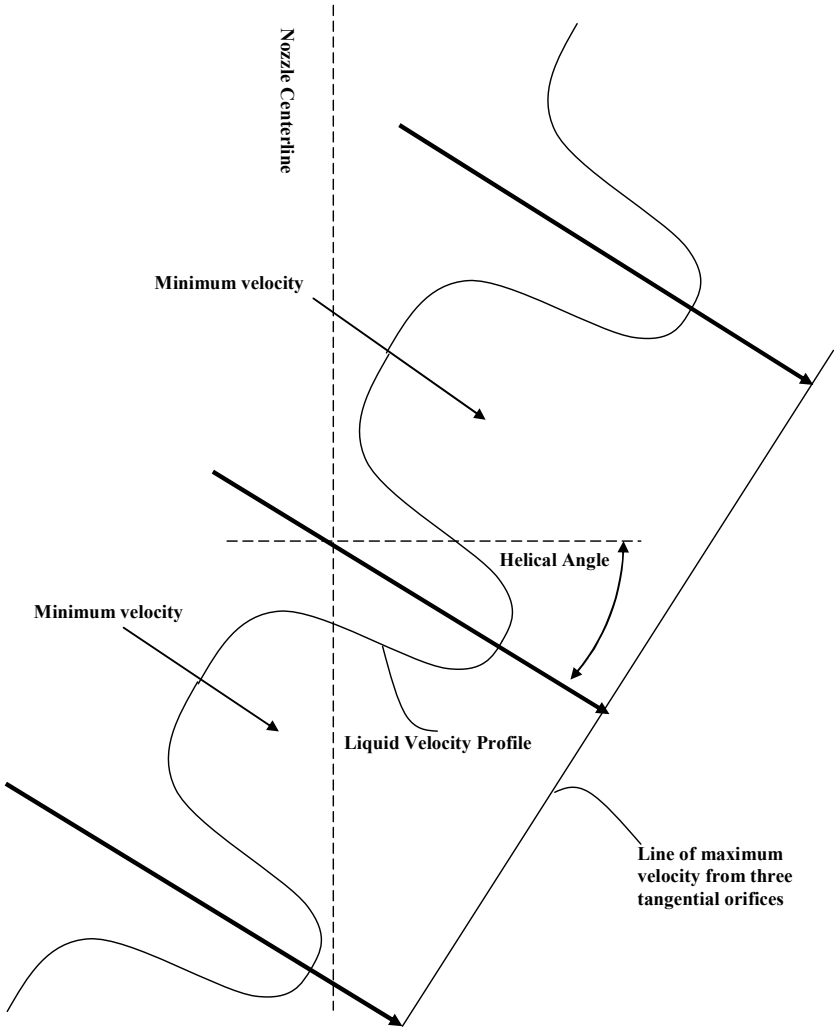

Figure 1.9 Internal swirling flow profile with flow striations

1.3.3.3 Skobelkin Effect

Hutt's [31] and Cooper and Yule's [38] measurements have shown that as the flow approaches the nozzle exit, the local film thickness values decreases on order of 20% relative to the average film thickness along the nozzle. Bazarov explains that the film thickness decreases close to the nozzle exit is due to the Skobelkin effect [20]. As the flow reaches the exit, the energy associated with the centrifugal pressure is transferred to the axial momentum of the flow, increasing axial velocity and decreasing the liquid flow area due to continuity. As the flow area decreases, the film thickness decreases.

1.3.3.4 Flow Criticality

Both Yule's and Hutt's works showed that the helical structure of the swirling flow is spatially stationary. Hutt has claimed that the flow reaches a supercritical state within the vortex chamber [31]. The accepted measure of the flow's criticality is the local Froude number. This number is a ratio between the axial mean velocity and the surface wave speed along the inner vortex core. Much like the Mach number, a flow is supercritical when the Froude number is greater than unity, and subcritical if the Froude number is less than unity.

Discussions of supercritical flows in literature focus on open-channel flow through weirs [44]. However, some work does exist for flows down cylindrical tubes. A large portion of this work is from Binnie [39], [40], [41], [42], [43], who looked at swirling water flow down clear plastic tubes of varying geometry. Swirl was imparted to

the water by two tangential entry ports at the tops of the cylindrical tubes. Initially, Binnie derived the tangential and axial wave speeds for a disturbance propagating along the inner gas core [39]. These wave speeds were used to define the Froude number for the axial and tangential mean velocities. Binnie related the wave speeds to the mode number of the tangential and axial disturbances, and found that the swirling flow will assume an n-threaded helical structure for n tangential modes.

By his calculations, Binnie showed most of his experimental flows were introduced at a supercritical state [40], [41], [42], [43]. As the mean velocity components were reduced due to friction, the flow transitioned from a supercritical to subcritical. This situation is analogous to Fanno flow for gas motion in pipes [44]. This transition is seen visually as a hydraulic jump, common in open-channel flows [44]. A sudden increase and wider spatial variance in film thickness is associated with these jumps. Binnie used a number of methods to create a hydraulic jump in the flow, including adding a 90° bend at the end of the pipe. This bend created a flow resistance to the axial velocity. At lower mass flow rate, a hydraulic jump was formed inside the vertical section of the pipe upstream of the bend. The structure consisted of a swirling vortex, then a jump where a large increase of film thickness was recorded. Static wall pressure taps measured a large increase in fluid pressure at the jump location. Downstream of the jump, the flow structure became helical and spatially stationary. However, the jump moved downstream around the bend and was eventually 'pushed out' of the pipe above a certain mass flow rate.

Sarpkaya [45] qualified hydraulic jumps as vortex breakdown 'bubbles.' Once these bubbles were established, the flow upstream remained relatively insensitive to

downstream changes; much like a shock wave created within a converging-diverging nozzle. Generally, for low circulation (or tangential velocity component), increasing the Reynolds number moved the vortex breakdown bubble upstream. For a fixed Reynolds number, lowering circulation worked to move the breakdown downstream, and vice-versa.

Historical swirling flow research has not considered ambient pressure effects on vortex breakdown formations, but a more recent review done by Shtern and Hussain [46] makes the following observation: moving the swirling flow against an axial pressure gradient can require pressure recovery via a vortex breakdown because the vortex core pressure along the vortex centerline is less than the ambient pressure. The swirling motion of the flow creates a radial pressure gradient, causing the centerline static pressure along the vortex to be less than ambient pressure. The centrifugal force created by tangential momentum balances this radial pressure gradient. For a fixed amount of total flow momentum, more tangential momentum needed to balance out the radial pressure gradient means less axial momentum available to move the flow against the axial pressure gradient. The axial pressure gradient can increase with increasing chamber pressure and potentially cause axial flow recirculation within the liquid flow. This axial flow recirculation is considered the vortex breakdown phenomenon. Thus, the possibility of vortex breakdown existence in a swirl injector element is a primary topic in this work.

1.4 Research Plan

Much material has been covered in this chapter, so it is useful to review the conclusions made in preparation for defining a cohesive research objective. This work's research objective and the associated research plan will be presented in this section.

1.4.1 Review of Findings

With respect to the material reviewed in this chapter, findings are as follows:

- Liquid rocket engine (LRE) performance is extremely sensitive to the quality for the propellant injection and combustion process within the LRE thrust chamber [3].
- While a full-scale LRE injector consists of many injection elements, typical injector designs are begun by focusing on a single element. Therefore, it is essential to understand the single element's behavior prior to assembling multi-element injectors [17].
- Test and development procedures for LRE single elements can include a preliminary series of cold flow studies to assess injector spray features. These spray features influence the behavior of the reacting flow field [30].
- A common propellant combination used for high thrust engines is LOX/GH2. Historical LOX/GH2 injection elements have been shear – coaxial. This element

type has a large heritage of research work that can be drawn from to aid in element design [31].

- Relative to shear – coaxial elements, swirl – coaxial elements has a smaller research history. The design features of interest for a swirl – coaxial spray, which are grounded in the fluid mechanics of the liquid swirl process itself, are based on data from low pressure, low mass flow rate experiments. The influence of high ambient pressures and varied mass flow rate on internal and external swirl features needs to be investigated.

1.4.2 Statement of Problem

This work investigates both internal and external spray features of a liquid swirl injector as a function of varying ambient pressure and liquid flow rate. Film thickness inside the injector will be measured directly through image analysis. Discharge coefficient of the injector will be calculated from flow measurements. Sheet boundaries and spray cone angles downstream of the injector will be measured directly through image analysis. Ambient pressure on order of liquid rocket engine operation captures internal and external gas environmental effects on the spray. Liquid flow rate will be varied down to approximately 15% of the design flow rate value to represent variable thrust engine operation.

1.4.3 Research Approach

1. A dimensional analysis of the atomization process for a swirled liquid sheet has been performed. Important independent parameters have been identified and used to understand physical implications of changing mass flow rate and chamber pressure.
2. A swirl element has been designed, fabricated, then tested in a high-pressure cold flow chamber. Steady and unsteady phenomena have been measured and analyzed with respect to spray features reviewed earlier.
3. Empirical correlations describing the behavior of measured spray features have been developed using the results from the dimensional analysis.
4. The design methodology used to design the swirl injector has been revisited and updated to include several new parameters. These parameters have been identified in the literature as relevant to swirl injector flows and offer increased fidelity to the design methodology. The results from this work have been assessed using the updated design methodology, and the implications assessed for the swirl injector design engineer.

CHAPTER 2

EXPERIMENTAL HARDWARE AND DIAGNOSTICS

2.1 Cold Flow Facility

The Water/Nitrogen Injector Spray Test Rig (WNIST), was selected for this work. It is located at the East Test Area of NASA Marshall Space Flight Center. WNIST uses cross country nitrogen gas (GN2) feed lines to operate hardware, pressurize the water supply tank, and pressurize the chamber. Figure 2.1 shows a picture of WNIST, with an associated profile view. The injector was fed from a 0.13 m^3 water run tank. The water tank can be pressurized using a GN2 feed line, giving water mass flow rate up to 0.45 kg/s. The water flow rate can be measured by a volumetric flow meter. The water fluid circuit from the supply tank to the chamber was monitored by several pressure transducers. All water temperatures were measured by type K thermocouples. The water flow rate was controlled by a variable position valve (VPV), which was pneumatically actuated by a current to pressure transducer. The water VPV, along with all other

actuated hardware, was remotely controlled in real-time by a Labview interface. An additional GN2 feed line supplied simulant gas for coaxial injector tests, but was not used in this work.

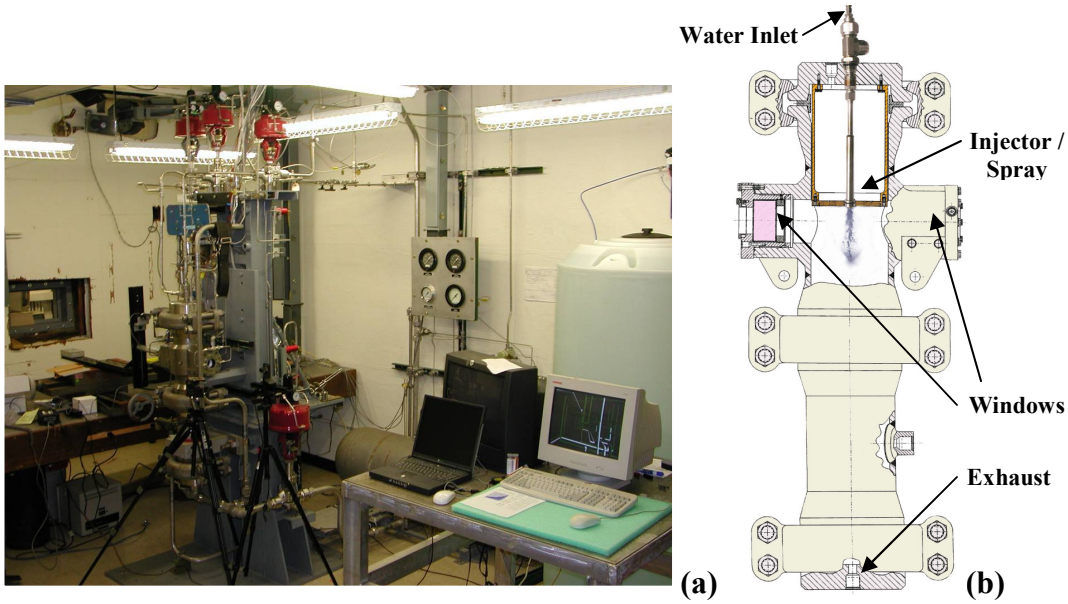

Figure 2.1 (a) WNIST facility and (b) WNIST operation schematic

The injected water spray entered a chamber pressurized by GN2 feed lines attached to port windows mounted opposite each other. These feed lines also acted to dry, or 'purge,' the chamber windows of any water splatter. The GN2 supply was heated in a hot water bath prior to reaching the windows. The system could raise the GN2 temperature up to about 100°C to counteract against Fanno flow cooling. The chamber pressure could be regulated up to 9.65 MPa, but only 4.83 MPa was used in this work.

Chamber and window purge pressures and temperatures were monitored by static pressure transducers and type K thermocouples, respectively. The combination of water and GN2 was exhausted through a set of VPV's. These valves were controlled in real time by a feedback loop to maintain a desired chamber pressure. After passing through the exhaust lines, the water/GN2 mix was vented outside of the facility building. Appendix A describes the operating procedure for the WNIST facility in detail.

All measurements were recorded electronically through an acquisition program. This program recorded data at 50 samples / sec, allowing for calculations of standard deviations and measurement repeatability. Using the measurement accuracies and repeatabilities, the systematic and random uncertainties were calculated and the total uncertainty for each measurement was found using methods outlined by Coleman [59]. The measurement uncertainty analysis is given in Appendix B, and the results are summarized in Table 2.1 for 95% confidence intervals. Optical diagnostic methods used during this work had their own uncertainty, and are presented in a case-by-case basis later in the next two chapters.

2.2 Swirl Injector Design

The swirl injector operating parameters were chosen to mesh with WNIST's capabilities. WNIST can provide up to 0.45 kg/s of water at atmospheric conditions, but running at this flow rate would only give five minutes of flow time from the run tank. An injector flow rate of 0.09 kg/s was chosen to allow approximately 25 minutes of run time before the run tank emptied. The design free cone spray angle was set at 50 degrees to

reduce spray impingement on the chamber walls, but still give a wide enough spray as to be able to image properly.

Table 2.1 WNIST measurement nominal ranges and uncertainties

Measurement	Device	Nominal Range	Accuracy (Systematic Uncertainty)	Repeatability (Random Uncertainty)	Total Uncertainty ($2U$)
Volumetric Flow Rate	Flow - Safe Flow Meter	0.03 – 0.32 m^3/hr (0.01 – 0.1 kg/s)	2% of reading	0.9% of reading	4.39% of reading
Temperature	Omega Type K Thermocouple	-200°C - 1250° C	0.75% of reading	0.14° C (max)	0.46° C (max)
Static Pressure	Setra Pressure Transducer	0.10 – 10.34 MPa	0.1% of reading	Reading Dependant	0.013 MPa (max)
Pressure Difference	Setra Pressure Transducer (2x)	0.10 – 10.34 MPa	0.1% of reading	Reading Dependant	0.016 MPa (max)

Figures 2.2, 2.3, and 2.4 show the internal and external operation of a swirling liquid sheet steadily issuing into a quiescent gaseous environment. The variables used to describe geometric, fluid, and flow features are listed in Tables 2.2 through 2.5.

The design processes for the swirl injection element are outlined in Appendix C. Both design procedures of Bazarov [20] and of Doumas and Laster [21] were used to size geometric features and predict spray properties. Table 2.6 gives a comparison of predicted injector parameters from these two methodologies. The fluid property values for water and GN2 were taken from NIST standards [60].

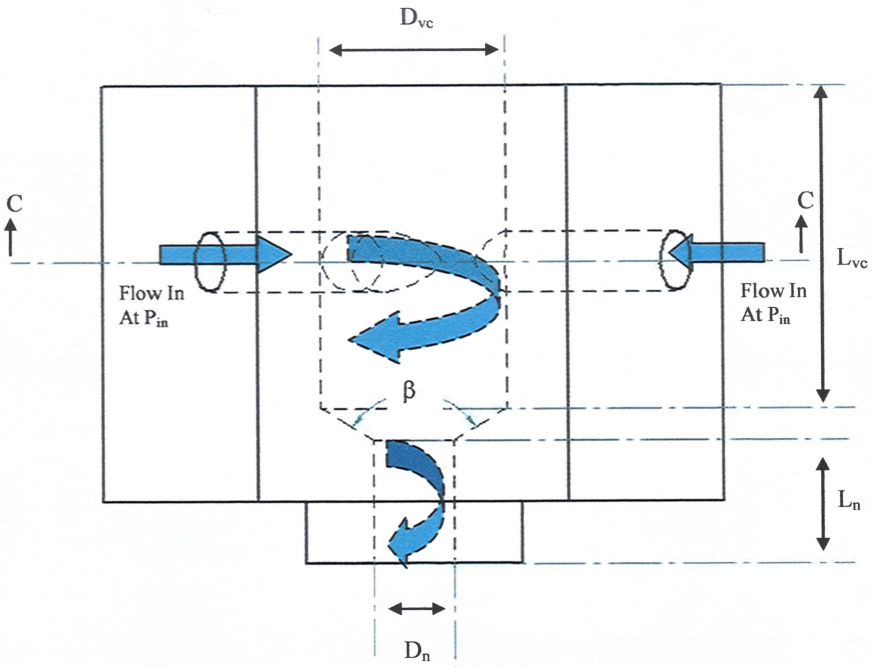

Figure 2.2 Profile view of swirl injection element

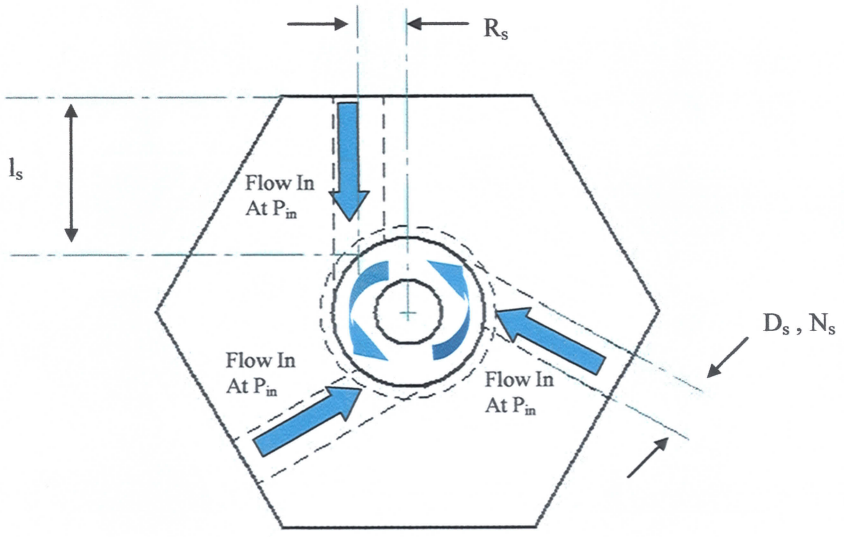

Figure 2.3 Top view (Section C-C) of swirl injection element

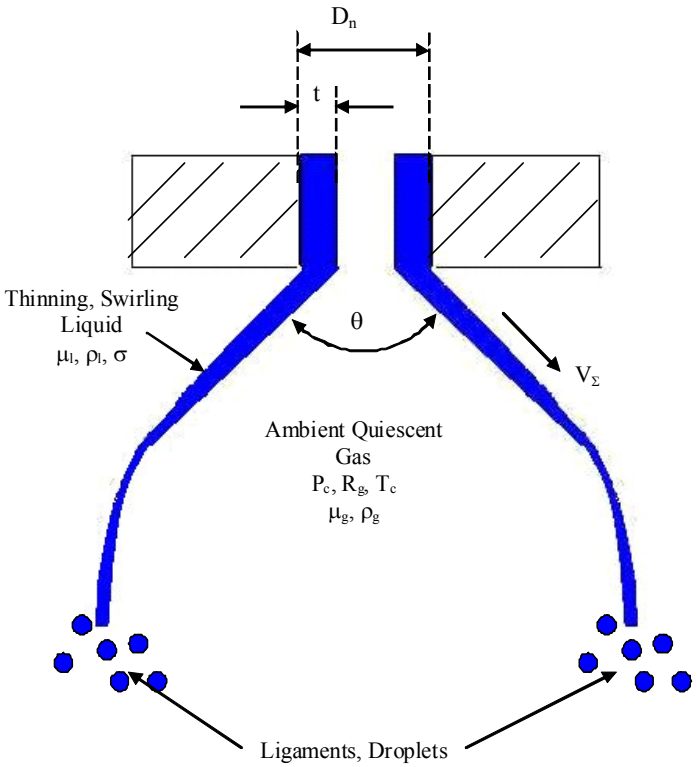

Figure 2.4 Spray features of swirl injection element

Table 2.2 Geometrical features of a liquid swirler

Tangential Slot Length	l_s
Tangential Slot Diameter	D_s
Radius from Slot Exit to Vortex Chamber Centerline	R_s
Number of Tangential Slots	N_s
Vortex Chamber Diameter	D_{vc}
Vortex Chamber Length	L_{vc}
Transition Angle	β
Nozzle Length	L_n
Nozzle Diameter	D_n

Table 2.3 Fluid properties of a swirling liquid sheet

Liquid Density	ρ_l
Liquid Viscosity	μ_l
Gas Density	ρ_g
Gas Viscosity	μ_g
Specific Gas Constant	R_g
Liquid / Gas Surface Tension	σ

Table 2.4 Flow properties of swirling liquid sheet

Liquid Inlet Pressure	P_{in}
Quiescent Gas Pressure	P_c
Quiescent Gas Temperature	T_c
Total Injection Velocity	V_Σ

Table 2.5 Spray properties of swirling liquid sheet

Film Thickness	t
Free Cone Spray Angle	θ
Discharge Coefficient	C_D

Variation of these properties with temperature and pressure were considered negligible, so the reported values were assumed constant throughout this work.

Table 2.6 Element operational and geometrical values

Design values	Design	Bazarov	Doumas and Laster
Mass Flow Rate (kg/s)	0.09	0.09	0.09
Pressure Drop (MPa)	-	1.65	2.06
Free Cone Spray Angle, θ (deg)	50	49.1	51.8
Tangent (Half Free Cone Spray Angle)	0.47	0.46	0.49
Film Thickness, t_n (mm)	-	0.43	0.40
Area Fullness Coefficient, α		0.66	0.62
Discharge Coefficient, C_D	-	0.46	0.41
Total Velocity Magnitude, V_Σ (m/s)	-	57.49	48.03
Tangential Orifice Diameter, D_o (mm)	-	1.56	1.56
Tangential Orifice Length, L_o (mm)	-	3.73	N/A
Number of Tangential Orifices, N_o	3	3	3
Radius from Orifices to Swirl Body Centerline, R_{in} (mm)	-	1.61	1.61
Vortex Chamber Diameter, D_{vc} (mm)	-	4.78	4.78
Vortex Chamber Length, L_{vc} (mm)	-	3.93	N/A
Transition Angle, β (deg)	118	118	118
Nozzle Diameter, D_n (mm)	-	2.08	2.08
Nozzle Length, L_n (mm)	-	3.12	N/A

Doumas and Laster's methodology does not give guidelines for calculating various swirl geometrical lengths. These include the orifice channel length, the vortex chamber length, and the nozzle length. Bazarov's guidelines generally direct the designer to make the orifice length approximately $l_s \sim 2.5D_s$, the vortex chamber length $L_{vc} \sim 5R_s$, and the nozzle length $L_n \sim D_n$. In order to have enough nozzle length for flow

visualization, the nozzle length built into the swirl body was extended by $6.71D_n$, to give a total nozzle length of $L_n = 7.71D_n$. This extended nozzle length will be discussed in more detail later in this section.

Table 2.6 only gives the mass flow rate for one value of pressure drop across the injector. Since this work will look at mass flow operation rate off the design point, it is important to know how the mass flow rate changes with injection pressure drop. Equation (1.4) gives the link between mass flow rate and pressure drop. This equation is accepted by both design methodologies, allowing both predictions to be graphed together on Figure 2.5. Also plotted on Figure 2.5 is the measured pressure drop versus mass flow rate for the fully-assembled swirl injector.

As seen in Figure 2.5, the Doumas and Laster prediction yields a higher pressure drop for a given mass flow rate than Bazarov's prediction. This shows a main difference between the two design methodologies: Bazarov's theory is inviscid and does not need empirical input to calculate values. Conversely, Doumas and Laster's design method is grounded in empirical input, but implicitly takes into account frictional losses of the liquid traveling through the swirler. This is why the Doumas and Laster prediction matches the measured data better than the Bazarov prediction. It is possible to modify the Bazarov prediction method to account for frictional losses, but for this work no modifications of the two methods will be used.

The injector setup consisted of three main parts, the water manifold, the swirl body, and the acrylic nozzle extension. The water manifold was a cylindrical cavity which water was delivered into via an AN male fitting. The fitting was attached to a set

length of stainless steel tubing, hung from underneath the top hub of WNIST. The cavity itself was a piece of 51 mm outer diameter tubing, 32 mm long.

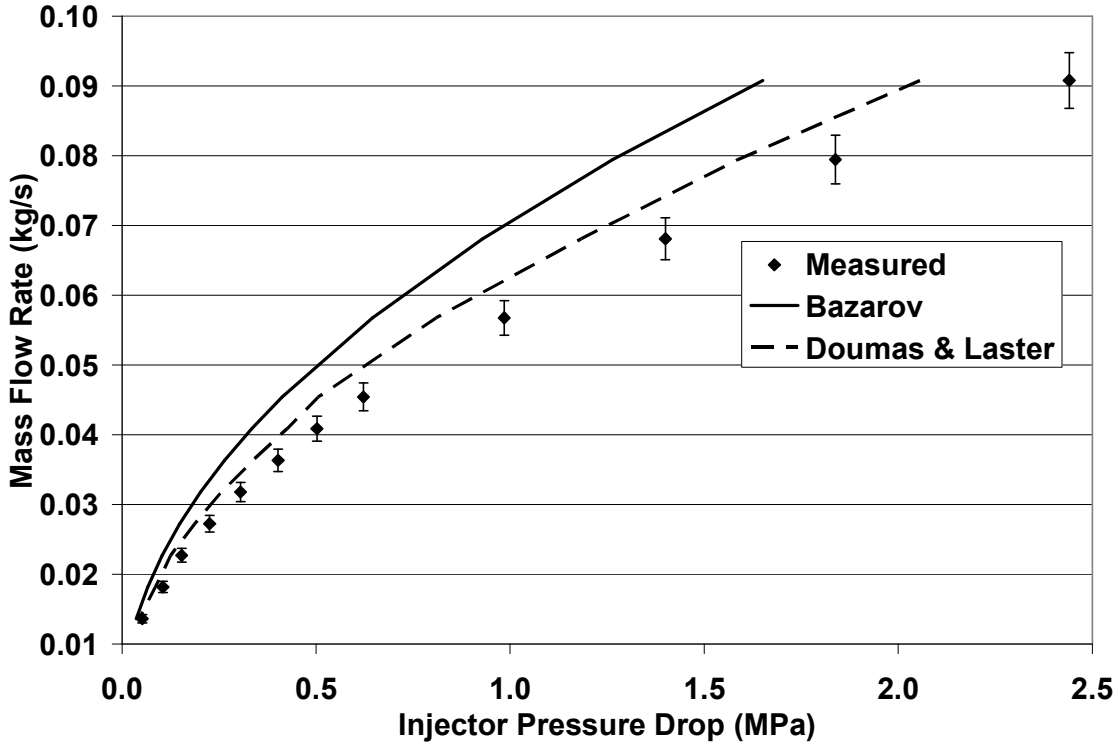

Figure 2.5 Element mass flow rate versus injection pressure drop

The inner diameter of 45 mm was chosen to provide a water flow path into the swirl element tangential orifices of at least $10D_s$. This length helps to promote steady state flow distributions at the orifices' inlets prior to entering the swirler. The tubing has stainless steel top and bottom sections welded to it. The top piece was a 51 mm diameter disk with an AN male fitting welded at the top. The bottom disk has twelve #8-32 tapped

holes in its bottom surface for bolting other injector parts. Figure 2.6 shows the water manifold.

Figure 2.6 Water manifold

The swirl body was machined out of stainless steel hex bar stock. The hex design gives planar surfaces which the three tangential orifices were easily drilled into. The swirl body was manufactured to the specifications given in Table 2.6. The vortex chamber was drilled from the top of the swirl body, and the top hole was blocked by a stainless steel plug. The bottom of the swirl body has a thin 51 mm diameter disk welded on to provide a mating surface from the swirl body to the manifold. This disk has twelve imbedded holes to allow the #8-32 bolts to slide through and tighten against. The water within the manifold system was contained by an o-ring seated on the swirl body disk. Figure 2.7 shows the swirl body design.

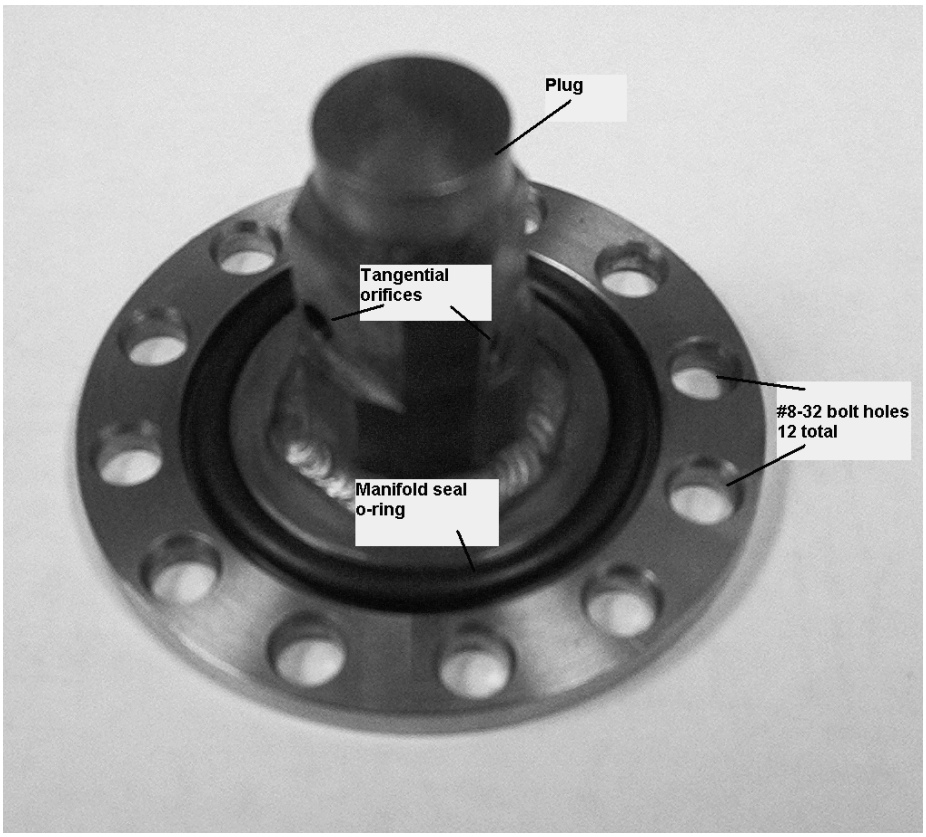

Figure 2.7 Swirl element body

The water supply system, inclusive of the manifold, was designed to minimize pressure drop losses between the upstream static pressure measurement and the water inlet location into the tangential channels. Calculations of the pressure drop losses from supply pipe friction and manifold sudden expansion give a total pressure drop small enough to be neglected during facility operation and for the calculation of discharge coefficient values seen later in Chapter 3.

The final piece of the swirl element was the acrylic nozzle extension. This part was designed to extend the swirling flow into an optically clear nozzle section, allowing

for visualization of the swirling film thickness. The nozzle extension length divided by the nozzle diameter was chosen to be 6.71, giving an additional acrylic nozzle length of 13.97 mm. This additional nozzle length has been shown by Rahman to have little effect on the resulting film thickness and free cone spray angle [61]. The acrylic section was a 51 mm disk, with twelve #8-32 bolt holes cut circumferentially. The nozzle extension was essentially a square-shaped post with a drilled orifice through the center to match the internal diameter of the swirl element. The lengths of the four square faces were double the center post's diameter. To protect against strain from the bolt heads, a stainless steel cuff, eighth of an inch thick, was placed against the bottom of the acrylic disk. Figure 2.8 shows both the acrylic section and the steel cuff. Figure 2.9 gives the assembled picture of the manifold, swirler, and acrylic section. Flow is from top to bottom in Figure 2.9(a).

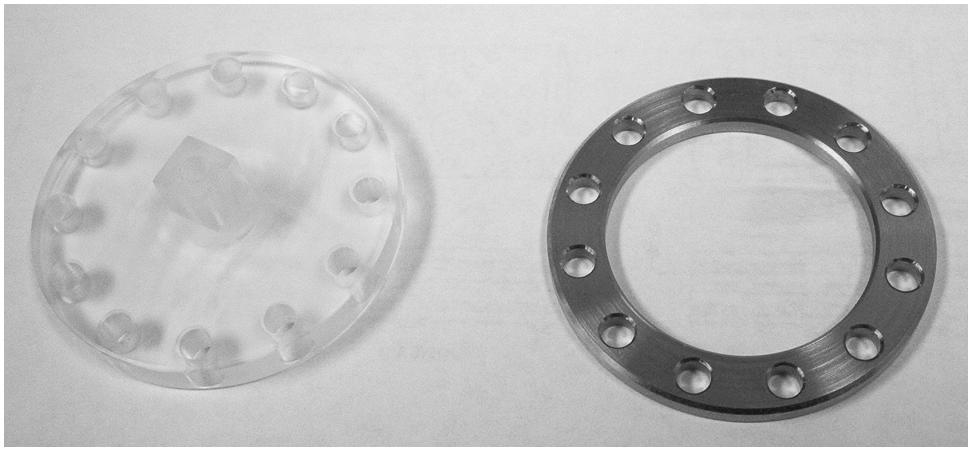

Figure 2.8 Full scale acrylic section and protective steel cuff

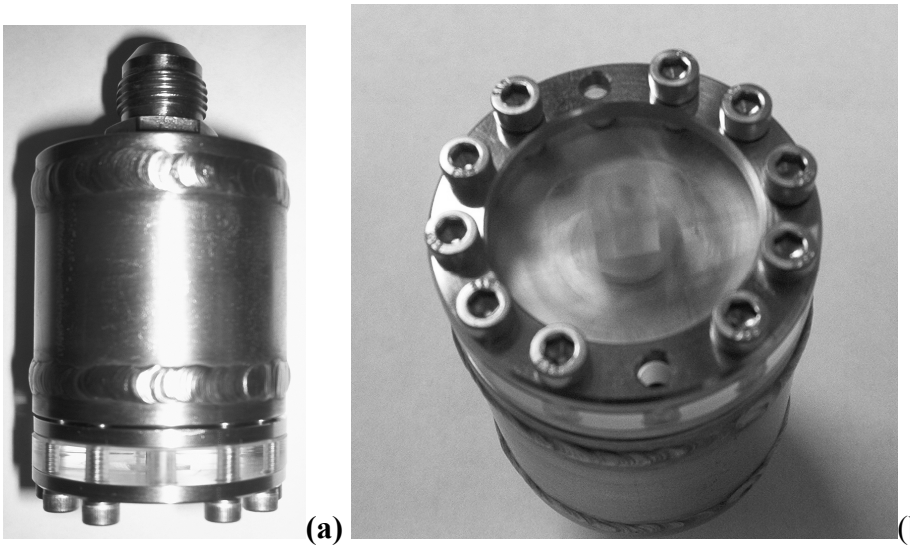

Figure 2.9 (a) Profile view of assembled element and (b) end view of acrylic section

It was later decided that the square-shaped post section distorted some of the light passing through it, making the film thickness measurement difficult. For measurements of the internal swirling structure, a solid 51 mm acrylic section was made. This section had the same length, o-ring seal, and nozzle diameter as the square-end post. Because the outer diameter of the solid acrylic piece was so much greater than the inner post diameter, the optical distortion through the acrylic was correctable. The optical correction applied is discussed in detail in Chapter 3. Figure 2.10 shows a profile of the solid acrylic section, along with a picture of the assembled swirl element.

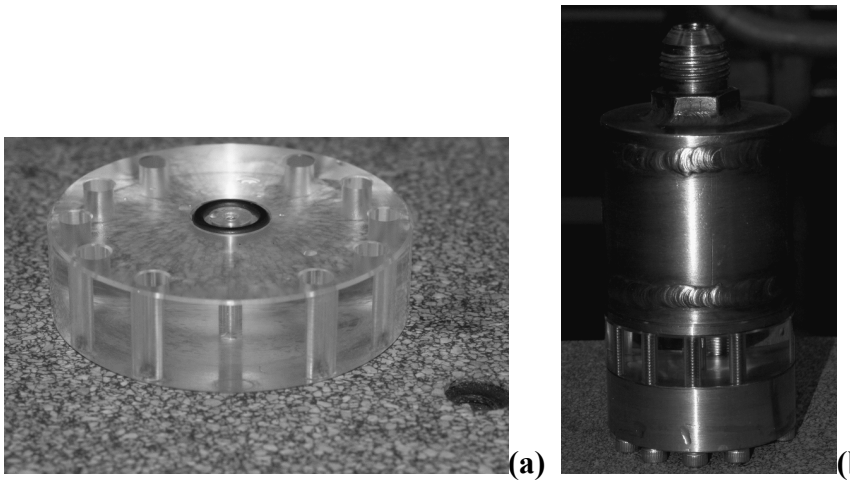

Figure 2.10 (a) Solid acrylic section and (b) profile view of assembled element

2.3 Dimensional Analysis

Steady operation of swirling flows is dependant on many variables, some of which are listed in Tables 2.2 through 2.5. The number of variables listed totals to 24. For this work, the absolute values of the flow variables will change. However the geometric parameters will remain the same since only one injector was used. Dimensional analysis allows for the identification of fixed geometric ratios, as well as the potential reduction of the number of degrees of freedom needing to be investigated. The following dimensional analysis, and subsequent non-dimensional groupings, is based off of the general ideas put forth by Bazarov [20] and Ruiz [62]. The first grouping chosen, shown below as Equation (2.1), is Bazarov's geometrical constant defined earlier as Equation (1.9).

$$A = \frac{2R_s D_n}{N_s {D_s}^2} \tag{2.1}$$

Use of Equation (2.1) leaves 21 variables to non-dimensionalize. The basic dimensions needed to describe this system are those corresponding to mass, length, and time. The rest of the groupings are found by using the Buckingham Pi Theorem outlined by White [63]. First, three variables representing the three basic dimensions are needed to non-dimensionalize the rest of the variables. The three variables chosen are: the liquid density (ρ_l), the total injection velocity (V_Σ), and the nozzle diameter (D_n). Selection of the liquid density and injection velocity are based primarily by suggestion from White, while the nozzle diameter was picked in accordance with the geometric constant grouping.

Equation (2.2) is derived using these three variables. On the left-hand-side, the two spray features of interest are listed. On the right-hand-side, the values related to swirler geometry, fluid properties, and flow properties are listed. Note that the two static pressures, P_{in} and P_c, have been combined into a total pressure drop across the swirl element.

$$\left(\frac{t}{D_n}, \theta\right) = f\left(\begin{array}{l} A, \frac{l_s}{D_n}, \frac{R_s}{D_n}, \frac{L_{vc}}{D_n}, \frac{L_n}{D_n}, \frac{\rho_g}{\rho_l}, \frac{\mu_g}{\rho_l V_\Sigma D_n}, \frac{\mu_l}{\rho_l V_\Sigma D_n}, \frac{\sigma}{\rho_l {V_\Sigma}^2 D_n}, \\ \frac{\dot{m}_l}{\rho_l V_\Sigma {D_n}^2}, \frac{P_{in} - P_c}{\rho_l {V_\Sigma}^2} \end{array}\right) \tag{2.2}$$

Any variables deemed constant will be simply 'absorbed' into the arbitrary relation function, *f*. Because all of the geometric ratios are held constant, Equation (2.2) reduces to Equation (2.3).

$$\left(\frac{t}{D_n},\theta\right)=f\left(\frac{\rho_g}{\rho_l},\frac{\mu_g}{\rho_l V_\Sigma D_n},\frac{\mu_l}{\rho_l V_\Sigma D_n},\frac{\sigma}{\rho_l {V_\Sigma}^2 D_n},\frac{\dot{m}_l}{\rho_l V_\Sigma {D_n}^2},\frac{P_{in}-P_c}{\rho_l {V_\Sigma}^2}\right) \tag{2.3}$$

It is common in atomization studies to define a liquid Reynold's number relating liquid momentum forces to viscous forces, and an aerodynamic Weber number relating relative liquid/gas shearing forces to liquid surface tension forces. Both of these numbers use the total liquid velocity value as the characteristic velocity. The nozzle diameter is used as the characteristic length. Typically, the accepted diameter to use is the hydraulic diameter for annular flow, which is equal to twice the exit film thickness for a swirling sheet. The viability of using the flow's hydraulic diameter instead of the nozzle diameter will be deferred for later chapters.

$$\mathrm{Re}=\frac{\rho_l V_\Sigma D_n}{\mu_l} \tag{2.4}$$

$$We=\frac{\rho_l {V_\Sigma}^2 D_n}{\sigma} \tag{2.5}$$

Substituting Equations. (2.4) and (2.5) into Equation (2.3) gives Equation (2.6). Note that the density associated with the Weber number in Equation (2.5) is the liquid density.

But multiplying the Weber number by the gas to liquid density ratio gives the more typical definition of the aerodynamic Weber number, defined with respect to the gas density.

$$\left(\frac{t}{D_n},\theta\right) = F\left(\frac{\rho_g}{\rho_l},\frac{\mu_g}{\mu_l}\frac{1}{\mathrm{Re}},\frac{1}{\mathrm{Re}},\frac{\rho_g}{\rho_l}\frac{1}{We},\frac{\dot{m}_l}{\rho_l V_\Sigma {D_n}^2},\frac{P_{in}-P_c}{\rho_l {V_\Sigma}^2}\right) \tag{2.6}$$

It is important here to address the gas to liquid viscosity ratio. Discussions by White [64] give a general rule of assuming low-density gas behavior for gases that have critical pressures above 1 MPa. The critical pressure of GN2 is approximately 3.39 MPa, and the maximum pressure to be seen in this work is up to 6.90 MPa. The critical temperature of nitrogen is 126 K, and the operating range of gas temperatures measured during testing is 311 – 327 K. Figure 2.11 shows the dependence of the normalized gas viscosity to static pressure and temperature. Marked on the graph is the general operating region in for these studies, giving a relatively small change in gas viscosity versus changes in pressure and temperature.

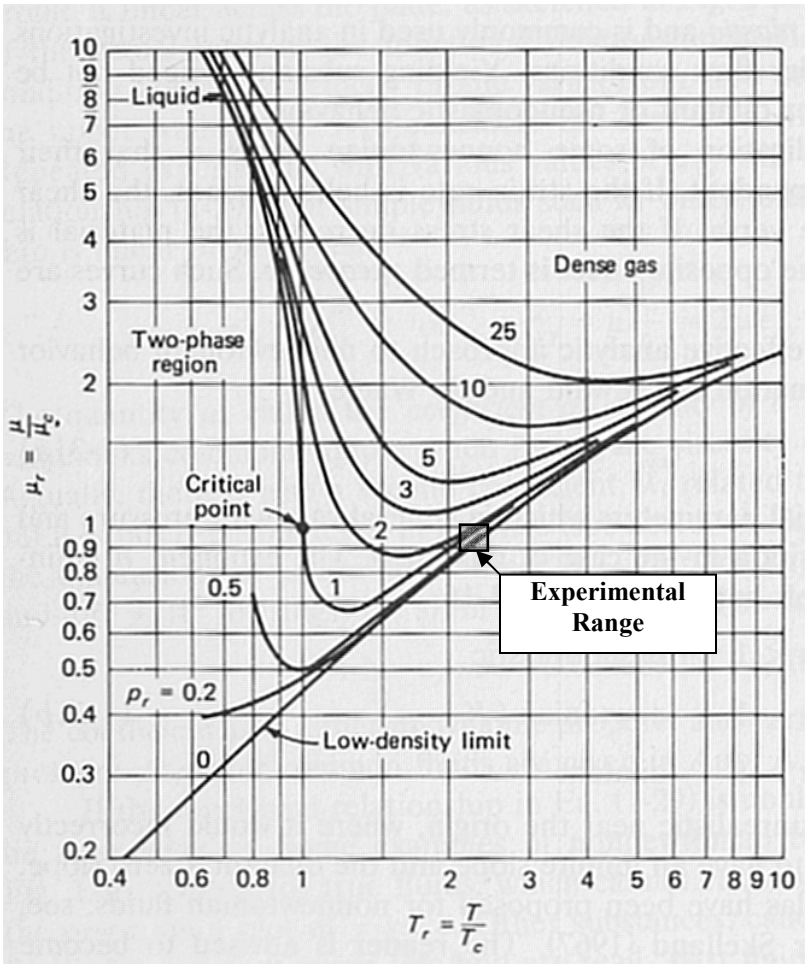

Figure 2.11 Normalized viscosity values versus pressure and temperature [64]

(Reprinted by permission)

Referring to Figure 2.11 above, the variation in nitrogen viscosity with pressure and temperature is small, justifying the use of the low-density approximation. This approximation defines viscosity to be solely dependant on temperature, and is represented by the Sutherland Law. Over the temperature operating range considered, the gas viscosity varies only about +/-10%. Because of the relatively small changes in gas

viscosity, as well as liquid viscosity, the viscosity ratio is assumed constant in this work, and is absorbed as part of the arbitrary relation function, giving Equation (2.7).

$$\left(\frac{t}{D_n},\theta\right) = f\left(\frac{\rho_g}{\rho_l},\frac{1}{\mathrm{Re}},\frac{1}{We},\frac{\dot{m}_l}{\rho_l V_\Sigma {D_n}^2},\frac{P_{in}-P_c}{\rho_l {V_\Sigma}^2}\right) \tag{2.7}$$

The mass flow rate term on the right-hand-side of Equation (2.7) can be related to the general definition of the discharge coefficient, given as Equation (2.8) [20].

$$C_D = \frac{\dot{m}_{actual}}{\dot{m}_{ideal}} = \frac{\dot{m}_l}{\rho_l V_\Sigma \frac{\pi}{4} {D_n}^2} \tag{2.8}$$

The last term on the right-hand-side of Equation (2.7) is the ratio of total pressure drop through the swirler to the total dynamic pressure of the injected flow. Assuming the liquid is incompressible, this ratio becomes equal to ½. Substituting the discharge coefficient and the dynamic pressure definition into Equation (2.7) gives Equation (2.9).

$$\left(\frac{t}{D_n},\theta\right) = f\left(\frac{\rho_g}{\rho_l},\frac{1}{\mathrm{Re}},\frac{1}{We},\frac{\pi}{4}C_D,\frac{1}{2}\right) \tag{2.9}$$

The constants of $\pi/4$, and ½ are absorbed into the arbitrary relating function. The discharge coefficient is moved from the grouping of independent variables to the dependent grouping. This variable is typically related to injector geometry and the

nondimensional film thickness. For this work, measured discharge coefficient values will be correlated against the independent variables to see if any dependency exists. The final non-dimensional groupings of interest to this work are given in Equation (2.10).

$$\left(\frac{t}{D_n}, \theta, C_D\right) = f\left(\frac{\rho_g}{\rho_l}, \mathrm{Re}, We\right) \tag{2.10}$$

Equation (2.10) shows that the independant non-dimensional groupings of interest are the quiescent gas to liquid density ratio, the injection liquid Reynold's number, and the injection Weber number. These nondimensional groupings are confirmed by Ruiz [62] as being important factors for defining swirling spray features. The normalized film thickness, free cone spray angle, and discharge coefficient all are possible functions of only the gas to liquid density ratio, the liquid Reynolds number, and the Weber number. These three variables will be used to correlate and understand spray feature measurements reported in later chapters.

2.4 Digital Imaging Diagnostic Methods

All spray features of interest were captured by shadowgraphs. A high-intensity strobe and digital camera combination were placed directly across from each other, on either side of the pressure chamber. Figure 2.12 shows how the camera and strobe system were situated during testing.

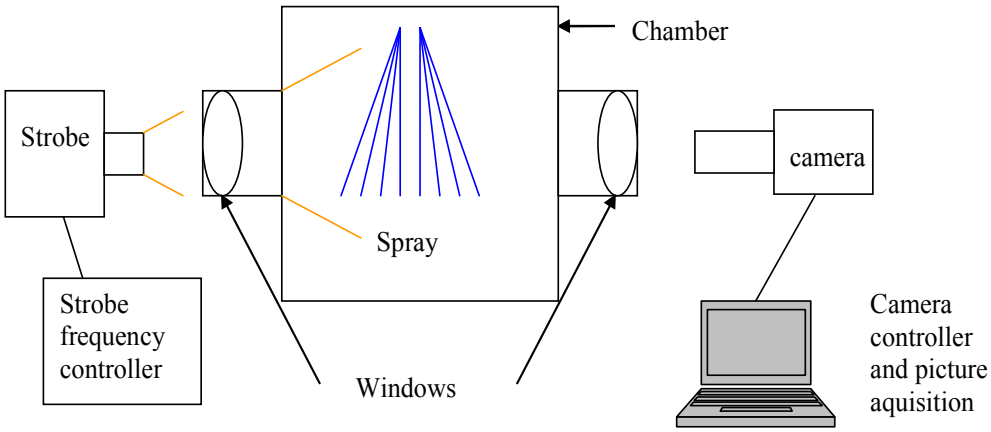

Figure 2.12 Shadowgraph acquisition system

The light source is a Model MVS-7010 High Intensity Xenon Strobe, made by the Machine Vision Corporation. Light pulse duration is 20 μsec per flash, with a maximum strobe frequency of 10 Hz. The strobe frequency was set by a voltage controller, at either 1 Hz for short exposures, or at 10 Hz for long, time-averaged pictures. Images were captured by a Kodak Model DCS Pro/SLRn digital camera. This CCD camera was set to take pictures at a 13.5 megapixel resolution, which was oriented as 4500 X 3000 pixel grid. Attached to the camera was a Nikon AF Micro-Nikkor telephoto lens, with a focal length of 200 mm and maximum aperture of 4. This telephoto lens allows for increased resolution at focal lengths of interest, which are critical for focusing on spray features within the chamber. The camera was controlled by a laptop, which can be used to change camera settings and acquire images remotely during testing. Accepted images were adjusted to a horizontal reference, and were converted to grayscale for further analysis.

In order to capture unsteady content, a high-speed video camera was set in place of the Kodak camera, and the strobe light was replaced by a 500W steady halogen lamp. The camera model is a Phantom v7.3 from Vision Research, Inc. The frame resolution was set at 512 pixels by 512 pixels, and the shutter speed was set for 10 μsec. To aid in picture resolution, the same telephoto lens used for still camera pictures was used for the video captures as well. A variety of frame rate settings were tried to maximize unsteady event capture and minimize individual memory size of the movies. A frame rate of 4000 frames per second (fps) was ultimately decided to be fast enough to capture the majority of the timescales needed during testing. The control and acquisition of high-speed movies was done in the same way as the still image capture: a laptop controlled the camera and recorded movies during a selected window of time, typically one second in length. The movies were then processed and saved as grayscale TIF images to preserve the resolution, and a selected number of images were saved for image analysis.

The main image processing software used was ImageJ 1.37(c), created by Wayne Rasband under the National Institute of Health [65]. This image processing and analysis program is written in Javascript and has features such as image thresholding, edge detection, pixel intensity histogram generation, and local zoom selection. Depending on the spray feature of interest, different tools of ImageJ were used to aid in the analysis. Details on which ImageJ tools were used will be given as the different spray features measured are discussed below.

CHAPTER 3

INTERNAL INJECTOR FLOW MEASUREMENTS

This chapter is dedicated to the measurement results of two main internal flow features of the swirl injector: the film thickness profile along the swirl injector's nozzle, and the overall injector discharge coefficient. Both features are important indicators of swirl injector performance and are fundamental to all swirl injector design processes.

3.1 Film Thickness Definitions

The film thickness varies appreciably as the liquid flow moves through the swirl element. Liquid entering from the tangential slots forms swirling streamlines which interact and mix with each other along the vortex chamber. The mixing streamlines coalesce to form a swirling annular body with a gas core in the center. The average distance from the liquid/gas interface to the vortex chamber inner wall is the vortex chamber film thickness. After the swirling flow moves downstream to the injector nozzle length, the nozzle film thickness decreases with respect to the vortex chamber film

thickness values. While both film thickness quantities are important in swirl injector design, the values of film thickness along the nozzle length are those referenced in previous works to relate swirl injector discharge coefficients and free cone spray angles. Empirically [21] and theoretically-based [20] design correlations are referenced to one of three nozzle film thickness definitions, (a) an 'average' film thickness, (b) an 'exit' film thickness, or (c) a 'maximum' film thickness.

The 'average' film thickness is defined here as a constant film thickness value along the nozzle length of the swirler. Regardless of any distortions along the liquid surface that may exist, the film thickness is considered spatially constant, thus representing the swirling flow as a liquid annulus. Swirling flow film thickness down the nozzle is assumed constant by Bazarov [20] in his design correlations. As the flow nears the nozzle exit, Bazarov notes that the film thickness actually decreases slightly due to the Skobelkin effect described in Chapter 1. His works relate this 'exit' film thickness to the average film thickness along the nozzle. Thus, there is an exit film thickness to be considered during the measurement process.

If the liquid/gas interface has any distortions present, the film thickness will vary spatially and temporally. Hutt [31] confirmed that even in atmospheric flow conditions, the swirling flow has a spatially varying film thickness down the nozzle. Hutt's work showed that not only does the film thickness decrease gradually through the nozzle length, but also varies temporally due to liquid/gas surface undulations. These distortions can cause the presence of maximum and minimum values of film thickness along the nozzle length. For the empirical work that Doumas and Laster [21] performed, the film thickness was obtained from visual measurements looking directly upstream into the

swirl injector. Visual perception, and subsequent measurements, would lend the reported film thickness to be a maximum value. Figure 3.1 shows the conceptual versions of the various film thickness values reported by Bazarov and Doumas and Laster. Assuming that all swirl injectors display a similar spatial variance in the nozzle film thickness, recognition of these various film thickness measurements gives direction on how to post process measured film thickness profiles.

Optical access to the swirling liquid flow profile was attained using the acrylic extension discussed in Chapter 2. Both high speed video and high resolution digital images were taken for various flow conditions. High speed video qualified any unsteady swirling flow behavior, but film thickness quantification came from high resolution digital image processing. Both the high speed video captures and the digital images were processed using the ImageJ software. By measuring a film thickness profile along the nozzle length, the average, maximum, and exit film thickness values can each be addressed and compared to each other.

3.2 Morphological Observations of Internal Swirling Flow

The swirl injector nozzle flow, with the acrylic extension attached, was filmed over various operation conditions using the experimental setup shown in Figure 2.9. A standard video capture session began with selecting the mass flow rate and chamber pressure combination within WNIST. Once these conditions were established, which took approximately ten seconds upon engaging the system, the high speed video camera was commanded to film the swirling flow for 100 frames.

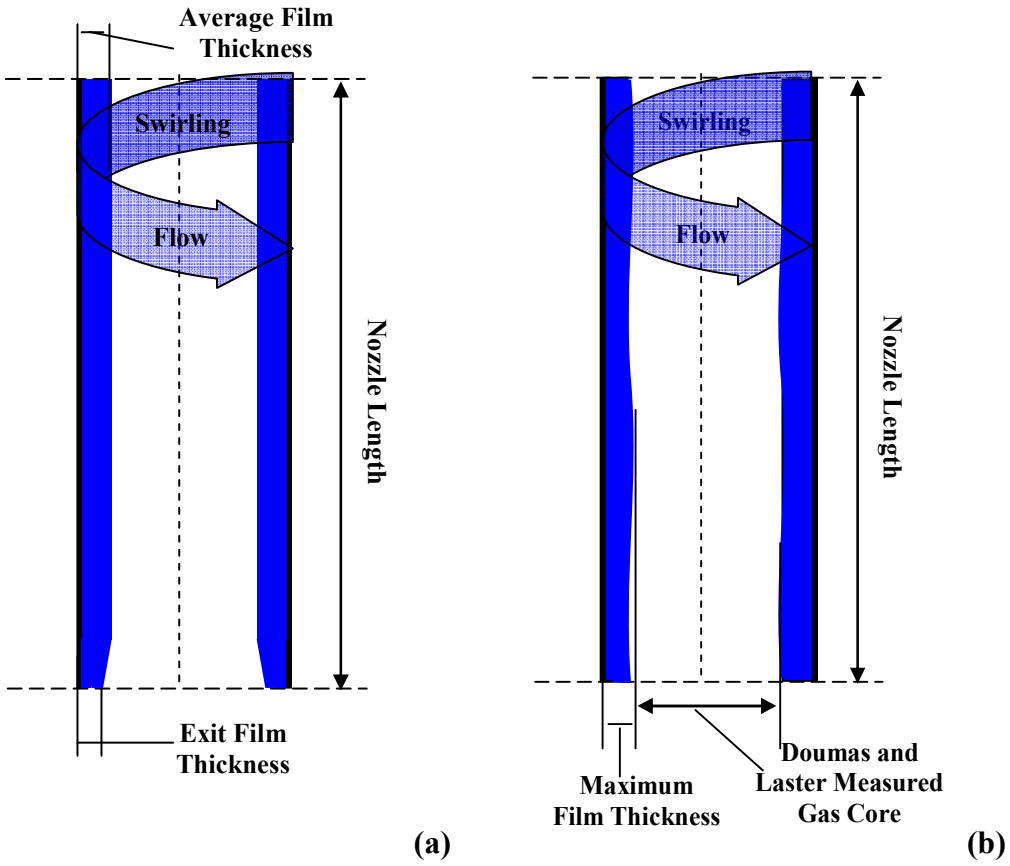

Figure 3.1 Conceptual film thickness from (a) Bazarov and (b) Doumas and Laster relations

At 4000 fps, a 100 frame capture session corresponded to a time record of $1/40^{th}$ sec. After 100 frames were recorded, the video capture software saved the session to a multi-page TIF format, best preserving image resolution. Because the constant light source used was powered by a 60 Hz AC power supply, the high speed camera picked up

a ‘breathing’ effect in the background lighting. To mitigate against this effect, the auto-exposure setting [66] was used on the video capture software.

Image resolution was chosen to be 512 x 512 pixels. This resolution was the highest offered by the video camera, while still keeping a moderately fast capture rate of 4000 fps. Each image session was cropped and magnified into the region of interest along the nozzle length. Except for a relatively small set of operating conditions that gave transitional behavior, the video captures generally showed spatially stationary behavior of the internal nozzle flow. Therefore, it was deemed accurate to use digital high resolution image stills to quantify internal flow features and let those quantifications be time independent.

Some horizontal movement of the swirler was noticed frame to frame, which visually looked as if the camera was vibrating during a capture session. However, inspection of the swirler body at higher chamber pressure showed the swirl body itself was shaking slightly. The cause was determined to be the GN2 window purge flow buffeting the swirler body. This effect is considered the classical case of a cylinder in cross flow being vibrated by vortex shedding [63]. Even though this influence is visually discernable, the actual displacement was deemed small and assumed to be only oriented perpendicular to the windows. For all image comparisons and measurements, the image stack alignment feature of ImageJ was used to correct this vibration effect out.

3.2.1 Fixed Mass Flow Rate and Elevated Chamber Pressure

Figure 3.2 shows how the internal flow profiles changed with increasing back pressure and fixed mass flow rate of 0.091 kg/s. Flow is from top to bottom of each picture. At atmospheric chamber pressure, the flow structure appeared helical. The helical flow structure came from liquid injection into the swirl chamber by three tangential slots, causing three main streamlines to form. Alignment of the three main streamlines created a helical pattern along the nozzle, with a flow profile showing striations in the direction of the swirling flow's helix angle. The helical flow film thickness varied minimally due to turbulence, but generally remained constant over the duration of the video. As the chamber pressure was increased to 0.34 MPa and 0.69 MPa, the same helical appearance was retained in the swirling flow.

At 1.03 MPa chamber pressure, the swirling flow began to show asymmetric variations in its profile, of which a portion with a thicker film (or smaller air core diameter) is labeled in Figure 3.2 as a 'neck.' The location of this neck, denoted by the right-side arrow in Figure 3.2, was centered roughly 2/3 of the nozzle length down from the bottom of the O-ring groove between the swirl body and the acrylic nozzle, and moved approximately ±2 mm about this point randomly. Flow upstream and downstream of the neck location maintained the same helical flow morphology and film thicknesses as at ambient chamber pressure. Increasing the chamber pressure to 1.38 MPa moved the neck further upstream to roughly ½ of the nozzle length, with the same random variations and film thicknesses upstream and downstream of the neck as measured at ambient chamber pressure.

At 1.72 MPa, the neck moved further upstream from the nozzle exit and the film thickness at the neck increased. The flow upstream of the neck maintained the same film thickness profile as at ambient chamber pressure, but the flow downstream of the neck was distorted and film thickness increased. Also, a second neck appeared that did not have the same appearance as the first neck. For clarification, this upstream neck was labeled a "jump." At 1.72 MPa, both the upstream jump and the downstream neck were spatially stationary in time. In Figure 3.2, left-side arrows denote jumps, and right-side arrows denote necks.

Increasing the chamber pressure to 2.07, 2.41, and 2.76 MPa moved the upstream jump location upstream towards the swirl chamber of the injector, and one to two downstream necks were formed in the flow. The location of the upstream jump and downstream necks stayed spatially stationary. However, in addition to the changes in film thickness due to jump and necks, the film thickness downstream of the jump increased.

For 3.10 to 4.83 MPa, the flow profile no longer had a visually notable upstream jump. It was assumed that the jump had moved upstream out of the viewable nozzle length. Multiple necks (three to four) were noticed along the nozzle length, and the location of these necks did not greatly vary with increasing chamber pressure. The film along the nozzle was the thickest seen over the chamber pressure range investigated.

The morphological changes of the flow in Figure 3.2 can be compared to observations from work performed by Binnie et al. [40] – [43]. Binnie's work focused mainly on observing the swirling flow morphology and the static wall pressure.

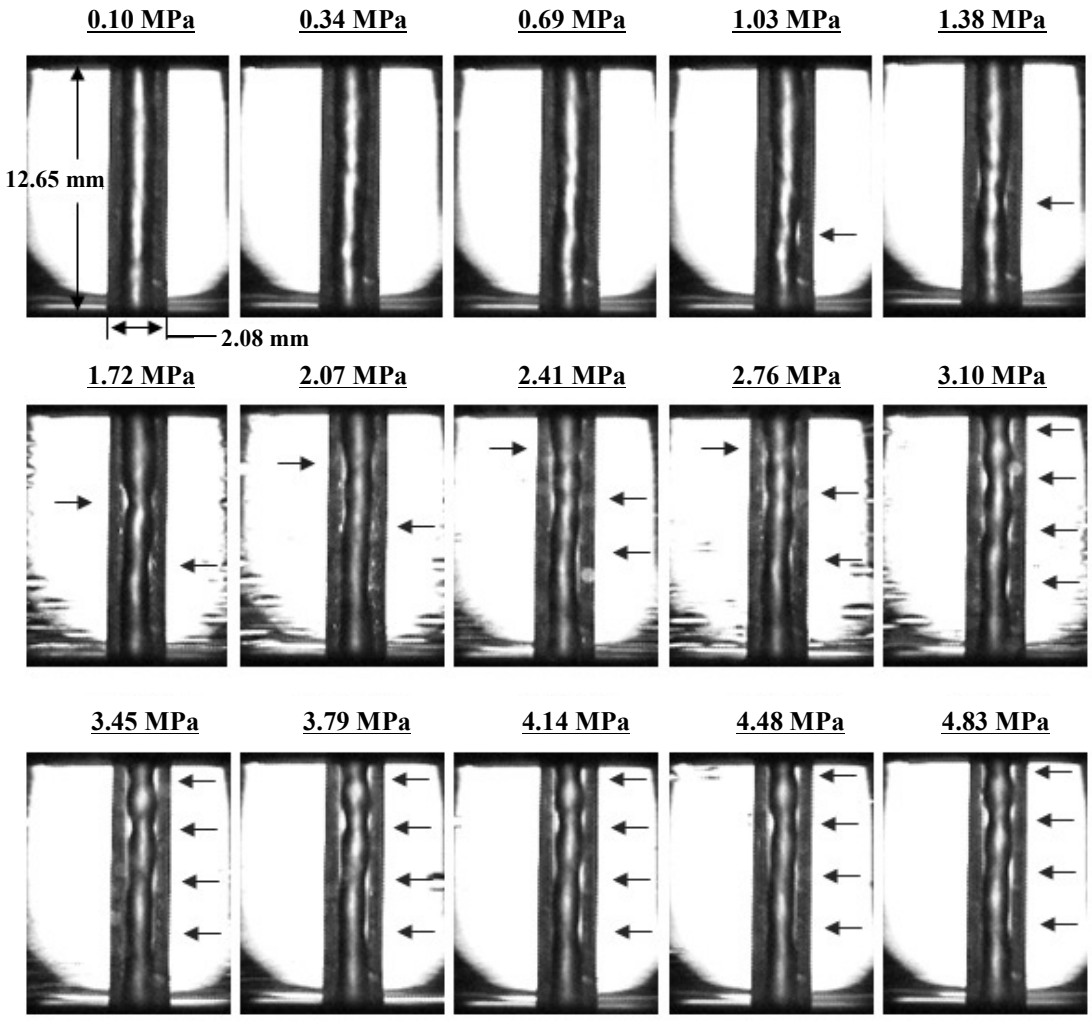

Figure 3.2 Internal flow profiles at fixed design mass flow rate and various chamber pressure operating points

The mass flow rate was held constant, but a gate valve was placed at the tube's exit to provide a downstream flow obstruction. Liquid static pressure was measured through a series of pressure taps flush mounted along the tube wall. Binnie showed that, for a given mass flow rate, the gate valve closing caused the flow to generate a swirling

flow jump phenomena a number of different ways. Binnie identified the jump seen in his swirling flow as a vortex breakdown event. Drawing an analogy to the two dimensional hydraulic jump process, increased mass flow rate for a fixed obstruction (gate valve setting) changed the morphology of the vortex breakdown from a smooth, laminar-like pattern to a highly turbulent one. Figure 3.3 shows a set of representative images of the vortex breakdown phenomena occurring within swirling flow studied by Binnie. The jump noted in Figure 3.2 is considered to be in the same family as the vortex breakdown phenomena in Figure 3.3.

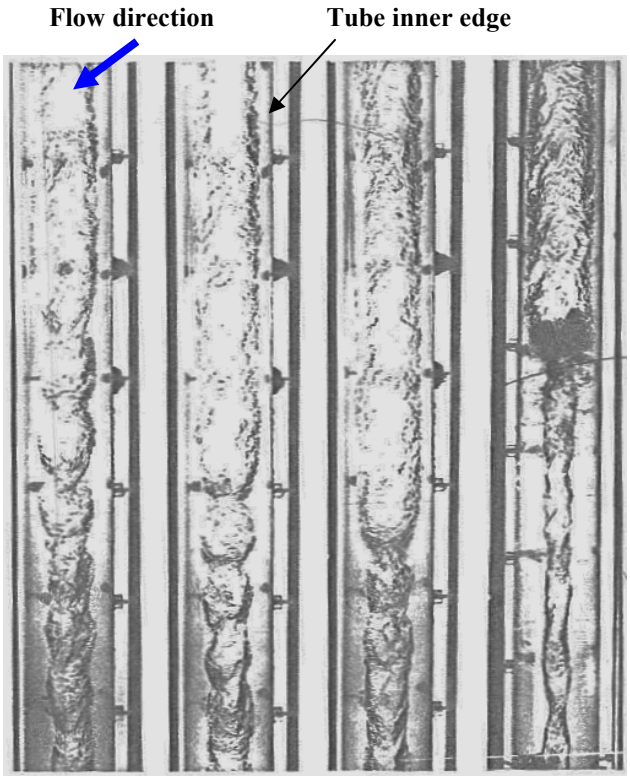

Figure 3.3 Internal swirling flow profiles from Binnie [42]

Lucca-Negro and O'Doherty [67] have reviewed a large body of literature regarding the vortex breakdown phenomena in swirling flows. Generally speaking, the vortex breakdown event is a fluid mechanic transition between swirling flow with no axial recirculation to swirling flow with large axial recirculation. Typically, as in the case of this work, the vortex breakdown causes a global change in flow structure downstream of the breakdown event. The effective flow area downstream of the breakdown is different than the effective flow area upstream. Figure 3.3 shows that the effective flow area increases as the flow moves through the vortex breakdown event. An increase in effective flow area correlates to a momentum loss/pressure recovery mechanism within the flow.

There are many types of vortex breakdown structures, which depend on flow geometry and operating ranges. Lucca-Negro implied that multiple non-dimensional variables play into the development of a vortex breakdown, most especially the swirl number of the flow. This swirl number has been defined as the ratio of tangential momentum axial flux to axial momentum axial flux times the flow exit radius. Equation 3.1 analytically defines the swirl number, recommended by Gupta [68] for swirling flows.

$$S = \frac{M_u}{M_a R_n} = \frac{\int_{r_{mn}}^{R_n} (\rho_l U_a U_u) 2\pi r^2 dr}{\int_{r_{mn}}^{R_n} \rho_l \left(U_a^2 - \frac{U_u^2}{2} \right) 2\pi R_n r dr} \tag{3.1}$$

According to Binnie, the inception and apparent intensity of a vortex breakdown was related to the flow's Froude number. The Froude number is the ratio of the swirling flow's axial velocity to the wave speed of a disturbance along the liquid/gas surface. Binnie derived the Froude number to be Equation (3.2).

$$Fr = \frac{U_a}{(\omega)\sqrt{\frac{1}{2}\left(R_n^2 - r_{mn}^2\right)}} = \frac{\left(\frac{U_a}{U_u}\right)}{\sqrt{\frac{1}{2}\left(\left(\frac{R_n}{r_{mn}}\right)^2 - 1\right)}} \tag{3.2}$$

Equation (3.2) shows that the only two parameters that can increase the Froude number are higher axial to tangential velocity ratios or lower tube radius to gas core radius ratios. In the images of Figure 3.3, the flow Froude number was calculated to be increasing from the left to the right of the figure.

Lucca-Negro noted that for low swirl numbers ($S < 0.6$), the axial and tangential velocity components operated independently from each other. That is, any radial pressure gradients existing in the flow are not strong enough to cause significant axial pressure gradients. However, as the swirl number is increased, the radial pressure gradient grows in conjunction with the centrifugal forces of the flow. Increases in the radial pressure gradient will continue to raise the axial pressure gradient until the axial momentum of the flow cannot overcome the axial pressure gradient. At this point, axial flow recirculation will occur within the flow field and a vortex breakdown will occur.

To estimate the swirl number for this swirl injector flow, the Doumas and Laster based predictions within Appendix C were used. The axial velocity component was

estimated to be 43.2 m/s, and the tangential velocity component was estimated to be 21.0 m/s. Both of these velocity components and the estimated gas core radius were used in Equations (3.1) and (3.2) to find the representative swirl number and Froude number. Calculations showed that $S = 0.55$ and $Fr = 3.70$. Because the Froude number was so high, downstream disturbances were believed not to propagate upstream and cause axial flow instabilities. However, since the swirl number was close to 0.6, the potential for axial flow recirculation was considered very high and could have been definitely active within the internal swirling flow.

Work performed by Wang [69] used digital particle image velocimetry (DPIV) to study the internal flow field of a large scale swirl injector. At the full flow design mass flow rate, the axial velocity profile was shown to have a somewhat parabolic shape with radius. The maximum axial velocities were typically found at the liquid/gas interface, with the profile reaching a minimum value approximately halfway between the liquid/gas interface and the tube inner wall. For several axial stations down the nozzle tube length, the minimum value actually turned negative, showing axial recirculation in the flow. Assuming the same flow behavior scales down to the injector of this work, a weaker vortex breakdown could exist in the swirl injector flow at even ambient chamber pressure conditions.

Upon creation of a strong vortex breakdown, the nature of the flow will change downstream of the breakdown location. Upstream of the breakdown, the flow is still behaving like constant angular velocity flow, with a helical look. Downstream of the breakdown, the film thickness profile values increases, decreasing the average gas core diameter. This decrease in gas core diameter is indicative of a large loss in swirl velocity

due to the breakdown. This observation was seen by Binnie when he measured the liquid wall static pressure downstream of a vortex breakdown, which showed a higher static pressure than upstream. If one draws an analogy to supersonic flow, then this process is much like high Mach number flow moving through a shock. High Mach number flow exists upstream of the shock, which will move through the shock at the cost of a large loss of total pressure. Downstream of the shock, the flow is now subsonic, with a Mach number less than unity.

For the swirling flow, the upstream flow has a Froude number less than unity, but as the flow moves through the swirl chamber to the nozzle section, the Froude number becomes greater than unity (or supercritical). As the chamber pressure increases and losses occur along the nozzle flow, the velocity ratio decreases and the Froude number lowers to below unity (subcritical), creating a vortex breakdown. Downstream of the jump, the flow continues to be subcritical, subject to notable gravity wave disturbances on the liquid/gas interface. Further increases in chamber pressure will force the flow to transition from super- to subcritical further upstream, until the transition reaches the swirl chamber to nozzle converging section. Observations of the swirling flow show that the vortex breakdown is no longer noted at the converging section, implying that the breakdown potentially exists within the swirl chamber itself. Unfortunately, no optical access was available in this section of the swirler body to confirm this implication.

3.2.2 Reduced Mass Flow Rate and Elevated Chamber Pressure

The other parameter varied to investigate internal flow structure changes was the liquid mass flow rate injected into the swirler. For a fixed chamber pressure, liquid mass flow rate values were reduced from 0.091 kg/s to 0.014 kg/s. This range corresponded to values of 100% to 15% relative to the design mass flow rate. For ambient chamber pressure values, decreasing the mass flow rate below the design value of 0.091 kg/s displayed similar transition structure seen for a mass flow rate of 0.091 kg/s and a chamber pressure of 1.03 MPa. This transition structure was seen from 0.079 kg/s to 0.057 kg/s, for ambient chamber pressure. Below 0.057 kg/s, the internal structure changed to display a vortex breakdown within the flow. This vortex breakdown was not as visually 'drastic' as the vortex breakdown seen for the 0.091 kg/s condition at higher chamber pressure. Further decreases in mass flow rate below 0.023 kg/s gave similar wavy structure as was seen for the 0.091 kg/s mass flow rate condition at the highest chamber pressure. The liquid/gas surface of the swirling flow had notable fluctuations, but the overall flow shape maintained a generally constant gas core radius. The mass flow rate was not decreased below 0.014 kg/s, where the flow still showed the same wavy structure. Figure 3.4 shows the flow structures for varying mass flow rate.

Referring back to Equations (3.1) and (3.2), the main variable that causes internal structure changes is the ratio of axial to tangential velocity. Hutt noted that inner wall friction decreases tangential momentum more than axial momentum [31], causing a decrease in flow helical angles. An additional flow loss comes from shear friction increases at the liquid/gas interface, which increases with increasing chamber pressure.

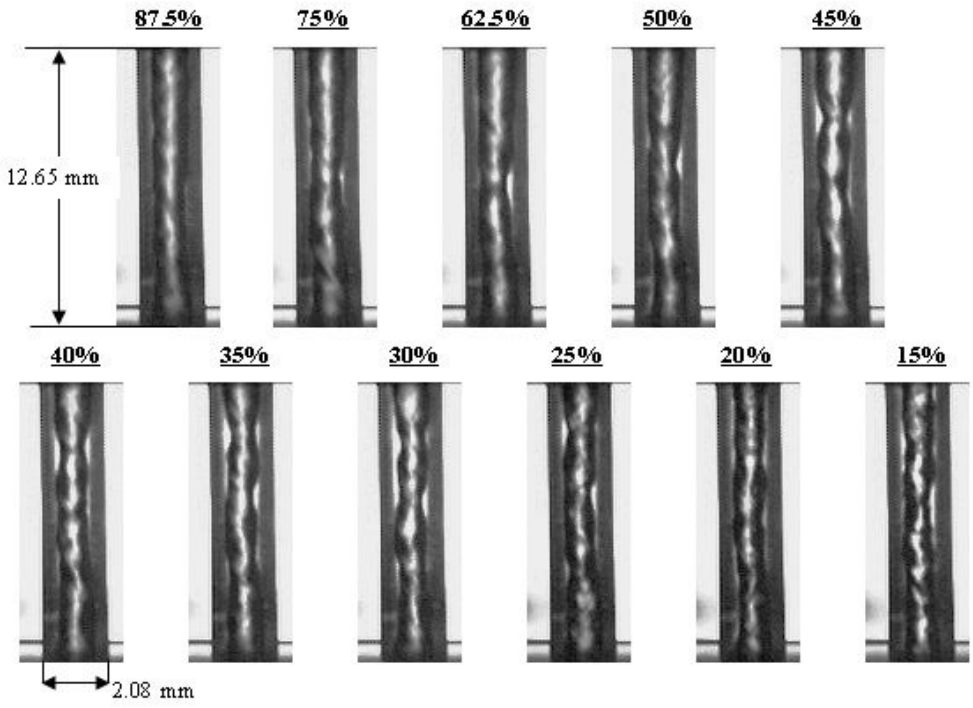

Figure 3.4 Internal flow profiles for decreasing relative mass flow rate at ambient chamber pressure

Any pre-existing vortex breakdown structure within the flow will potentially increase in size and move upstream. For a certain value of chamber pressure, the flow's swirl number will grow large enough that the vortex breakdown becomes notably stronger and the flow displays an unsteady transition structure. The drastic change in the flow field downstream of the vortex breakdown causes a decrease in the gas core radius, which causes the flow Froude number to decrease with respect to Equation (3.2). Because the swirling flow downstream of the vortex breakdown exhibits spatial contours at the liquid/gas interface, the Froude number is assumed to be below unity and downstream

disturbances from the chamber can propagate back up along the subcritical flow. Further increases in chamber pressure at a fixed mass flow rate continually increases the swirl number and moves the vortex breakdown further upstream, moving the transition location of super- to subcritical flow upstream as well.

Decreasing mass flow rate at a fixed chamber pressure lowers the swirl number relative to the value at the design mass flow rate. For lower swirl numbers, the intensity of the vortex breakdown is less and the disturbance of the breakdown on the flow field is smaller. Still, increasing chamber pressure at lower mass flow rate gives the same transition structure seen at the design mass flow rate. The only difference is the chamber pressure value needed to convert the weak vortex breakdown to a strong one.

Finally, decreasing the mass flow rate to very low values is assumed to bring the swirl number to less than a critical value of 0.6. At these swirl numbers, the weak vortex breakdown structure does not exist in the flow at ambient pressure conditions. Increasing the chamber pressure can cause enough axial to tangential velocity losses to drop the Froude number below unity if flow conditions do not already establish subcritical flow. The flow structure at the low mass flow rate confirms this assumption, with the liquid/gas interface displaying notable surface contortions at ambient chamber pressure.

3.3 Internal Film Thickness Measurements

While high speed videography offers qualitative insight into the internal swirling flow behavior, the main quantity that is needed to compare these observations to other spray features is film thickness. For a given image of the internal flow, the film thickness

can be perceived visually as the difference between the nozzle diameter and the liquid/gas interface. Figure 3.5 shows an example image of the internal flow along the nozzle, with the flow features labeled. The swirling water, through refraction effects, gives an optical distinction of the nozzle inner diameter. Also seen is the edge of the water/gas interface. It is the difference between the nozzle edge and the water/gas interface edge which defines the film thickness. In the process of defining the film thickness, care must be taken to a) define an accurate image pixel to physical length relation, and b) correct for optical refraction effects.

3.3.1 Fixed Mass Flow Rate and Elevated Chamber Pressure

As mentioned in Chapter 2, the resolution associated with the high quality images was 4500 x 3000 pixels. During a given operating condition, the camera and optically accessible section of the swirler were oriented towards each other so that the entire vertical length of the nozzle was captured. Because the camera was mounted on a multi-axis tripod, the alignment of the swirler and the camera was performed by adjusting the camera orientation until swirler features were best aligned with the camera's lens reticule. Minor adjustments to the image orientation were performed as needed using image processing software.

Figure 3.5 shows an example of a captured image used for film thickness measurements. Labeled on Figure 3.5 are the geometric features of the nozzle, as well as the relevant length scales used to quantify film thickness. The sealing o-ring optically blocked the first 10% of the nozzle length approximately, but the large majority of the

swirling flow can be easily seen along the nozzle. The swirling flow exhibits an asymmetric look over halfway downstream the optical nozzle length. This asymmetry was noted for all mass flow rate at atmospheric conditions, and was considered part of the 'nominal' flow and not as a vortex breakdown. Also seen is the notable decrease in film thickness, predicted by Bazarov, just as the flow reaches the exit plane of the nozzle.

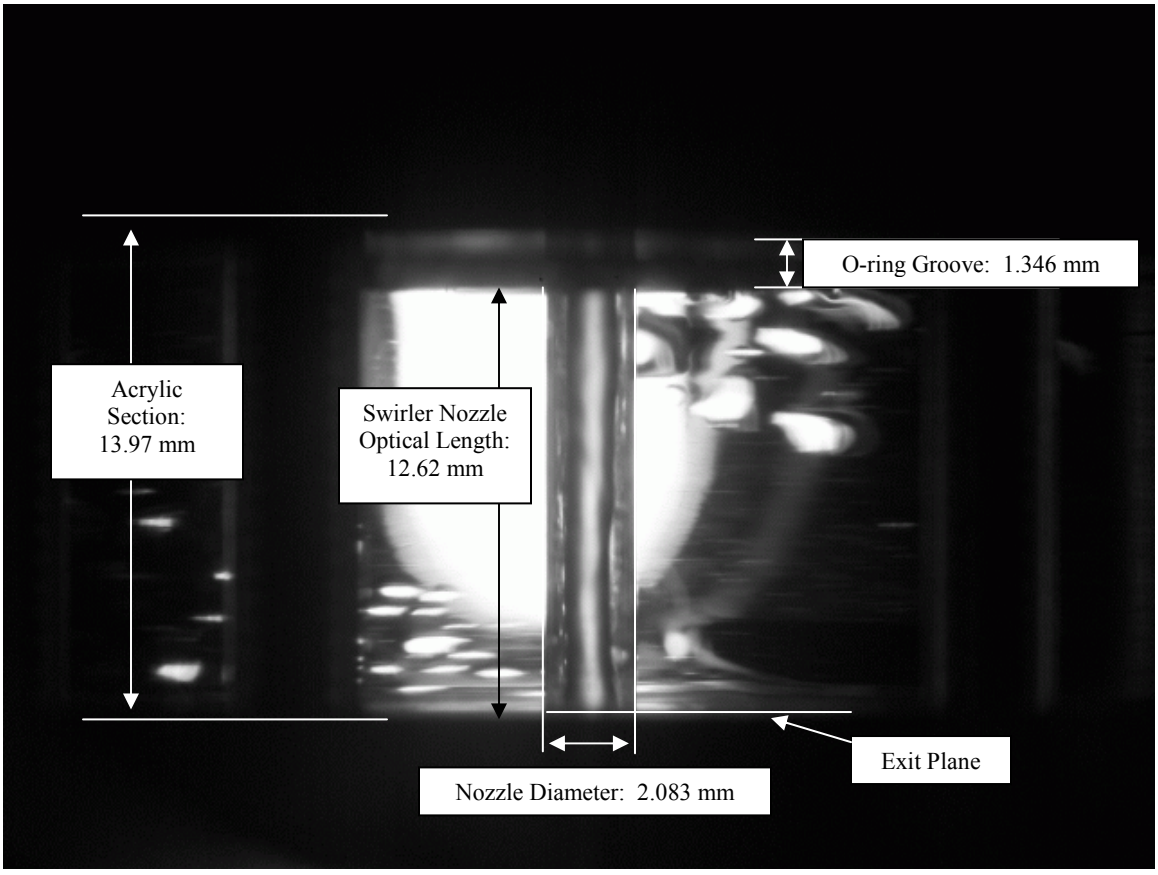

Figure 3.5 Geometric lengths associated with optically accessible swirler nozzle

Quantification of the film thickness along the nozzle length consisted of three steps: 1) determination of the pixel-based film thickness profile, 2) conversion of image pixels to actual physical lengths, 3) correction of film thickness measurement errors due to optical distortion. The two software packages used during the implementation of all three steps were ImageJ and Microsoft Excel. Each of the three steps will be discussed in detail below.

The first step consisted of determining the pixel-based values for average film thickness along the nozzle length. Figures 3.6 to 3.8 show the procedure for finding the pixel-based film thickness. First, an image at a given operating condition was selected for analysis, loaded into ImageJ, and irrelevant image sections cropped to reduce storage size (Figure 3.6). Next, fourteen axial locations along the nozzle length were selected to measure film thickness (Figure 3.7). ImageJ's rectangular selection feature was used to select a 50 pixel high region per axial location (Figure 3.7). This selection contained multiple rows of line selections with individual intensity values (Figure 3.8). ImageJ was then used to take the spatial average of each pixel row within the rectangular selection, giving composite average pixel intensity values versus horizontal pixel location.

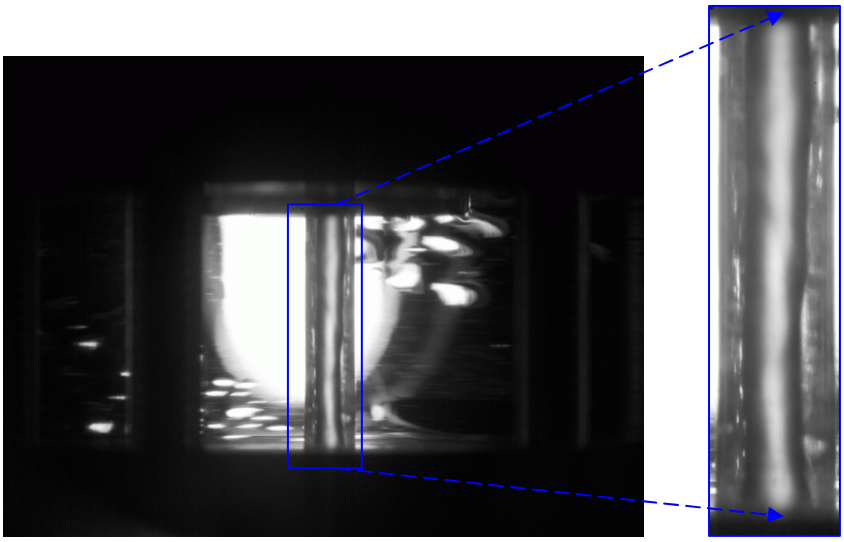

Figure 3.6 Example image cropped selection for film thickness quantification

As seen in Figure 3.7, the intensity profile vs. x-pixel location denotes the four necessary features needed to define average film thickness: the left-most nozzle diameter edge, the left edge of the liquid film/gas interface, the right edge of the liquid film/gas interface, and the right-most nozzle diameter edge. At locations where the nozzle diameter edge distorts the background light, the intensity derivative is either a minimum or a maximum. For the left nozzle edge, the intensity values change from high to low, denoting a large negative derivative. For the right nozzle edge, the intensity values change from low to high, denoting a large positive derivative.

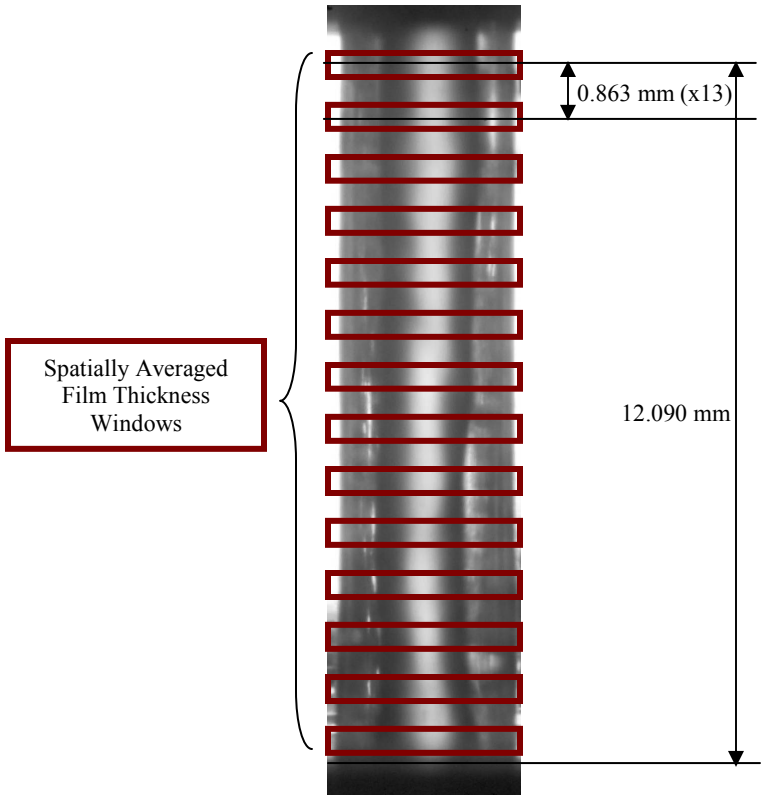

Figure 3.7 Axial locations for average film thickness selections

Detection of the left and right liquid film/gas interfaces corresponds to the local minimums of the intensity vs. x-pixel location values. It is this local minimum that gives the lowest mean intensity, corresponding to the darkest sections of the captured image. Physically, these dark sections are where the liquid film has the most refraction of the background light, a good indicator of where the swirling fluid's index of refraction changes at the liquid/gas interface. The difference between the left film edge and the left nozzle edge gives the left-side film thickness. The similar case is true for the right film edge and the right nozzle edge.

The accuracy of this pixel-based film thickness process was determined to be a summation of two biases, the bias due to nozzle diameter edge resolution and the bias due to the liquid/gas interface edge resolution. The x-pixel width for each image analyzed was 385 pixels. With respect to the average intensity vs. x-pixel location plot in Figure 3.7, both nozzle edge x-pixel location and liquid/gas pixel location could be discerned within 2 pixels each. Thus, a pixel-based film thickness value has a composite bias of ±4 pixels. Repeated measurements of the same images, using the same pixel-based edge detection process, gave a repeatability of ±6 pixels. Using uncertainty methods defined by Coleman [59], the composite total uncertainty associated with the average film thickness value was ±10 pixels.

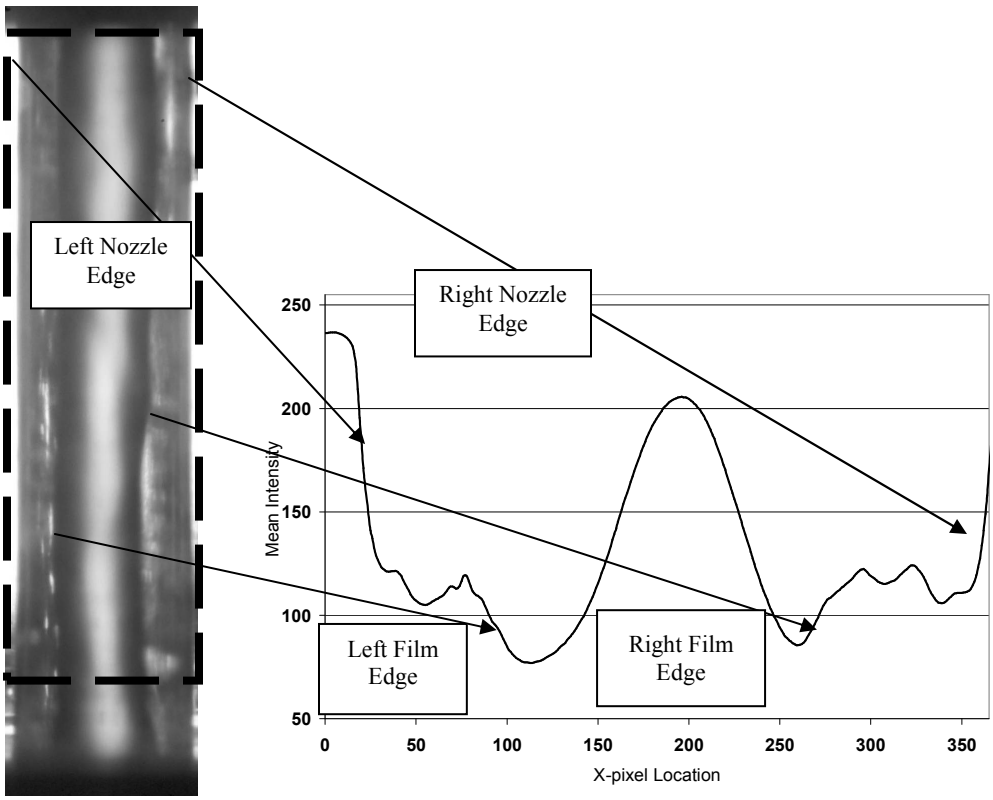

Figure 3.8 Horizontal pixel intensity values correlated to film thickness features

The first set of average intensity values are shown below in Figure 3.9. Conditions for fixed mass flow rate and varied chamber pressure were the same as shown in Figure 3.2. Comparison between each measured mean intensity shows the same general trends outlined in Figure 3.8. However, the mean intensity values for 2.76 MPa and higher show higher mean intensity values compared to the intensity values for less than 2.76 MPa. During testing, it was noticed that for chamber pressure values 2.76 MPa and greater, the opacity of the surrounding GN2 had been increased. This opacity increase was attributed to the increased gas density with increasing chamber pressure. To counter the dimming effect that the increasing gas opacity caused, the digital camera aperture was opened to collect more background illumination per capture. As a result, the lowest possible values of mean intensity were raised. This 'offset' in mean intensity readings was noted, but the trends in the mean intensity readings were still considered preserved.

To better compare the lower chamber pressure data to the higher chamber pressure, the mean intensity offset was normalized by the mean intensity values. For every mean intensity plot, the maximum and minimum intensity values were recorded. Then, the measure mean intensity values were normalized according to Equation 3.2.

$$I_{nom} = \frac{\bar{I} - I_{\min}}{I_{\max} - I_{\min}} \tag{3.2}$$

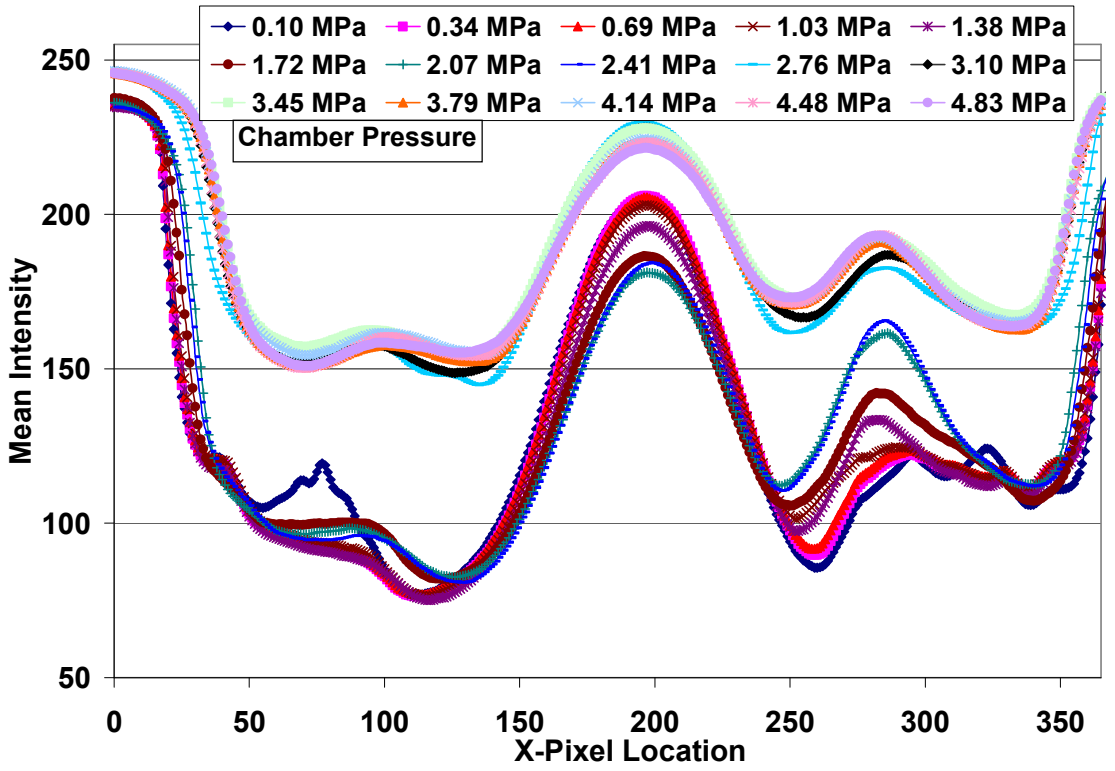

Figure 3.9 Mean pixel intensity vs. horizontal distance for average film thickness selections

Application of Equation (3.2) to the mean intensity values yields Figure 3.10, with all mean intensity trends normalized to the same references. The same trends as seen in Figure 3.9 are preserved, allowing for mean intensity gradients to be determined for the datasets.

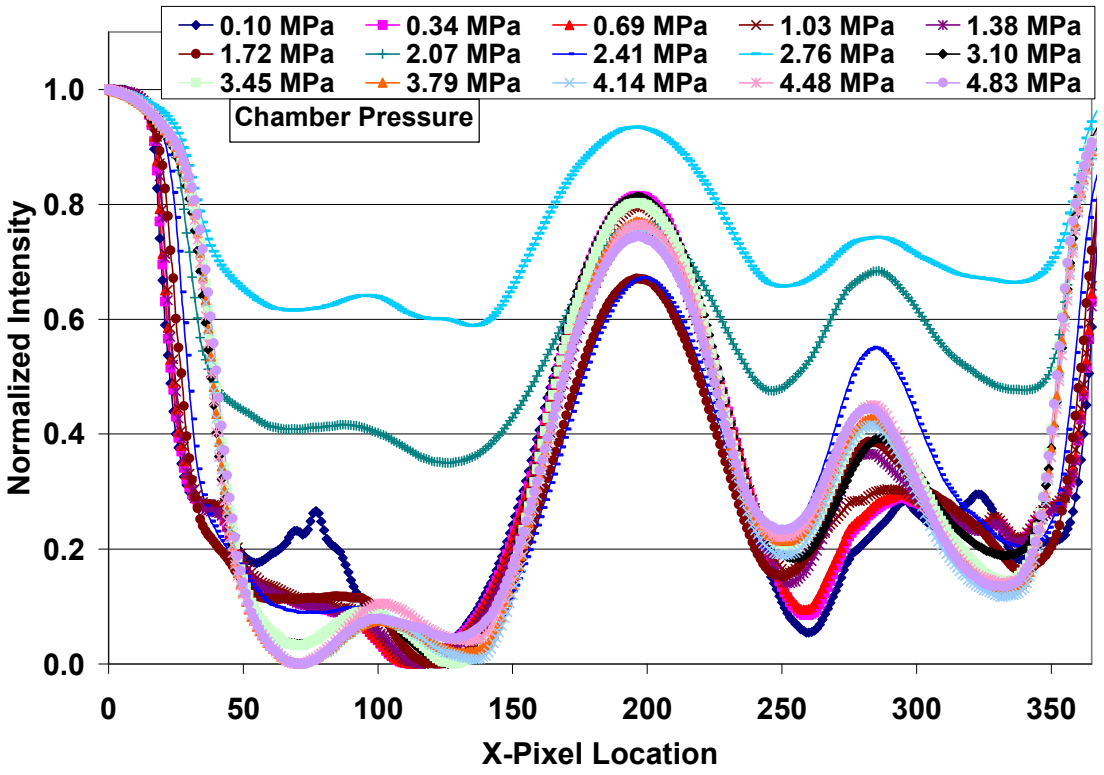

Figure 3.10 Normalized mean pixel intensity vs. horizontal distance

Traditionally, digital image processing methods lean towards edge detection algorithms to quantify changes in illumination, which in this case signifies the nozzle diameter edge and the liquid/gas interface denoting film thickness. In general, the edge detection processes use a gradient operator to delineate edges. Similarly, the derivative of the normalized mean intensity data from Figure 3.10 was numerically calculated, using a central difference relation defined as Equation (3.3).

$$I'_{nom\,i} = \frac{I_{nom\,i+1} - I_{nom\,i-1}}{X_{i+1} - X_{i-1}} \tag{3.3}$$

Application of Equation (3.3) to the data in Figure 3.10 gives Figure 3.11.

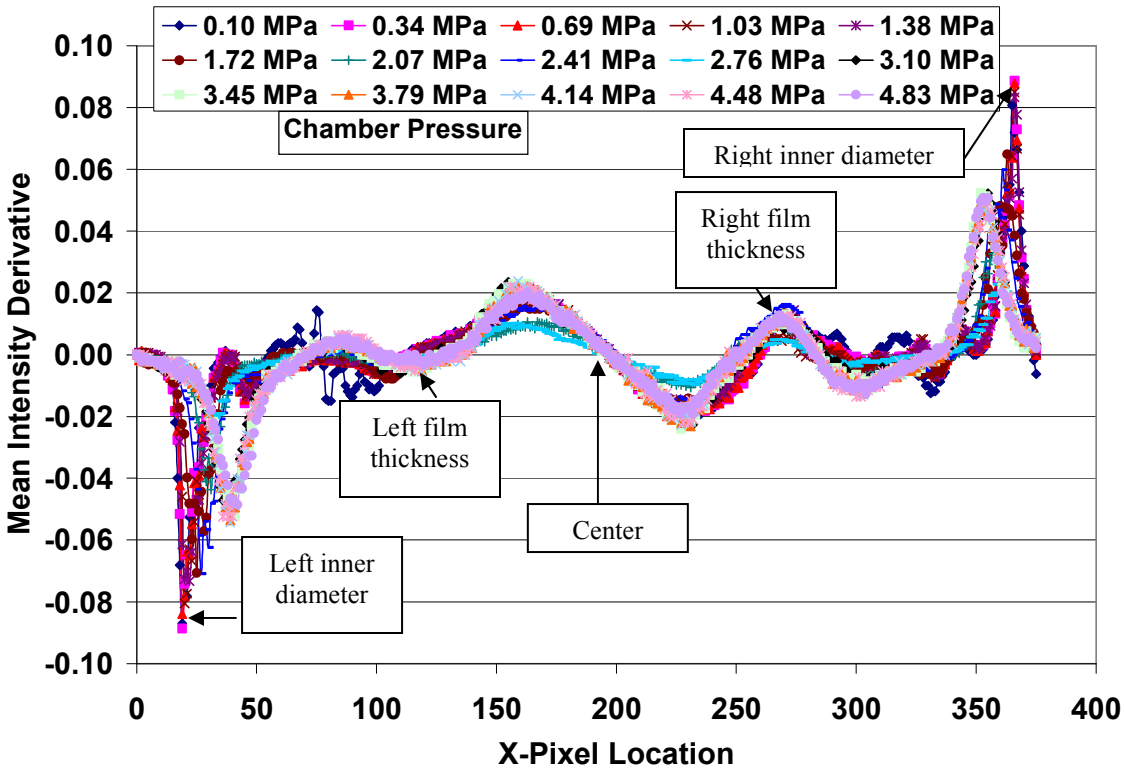

Figure 3.11 Derivative of normalized mean pixel intensity vs. horizontal distance

Figure 3.11 shows the locations where notable edges exist in the picture. Between 0 and 50 pixels, the left-side nozzle diameter edge exists, which visually

represents a change from high intensity to low. This change is mathematically represented by a large negative intensity gradient. Changes in the intensity values to signify the left-side liquid/gas interface was deemed best represented by the intensity gradient crossing zero between 100 and 150 pixels. The centerline of the image is where the intensity derivative plots cross zero at approximately 200 pixels. The right-side liquid/gas interface edge is captured between 250 and 300 pixels, and the right side nozzle diameter edge is easily seen between 350 and 400 pixels. To aid in determining the best zero-crossing of the derivative, each measured intensity curve was replaced with a smoothed curve generated by a median processing technique. For each point along a given curve, the value was replaced by the average of that point and two points on either side. This process helped to suppress much of the measurement noise that was amplified in the derivative curve. This technique is known as a 'running' or 'moving' average.

The last step in determining the film thickness from the mean intensity values consists of recording, for each chamber pressure value, all four x pixel locations corresponding to the left-side nozzle diameter edge, the left-side liquid/gas interface, the right-side liquid/gas interface, and the right-side nozzle diameter edge. The difference between the left-side nozzle diameter edge and the left-side liquid/gas interface is the left-side film thickness and the right-side film thickness is similarly defined. Conversion of pixel-based film thickness to length-based film thickness was performed using a defined reference length scale from the captured images. The reference length scale chosen was the nozzle diameter, taken as the known value of the nozzle diameter divided by the distance from left to right nozzle diameter edges. The nozzle diameter was confirmed to be 2.083 mm ± 0.025 mm by physically placing a calibrated centering pin

into the acrylic nozzle and verifying a tight fit. Accommodating for the image-to-image variation, the pixel to inches conversion used was 0.0064 mm/pixel. Using this conversion, the average film thickness bias was defined as ±0.025 mm, the average film thickness repeatability was defined as ±0.041 mm, and the total uncertainty of the average film thickness was defined as ±0.071 mm.

Binnie et al. noted that refraction effects at the liquid/gas interface could distort the visually-perceived edges of the swirling flow. Optical correction methods were developed and simplified to account for these refraction effects seen in Binnie's results. The refraction correction method stipulated certain criteria on the ratio of the nozzle diameter to the outer plastic diameter, as well as the viewing angle of the camera. Since the acrylic nozzle geometry and experimental setup in the current study satisfied both of the refraction correction criteria, it was deemed viable for use with these data. Using Snell's law, the physical gas core radius (or the nozzle radius less the film thickness) is the visually-determined gas core radius divided by the index of refraction of water, taken to be 1.33. For each flow condition, the measured left and right film thicknesses were divided by the index of refraction for water to give the corrected profile values. Figure 3.12 gives a representative comparison between left and right-side profile values to the original image. Values are reported in radial locations referenced to the nozzle radius, and axial spatial location along the nozzle length relative to the nozzle diameter. Error bars, reflecting the measurement uncertainty as discussed above, are plotted with the measured values.

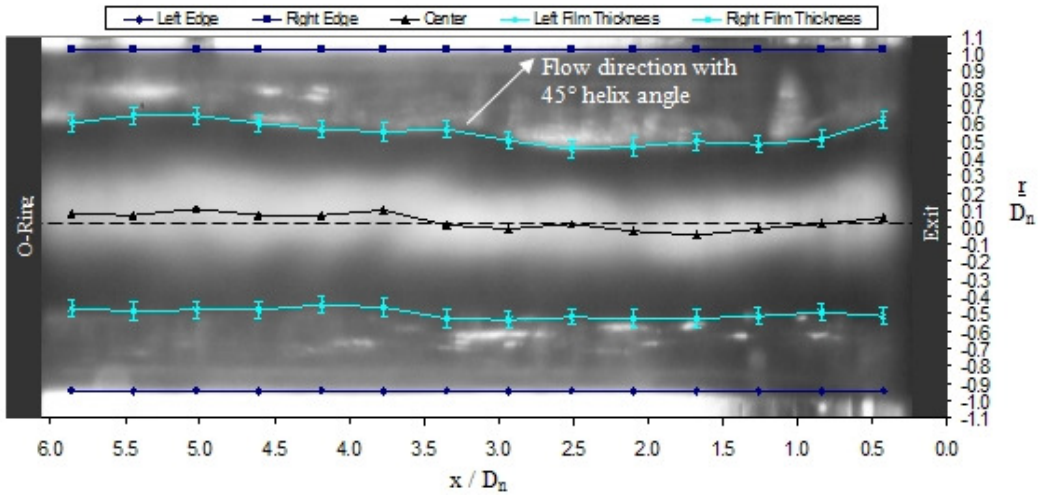

Figure 3.12 Measured film thickness profile comparison

Comparison between the left and right film thicknesses in Figure 3.12 show that they are notably different, partly due to the asymmetry of the helical flow. Figure 3.13 better highlights the left and right film thickness profiles' axial asymmetry for varying chamber pressure. To compare measurements from this work to both design methods, the two film thickness profiles from Figure 3.13 were averaged per spatial location and chamber pressure. The results, along with the predicted film thickness values, are shown in Figure 3.14.

Plotted in conjunction with the average film thickness values are the film thickness predictions from both Doumas and Laster's and Bazarov's methodologies.

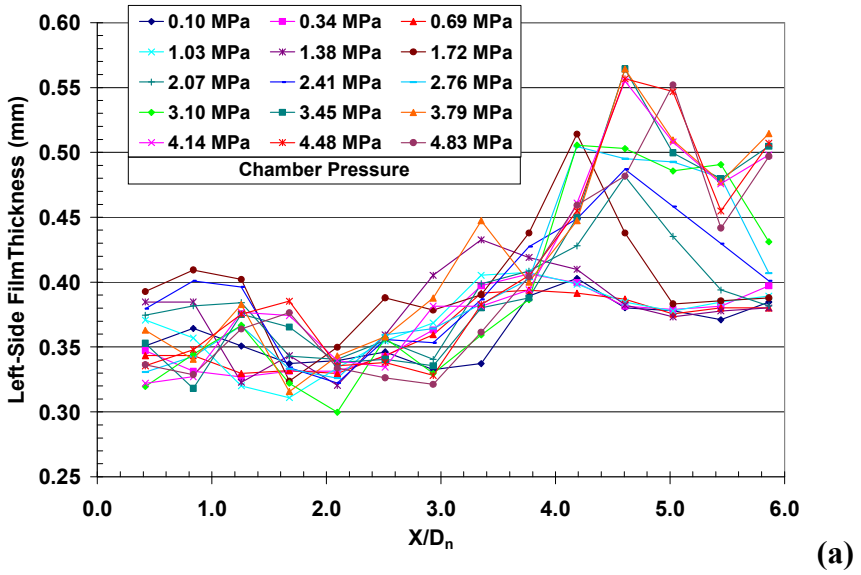

(a)

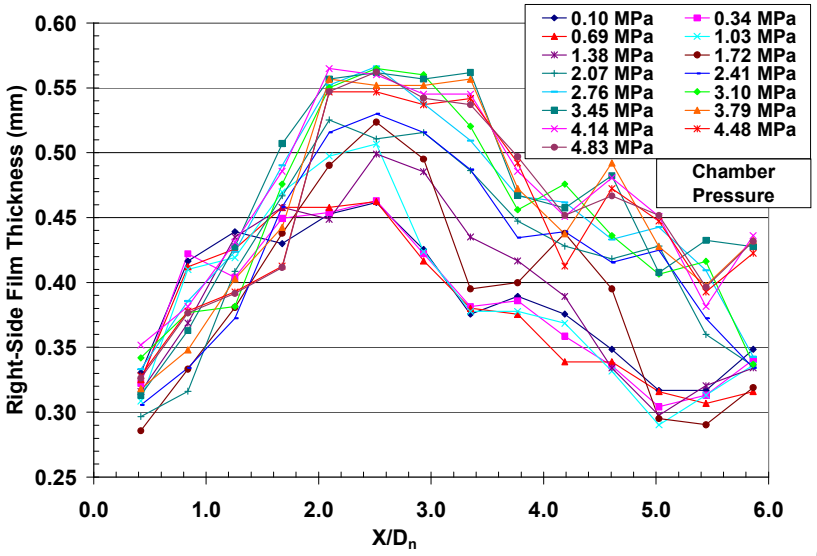

(b)

Figure 3.13 Comparison between (a) left and (b) right film thickness profiles over various chamber pressure operation at the design mass flow rate

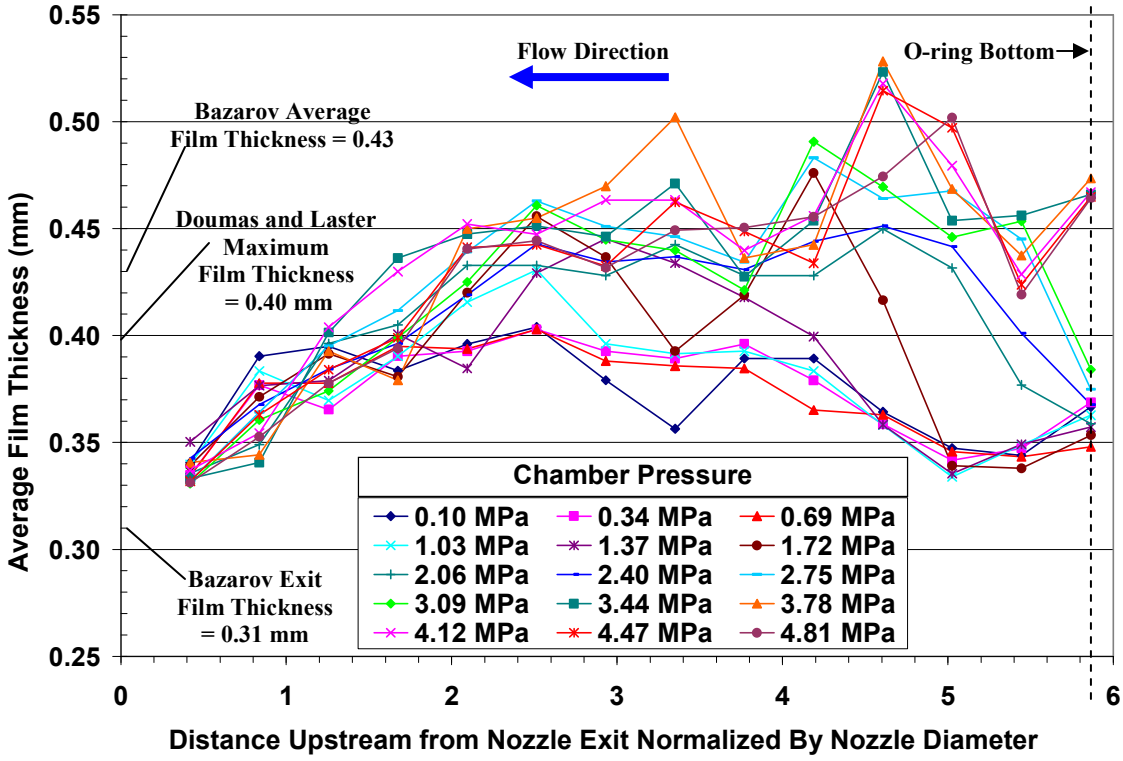

Figure 3.14 Optically corrected average film thickness profiles at the design mass flow rate

As discussed earlier, the predicted film thickness using Doumas and Laster's method should predict a value corresponding to the maximum value along the nozzle length. This prediction is in good agreement with the measured average film thickness at a normalized exit diameter of 0.20 and at ambient chamber pressure.

Figure 3.14 shows that the film thickness changes notably based just on the ambient chamber pressure data points. Hutt noted a similar trend in film thickness profile in his work with larger swirl injectors [31]. The spatial variation in film thickness was

attributed to a long wavelength shape along the nozzle. Based on the high-speed video observations discussed earlier, any spatially distributed wavelengths are generally fixed in time along the nozzle, as in agreement with Hutt's observations. Hutt also stated that because the spatial wavelength pattern was resolute in time, the liquid flow was considered supercritical in nature. Namely, any downstream disturbances cannot propagate upstream and influence the liquid flow. However, not all of the film thickness variation can be solely attributed to the spatial wavelength pattern. As the flow moves towards the nozzle exit, the Skobelkin effect begins to influence the film thickness by causing the swirling flow to thin. As described by Bazarov, the exit film thickness will always be less than the average film thickness upstream inside the nozzle due to the Skobelkin effect [20].

Increasing the chamber pressure up to 0.69 MPa (at constant mass flow rate) does little to deviate the spatial character of the film thickness from atmospheric chamber pressure values. It is assumed that the increase of chamber pressure within this range does not significantly cause enough flow effects to notably alter the flow structure. However, at 1.03 MPa chamber pressure the swirling flow exhibited unsteady behavior as the swirling flow morphology transitioned to vortex breakdown. The transition morphology exhibited a necking of the flow, which causes the maximum film thickness values to increase. Further chamber pressure increase to 1.38 MPa shows even greater necking phenomena occurring within the nozzle. At 1.73 MPa, the internal flow has established a vortex breakdown, raising the maximum film thickness 26% higher relative to the atmospheric maximum film thickness. This maximum film thickness location also moves upstream relative to the atmospheric location.

Further increase in chamber pressure continues to raise the average film thickness and the upstream location of the vortex breakdown within the nozzle. At 3.45 MPa, the increase of average film thickness with increasing chamber pressure begins to diminish. Inspection of Figure 3.2 shows that the internal structure of the swirling flow changes slightly from 3.45 MPa up to 4.83 MPa. As a result, the average and maximum film thickness values do slightly decrease.

To best compare between the chamber pressure combinations tested at the design mass flow rate, Figure 3.15 shows the spatially averaged film thickness and the maximum observed film thickness measured. The average film thickness was determined by spatially averaging over the film thickness profile values between $2 - 4D_n$. The maximum film thickness was taken as the largest film thickness value over the film thickness profile values between $2 - 4D_n$. It was within this range that the values were considered always downstream of the strong vortex breakdown phenomena, and upstream of the film thickness exit profile.

Figure 3.15 shows how far the swirling flow's average film thickness can deviate from the predictions based on both Doumas and Laster's and Bazarov's methods. The influence is relatively small up until 1.73 MPa, where the vortex breakdown occurs within the nozzle. The character of the swirling flow at this chamber pressure has changed significantly, making the ideal case of simple swirling flow highly questionable. At least two flow states, upstream and downstream of the vortex breakdown position, are needed to better capture the swirling flow features. These observations are continued in the next section, where mass flow rate is changed as chamber pressure.

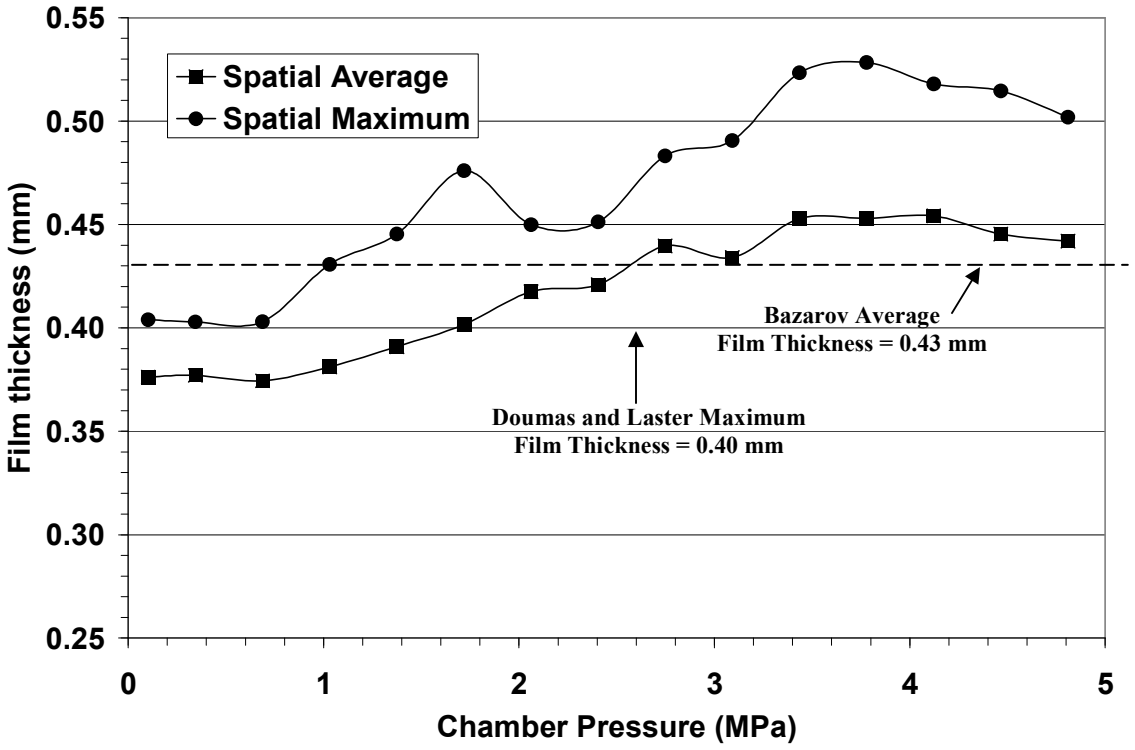

Figure 3.15 Spatially averaged film thickness values

3.3.2 Reduced Mass Flow Rate and Elevated Chamber Pressure

Changing the mass flow rate as well as the chamber pressure showed different behavior, as noted in the high speed videos. In general, as the mass flow rate was reduced, the swirling flow profile changed less with increasing chamber pressure. Figures 3.16 through 3.25 show the various film thickness profiles at set mass flow rate and varying chamber pressure.

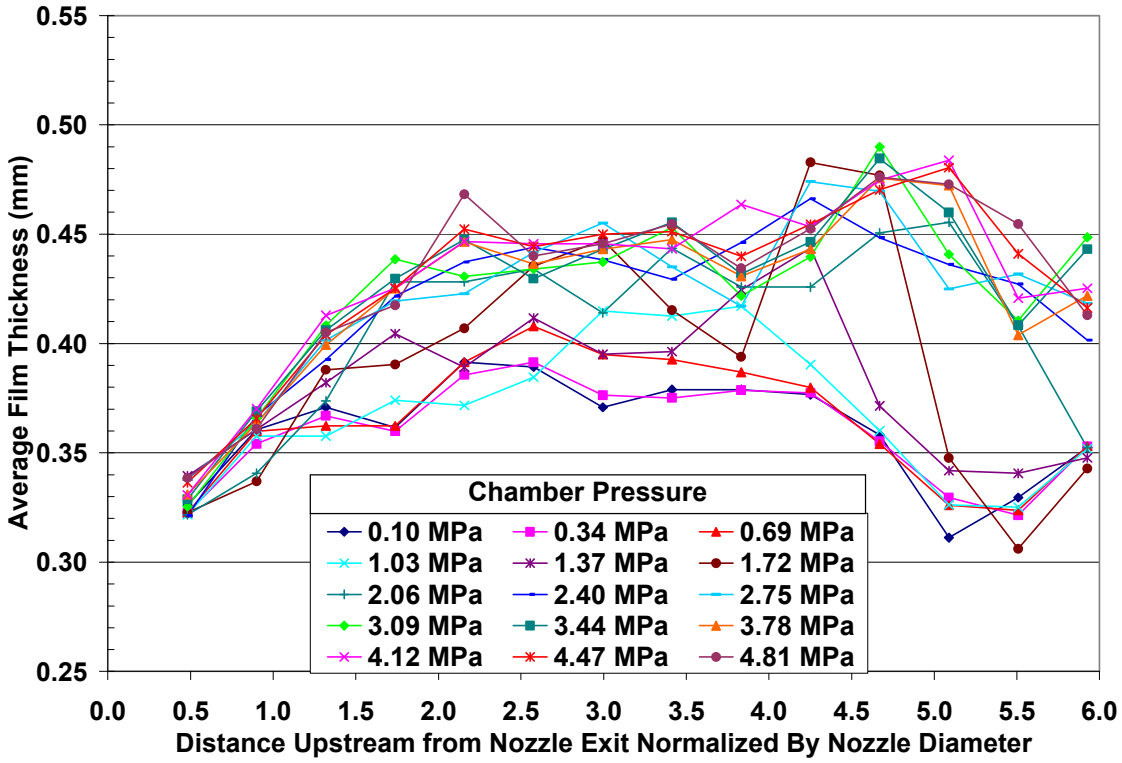

Figure 3.16 Film thickness profiles at 75% relative mass flow rate

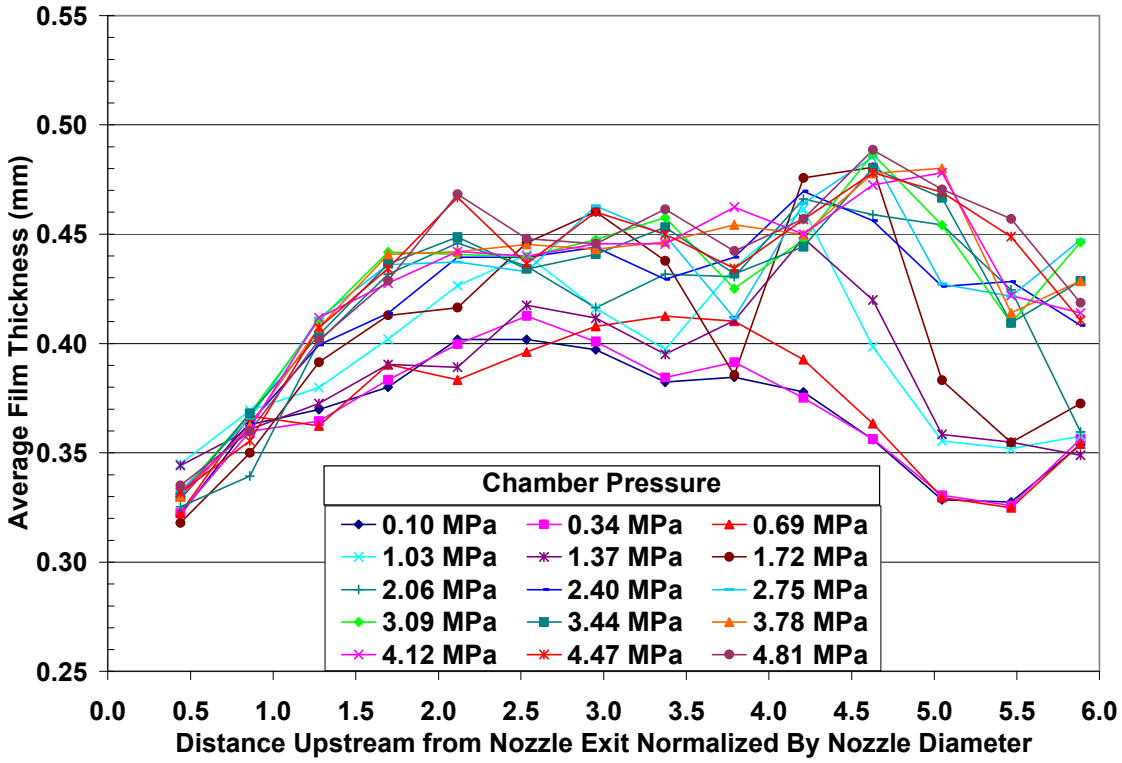

Figure 3.17 Film thickness profiles at 62.5% relative mass flow rate

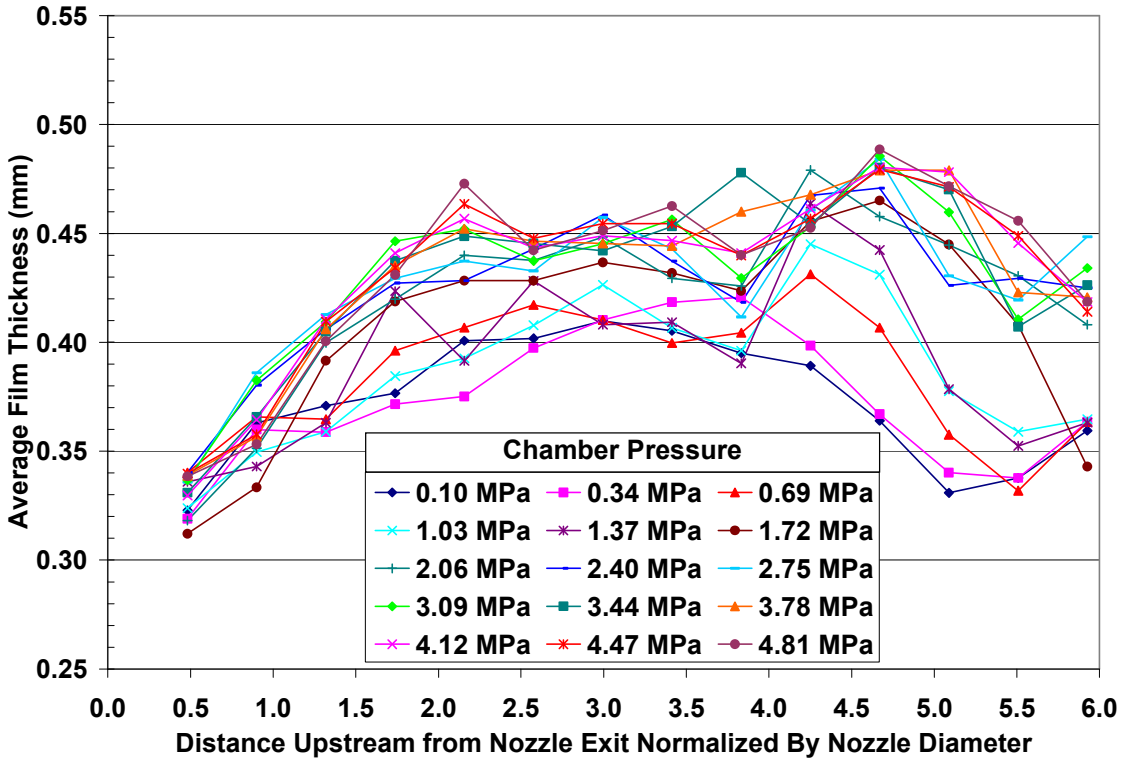

Figure 3.18 Film thickness profiles at 50% relative mass flow rate

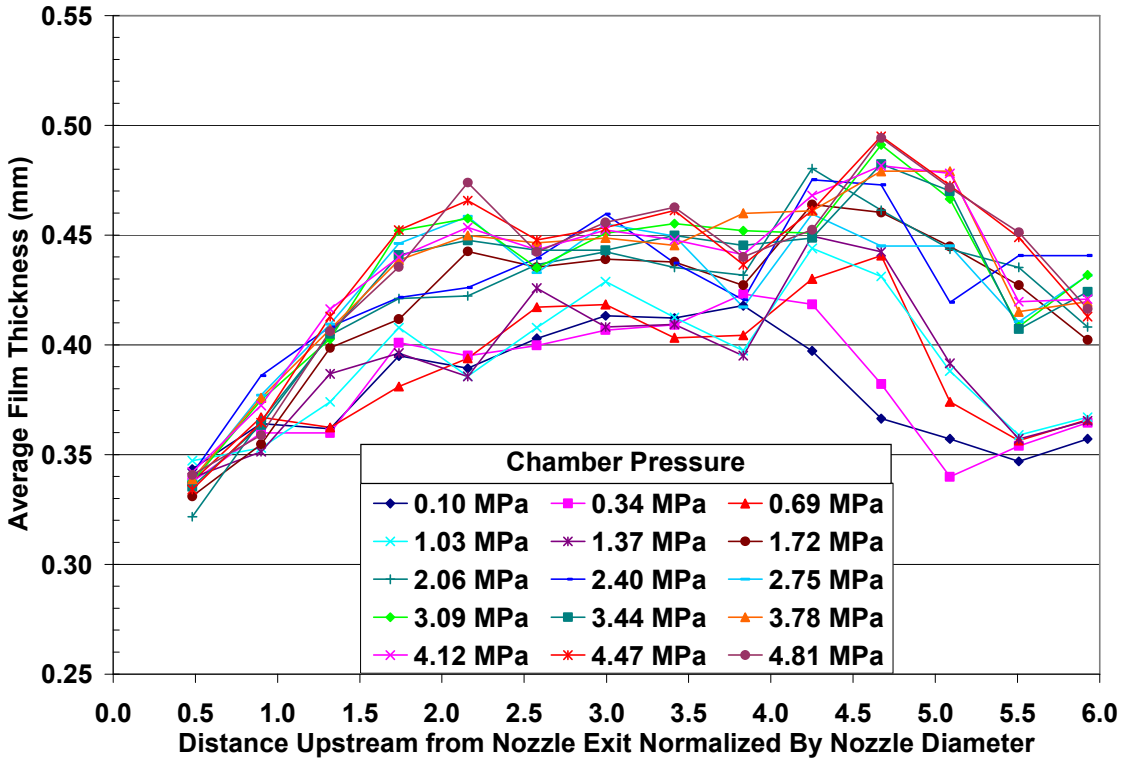

Figure 3.19 Film thickness profiles at 45% relative mass flow rate

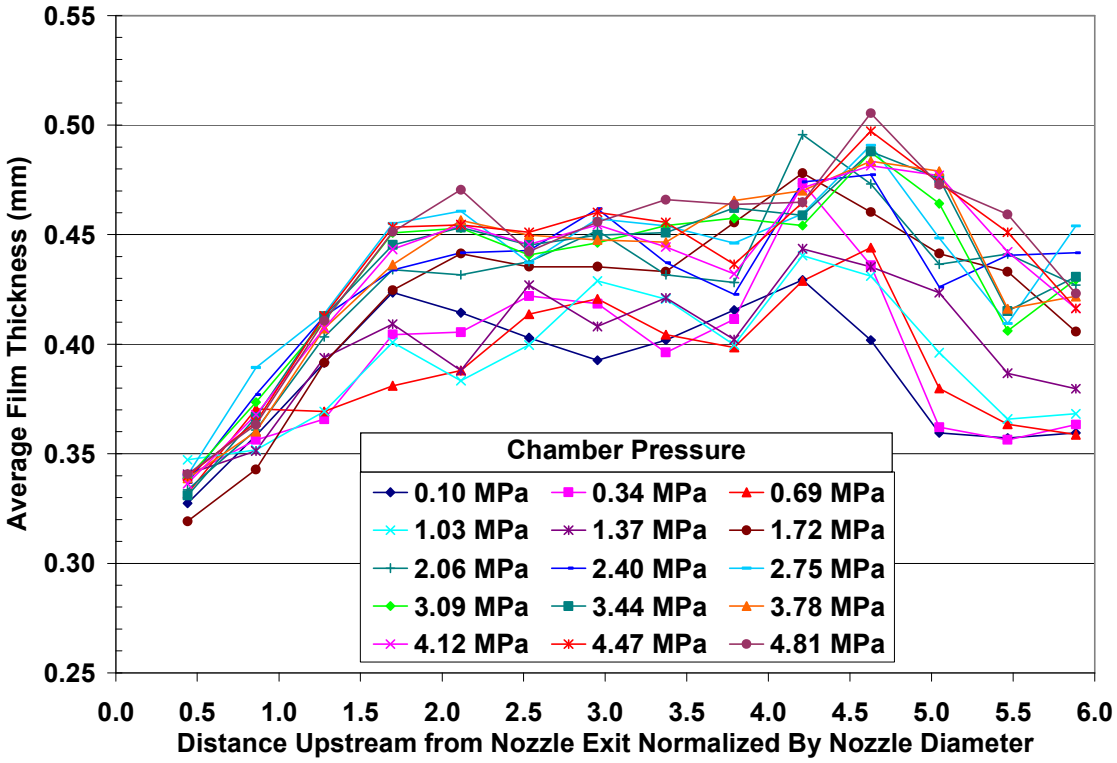

Figure 3.20 Film thickness profiles at 40% relative mass flow rate

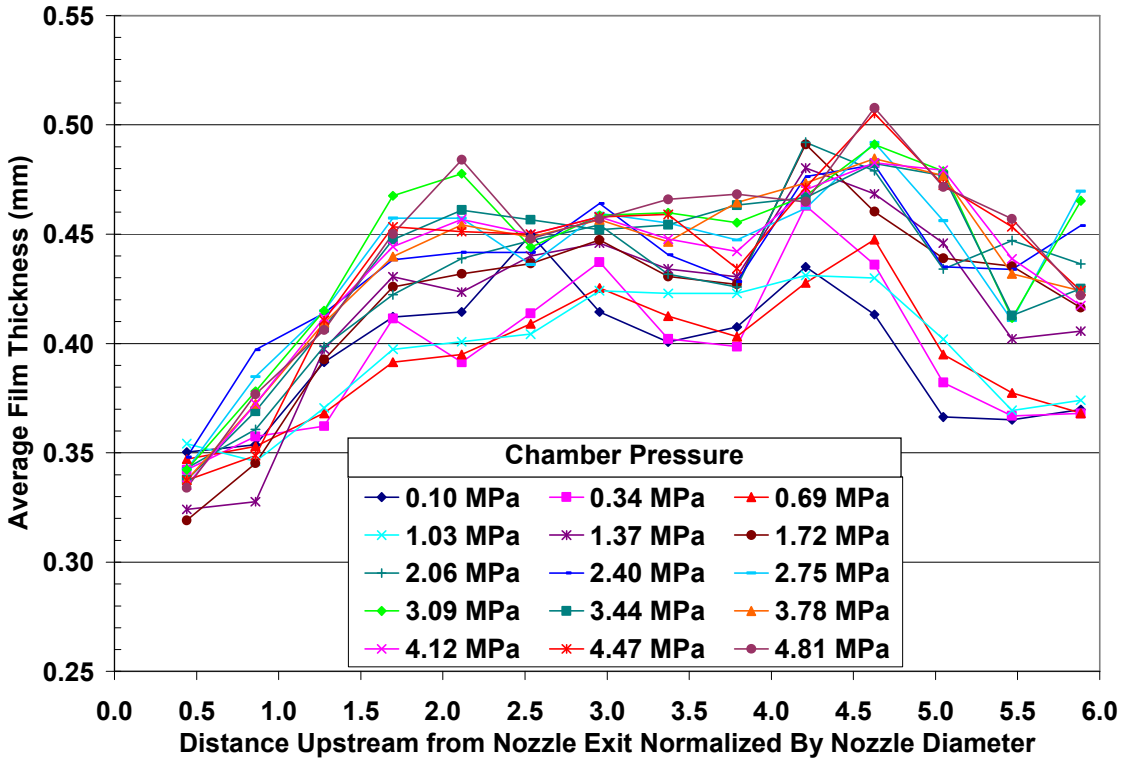

Figure 3.21 Film thickness profiles at 35% relative mass flow rate

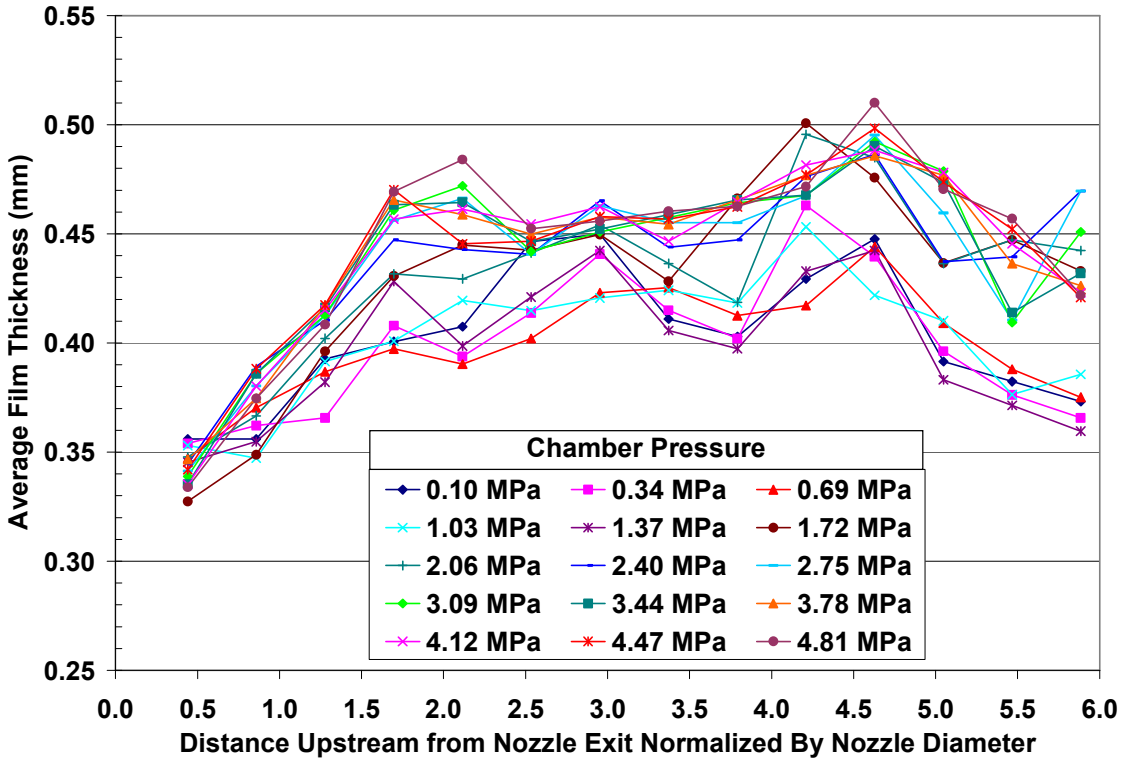

Figure 3.22 Film thickness profiles at 30% relative mass flow rate

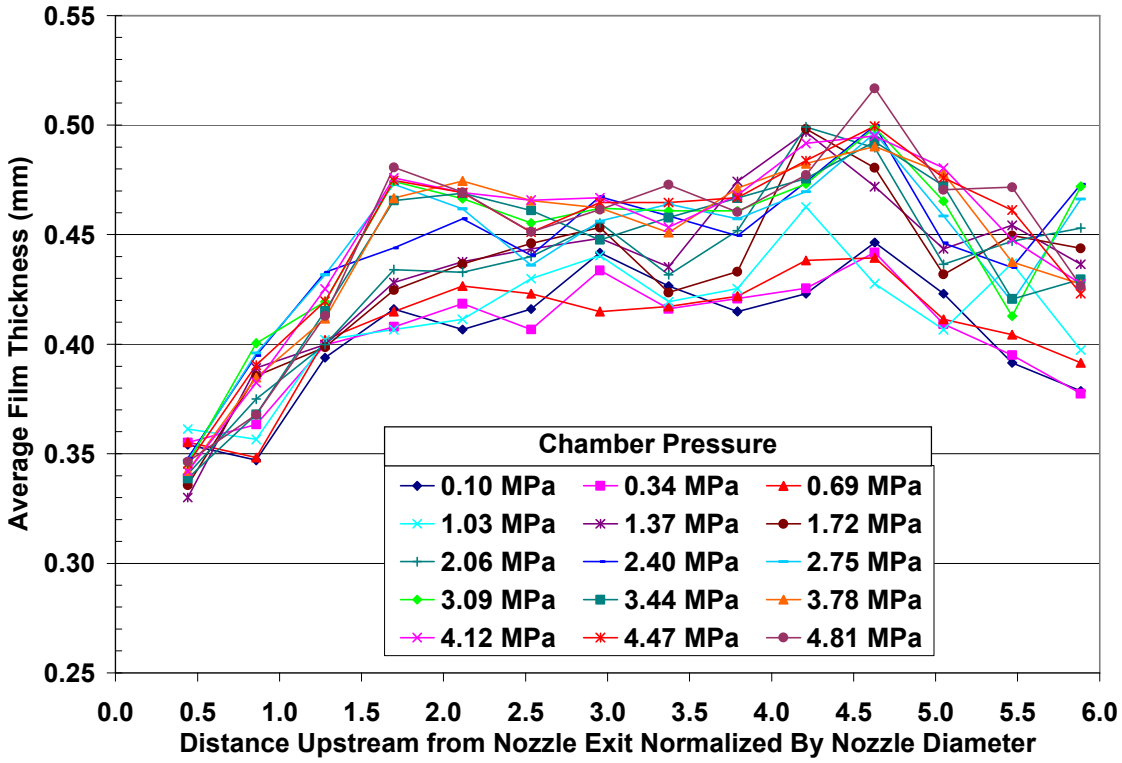

Figure 3.23 Film thickness profiles at 25% relative mass flow rate

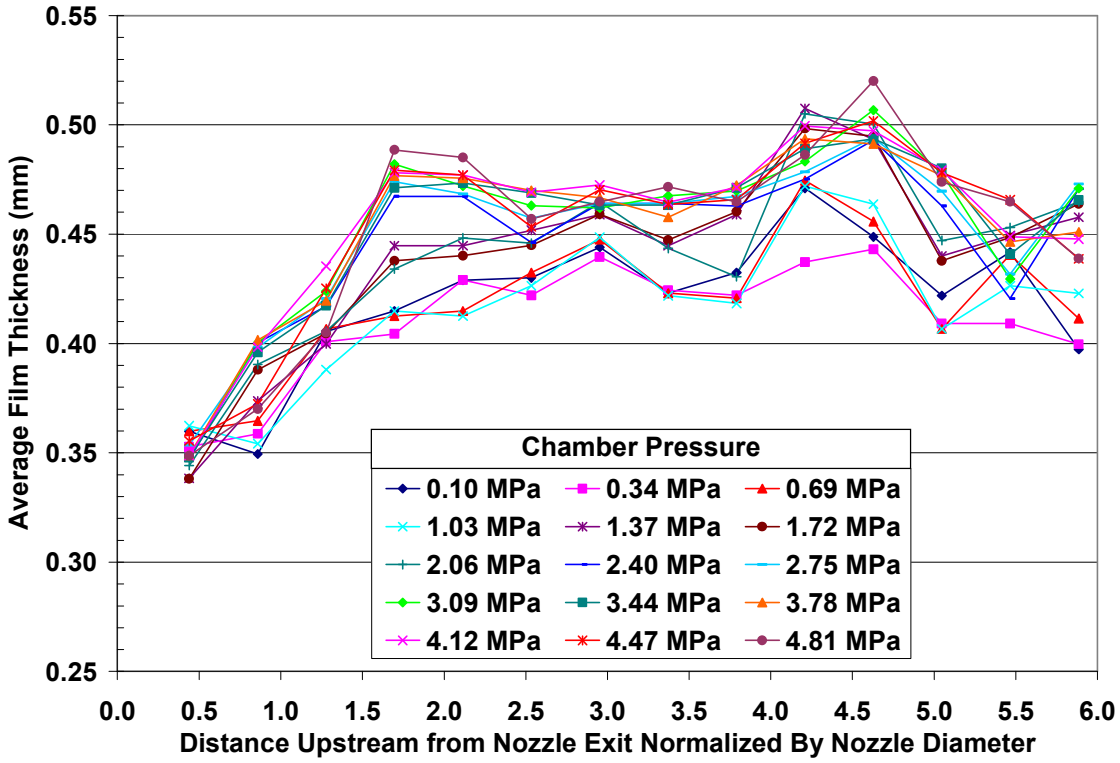

Figure 3.24 Film thickness profiles at 20% relative mass flow rate

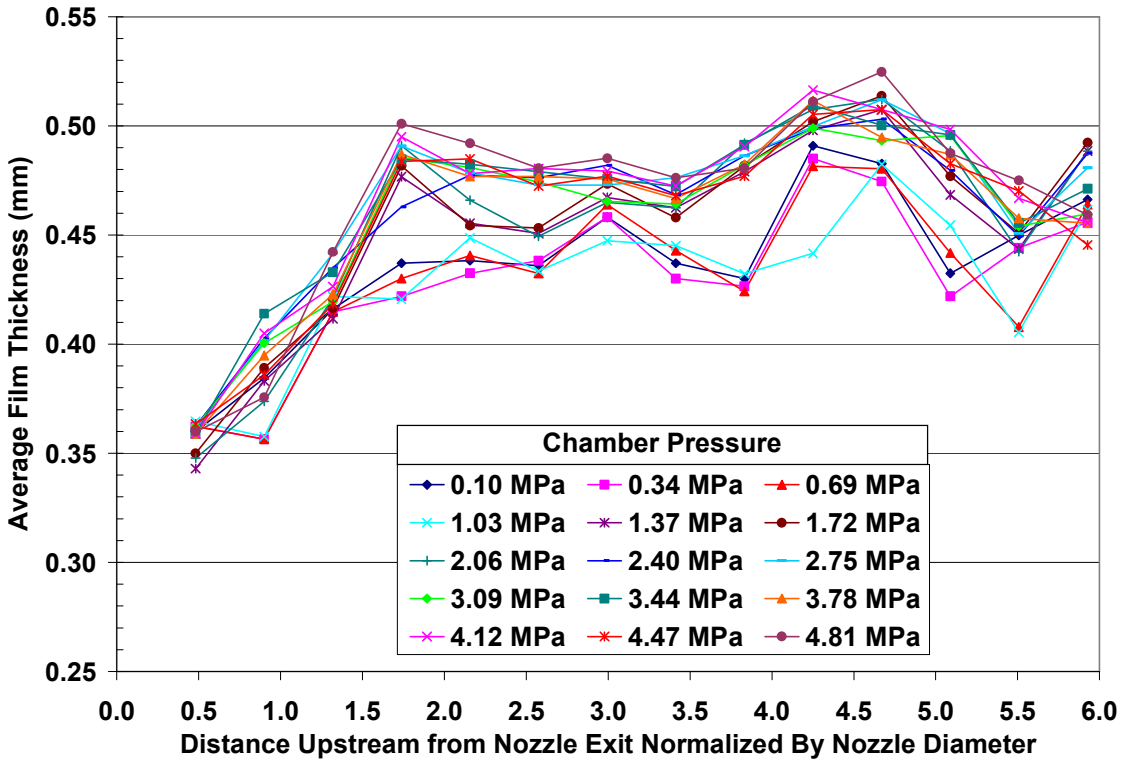

Figure 3.25 Film thickness profiles at 15% relative mass flow rate

As the figures above show, the change in film thickness profile with chamber pressure is relatively the same for mass flow rate as low as 45% of the design mass flow rate. Below 45%, the profile changes become less drastic with increases in chamber pressure. By a relative mass flow rate of 15%, the profiles are still changing with chamber pressure, but the overall spatial distribution of the film thickness along the nozzle length remains somewhat similar. A consistent trend between all mass flow rate values is that the film thickness profiles near the nozzle exit are very insensitive to changes in chamber pressure. Figure 3.26 shows the spatially averaged film thickness for

various mass flow rate and chamber pressure and Figure 3.27 shows the maximum film thickness measured for all operating conditions.

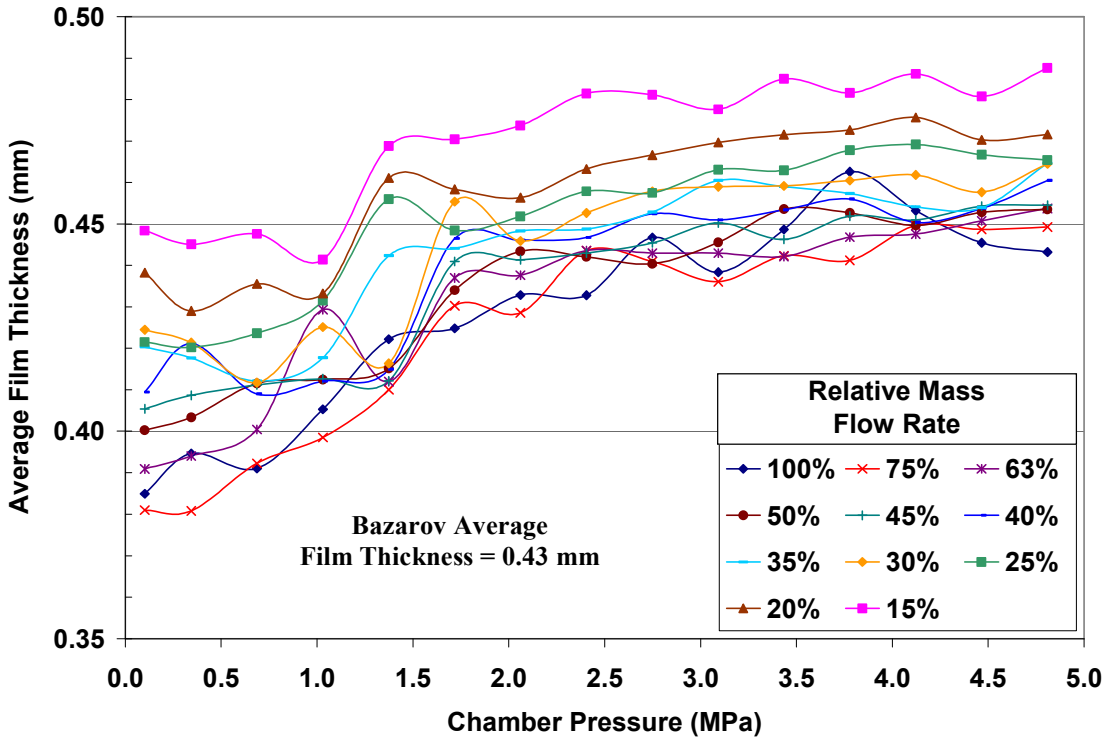

Figure 3.26 Spatially averaged film thickness values

Comparison between the different operating conditions of Figures 3.26 and 3.27 shows that decreasing the mass flow rate works to increase both the spatially averaged film thickness and the maximum film thickness. This trend is similar to that seen when increasing chamber pressure for a fixed mass flow rate, but the reasons for the trends may not be the same. Decreasing the mass flow rate lowers the swirling flow momentum

through the injector. As Lucca-Negro describes [67], swirling flow at low mass flow rate behave more like a solid body rotation with superimposed axial flow.

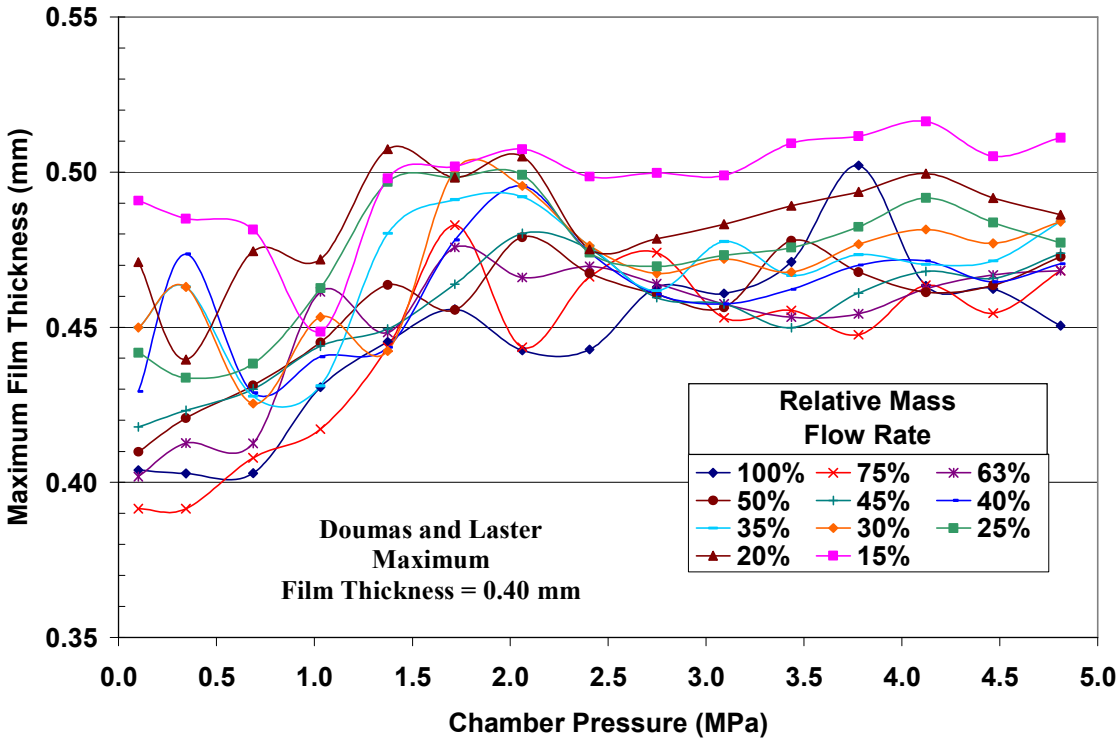

Figure 3.27 Spatial maximum film thickness values

Continually decreasing the injected mass flow rate can effectively decouple the tangential and axial liquid velocity components from each other, letting both components react to increasing chamber pressure separately. Hence, the tangential and axial momentum losses occur independently from each other, simply slowing the flow rotation and causing a net increase in flow cross-sectional area from continuity considerations.

As seen in Figure 3.26, just decreasing the mass flow rate at ambient chamber pressure causes a notable change in the average film thickness.

Conversely, higher mass flow rate can cause a coupling between the axial and tangential momentum components of the flow. At this coupled state between the flow components, effects of chamber pressure on the axial component can easily influence the behavior of the tangential component. Figure 3.26 shows that at higher mass flow rate the film thickness stays relatively close to the value at ambient chamber pressure, but the film thickness changes rather sharply at higher chamber pressure, indicating an overall change in the flow components. This sharp change is somewhat in contrast with the smaller change in film thickness profiles associated with lower mass flow rate. Both situations of high and low mass flow rate are subject to the effects of liquid/gas interface friction from chamber pressure related shear, but the morphological effects on film thickness profiles are exhibited in different ways.

3.4 Discharge Coefficient Measurements

By taking real-time measurements of the liquid volumetric flow rate, the upstream supply pressure, and the downstream chamber pressure, the subsequent mass flow rate and injector pressure drop can be defined for the injector at various operating conditions. Using these variables in conjunction with the defined nozzle diameter from Table 2.6, values of the discharge coefficient can be defined using Equation (1.4). In the same spirit as Figure 2.5, values of mass flow rate as a function of injector pressure drop

were found for the swirl injector, but Figure 3.28 below will also show the influence of downstream chamber pressure.

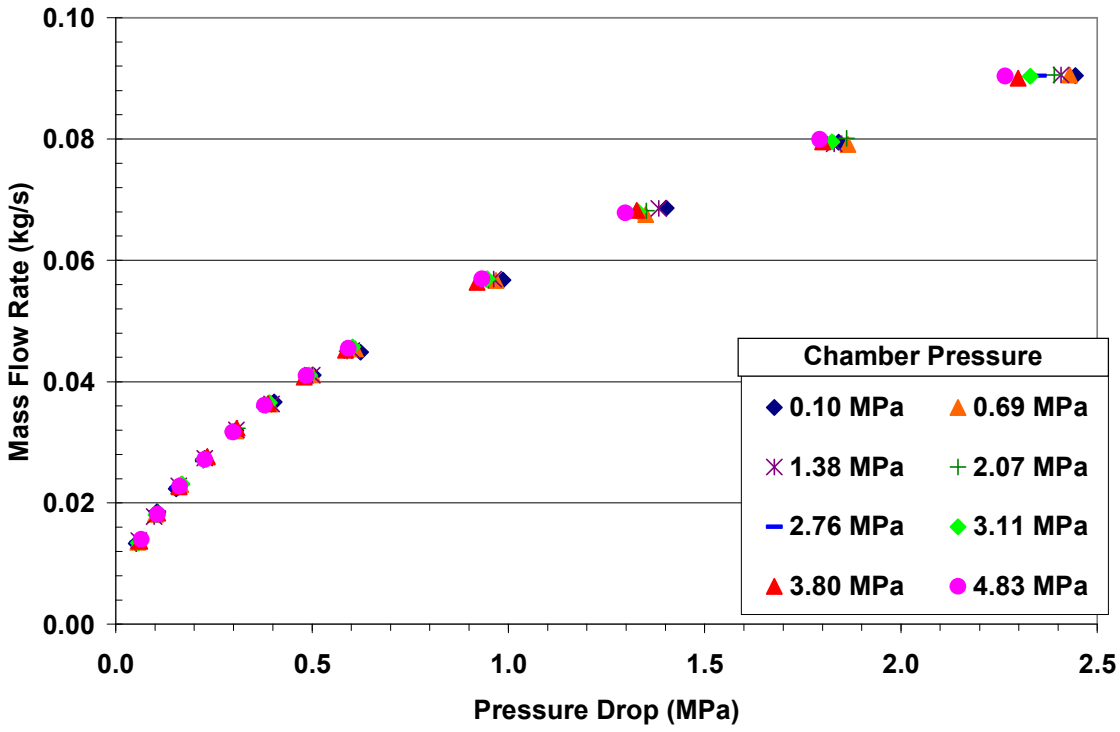

Figure 3.28 Measured mass flow rate versus injector pressure drop and chamber pressure

Figure 3.28 shows that increases in chamber pressure will lower the injector pressure drop needed to give a set mass flow rate. This is more obvious in plots of the needed injector pressure drop relative to the needed injector pressure drop at ambient chamber pressure for a given mass flow rate. Different normalized injector pressure

drops are plotted for varying chamber pressure as the ordinate and abscissa axes in Figure 3.29, respectively.

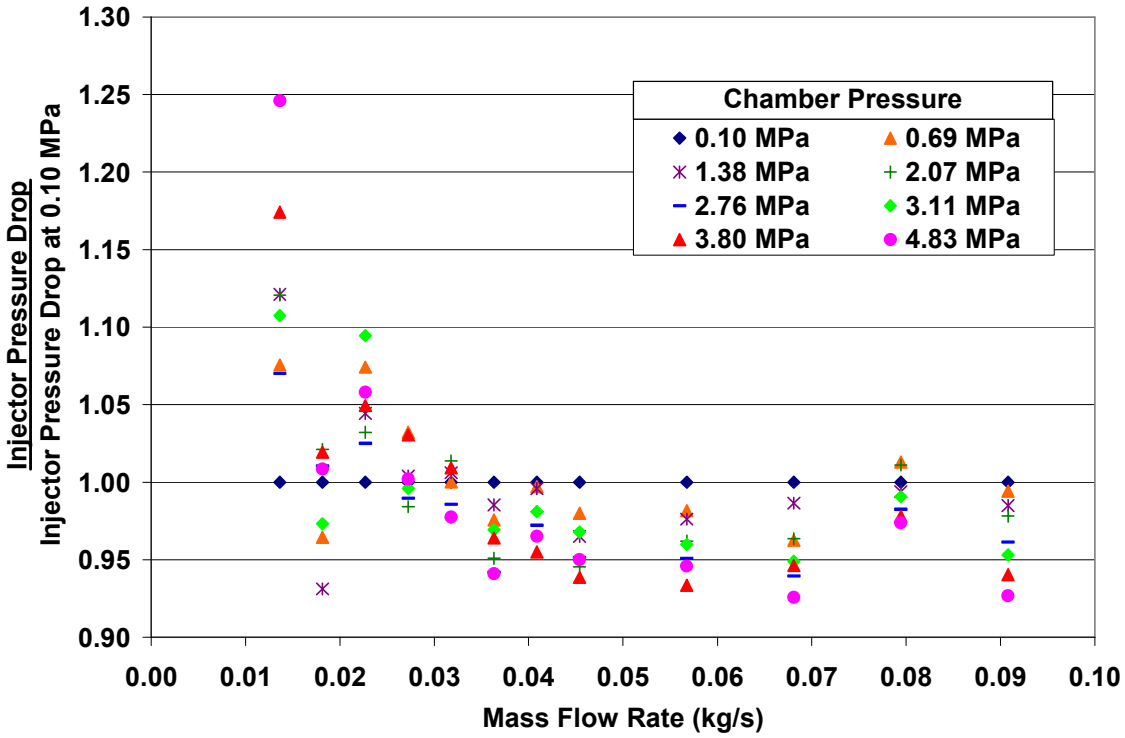

Figure 3.29 Normalized injector pressure drop for varying mass flow rate and chamber pressure

Figure 3.29 shows that as the downstream chamber pressure is increased, the required injector pressure drop to sustain a given mass flow rate decreases. This trend generally stays consistent for every mass flow rate, except for the 'notch' at a mass flow rate of 0.018 kg/s. At this point, the overall data trend of higher chamber pressure

yielding lower needed pressure drops is similar, but a large downward shift in the data is evident. For the relative pressure drop values below 0.018 kg/s, the variance of the data between different chamber pressure is greater than for pressure drop values above 0.018 kg/s. A potential indicator for this change could be the discharge coefficient, plotted as a function of mass flow rate and chamber pressure in Figure 3.30. Equation (1.4) was used to define the discharge coefficient, using the same values measured from Figure 3.28.

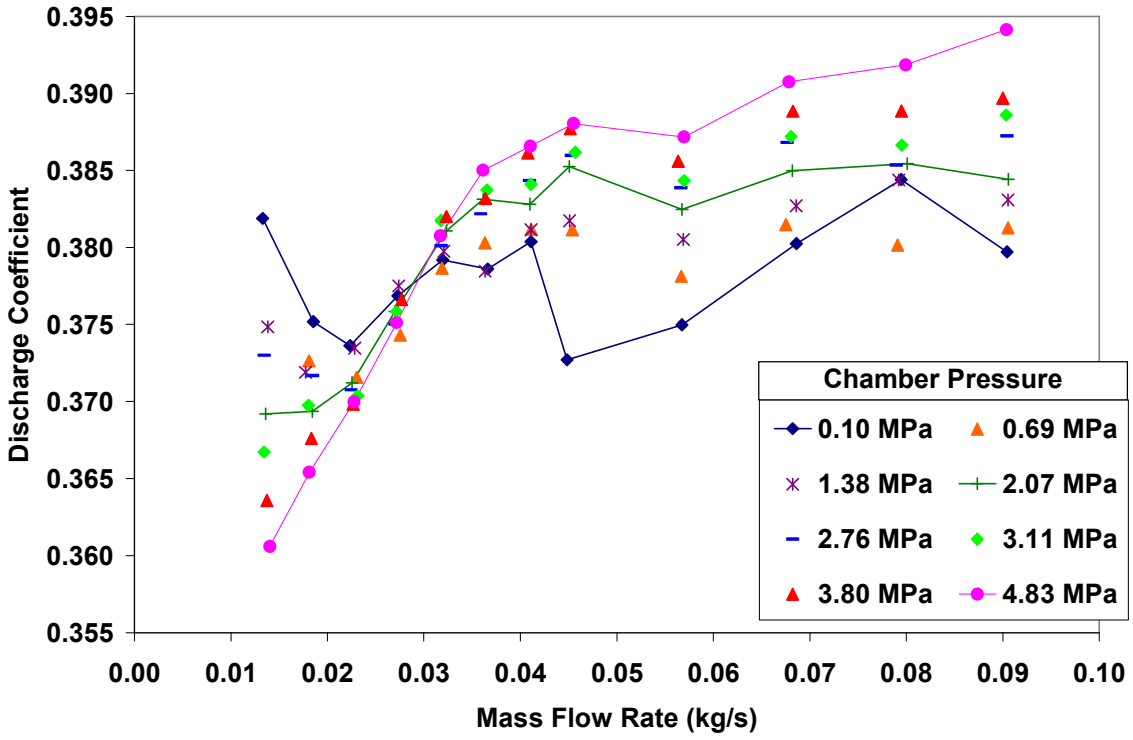

Figure 3.30 Discharge coefficients for varying mass flow rate and chamber pressure

Figure 3.30 shows several interesting features. Discharge coefficient trends change with certain combinations of mass flow rate and chamber pressure. At atmospheric chamber pressure, the discharge coefficient values display three different trends in Figure 3.30. From the highest mass flow rate down to approximately 0.045 kg/s, the discharge coefficient values generally decrease with decreasing mass flow rate. From 0.045 kg/s to 0.04 kg/s, the discharge coefficient trend changes notably, giving a steeper decrease in discharge coefficient values with decreasing mass flow rate. Also, the absolute values of the discharge coefficient at 0.04 kg/s and less are higher than at 0.045 kg/s. This change in discharge coefficient trend is believed to be related to a tangential slot hydraulic flip phenomenon and is discussed in the next section. At 0.023 kg/s, the discharge coefficient changes again to give increasing discharge coefficient values with decreasing mass flow rate.

The discharge coefficient trends also show sensitivity to increasing chamber pressure. Increasing the chamber pressure at a fixed mass flow rate raises the discharge coefficient for mass flow rate of 0.036 kg/s and greater. Below 0.036 kg/s, increasing chamber pressure actually decreases the discharge coefficient. The trend of increasing discharge coefficient with decreasing mass flow rate at 0.023 kg/s is exhibited at moderate chamber pressure. However, increasing the chamber pressure to levels of 3.11 MPa and above actually 'suppress' this trend to exhibit the same behavior of discharge coefficient with mass flow rate seen between 0.023 kg/s and 0.04 kg/s.

The uncertainty associated with the flow rate and pressure drop measurements must be taken into account when viewing this data's viability in quantifying trends of the discharge coefficient. Figure 3.31 shows the calculated 95% uncertainty bands of the

discharge coefficient values show in Figure 3.30 relative to the nominal discharge coefficient values, denoted $2U_{CD}/C_D$. Chamber pressure uncertainty has a large influence in the discharge coefficient uncertainty, especially at the highest chamber pressure of 4.83 MPa. Also noted at the low mass flow rate values of 0.014-0.018 kg/s is again the large variance of discharge coefficient values with chamber pressure.

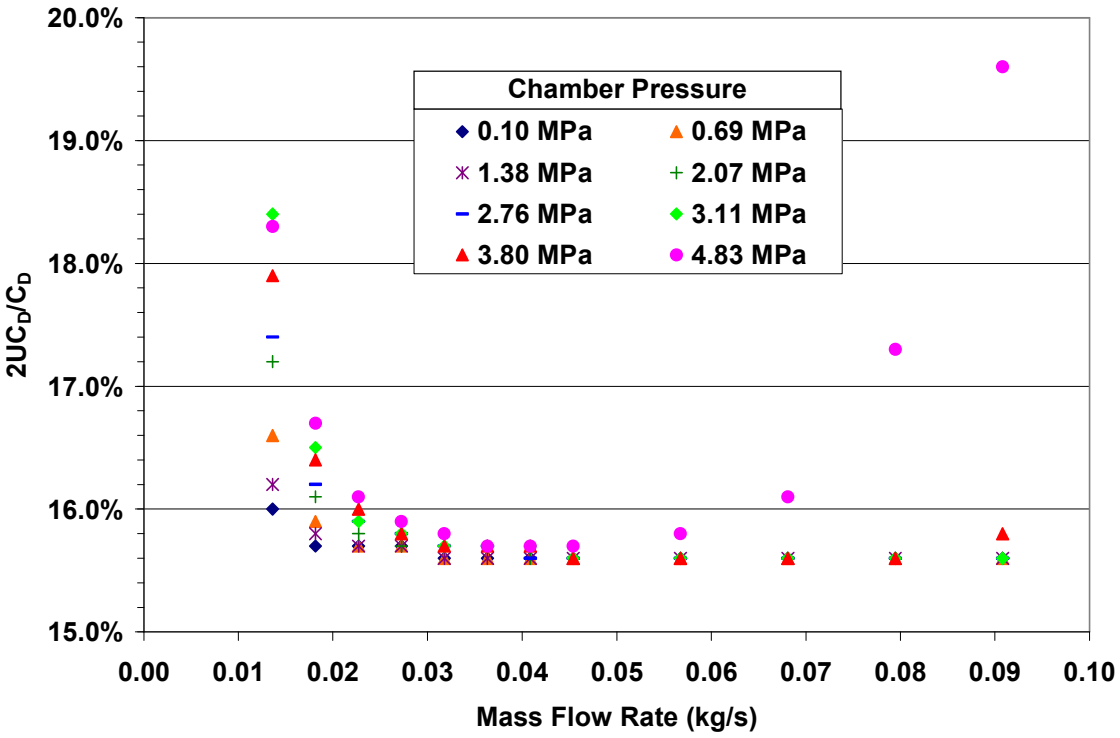

Figure 3.31 Relative 95% confidence total uncertainty band of the discharge coefficient for varying mass flow rate and chamber pressure

Even though the uncertainty values associated with each average discharge coefficient values are large, the trends associated with the discharge coefficient averages in Figures. 3.28 to 3.30 are still believed viable. Higher measurement uncertainties mainly place a demand to collect a large number of samples per reading to attain a trustworthy average. It is true that the uncertainty values seen in Figure 3.31 above denote large variances between two sample readings for the same operating condition, but given enough samples a viable reading average can be taken and trends, as seen in Figure 3.28 to Figure 3.30, can be established. Since each reading had over 500 samples, it was believed that the sample average per operating condition is viable and that the trends seen in the data are real.

In order to better illuminate this sensitivity of flow rate dependence on discharge coefficient, Figure 3.29 is plotted again as Figure 3.32, but this time with chamber pressure on the abscissa axis. As Figure 3.32 clearly shows, there is a notable change in how the discharge coefficient varies with set mass flow rate values. For flow rate above 0.027 kg/s, increasing the chamber pressure clearly increases the discharge coefficient. However, at 0.027 kg/s, the influence of chamber pressure is relatively little. Below 0.027 kg/s, the increase of chamber pressure actually works to decrease the corresponding discharge coefficient. This trend is believed to be related to a switching of the tangential slot flow regime and is discussed later in this chapter.

To quantify this trend of discharge coefficient to variables of chamber pressure and mass flow rate, two curve fits were performed. Variables chosen to curve-fit against are the slot Reynolds number, and the density ratio between the ambient gas density and the liquid density. These two variables were chosen to match the results from the

dimensional analysis in Chapter 2. Weber number was not considered in this curve fit, since the effects of surface tension were deemed not important to account for the pressure drops within the injector.

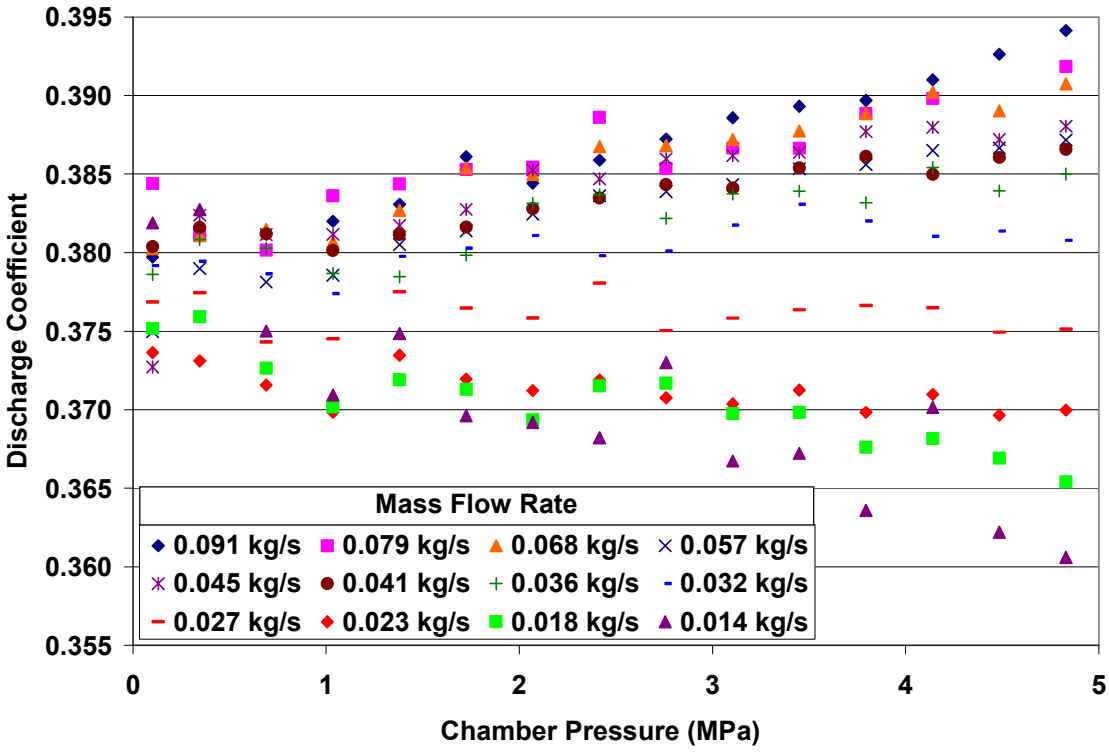

Figure 3.32 Discharge coefficient variation with set mass flow rate and changing chamber pressure

A linear function was defined for each flow rate, represented as a slot Reynolds number. This linear function is listed as Equation (3.4).

$$C_D\left(\frac{\rho_g}{\rho_l}, \mathrm{Re}_o\right) = S(\mathrm{Re}_o)\left[\frac{\rho_g}{\rho_l}\right] + C_{Do}(\mathrm{Re}_o) \tag{3.4}$$

In Equation (3.4), the slope, S, and intercept, C_{Do}, are both assumed functions of slot Reynolds number only. Figure 3.33 shows the same discharge coefficient values as in Figure 3.32, but with slot Reynolds number in place of mass flow rate and gas to liquid density ratio in place of chamber pressure. Table 3.1 gives the slope and intercept for each measured slot Reynolds number set of values shown in Figure 3.33.

Table 3.1 Slope and intercept of discharge coefficient trends in Figure 3.33

Slot Reynolds Number	Slope	Intercept
11260	0.256	0.379
8411	0.202	0.380
7050	0.206	0.377
5566	0.200	0.379
5071	0.123	0.380
4453	0.120	0.379
3958	0.060	0.379
3340	-0.012	0.376
2845	-0.055	0.373
2226	-0.150	0.375
1732	-0.324	0.379

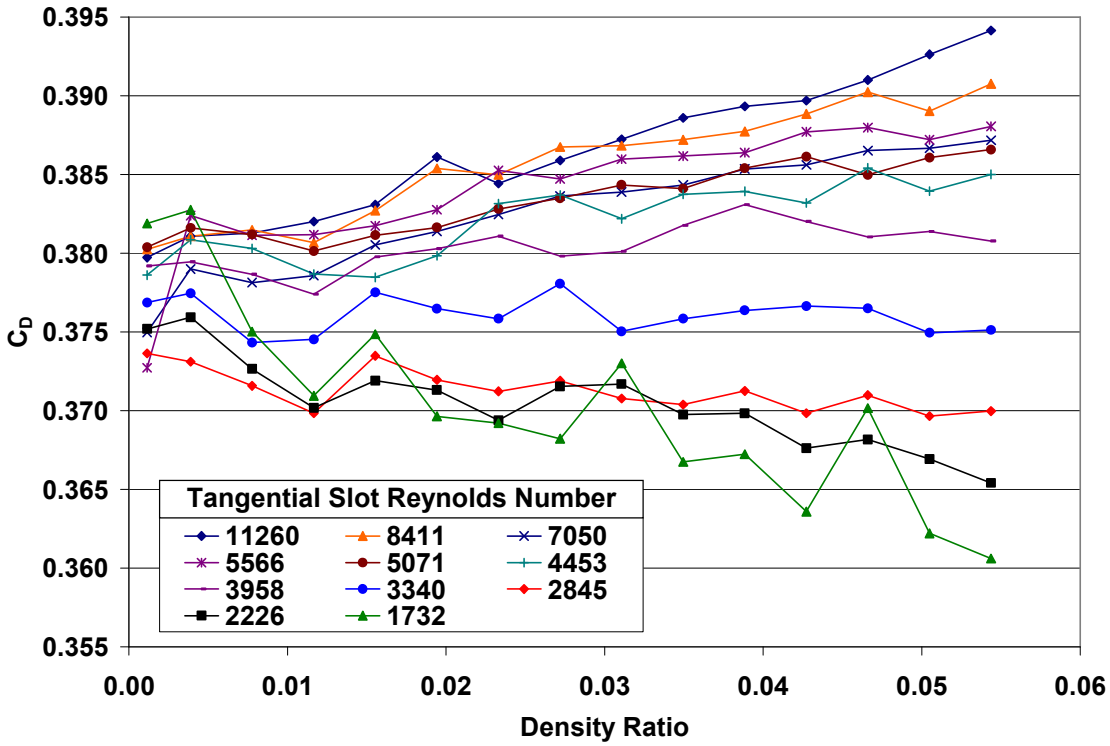

Figure 3.33 Discharge coefficient variation with slot Reynolds number and gas to liquid density ratio

The second curve-fit operation captures how the slopes listed in Table 3.1 change with slot Reynolds number. A cubic curve-fit was found to best match the trend shown from the slope values. This cubic fit is given as Equation (3.5).

$$S(\mathrm{Re}_0) = (2\cdot 10^{-12})(\mathrm{Re}_0)^3 - (5\cdot 10^{-8})(\mathrm{Re}_0)^2 + 0.0004(\mathrm{Re}_0) - 0.8381 \qquad (3.5)$$

The slot Reynolds number at which the discharge coefficient trend changes is where Equation (3.5) goes to zero. The zero-crossing value corresponds to a slot Reynolds number of 3443, equal to 0.013 kg/s. Figure 3.34 shows the slope and intercept values of Equation (3.5).

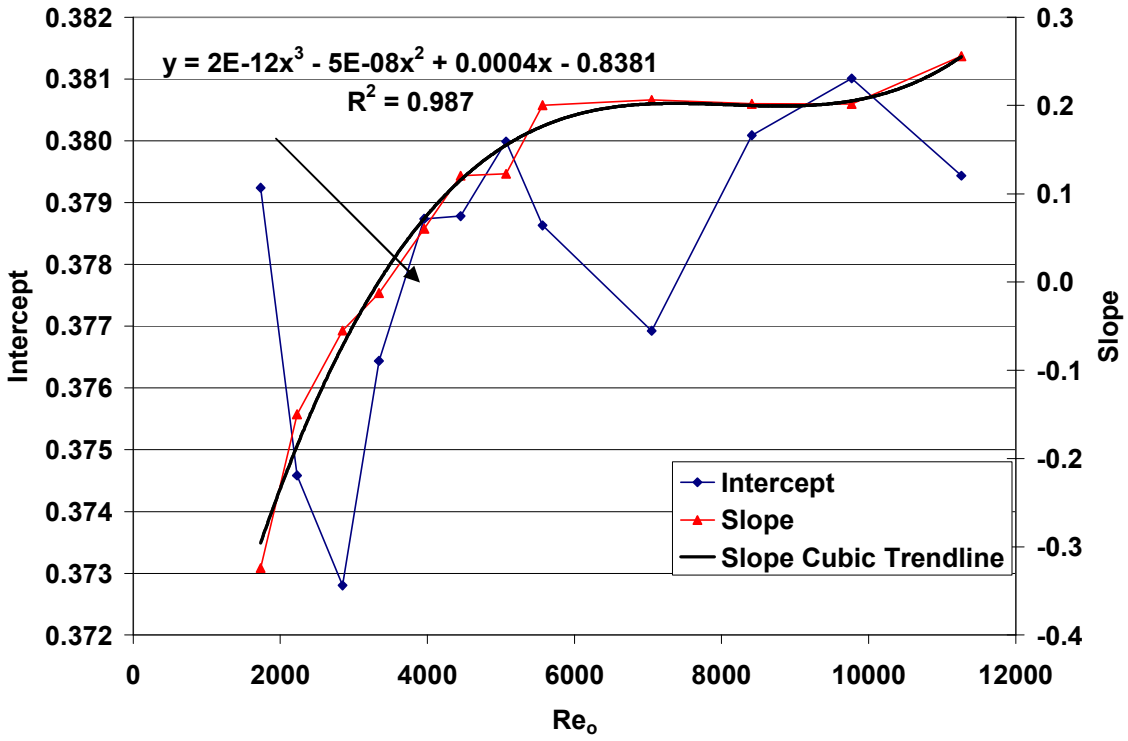

Figure 3.34 Slope and intercept values for Equation (3.5)

The following two sections will give possible explanations on the observed changes in discharge coefficient trends with injector operating conditions. These

explanations are not considered the absolute answers to the observed changes, but rather potential explanations which warrant further investigation and study in future works.

3.4.1 Tangential Orifice Hydraulic Flip

For this swirl injector design, the tangential slots were considered sharp edged jet orifices. The change in discharge coefficient trend with decreasing mass flow rate at 0.045 kg/s is very similar to hydraulic flip effects seen in jet orifice flow. A given orifice design can have several different flow structures, which 'flip' from one structure to another at certain combinations of injected mass flow rate and chamber pressure. Flow into a circular orifice typically detaches from the orifice inlet edge, creating a separated jet flow through the orifice surrounded by a recirculation bubble. The separated flow can reattach itself to the orifice wall, provided that the orifice length is long enough and the flow conditions are favorable. The recirculation zone can exhibit low static pressures, which can induce flow cavitation if these static pressures reach levels below the fluid vapor pressure. If the flow does not reattach along the orifice walls, then the local cavitation at the recirculation zone can exist all along the orifice length. The transition between separated flow and reattached flow has been defined as the hydraulic flip phenomenon and is important in understanding orifice cavitation.

Hoehn et al. identified trends of discharge coefficient with orifices experiencing hydraulic flip [70]. If the orifice flow structure is separated, then the discharge coefficient can show low values relative and the flow is considered flipped. If the flow structure is attached (or reattaches) inside the orifice, the discharge coefficient shows

higher values than expected and the flow is considered unflipped. Hoehn et al. used a metric based on orifice cavitation to evaluate onset of hydraulic flip. The orifice was considered flipped if the predicted orifice discharge coefficient was above the cavitation metric, and unflipped if the predicted discharge coefficient was below the metric. Equation (3.6) gives the cavitation metric used by Hoehn [70].

$$\Delta P_{critical} = \frac{P_c - P_V}{\left(\frac{C_{D,v}}{C_C}\right)^2 - 1} \tag{3.6}$$

In Equation (3.6), $\Delta P_{critical}$ is the orifice pressure drop needed to cause cavitation at a sharp edged inlet. P_V is the fluid vapor pressure, which is taken as 3.165 kPa for water. $C_{D,v}$ is the predicted orifice discharge coefficient, and C_c is the orifice contraction coefficient. The orifice contraction coefficient is the ratio of the separated flow's cross-sectional area to the orifice's geometric cross-sectional area. This work used $C_c = 0.62$ for cavitation limit calculations, as used for sharp edged inlets by other researchers [70, 71]. The orifice discharge coefficient was evaluated using a relation reported by Khavkin [34], given below as Equation (3.7).

$$\mathrm{Re}_o = \frac{V_o(2r_0)}{\upsilon} = \left(\frac{\dot{\forall}}{N_o \pi r_o^2}\right)\left(\frac{2r_o}{\upsilon}\right) = \frac{2\dot{\forall}}{N_o \pi \upsilon r_0} \tag{3.7a}$$

$$C_{D,o} = \left[1 + \frac{5.843}{\log\left(\mathrm{Re}_o^{1.432}\right)}\right]^{-0.5} \tag{3.7b}$$

Inlet centerline velocity is used to define a tangential slot Reynolds number, which is then used to calculate an orifice discharge coefficient. Figure 3.35 shows the comparison between the predicted orifice discharge coefficient for this work, and the cavitation limit for several chamber pressure values using Equation (3.6).

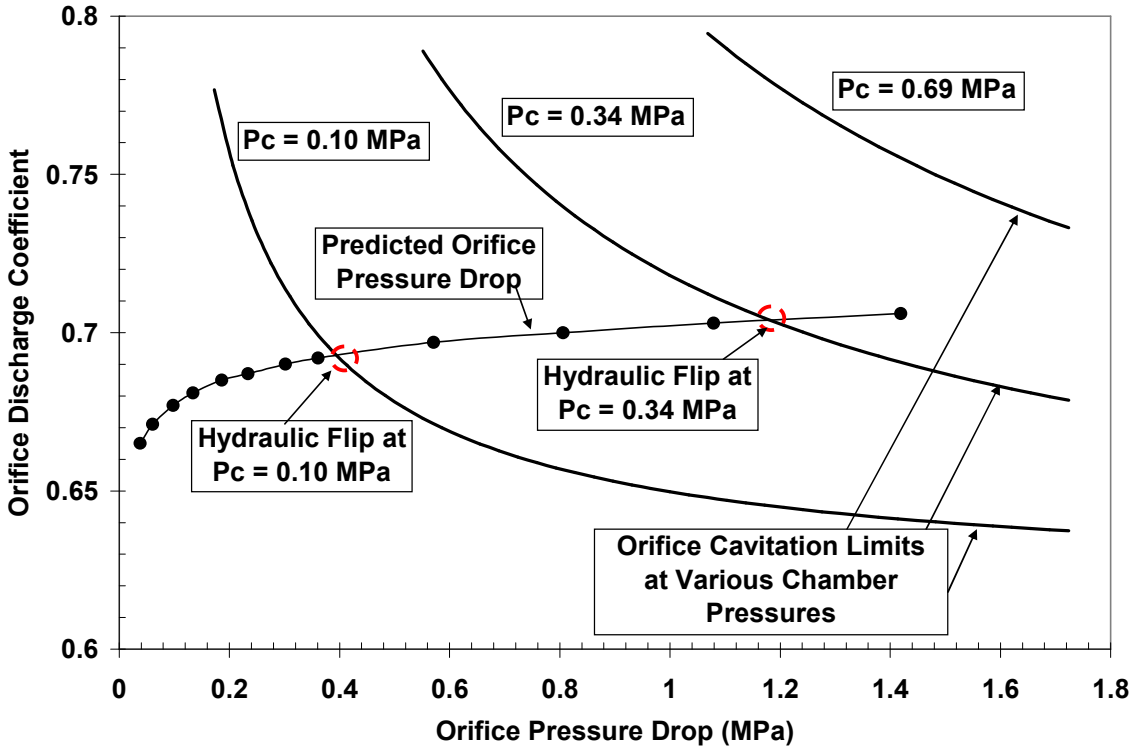

Figure 3.35 Orifice discharge coefficient and cavitation limits

Figure 3.35 shows the predicted discharge coefficient values from Equation (3.7b) intersecting with predicted discharge coefficient values from Equation (3.6) at an orifice pressure drop of 0.414 MPa and chamber pressure of 0.10 MPa. It is at this pressure drop and chamber pressure that hydraulic flip will occur within the orifice. Increasing the chamber pressure will increase the orifice pressure drop at which hydraulic flip will occur. At 0.34 MPa chamber pressure, the orifice pressure drop at which hydraulic flip will occur increases to 1.207 MPa. For 0.69 MPa chamber pressure and higher, the flow is not expected to cavitate inside the orifice.

Figure 3.36 re-plots the injector discharge coefficient values from Figure 3.30, with the addition of the predicted orifice discharge coefficient values. Both data sets are plotted versus the tested mass flow rate operating points. The orifice slots are predicted to have a hydraulic flip point at a mass flow rate of approximately 0.05 kg/s, corresponding to the orifice pressure drop of 0.414 MPa. The measured injector discharge coefficient values also show a notable change in discharge coefficient trends between 0.04 and 0.06 kg/s, reflecting the influence of orifice hydraulic flip. At 0.10 MPa chamber pressure, lowering injector mass flow rate below 0.05 kg/s causes the tangential slot orifices to become unflipped and the orifice discharge coefficient to rise. If the orifice discharge coefficient rises, then the injector discharge coefficient rises as well. Above 0.05 kg/s, the orifice becomes flipped, the orifice discharge coefficient lowers, and the injector discharge coefficient lowers as well.

Figure 3.36 shows some disagreement with the predicted orifice behavior in Figure 3.35. As the chamber pressure is increased, the injector discharge coefficient values still display trends associated with orifice hydraulic flip. Increasing the operating

chamber pressure does lessen the gap between the flipped and unflipped injector discharge coefficient values around the mass flow rate of approximately 0.05 kg/s. By 4.83 MPa chamber pressure, the injector discharge coefficient trend is similar to that of the orifice discharge coefficient. Orifice flow reattachment could have started to occur for higher chamber pressure, giving higher discharge coefficient values for all mass flow rate operation.

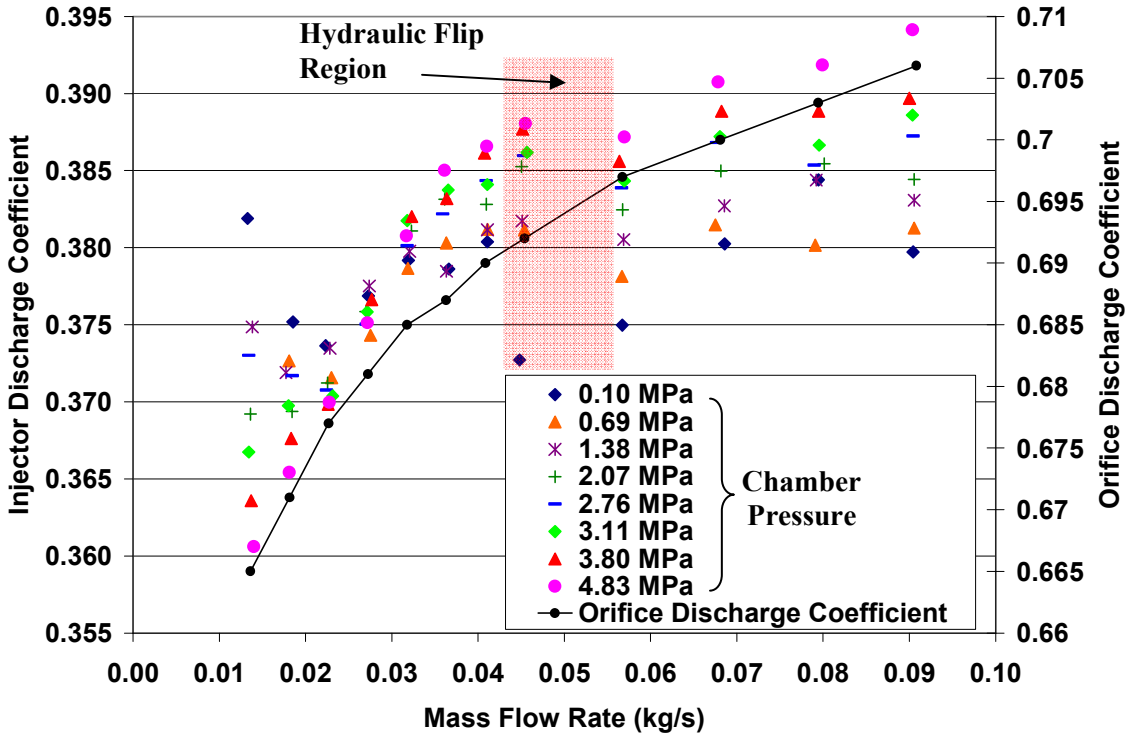

Figure 3.36 Comparison between tangential slot orifice and injector discharge coefficients

Also, Equation (3.6) is derived assuming that the downstream static pressure of the orifice flow is the same as the chamber pressure. For swirl injectors, the downstream static pressure is actually the liquid static pressure of the swirling vortex chamber flow. While the static pressure in the swirling flow's gas core may be the same as the chamber pressure, the downstream liquid static pressure is not the same as the chamber pressure. The most appropriate value to use in Equation (3.6) instead of chamber pressure is the actual liquid downstream static pressure, but estimates of these values were not considered in this work.

3.4.2 Flow Coefficient Effects

Handbooks on orifice flow show that below a certain orifice Reynolds number, the flow can display increasing tangential slot discharge coefficient values for decreasing Reynolds numbers. Equation (3.8) defines the orifice flow coefficient with respect to the orifice discharge coefficient and the orifice geometric parameter, β [72]. Figure 3.37 shows how the orifice flow coefficient and the subsequent orifice discharge coefficient, changes with slot Reynolds number. The highlighted section of Figure 3.37 corresponds to the mass flow rate range in Table 3.1.

$$C_D = \frac{C}{\sqrt{1-\beta^2}} \tag{3.8a}$$

$$\beta = \frac{d_1}{d_2} \approx \sqrt{C_C} \tag{3.8b}$$

The contraction coefficient was defined in the previous section as 0.62. The corresponding orifice geometric parameter is taken as approximately 0.8 according to Equation (3.8b). At a fixed geometric parameter of 0.8, Figure 3.37 shows that the orifice flow coefficient increases notably as the Reynolds number decreases below approximately 4000. Table 3.1 showed that the trend of injector discharge coefficient with slot Reynolds number changed at a Reynolds number of 3443. For mass flow rates below this value, the slot discharge coefficient and the composite injector discharge coefficient should increase. At low Reynolds numbers and increasing chamber pressures, the injector discharge coefficient decreases. Ref. [72] does not offer any link between the orifice flow coefficient and the downstream liquid static pressure, so no explanation could be generated at the time of this work. Figure 3.34 is replotted as Figure 3.38 below, relating the observed flow regimes of the tangential slot orifices to the measured injector discharge coefficients.

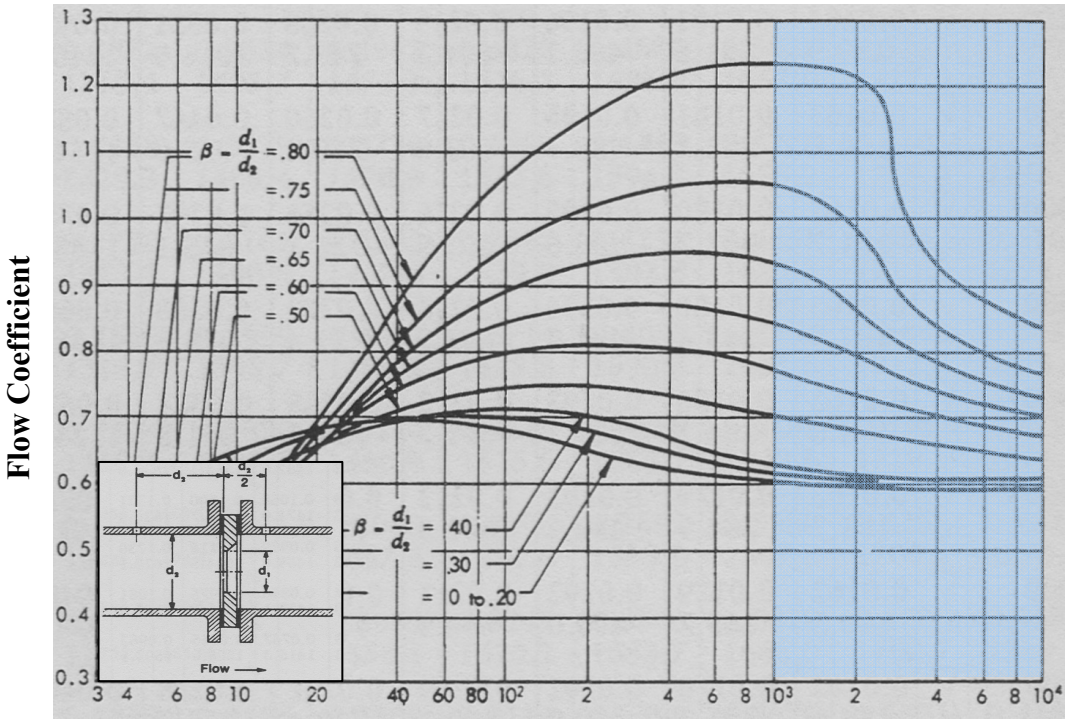

Figure 3.37 Orifice Flow Coefficient vs. Slot Reynolds Number

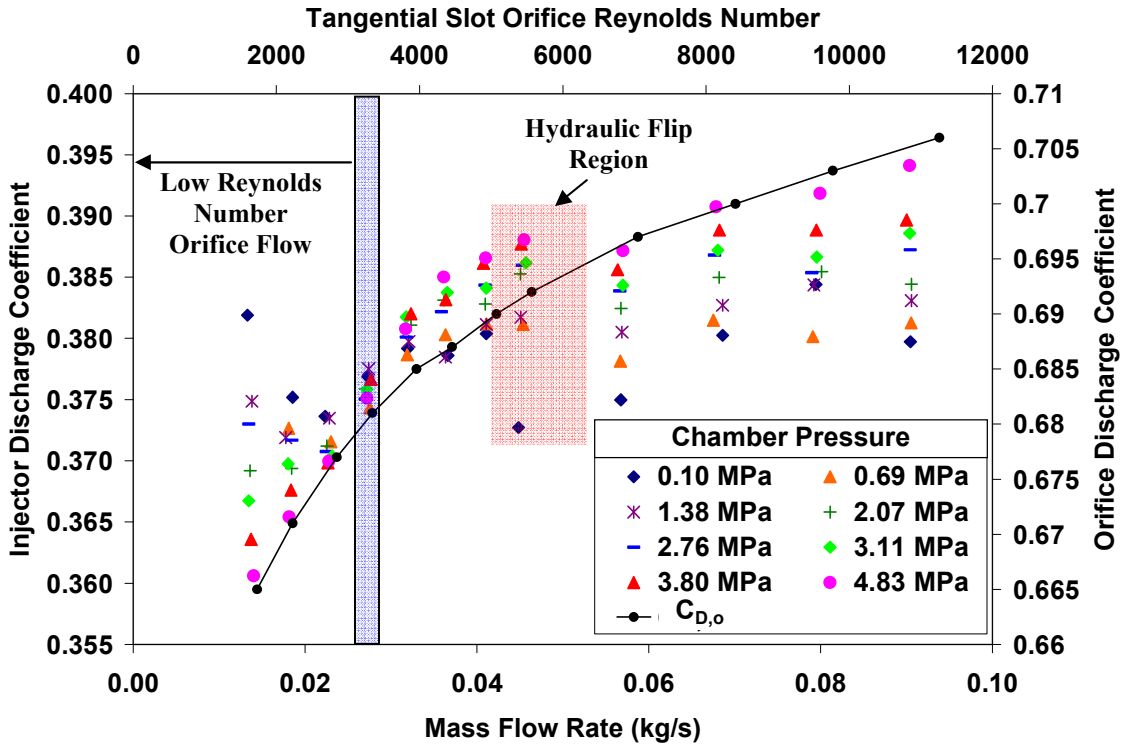

Figure 3.38 Injector discharge coefficients compared to tangential slot orifice flow regimes

CHAPTER 4

SPRAY ANGLE MEASUREMENTS

Issuing downstream of the nozzle exit plane, the swirling flow has enough tangential and axial momentum to spray outward into the open chamber. At the injector design flow rate, the spray has a conical shape with a spreading angle to the design free cone spray angle. The measurement of this angle, over varying mass flow rate and chamber pressure, is the focus of this chapter. It was discussed in Chapter 1 that the internal film thickness of the swirl injector strongly correlates with conical spray angle values. Historically, the exit film thickness is a commonly-used variable to predict free cone spray angles expected through correlations. However, relations have also been made between free cone spray angles and other flow parameters such as mass flow rate, pressure drop, average film thickness, and discharge coefficient. Because this work is oriented toward variable thrust operation, the relations generated in this chapter will be weighted toward liquid mass flow rate and chamber pressure.

4.1 Spray Angle Definition

Definition of the conical spray angle for image quantification is an important first step prior to actually making measurements. In reviewing previous works determining free cone spray angles of swirling sprays, the most consistent definition given is that helmed by Lefevbre [22], shown schematically in Figure 4.1. As the swirling sheet exits the nozzle at full flow conditions, the flow moves to create a conical structure with a quasi-symmetric profile. This profile moves outward at a near-constant angle with a value theoretically equal to the inverse tangent of the ratio of tangential liquid velocity to axial velocity. This angle is commonly defined as the free cone spray angle.

The conical structure is the result of the spray sheet's momentum overcoming its surface tension. The surface tension works to collapse the spray sheet towards the flow centerline, and the sheet momentum counters this trend. Ultimately, the swirling flow will lose enough momentum through liquid/gas shear friction that the near-constant free cone spray angle is decreased, and the profile displays an inflection point along the liquid surface. This inflection point is the reference point for free cone spray angle measurement for this work.

Lastly, recall the discussion of the spray angle definition in Chapter 1 with respect to the difference between free cone spray angle and chamber angle. Hulka and Makel [33] made a clear definition that the free cone spray angle was related solely to the injector geometry and internal flow conditions, and that the chamber angle was related to the free cone spray angle, injected liquid momentum, and ambient chamber pressure.

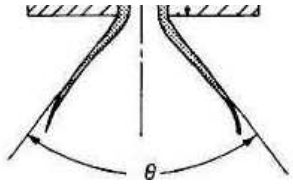

Figure 4.1 Definition of Free Cone Spray Angle from Lefevbre [22]

For this work, there is a predicted spray angle and a measured spray angle. Later in this chapter the ideas of free cone spray angle and chamber angle will be revisited in light of this work's findings.

4.2 Morphological Characteristics of Swirling Sprays

The morphology from swirl atomizer sprays is highly dependant on the liquid mass flow rate. Even before chamber pressure effects are considered, the variance of free cone spray angles to liquid mass flow rate must be first noted. This is needed for this work since later the measured spray angles at increased chamber pressure will be referenced to the spray angles at ambient conditions. Any significant changes in spray morphology for ambient conditions can be retained and displayed for spray structures (and their subsequent spray angles) at increased chamber pressure.

Figure 4.2 shows the effect of changing liquid mass flow rate on the overall spray structure. The images were generated from time-averaged photographs, with a strobe illumination frequency of 10 Hz, and the camera set at maximum aperture and 1 second

shutter speed. Picture-to-picture scales were not retained in the photo sessions for these images; they were used just to give qualitative observations of the flow profiles.

Both Lefevbre [22] and Khavkin [34] have qualitatively noted these structure changes and have named the various spray morphologies, as shown in Figure 4.3. Figure 4.3 below is the same figure as Figure 1.6, repeated here for the reader to easily compare to the morphologies seen in Figure 4.2. While these general morphologies are evident for every swirler design, there have been no quantitative standards found which relate where each morphology exists for a given swirl injector. Therefore, the swirling spray morphologies found in Figure 4.3 have only been qualitatively matched to this work's injector spray morphologies shown in Figure 4.2.

According to Figure 4.3, there is a lower limit at which the tangential momentum issuing from the swirler is so small that a sheet is not formed. Instead, a spiraling jet, named a 'distorted pencil' by Khavkin, is formed. For this spray structure and for those at even lower mass flow rate, a liquid free cone spray angle is not defined. For this work, the lowest mass flow rate attained still show the Onion stage, from which a sheet spray still exists and a free cone spray angle can still be identified.

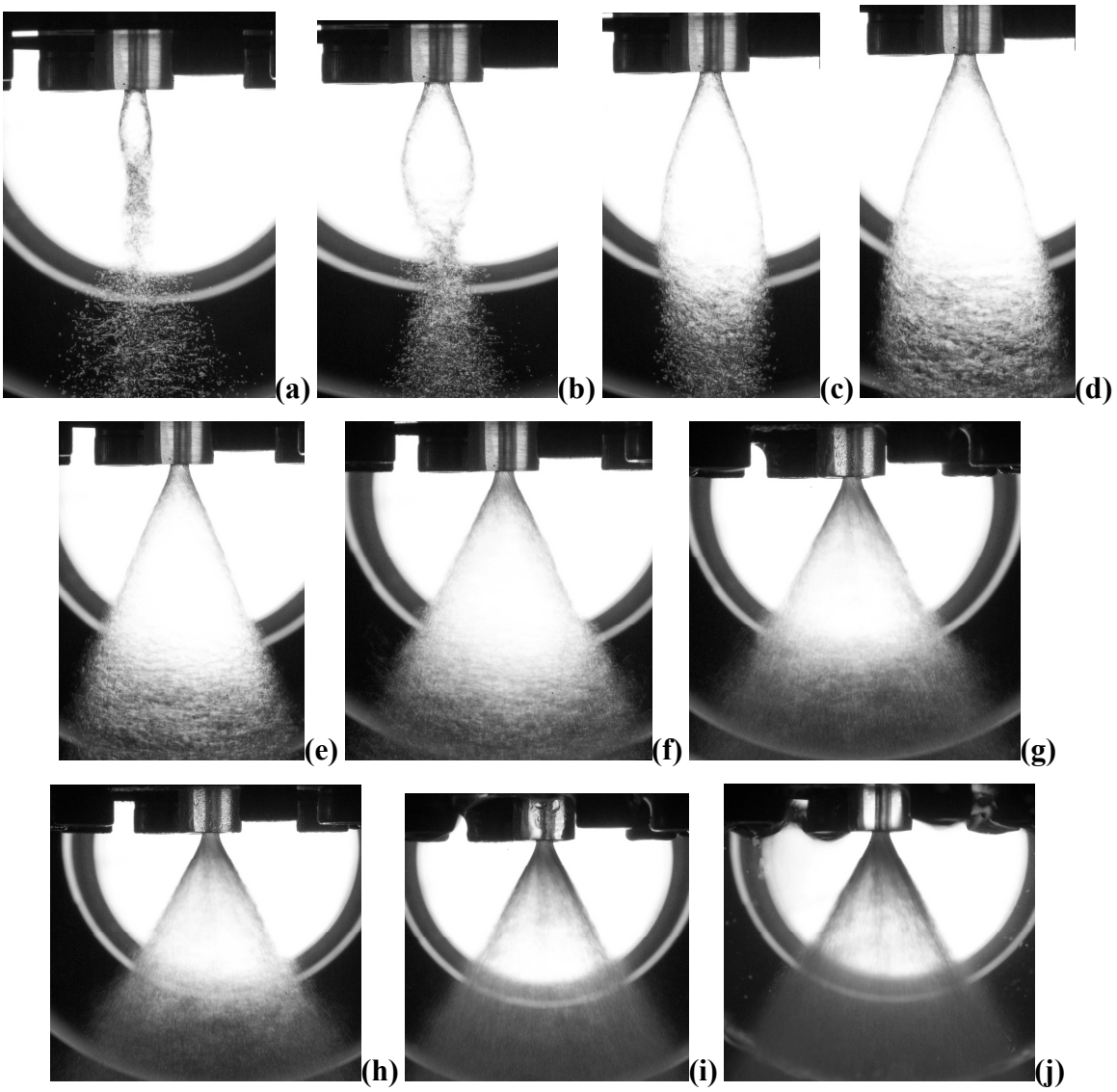

Figure 4.2 Ambient spray disintegration shapes at various relative mass flow rates ((a) 7.3% flow – Small onion stage, (b) 10.3% flow – Onion stage, (c) 12.4% flow – Pre-tulip stage, (d) 14.2% flow – Tulip stage, (e) 19.7% flow – End-tulip stage, (f) 30.3% flow – Cone stage/coarse atomization, (g) 40% flow – Cone stage/finer atomization, (h) 47% flow – Fully developed spray/coarse atomization, (i) 75% flow – Fully developed spray/finer atomization, (j) 100% flow – Fully developed spray/finest atomization)

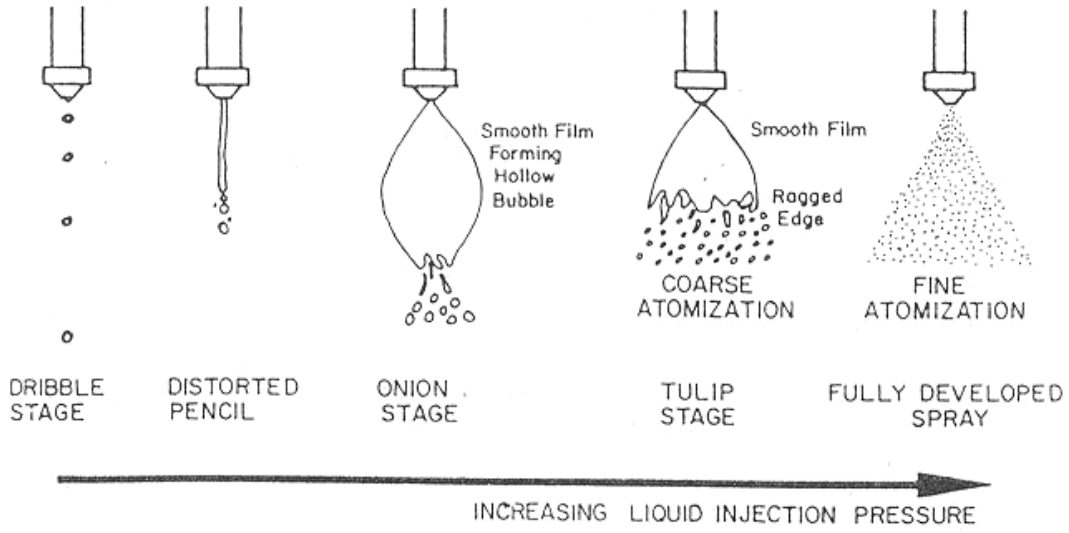

Figure 4.3 Swirling spray morphologies [34]

4.3 Spray Angle Measurements

Determination of the free cone spray angle first requires the spray sheet's boundary profile to be quantified. Because the spray sheet itself showed unsteady surface undulations, it was deemed important to use high speed digital video captures to give time averaging options with the images. The high speed video setup previous described in Chapter 2 was used. The operating conditions during which sprays were filmed were the same as noted for the film thickness measurements. The swirl injector configuration tested was that shown in Figure 2.9.

Typical test runs of the swirl injector consisted of operating conditions being chosen, then established within the facility. Once mass flow rate and chamber pressure

displayed steady values, the issuing spray was captured for 300 sample frames. At a sample rate of 4000 fps, a capture session corresponded to approximately 75 msec. Inspection of the video captures gave confidence that the spray boundary was fluctuating fast enough that multiple undulations or 'periods of unsteadiness' were within the capture period. A more quantitative check was done assuming the total exit velocity to be that predicted by Doumas and Laster of 51 m/sec. As discussed later, the region of interest within the capture frame was defined as six nozzle diameters downstream of the nozzle exit plane. Using this representative length scale and the total velocity, the travel distance for a fluid element to move downstream six nozzle diameters was 0.25 msec. A 75 msec capture time gave 300 'convection periods' of the spray, yielding an acceptable number of flow periods for a representative average.

Figure 4.4 shows an example session frame from a captured video of the spray at ambient chamber pressure and design mass flow rate. The nozzle diameter width, the exit plane, and the spray angle are all demarcated in the figure. To give the reader a sense of physical lengths, downstream distances of $1D_n - 6D_n$ are highlighted in Figure 4.4. Spray angle measurements were taken at several locations downstream of the nozzle exit plane. These locations were chosen through visual observations of where the spray boundary inflection point occurred nearby the nozzle exit plane. Using these observations, the spray angles were measured at downstream locations of $0.25D_n$, $0.5D_n$, $0.75D_n$, $1D_n$, $2D_n$, $3D_n$, $4D_n$, $5D_n$, and $6D_n$. The tighter spacing between measurement locations upstream of one exit diameter was chosen since the spray is observed to have notable changes of boundary shape in that region. Downstream of one exit diameter, the

spray boundary changes more smoothly on a larger length scale, so a wider spacing can be used.

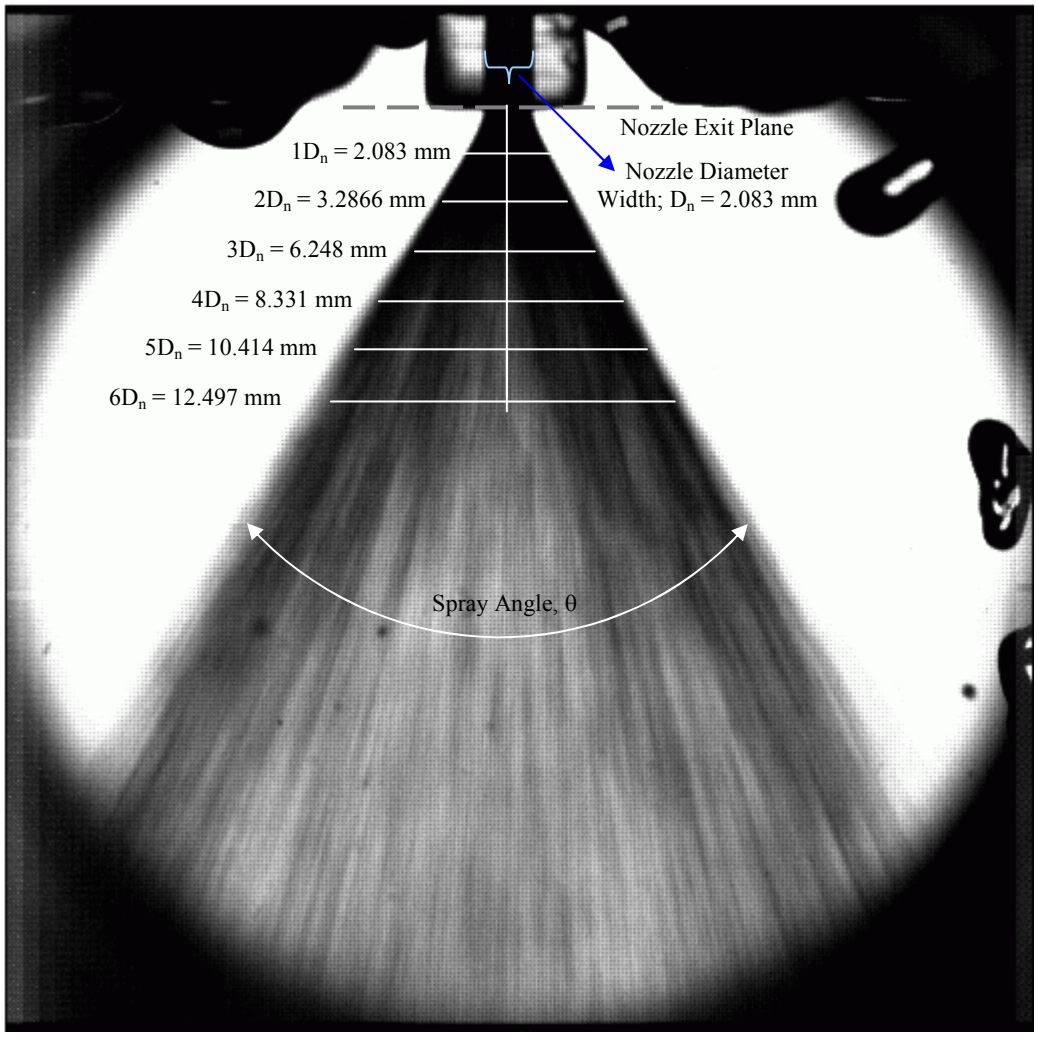

Figure 4.4 Representative video capture of downstream spray

Assessment of the free cone spray angle involved multiple steps, all of which were necessary to define the spray boundary from the captured videos, measure the spray angles at multiple locations, and finally quantify the representative free cone spray angle for the given operating conditions. Each of these three steps was made up of many constituent steps, each detailed below.

4.3.1 Spray Boundary Definition

To define the spray boundary, the captured video had to first be converted to an image processing-amenable format, and then post-processed. An example spray boundary capture process is as follows. The issuing spray is captured using the Phantom video camera in conjunction with the Phantom Cine Control Panel software [66]. A typical capture session lasted approximately 300 frames. From this frameset, a representative 100 sequential frames were chosen by finding the best time period where the spray was discernable within the image. The Phantom software is then used to save the frameset as a multipage TIF file, in order to best preserve image resolution.

Next, the multipage TIF file is opened using the ImageJ software for image post-processing. Image processing is necessary because high mass flow rate/high chamber pressure spray images do not consistently display an obvious contrast between the background and the spray boundary. Thus, the main goal of image post-processing is to establish an accurate spray boundary contrast, using a repeatable method per processed image. The first operation performed on the file is the determination of the image's mean pixel intensity. This operation finds the mean intensity value for every frame. This mean

intensity value is used as a metric to convert the TIF file from a grayscale format to a binary black/white format. For a given image, the threshold function from ImageJ is used to establish the binary threshold as the mean intensity value found. In other words, every pixel for every frame in the TIF file that has an intensity value equal to or above the mean intensity value will be assigned the value of 0, or 'black.' Every pixel below the mean intensity value will be assigned 255, or 'white.' The final result will be a binary image, whose colors are only black and white. Figure 4.5 shows, for two operating conditions, the difference between a grayscale image and binary image.

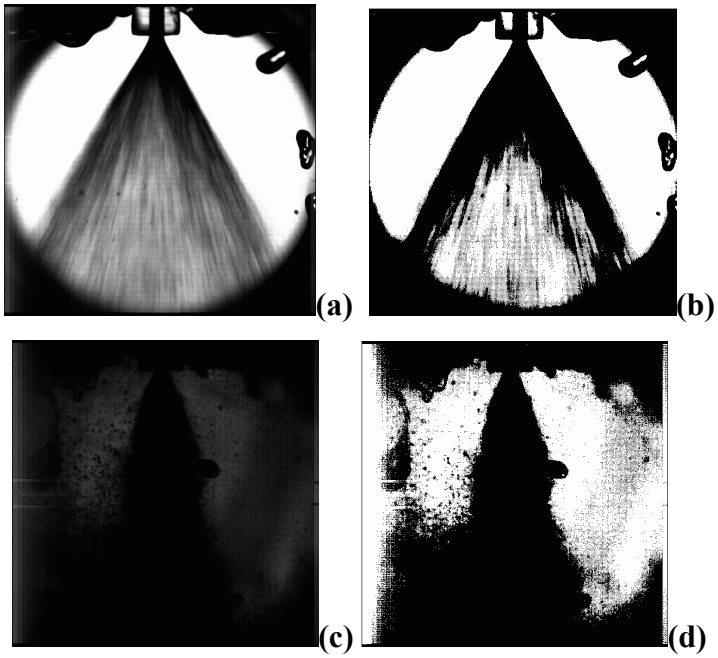

Figure 4.5 Comparison between grayscale and binary TIF files

(Operating conditions are 0.091 kg/sec, with chamber pressure of (a) 0.10 MPa, grayscale, (b) 0.10 MPa, binary, (c) 4.83 MPa, grayscale, and (d) 4.83 MPa, binary)

Observation of the TIF images showed many spurious droplets in the captured flow field. These droplets were usually near the spray boundary, potentially giving false answers when determining the spray boundary edge. To help de-emphasize the imaged droplets, two processes were applied to the binary TIF file: 'Open' and 'Erosion.' The 'Open' command first removes pixels from the edges of black objects within the image and in the surrounding image field [65]. Then, black pixels are added back to the black edges. The 'Erosion' command was used to remove isolated black pixels left in the surrounding image field [65]. The net sum of the two operations works to smooth black objects within binary images and to remove isolated pixels in the images. The Erosion command was applied twice to all of the frames, aiding in removing the final black pixels isolated through the 'Open' command applications. Figures 4.6 and 4.7 illustrate the 'Open' and 'Erosion' commands using the images from Figure 4.5.

Completion of the image post-processing generates a final TIF file that is ready for image measurement. This measurement process involves tagging pixels of interest, along the ten downstream locations shown in Figure 4.4. The spatial distribution of the tagged pixels is linear, defining rows of pixels at each downstream location. Figure 4.8 shows the tagged lines of pixels, which are constant for each TIF file.

For all downstream rows of pixels, there is a total of 1,190 points on the image tagged for analysis. Once the tagged pixels have been established on the image, the ImageJ software measures the intensity associated for each tagged pixel for each frame. After one analysis run, a text file is outputted, containing pixel intensity readings totaling 119,000 (1,190 pixels/frame X 100 frames). Because the TIF file is binary, the intensity at each pixel location is either 255 ('white') or 0 ('black').

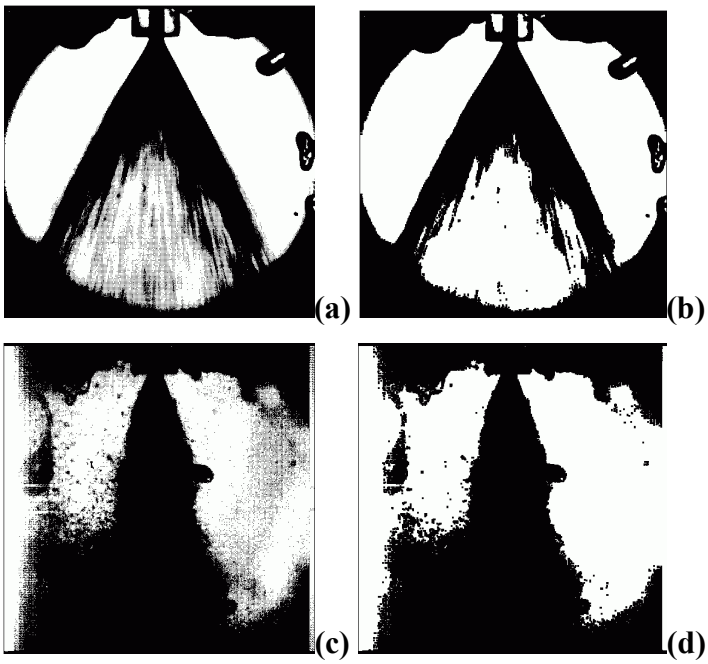

Figure 4.6 Effect of the 'Open' application to binary TIF images (Operating conditions are 0.091 kg/sec, with chamber pressure of (a) 0.10 MPa, binary, (b) 0.10 MPa, binary-open, (c) 4.83 MPa, binary, and (d) 4.83 MPa, binary-open)

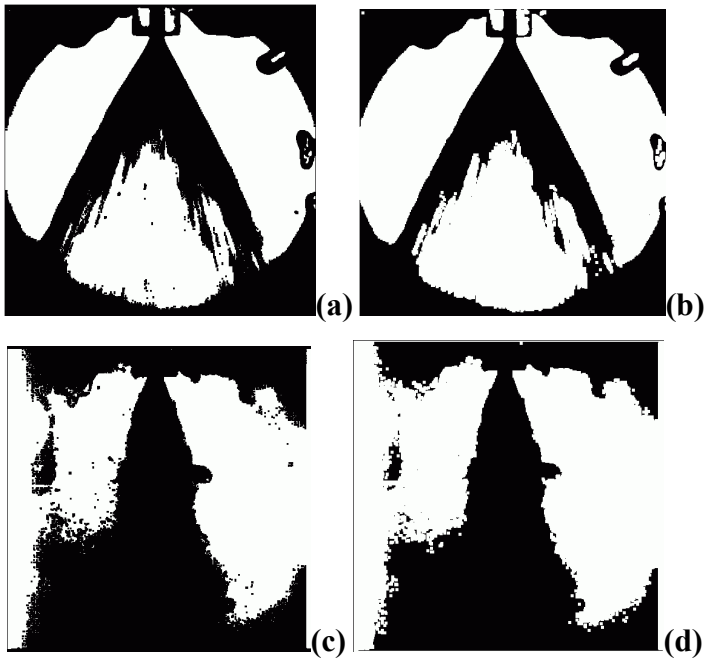

Figure 4.7 Effect of the 'Erosion' application to binary TIF images (Operating conditions are 0.091 kg/sec, with chamber pressure of (a) 0.10 MPa, binary-open, (b) 0.10 MPa, binary-erode, (c) 4.83 MPa, binary-open, and (d) 4.83 MPa, binary-erode)

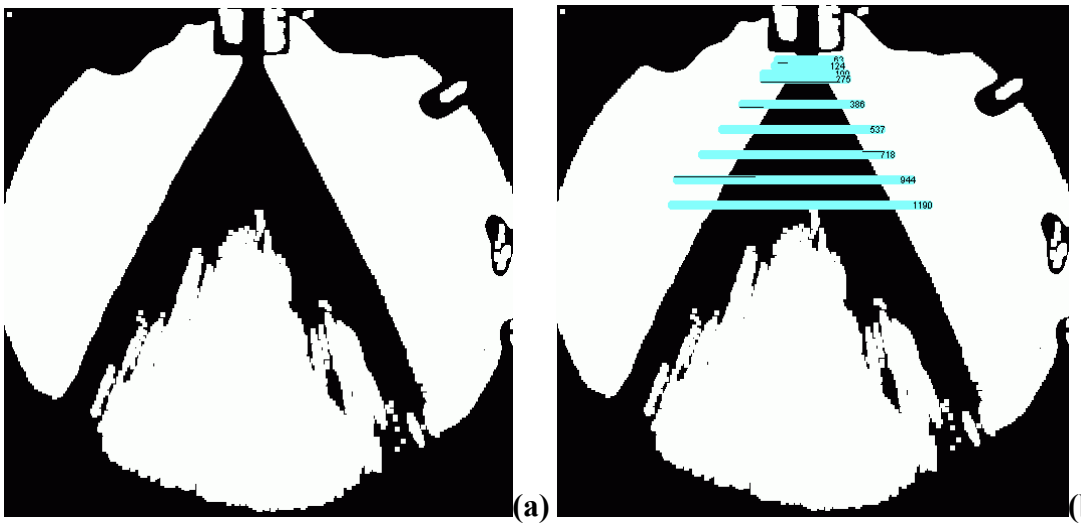

(a) **(b)**

Figure 4.8 Marked pixel locations for TIF image processing

(Example image shows post-processed (a) binary image and (b) binary image with tagged pixel locations)

The pixel intensity text file is read into a MathCAD document, where the data are grouped by readings pertaining to individual pixel locations. Then, the grouped data are fed into a MathCAD routine which calculates the mean intensity value for each pixel location, derived from averaging over all 100 frames. The mean intensity for each pixel location is then columnized for each downstream location. Finally, for each downstream location, the central difference numerical derivative is calculated, giving the intensity gradient at each pixel location. As one moves left to right along a pixel row in Figure 4.7(b), the pixel intensity changes from white, to black at the left-side spray boundary, then back to white at the right-side spray boundary. At the white-to-black boundary, the numerical derivative is the most negative value along that pixel row. At

the black-to-white boundary, the derivative is the most positive value along that pixel row. The spatial pixel locations at these positive and negative derivative values are defined as the spray boundary. Comparisons of spray boundary definitions to the images shown in Figure 4.7 are shown below in Figure 4.9. The red lines are the assessed spray boundary definitions.

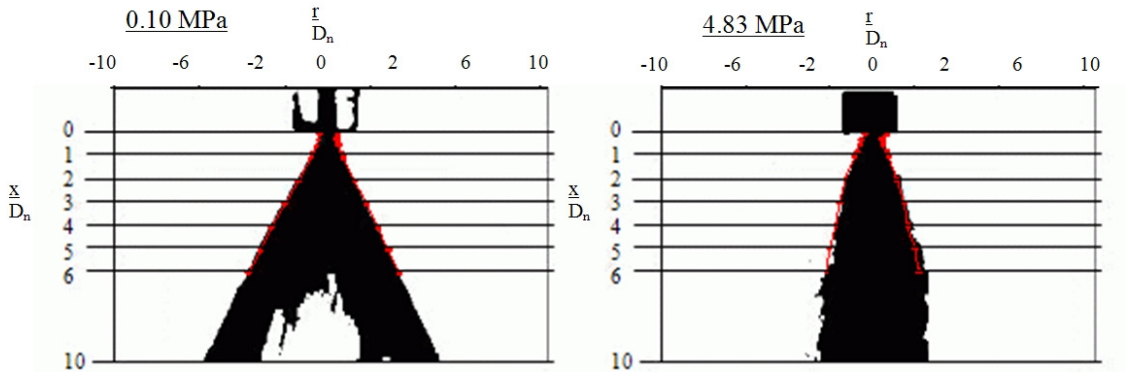

Figure 4.9 Comparison of average spray boundary definition to single frame capture

4.3.2 Spray Angle Quantification

Once the spray boundary has been defined, the next step is to measure local spray angles at the left and right sides of each downstream location. The calculation of the spray angle is done with respect to the 2-D spatial locations of the left and right edges of the nozzle exit diameter. The left and right 2-D locations of the nozzle exit diameter

edges are defined as (X_{Lo}, Y_{Lo}) and (X_{Ro}, Y_{Ro}), respectively. Then, the left and right 2-D locations of the spray boundary at a given downstream location are (X_{Li}, Y_{Li}) and (X_{Ri}, Y_{Ri}), respectively. For each downstream location then, the left (Φ_L) and right (Φ_R) spray angles are defined by Equations (4.1) and the total spray angle for each downstream location is simply the sum of the two angles.

$$\Phi_L = \arctan\left(\frac{X_{Lo} - X_{Li}}{Y_{Lo} - Y_{Li}}\right) \tag{4.1a}$$

$$\Phi_R = \arctan\left(\frac{X_{Ri} - X_{Ro}}{Y_{Ro} - Y_{Ri}}\right) \tag{4.1b}$$

From the pixel resolution available per TIF file, the angle measurement accuracy varied depending on what downstream location was being measured. Determination of the spray boundary was resolved to within ±1 pixel, giving the accuracies reported in Table 4.1. For normalized downstream locations close to the nozzle exit plane, the amount of pixels available to define the differences in Equation (4.1) were low. Thus, a ±1 pixel error caused a drastic change in the calculated spray angle. For downstream locations farther away from the nozzle exit plane, the number of pixels available for calculation of the spray angle using Equation (4.1) was much greater. For normalized downstream locations of one nozzle diameter or greater, the accuracy was deemed acceptable to use for free cone spray angle analysis. All free cone spray angles occurred at normalized downstream distances of one nozzle diameter or greater.

It is important to compare the spray angle measurement method against multiple chamber pressure conditions, since the captured spray is 'noisy' in an imaging sense at high chamber pressure. This image noise comes from secondary flows moving within the image capture zone. Secondary flows include droplet clouds and recirculation flows, which work to mask the discernable spray boundary.

Table 4.1 Spray angle measurement accuracy per downstream location

Downstream Location (Y/Dn)	Total Spray Angle Accuracy (±deg)
0	N/A
0.25	7
0.5	3.32
0.75	2.5
1	2
2	1
3	0.6
4	0.4
5	0.3
6	0.3

Results using the objectively-oriented spray angle measurement technique discussed above were compared to subjective measurements of the spray angle determined for multiple test cases. The subjective measurement consisted of observing the spray boundary over a number of frames for a given operating condition, and recording the pixel-based coordinates at each downstream location. The subjectively-determined spray boundary values were used to find the spray angles via Equation (4.1).

In Figure 4.10, the subjectively-determined spray angles are compared against the objectively-determined spray angles using the technique described earlier.

Observations of Figure 4.10 show that the objective measurements compare favorably with the subjective measurements at normalized downstream locations of two nozzle diameters or greater. For downstream locations of one or less, the comparison shows the objective measurements generally showing smaller spray angles than the subjective case. This difference is due mainly to the thresholding processing that the objective method utilizes. The subjective method determines the spray boundary by visual discernment, which can have difficulty in defining the boundary edge due to the gradual change from dark spray to light background. This gradual change is equivalent, in image processing terms, to a low-valued intensity gradient across the spray boundary. For low chamber pressure, the intensity gradient is high and it is 'easy' to visually discern the spray boundary. For higher chamber pressure however, the intensity gradient becomes low and the spray boundary is 'blurry.' Conversely, the objective method chooses an image threshold that divides the intensity values to either black or white. The intensity gradient at the spray boundary is always high in magnitude, and therefore, relatively simple to define. However, the additional erosion processes to the image can remove edge pixels from the spray boundary, lowering the spray angles measured at the downstream locations of one or less.

Because there is no clear 'true' answer for what the actual spray boundary is at the different downstream locations, the metrics chosen to justify using the objective method for free cone spray angle quantification are (a) the objectively-determined spray angles approach the subjectively-determined spray angles as one moves downstream, and

(b) the objectively-determined spray angles at design mass flow rate and ambient chamber pressure approach the predicted free cone spray angle as one moves downstream. As Figure 4.10 shows, both of these metrics are satisfied and so the objective method's values will be used to define the free cone spray angles for a given operating condition.

4.3.3 Spray Angle Measurement

Referencing Figure 4.1, the measured spray angle is defined as the local spray angle measured at the spray boundary inflection point. Thus, the measured spray angle was selected at each operating condition by choosing the largest local spray angle value over all of the downstream locations. Because the number of downstream locations measured was limited, it should be noted that the actual spray angle value may be higher than what was selected from the processed images. However, this potential difference between the actual and measured angles is considered negligible.

As with the film thickness measurements in Chapter 3, the first set of data viewed is that of full flow rate, with changing chamber pressure. Figure 4.11 below shows the measured chamber angles for a fixed mass flow rate of 0.091 kg/sec, and varying chamber pressure. The downstream location corresponding to chamber angle measurement ranges over a normalized distance of $2D_n$ - $6D_n$.

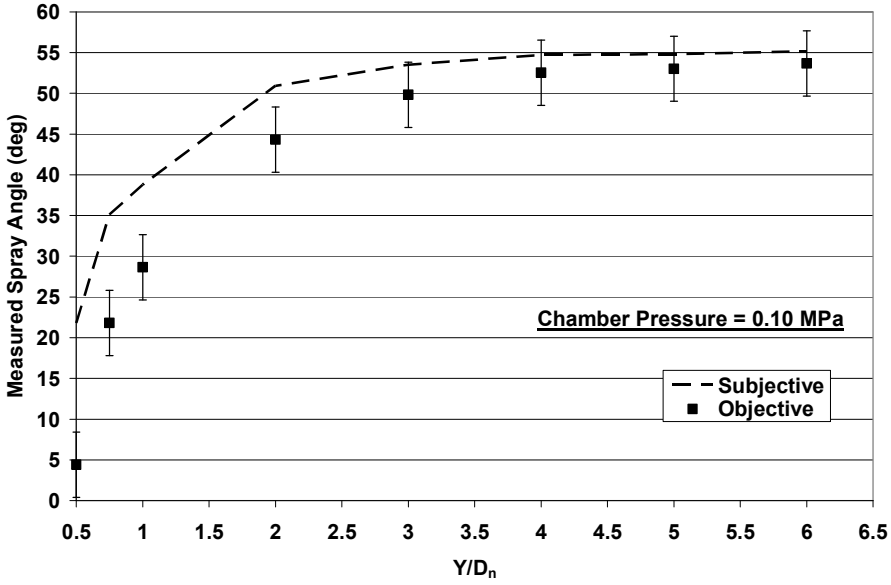

(a)

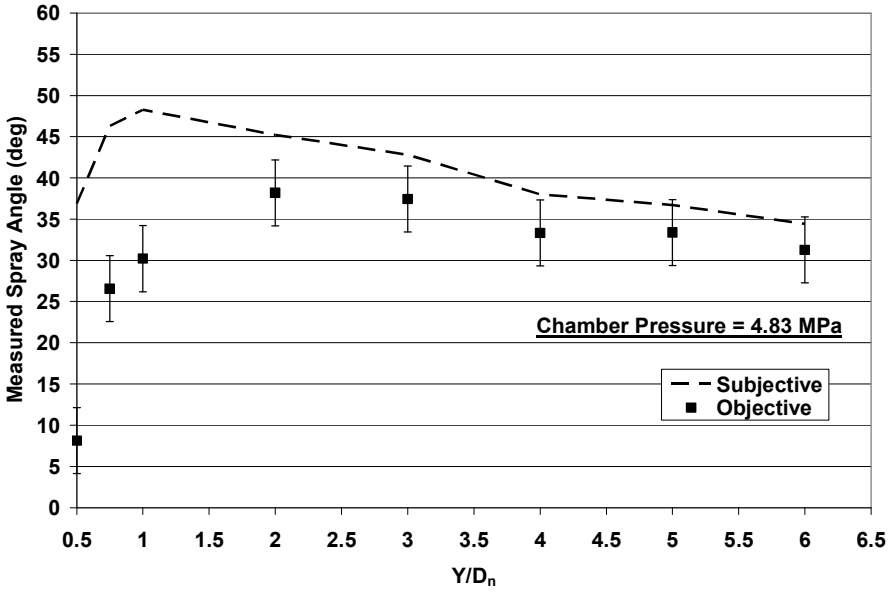

(b)

Figure 4.10 Comparison of subjectively and objectively measured spray angle values at chamber pressures of (a) 0.10 MPa and (b) 4.83 MPa

Error bars are chosen to match the accuracy reported in Table 4.1 for the normalized downstream distance of $2D_n$. With these error bars included per measurement, comparison to the predicted free cone spray angles from Doumas and Laster and Bazarov's methodologies show good agreement at the ambient chamber pressure value.

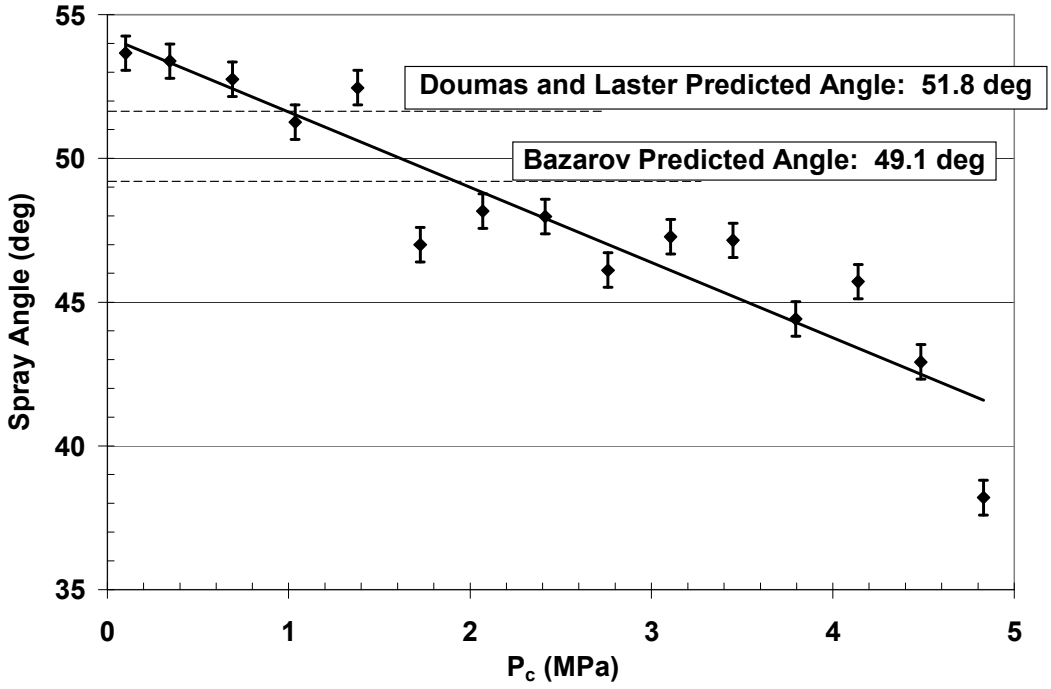

Figure 4.11 Chamber angle values at design mass flow rate and varying chamber pressure

Figure 4.11 displays a clear trend of decreasing chamber angle values with increasing chamber pressure. An explanation for this trend has been offered by DeCorso and Kemeny, through previous work related to chamber pressure influences on spray angles [55]. Figure 4.12 gives a graphical representation of what this explanation.

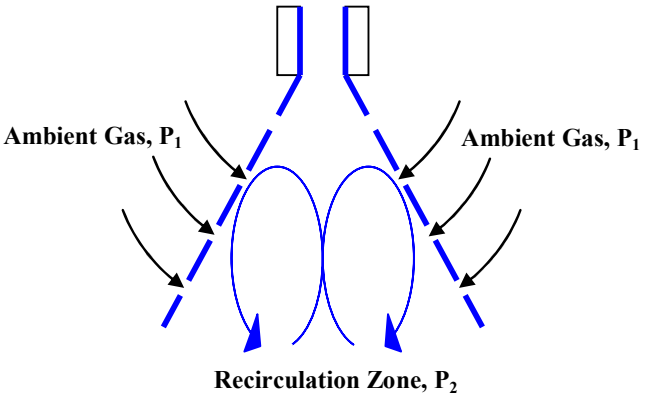

Figure 4.12 Schematic of liquid swirl sheet-induced recirculation and the motion of the ambient gas

As the spray issues out into the chamber and creates a swirling conical sheet, vortex recirculation zones are created within the gas volume bounded by the sheet. These vortices create a low static pressure region in the sheet-bounded volume, promoting gas flow from outside the spray boundary towards the volume. This gas flow induces drag on the liquid spray boundary and can actually work to increase sheet atomization. As the chamber pressure is increased, the gas density is increased as well, causing more drag on

the liquid sheet. As the drag is increased, enough of the liquid tangential momentum is lost to begin to actually contract the spray boundary in towards the centerline of the flow.

Continually increasing the ambient chamber pressure will promote gas flow towards the inner volume of the spray, with increasing drag effects further contracting the spray boundary. Increasing the chamber pressure also increases the gas density within the inner spray volume. As the gas density increases, higher chamber pressure is needed to continue contracting the spray boundary. This is considered the reason why the change in chamber angle with chamber pressure becomes insensitive between 1.72 and 3.45 MPa in Figure 4.11. DeCorso and Kemeny also noted this trend, but did not observe high enough chamber pressure to see whether or not the spray boundary contracted. In this work, chamber pressure of 3.79 MPa and greater are enough to resume contraction of the spray boundary with chamber pressure.

The flow mechanism explained above must be applied to this work's results with care. The spray angles were measured in the near injector exit region of the spray, so the same gas entrainment mechanism may not be as dominant an influence to the spray angle as it was with DeCorso and Kemeny's measurements at over ten nozzle diameters downstream of the injector exit. Sprays measured by DeCorso and Kemeny probably had already broken up in either primary or secondary atomization regimes that far downstream. At the downstream distances the spray angle was measured at in this work, the spray boundary could still be considered intact and the influence of the internal nozzle flow parameters should still be very important in defining the spray angles. Measured spray angles will be correlated against the internal nozzle film thickness values measured later in this chapter.

Influence of lowering the liquid mass flow rate at constant chamber pressure is seen in Figure 4.13. Figure 4.13 shows that the swirl injector has to be throttled down to 25% or less for larger than a 10% reduction in the measured spray angles. Explanation of this change can be related to the spray images shown in Figure 4.3. Below 30% throttled values of the swirl injector, the spray morphology is beginning to enter the Tulip stage. This stage is associated with lower spray momentum and less conical spreading of the spray sheet. This trend holds as the injector is throttled down even further and the spray morphology continues to be in the Tulip stage.

Combined effects of changing mass flow rate and chamber pressure are shown in Figure 4.14. Measured spray angles for all of the mass flow rate and chamber pressure conditions tested are plotted against each other. General trends show an approximately linear decrease in measured spray angle with increasing chamber pressure. This is true for each mass flow rate, relative to the ambient spray angle.

The dimensional analysis from Chapter 2 was used to select variables to better identify spray angle trends with the relevant fluid mechanic processes of the spray. The relative mass flow rate was replaced with Reynolds number, defined as Equation (4.2), and the chamber pressure was replaced by Weber number, defined as Equation (4.3).

$$\mathrm{Re}_n = \frac{V_\Sigma D_n}{\nu} \tag{4.2}$$

$$We_n = \frac{\rho_g V_\Sigma^2 D_n}{\sigma} \tag{4.3}$$

In both Equations (4.2) and (4.3), the nozzle diameter is the representative length scale, the gas density was calculated assuming 300K gas temperature for each chamber pressure, and the representative velocity was the total exit velocity estimated for each mass flow rate using Doumas and Laster predictions.

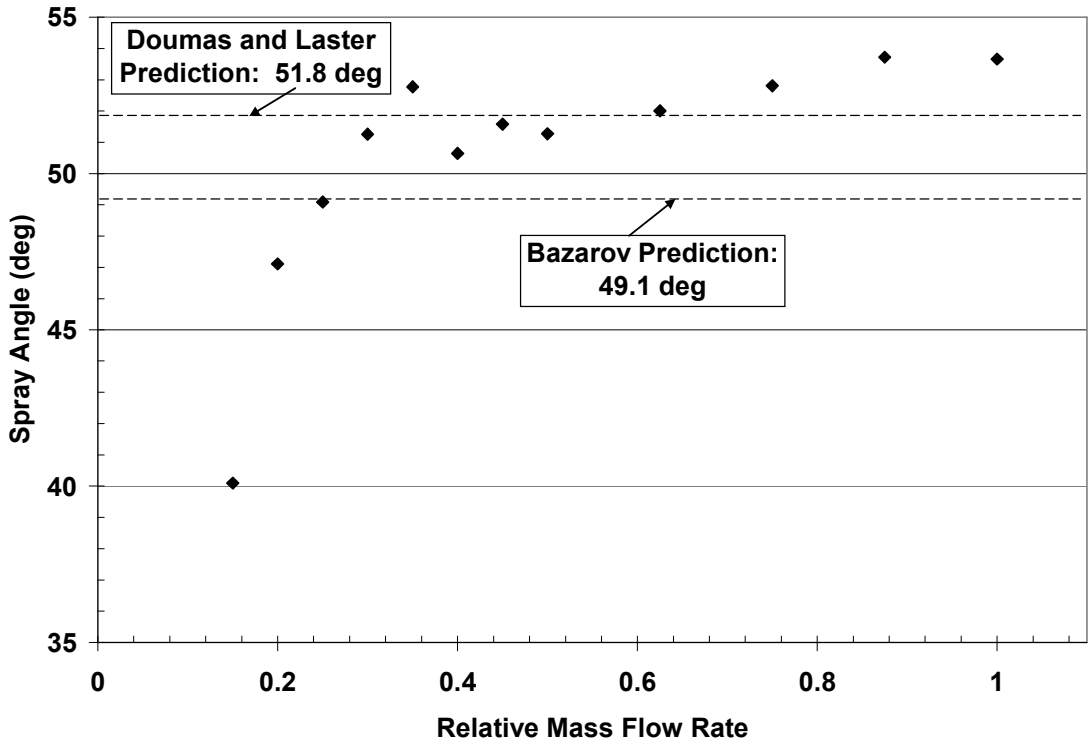

Figure 4.13 Measured spray angles for reducing relative flow rate at ambient chamber pressure

Figure 4.14 was re-plotted as Figure 4.15, using the variables defined in Equations (4.2) and (4.3). The measured spray angle was replaced by the tangent of half

of the spray angle for each nozzle Reynolds number. Figure 4.15 shows that as the nozzle Reynolds number is increased, the reduction in spray angle for increasing Weber number is decreased.

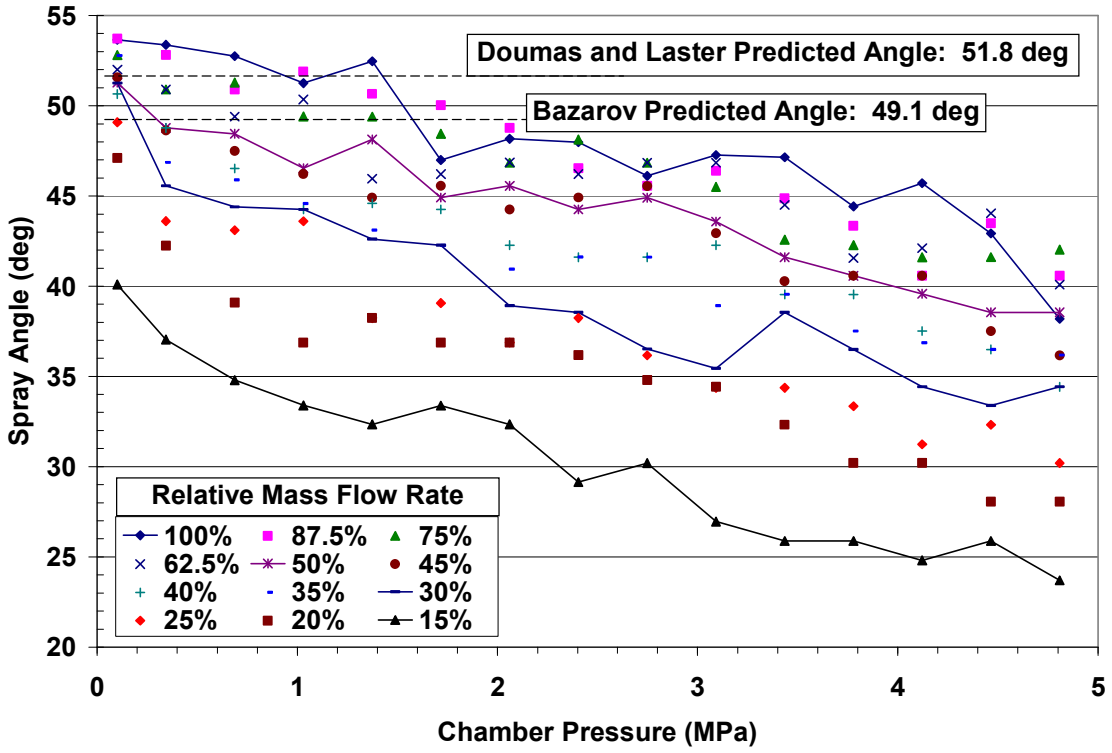

Figure 4.14 Measured spray angles for each relative mass flow rate and chamber pressure

Since the Reynolds number is related to total sheet velocity magnitude, high Reynolds number corresponds to high liquid sheet total momentum. A high liquid momentum requires a higher liquid/gas shear friction loss to reduce the spray angle.

Thus, higher Reynolds number values require a higher Weber number to notably reduce the spray angle from the reference ambient value. Lowering the nozzle Reynolds number below 50,000 begins to reduce liquid momentum enough that both liquid/gas interface shear and, potentially, surface tension begin to notably reduce the spray angle to lower values then seen for higher Reynolds numbers.

Observation of Figure 4.15 showed that each set of values generally follows a linear trend with respect to the nozzle Weber number. Similar to the approach in Chapter 3 for the discharge coefficient, a linear fit was made for each nozzle Reynolds number set of spray angles given in Figure 4.15. Equation (4.4) shows the generalized linear fit and the assumed variable dependences. The slope and intercept of Equation (4.4) was plotted against the nozzle Reynolds numbers, as shown in Figure 4.16. The trend of slope with nozzle Reynolds number fit best to a power relation, and the intercept fits best to a logarithmic trend.

$$f = \tan\left(\frac{\theta}{2}\right) \tag{4.4a}$$

$$f\left(\mathrm{Re}_n, We_n\right) = S_\theta\left(\mathrm{Re}_n\right) \cdot We_n + f_o\left(\mathrm{Re}_n\right) \tag{4.4b}$$

Equations (4.5) and (4.6) give the trend fits to slope and intercept values.

$$f_o\left(\mathrm{Re}_n\right) = 7.6555 \ln\left(\mathrm{Re}_n\right) - 33.187 \tag{4.5}$$

$$S_\theta(\mathrm{Re}_n) = \frac{1.905 \cdot 10^8}{(\mathrm{Re}_n)^{2.157}} \tag{4.6}$$

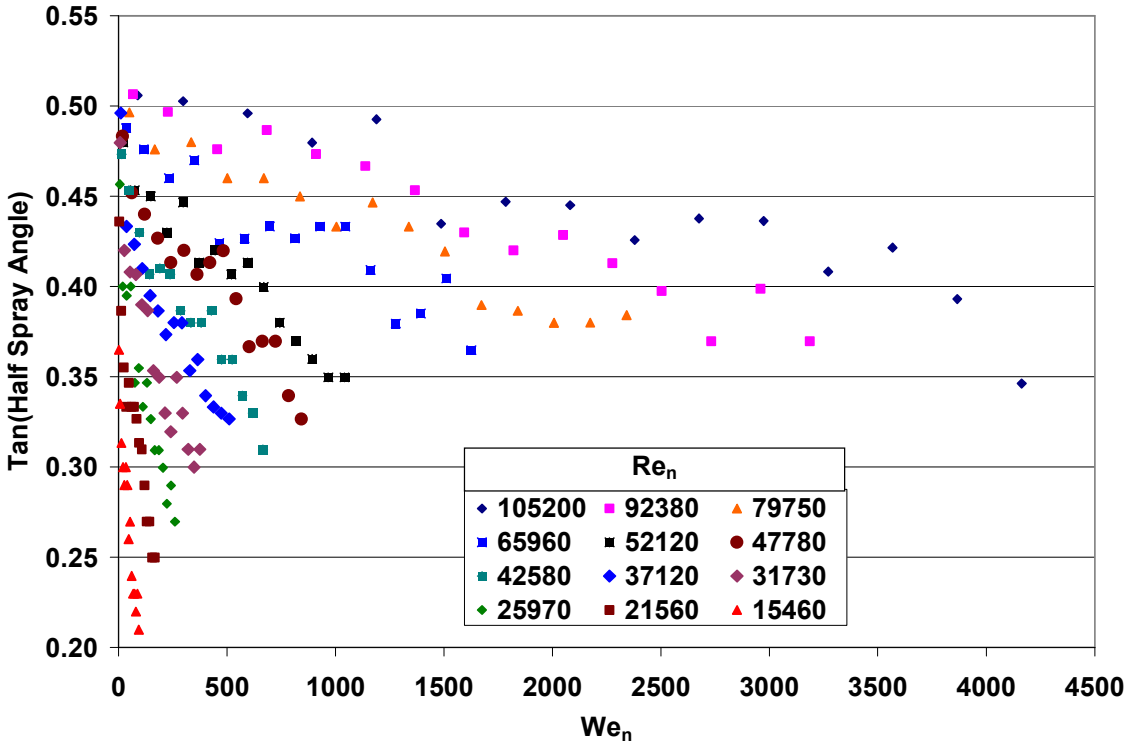

Figure 4.15 Tangent of measured spray angle for varying nozzle Reynolds and Weber number

Equations (4.5) and (4.6) show how changing the mass flow rate, and subsequently the nozzle Reynolds number, lowers the ambient spray angle and increases the effect of ambient chamber pressure on reducing the spray angle. For the ambient

spray angle, the Reynolds number reduction corresponds to a decrease in injected liquid momentum into the chamber. For the slope, the reduction in liquid momentum gives less resistance against ambient gas shearing friction effects.

As seen in Chapter 3, increasing the chamber pressure and/or decreasing the injected mass flow rate decreases available flow momentum to the liquid sheet. This reduced flow momentum is associated with an increased average film thickness along the injector nozzle.

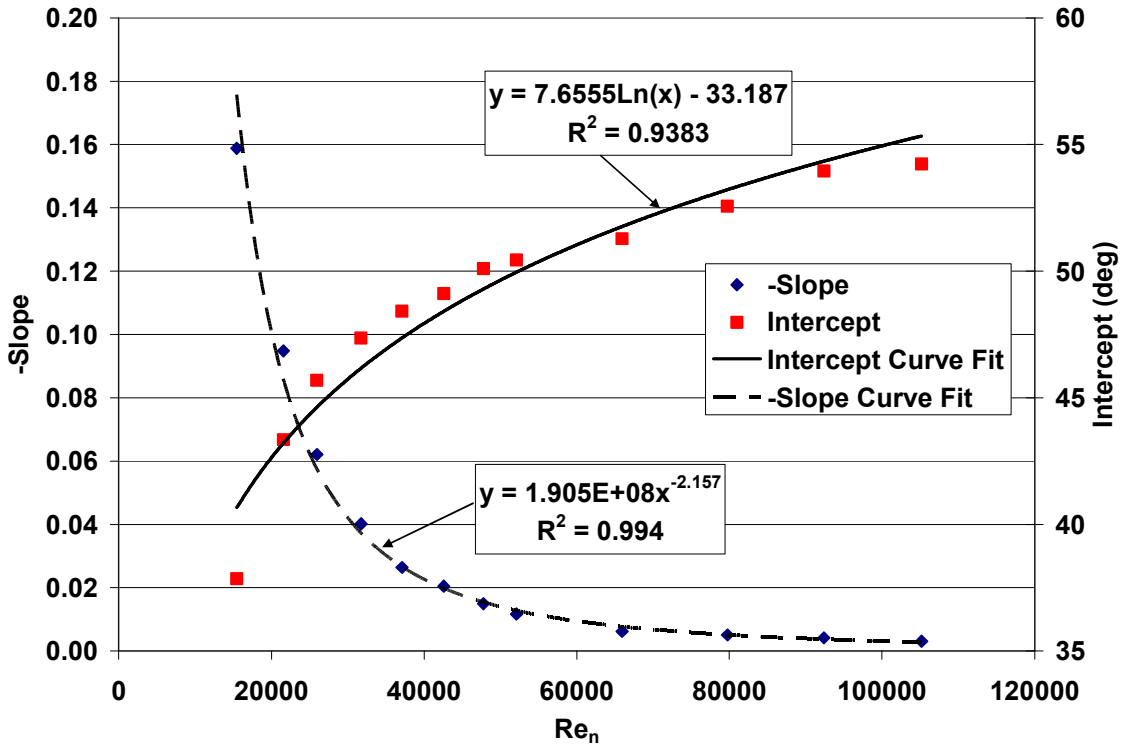

Figure 4.16 Slope and intercept fits for varying nozzle Reynolds numbers

Both the Bazarov and Doumas and Laster design methods used relate the spray angle solely to the area fullness coefficient within the swirl injector element. This area fullness coefficient is directly related to the average film thickness along the nozzle. Figure 4.17 shows how the tangent of the measured spray angles in Figure 4.15 vary with the area fullness coefficients calculated from the average film thickness values reported in Figure 3.36.

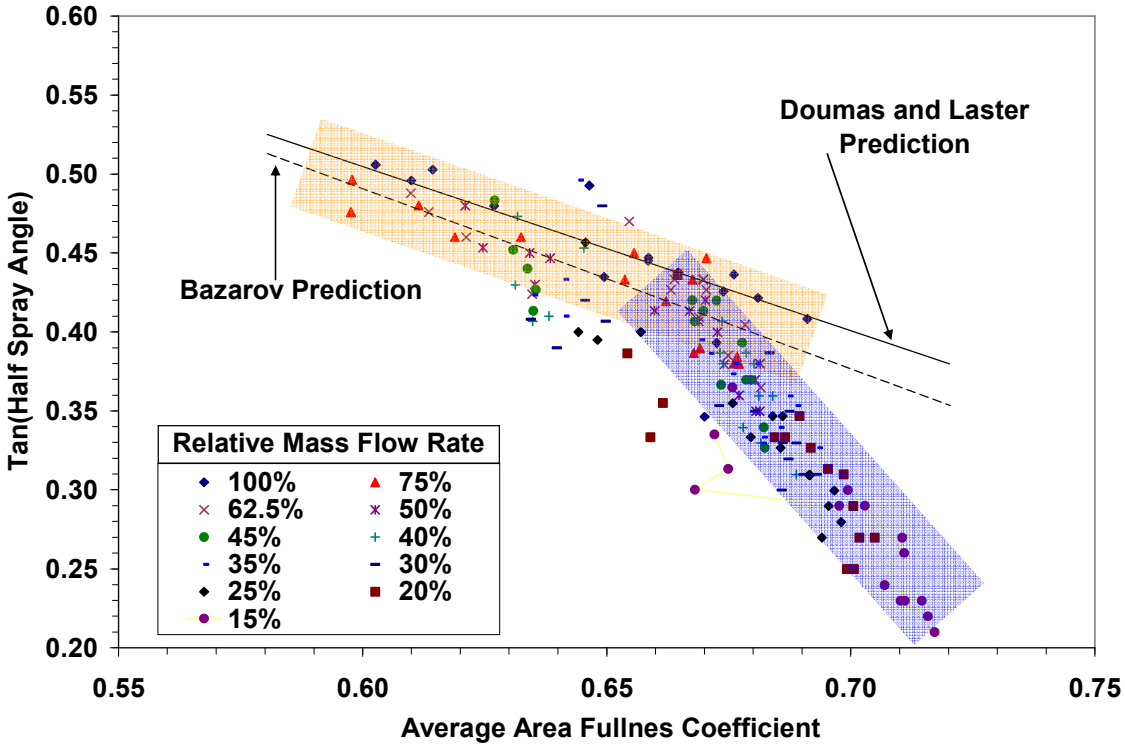

Figure 4.17 Spray angle trends with area fullness coefficient

Also plotted in Figure 4.17 are the predicted spray angles from the Bazarov and Doumas and Laster methods using the measured area fullness coefficient range seen from Chapter 3. The highlighted tan section on the plot groups the spray angle data whose trend follows the predicted trends from either Bazarov or Doumas and Laster predictions. Both sets of predictions show that increasing the area fullness coefficient corresponds to increasing the injector discharge coefficient, which also means that the injector liquid momentum is being reduced. Reduced liquid momentum does not give the liquid sheet enough resistance to surface tension and gravity forces and the sheet curves back towards the flow centerline. Since the spray angle values were measured close to the injector exit plane, this mechanism of reduced liquid mechanism is considered the dominant mechanism defining the spray angles values over the gas entrainment described earlier. This consideration implies that the measured spray angles can be used to define the free cone spray angles shown in Figure 1.18.

The highlighted blue section on Figure 4.17 shows that the spray angle data follows a different trend than that predicted by Bazarov or Doumas and Laster. This data consists mainly of spray angles measured at reduced mass flow rate / elevated chamber pressure operating conditions. At these operating conditions, it is estimated that the gas entrainment effects influence the spray boundary shape along with the effects of reducing injected liquid momentum. If both the injector liquid momentum and the gas entrainment mechanism are affecting the measured spray angle, then it is difficult to determine whether the measured angle represents the free cone spray angle or the chamber spray angle as defined in Figure 1.18. It is also equally difficult to determine if the spray sheet

is still intact or not at the measured spray angle location since the intact length was not measurable from the high speed videos.

CHAPTER 5

ANALYTICAL RELATIONS

As the previous chapters have shown, spray features display notable deviations when the injector's mass flow rate is lowered below the design point, and/or the chamber pressure is raised above atmospheric values. Results from the previous two chapters show that both the Bazarov and Doumas and Laster methodologies are unable to capture these deviations. The Bazarov design methodology is based on inviscid flow theory, which does not have the ability to capture flow effects from increasing chamber pressure and decreasing mass flow rate. The Doumas and Laster design methodology is grounded on inviscid relations, but is completed by empirical relations from data. It is understandable that neither methodology is unable to capture the effects of reducing mass flow rate and elevating chamber pressure, since data wasn't available at the time to modify the methodologies appropriately.

In this chapter, the Doumas and Laster methodology will be modified to better explain the observed results seen in the previous two chapters. This methodology was chosen since Doumas and Laster's original set of data was available to be combined with

the results collected in this work. The fundamental relations in Doumas and Laster's original work will be re-derived and expanded to incorporate: 1) a tangential momentum loss factor, and 2) an explicit dependence of the swirl flow features to the inlet slot losses. The second part of this chapter will extend the relations developed in the first part to include effects of changing injector mass flow rate and ambient chamber pressure.

5.1 Derivation of Fundamental Relations

A key concept for all swirl injector design relations is the definition of the tangential velocity profile within the injector itself. A review of the literature regarding internal physics of swirling liquid flows has shown that the tangential velocity profile has a shape indicative of a modified Rankine vortex [69], [73], [74], [75]. This vortex type consists of (1) a narrow solid vortex close to the central gas core, (2) a quasi-free vortex between the solid vortex and near the inner wall, and (3) a boundary-layer defined section next to the inner wall. Figure 5.1 shows the general shape of a modified Rankine vortex related to the swirl injector geometries.

Close to the liquid/gas interface, the tangential velocity is similar to solid body rotation shown as region (1) in Figure 5.1. As one moves radially outward towards the tube inner radius, the solid body rotation profile transitions to the quasi-free vortex profile of region (2). The quasi-free vortex profile is defined as having an index of frictional decay k, and circulation Γ. k is equal to unity for an inviscid free vortex, and is less than unity for a quasi-free vortex with viscous effects.

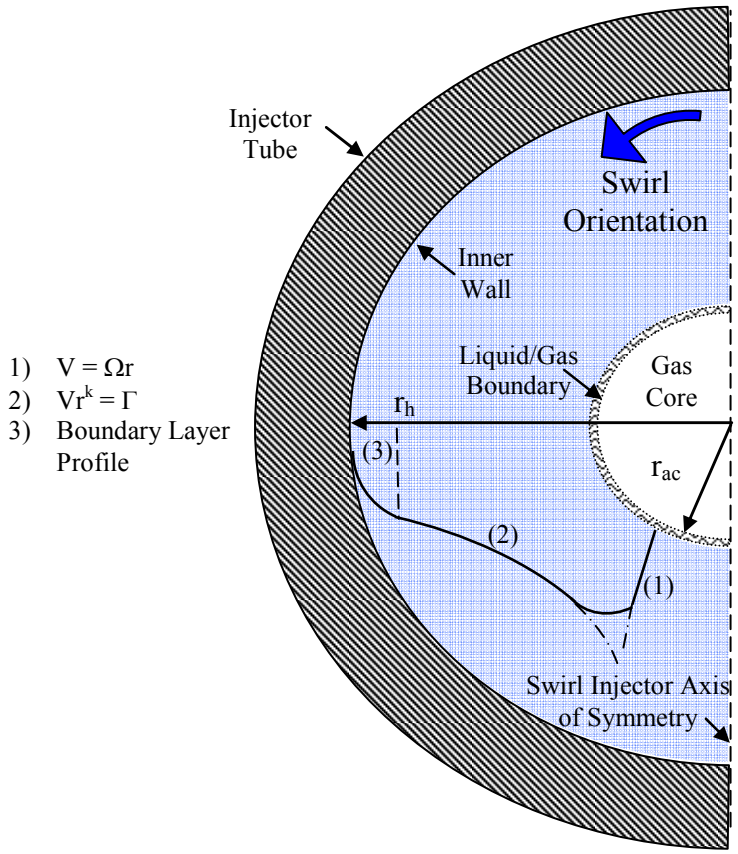

Figure 5.1 Definition of modified Rankine vortex

Measured data of confined rotating flow from Ogawa [75] showed a smooth transition profile connecting the solid body profile and the quasi-free vortex profiles for modified Rankine vortices, as shown in Figure 5.1. Continuing to move towards the inner tube radius, the tangential profile finally changes to a boundary layer profile.

Work performed by Wang [69] showed that the solid vortex profile is very thin and that the flow quickly changes to a quasi-free vortex. Wang used digital particle image velocimetry (DPIV) to show the solid body profile only represents 5% of the liquid

flow cross-sectional area moving down the swirl injector nozzle. In light of Wang's findings, the solid body rotation profile will be considered negligible in this work. By neglecting the solid vortex profile, the gas core radius is defined as where the viscous vortex profile reaches a maximum. This assumption is in concurrence with Dombrowski and Hasson [73] and Babu et al. [74] in their analysis of swirl injector internal flows.

Between the viscous vortex and the inner tube wall is the boundary layer velocity profile. Hutt [31] empirically investigated the boundary layer thickness within the swirl injector nozzle section. He concluded, through PIV measurements, that the boundary layer thickness is on order of 10% of the liquid cross-sectional area, which was small enough to neglect consideration of the boundary layer profile. Donjet et al. [76] showed that the boundary layer thickness normalized by the nozzle radius is on order of 5% of the liquid film thickness. This 5% corresponded to a flow area percentage of 9.75%, agreeing well with Hutt's conclusion. The boundary later profile will be neglected in this work, but the viscous effects will be indirectly accounted for through the measured pressure drop of the flow.

An important observation from Chapter 3 is that for all operating conditions tested, a gas core existed in the swirling flow. For the tangential velocity profiles used in this chapter, a gas core is also assumed to exist at any mass flow rate and chamber pressure. The tangential velocity profile is expected to be different for very low mass flow rate injection and the relations assumed in this chapter are not valid to quantify the flow. Subsequently, the area fullness coefficient can never be equal to unity and the tangential velocity profile will always be a quasi-free vortex type.

The other two velocity profiles needed to define the swirling flow are the radial and axial components. Measurements of swirling flow in pipes by Ogawa [75] show a net radial profile oriented towards the inner tube wall. With respect to swirl injector analysis, this radial velocity component has been neglected in the past for swirl injectors with relatively small to moderate swirl chamber to nozzle diameter ratios [20]. The swirl injector design used in this work has a ratio of 2.29, small enough to neglect radial velocity effects.

While the radial velocity components will be neglected in this derivation, the axial velocity is certainly non-zero. Wang [69] also showed the axial velocity profile to have a somewhat parabolic profile with radius. The maximum axial velocities were typically found at the liquid/gas interface, with the profile reaching a minimum value approximately halfway between the liquid/gas interface and the tube inner wall. For several axial stations down the nozzle tube length, the minimum value actually became negative, denoting recirculation in the flow. For derivation simplicity, the axial velocity profile will be replaced by an average value, constant across the nozzle cross-section. The issue of axial flow recirculation will be considered later in the second part of this chapter.

The list below combines the assumptions in velocity profiles listed earlier with the other assumptions used to simplify the governing relations of the swirl injector. These assumptions are

1. Steady flow
2. Inviscid axial flow
3. Axisymmetric flow about the center of the nozzle
4. Incompressible liquid flow
5. Swirling flow always has a gas core filled with chamber gas
6. Buoyancy, gravity, and surface tension forces are neglected
7. Radial velocity component is neglected
8. Axial velocity component is uniform across radius
9. Tangential velocity component solely consists of quasi-free vortex profile; this profile uses inviscid flow to relate any two points in the flow, but accounts for viscous losses through a frictional decay index
10. Liquid/gas interface is constant with no mass transfer, no heat transfer, and the local interface static pressure is equal to the chamber pressure

For the following derivations, Table 5.1 defines each variable used in this chapter. The geometrical variables and several of the flow features are shown in Figure 5.2.

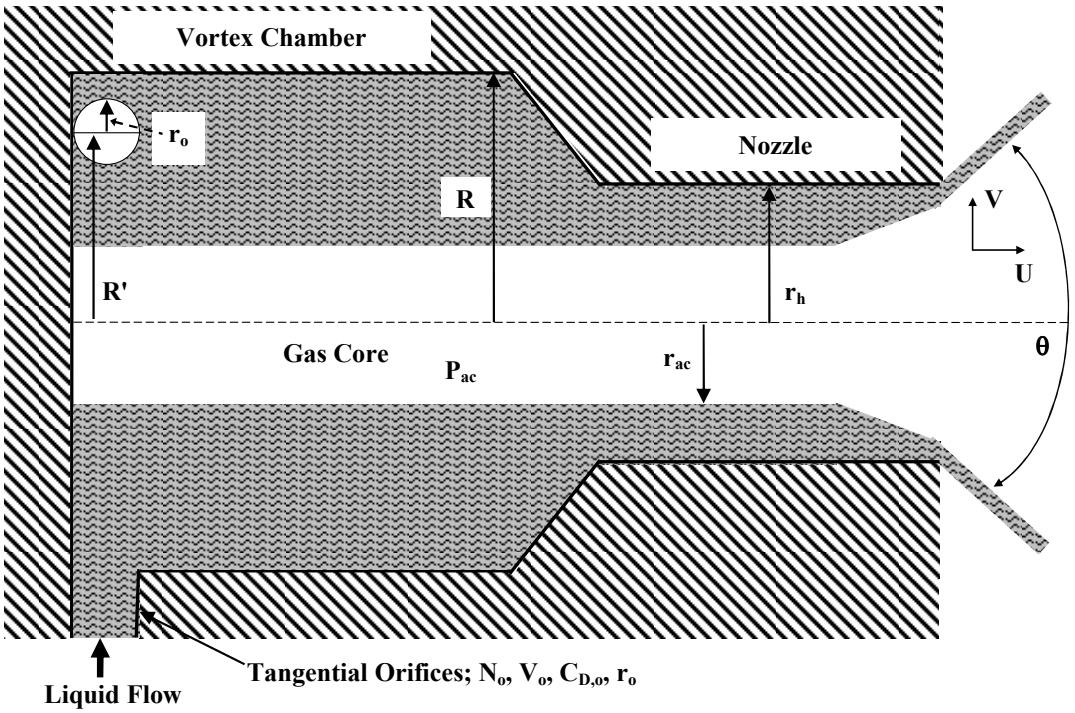

Figure 5.2 Swirl Injector Geometry and Features

To start, conservation of angular momentum is used to relate the tangential velocity anywhere inside the swirl injector to the initial angular momentum coming out of the tangential slots. Using assumption #9 above, the tangential velocity profile is defined as Equation (5.1).

$$V_o R'^k = U_u r^k = Const. \tag{5.1}$$

Table 5.1 Notation for fundamental relation derivations

Parameter	Symbol
Geometric constant	A'
Modified geometric constant defined by Doumas and Laster	A'_{DL}
Modified geometric constant with tangential loss factor	A'_k
Effective tangential orifice flow area	A'_o
Tangential orifice discharge coefficient	$C_{D,o}$
Frictional decay index	k
Number of tangential orifices	N_o
Liquid static pressure	P
Gas core static pressure	P_{ac}
Liquid stagnation pressure	P_o
Vortex chamber radius	R
Swirl arm; = R - r_o	R'
Gas core radius	r_{ac}
Nozzle radius	r_h
Tangential orifice radius	r_o
Spray angle	θ
Total liquid velocity	$\boldsymbol{V}_\Sigma$
Tangential velocity component	$\boldsymbol{U}_u$
Tangential orifice inlet velocity	V_o
Axial velocity component	$\boldsymbol{U}_a$
Volumetric flow rate	$\dot{\forall}$

Equation (5.1) shows that the tangential velocity, U_u, anywhere along the swirl injector length is only a function of slot inlet velocity V_o, the swirl arm radius R', and the resulting frictional decay index k. The range of k can fall anywhere between 0 and 1, but values cited from previous works range from 0.4 to 0.9 [69, 72 – 74]. The difference between the swirl arm and using the actual vortex chamber radius is the slot orifice radius. Previously, Doumas and Laster ignored this difference and used the vortex

chamber radius in place of the swirl arm for Equation (5.1). While for some swirl injector designs the difference between the swirl arm and the vortex chamber radius is small, this derivation will continue using the swirl arm as the representative radius for the inlet velocity.

A second difference between this work's derivations and Doumas and Laster's relations is the inclusion of the inlet slot discharge coefficient. As the flow enters the inlet slots, losses from inlet edges and wall friction cause differences between the average slot inlet and exit conditions. The definition of the volumetric inflow to the swirl chamber captures the inlet losses, shown as Equation (5.2a). In this work, the orifice area is circular and is defined by the orifice radius and the number of orifices in Equation (5.2b).

$$\dot{\forall} = V_o C_{D,o} A_o = V_o A_o' \tag{5.2a}$$

$$A_o' = C_{D,o} N_o \pi r_o^2 \tag{5.2b}$$

Inclusion of the slot discharge coefficient (always less than unity) decreases the effective slot inlet flow area, raising the flow velocity required for a fixed volumetric flow rate. Doumas and Laster considered the slot discharge coefficient equal to unity.

The next relation describing the swirling flow is the Bernoulli equation, written as Equation (5.3).

$$P + \frac{\rho_l V_\Sigma^2}{2} = P_o \tag{5.3}$$

Equation (5.3) is straightforward to understand: the sum of the static pressure and dynamic pressure is equal to a reference stagnation pressure value. No loss terms appear explicitly in this equation, but will be included later. Neglecting radial velocity components, the total velocity term in Equation (5.3) can be expanded to axial and tangential velocity terms as seen in Equation (5.4).

$$P + \frac{\rho_l U_u^2}{2} + \frac{\rho_l U_a^2}{2} = P_o \tag{5.4}$$

The tangential velocity U_u is the assumed quasi-free vortex profile defined in Equation (5.1), and the axial velocity U_a is constant for a given operating condition.

The last fundamental relation needed is mass continuity. For a swirling liquid flow with a gas core, the volumetric flow rate can be related to the average axial velocity and the slot inlet conditions by Equation (5.5).

$$\dot{\forall} = U_a \pi \left(r^2 - r_{ac}^2 \right) = V_o A_o' \tag{5.5}$$

Implicit in Equation (5.5) is that the swirling flow is operating at a steady state condition. This relation is only valid when the injector has been operating at a set mass flow rate and chamber pressure long enough to be considered steady state.

To begin relating Equations (5.2), (5.4), and (5.5) to each other, the derivative of Equation (5.4) is taken with respect to radius.

$$\frac{\partial P}{\partial r} + \rho_l U_u \frac{\partial U_u}{\partial r} = 0 \tag{5.6}$$

Again, the reader is reminded that the axial velocity term is assumed not a function of radius. Substitution of Equation (5.1) into (5.6) gives Equation (5.7).

$$\frac{\partial P}{\partial r} = k\left(\frac{\rho_l U_u^2}{r}\right) \tag{5.7}$$

Equation (5.7) gives an important relation between radial pressure gradient and the centrifugal force from the swirling flow. As tangential flow losses increase, k decreases and the amount of radial pressure gradient needed to balance liquid centrifugal forces is lessened. If there are additional forces to consider, such as aerodynamic forces at the liquid/gas interface, increasing tangential losses could cause force imbalance in the radial direction and create potentially unsteady undulations at the interface.

Integrating Equation (5.7) and substituting the slot inlet velocity conditions from Equation (5.2) gives Equation (5.8).

$$P = C_1 - \frac{\rho_l}{2}\left(\frac{V_o R'^k}{r^k}\right) \tag{5.8}$$

Equation (5.8) can be considered the component of static pressure related to tangential flow dynamic pressure. It is not yet inclusive of the axial momentum effects. The integration constant in Equation (5.8) is found by using the boundary condition of the static pressure at the gas core radius equaling that of the gas core pressure at the interface. Applying this boundary condition to Equation (5.8) gives Equation (5.9).

$$P - P_{ac} = \frac{\rho_l}{2}\left(\left(\frac{V_o R'^k}{r_{ac}^{\ k}}\right)^2 - \left(\frac{V_o R'^k}{r^k}\right)^2\right) \tag{5.9}$$

Equation (5.9) shows that the total pressure is conserved radially across the swirling liquid flow. The static pressure at the liquid/gas interface is converted to dynamic pressures at the gas core radius and at any other radial location within the flow.

Using the continuity relation of Equation (5.5), the inlet velocity term in Equation (5.1) can be replaced by the volumetric flow rate.

$$U_u = \frac{V_o R'^k}{r^k} = \left(\frac{\dot{\forall}}{A'_o}\right)\frac{R'^k}{r^k} \tag{5.10}$$

Substitution of Equations (5.5), (5.9), and (5.10) into Equation (5.4) gives Equation (5.11).

$$\left(P_{ac}+\frac{\rho_l}{2}\cdot\left(\left(\frac{V_o R'^k}{r_{ac}{}^k}\right)^2-\left(\frac{V_o R'^k}{r^k}\right)^2\right)\right)+\frac{\rho_l}{2}\left(\left(\frac{\dot{\forall}}{A_o'}\right)\frac{R'^k}{r^k}\right)^2+\frac{\rho_l}{2}\left(\frac{\dot{\forall}}{\pi\left(r^2-r_{ac}^2\right)}\right)^2=P_o \tag{5.11}$$

The inlet velocity on the left hand side of Equation (5.11) can be replaced with volumetric flow rate divided by effective cross-sectional flow area. The left hand side then simplifies, leaving Equation (5.12).

$$P_o-P_{ac}=\left(\frac{\rho_l}{2}\frac{\dot{\forall}^2}{\pi^2}\right)\left(\frac{1}{\left(A_o'\right)^2}\left(\frac{R'}{r_{ac}}\right)^{2k}+\frac{1}{\left(r^2-r_{ac}^2\right)^2}\right) \tag{5.12}$$

The reference stagnation pressure is chosen to be the liquid supply pressure and the gas core pressure is chosen to be the chamber pressure. The difference between the supply pressure and the chamber pressure is defined as the pressure drop across the injector. This pressure drop definition is the same as the measured values of pressure from the experimental part of this work. In accordance to Doumas and Laster, the appropriate radius to associate with this pressure drop relation is the exit radius of the nozzle.

$$\Delta P=\left(\frac{\rho_l}{2}\frac{\dot{\forall}^2}{\pi^2}\right)\left(\frac{1}{\left(A_o'\right)^2}\left(\frac{R'}{r_{ac}}\right)^{2k}+\frac{1}{\left(r_h{}^2-r_{ac}^2\right)^2}\right) \tag{5.13}$$

The geometric constant is defined as Equation (5.14).

$$A' = \frac{r_h R'}{N_o r_o^2} = \frac{\pi r_h R'}{A_o} \tag{5.14}$$

The area fullness coefficient, which the ratio of cross-sectional area filled by liquid to the nozzle cross-sectional area, is defined as Equation (5.15).

$$\alpha = \frac{\pi\left(r_h^2 - r_{ac}^2\right)}{\pi r_h^2} = 1 - \left(\frac{r_{ac}^2}{r_h^2}\right) \tag{5.15}$$

Substitution of Equations (5.14) and (5.15) into (5.13), with some additional simplification, yields Equation (5.16).

$$\Delta P = \left(\frac{\rho_l}{2}\frac{\dot{\forall}^2}{\left(\pi r_h^2\right)^2}\right)\left(\frac{A'^2}{{C_{D,o}}^2}\left(\frac{r_h}{R'}\right)^{2(1-k)}\frac{1}{(1-\alpha)^k} + \frac{1}{\alpha^2}\right) \tag{5.16}$$

The first bracketed term on the right hand side of Equation (5.16) is the total pressure drop if the swirl injector was flowing full and all volumetric flow rate is going towards jet flow through the nozzle cross-sectional area. The second bracketed term on the right hand side is the adjustment needed to accommodate the tangential velocity terms. The first term in the second bracket is related to the pressure drop associated with converting the slot inlet velocity to tangential momentum. The second term in the second bracket is related to the pressure drop associated with the axial velocity flow down the swirl injector.

Equation (5.16) represents an intermediate step towards a closed system of equations relating the various swirl parameters to each other. A key parameter now introduced is the injector mass flow rate discharge coefficient, which is defined as Equation (5.17).

$$C_D = \frac{\dot{\forall}}{\left(\pi r_h^2\right)}\sqrt{\frac{\rho_l}{2\Delta P}} \tag{5.17}$$

Substitution of Equation (5.17) into Equation (5.16) gives Equation (5.18).

$$C_D = \left(\frac{A'^2}{{C_{D,o}}^2}\left(\frac{r_h}{R'}\right)^{2(1-k)} \frac{1}{\left(1-\alpha\right)^k} + \frac{1}{\alpha^2} \right)^{-0.5} \tag{5.18}$$

Rearranging Equation (5.18) to match better the format that Doumas and Laster used gives Equation (5.19).

$$C_D = \frac{\alpha\sqrt{\left(1-\alpha\right)^k}}{\sqrt{\left(\frac{A'}{C_{D,o}}\left(\frac{r_h}{R'}\right)^{(1-k)} \alpha \right)^2 + \left(1-\alpha\right)^k}} \tag{5.19}$$

Equation (5.19) does not represent an independent relation from (5.16), just a different form. If a swirl injector geometry is specified, then the geometric constant can be

considered fixed. This leaves four variables to solve for: the slot discharge coefficient, the fullness coefficient, the tangential loss factor, and the injector discharge coefficient.

Clearly, another relation is needed to define how these variables relate to each other. The relation invoked is the principle of maximum flow used by Doumas and Laster [21], as well as Bazarov [20]. This principle states that the swirling flow area will adjust so that the maximum flow possible through the swirl injector is achieved. Analytically, this relation is written as Equation (5.20).

$$\left.\frac{\partial \dot{\forall}}{\partial r}\right|_{r=r_{ac}} = 0 \tag{5.20}$$

Replacing volumetric flow rate using Equation (5.17) gives Equation (5.21).

$$\left.\frac{\partial C_D}{\partial r}\right|_{r=r_{ac}} = \frac{\partial C_D}{\partial \alpha}\frac{\partial \alpha}{\partial r_{ac}} = 0 \tag{5.21}$$

Substitution of Equations (5.15) and (5.18) into (5.21), with some additional simplification, gives Equation (5.22).

$$\frac{2(1-\alpha)}{\alpha^3} = \left(\frac{A'}{C_{D,o}}\left(\frac{r_h}{R'}\right)^{(1-k)}\right)^2\left(\frac{k}{(1-\alpha)^k}\right) \tag{5.22}$$

Equation (5.21) also implies that the flow is choked at the swirl chamber to nozzle contraction point. In other words, no disturbances exist in the flow to "disrupt" the direct relation between slot conditions and the axial velocity values downstream. At the injector contraction point, the flow establishes a maximum axial velocity equal to the surface wave velocity at the liquid/gas interface [31].

Equation (5.22) gives a relation solely between the geometric constant, fullness coefficient, slot discharge coefficient, and the tangential loss factor. An important observation from both Equations (5.18) and (5.22) is the reoccurrence of the first bracketed term on the right hand side of Equation (5.22). In their work, Doumas and Laster noted that the discharge coefficient empirically correlated well against the geometric constant defined as Equation (5.23a). Equation (5.23b) shows a similar constant defined in Equation (5.22).

$$A'\big|_{Doumas\&Laster} = A'\left(\frac{r_h}{R'}\right)^{0.5} \tag{5.23a}$$

$$A'\big|_{k} = \frac{A'}{C_{D,o}}\left(\frac{r_h}{R'}\right)^{1-k} \tag{5.23b}$$

Equation (5.23b) offers two extra degrees of freedom that Equation (5.23a) does not have: the tangential loss factor and the slot discharge coefficient. The tangential loss factor term allows for additional frictional losses inside the swirl injector in addition to those captured by the changing cross-sectional areas of swirl chamber diameter to nozzle

tube diameter. This term will be important in the upcoming sections of the chapter to help explain additional loss mechanisms for a fixed geometry swirl injector. The slot discharge coefficient helps to account for losses associated with the inlet flow's Reynolds number.

Definition of the slot inlet discharge coefficient varies from author to author. Not only do the inlet edges of the slots affect the discharge coefficient, but so does the overall length of the slots. While the slot length was held constant in Doumas and Laster's work, the orifice radius and inlet velocity was changed notably as part of the test matrix. The actual slot length was not reported in Doumas and Laster's publication, so the actual loss due to friction through the slots cannot be calculated. But for standard pressure drop considerations, the inlet Reynolds number is adequate to use as a representative value. The inlet slot Reynolds number and discharge coefficient are defined as Equations (5.24a) and (5.24b), respectively. These definitions are those advocated by Khavkin [34] in his review of swirl injector research, and were previously used in Chapter 3.

$$\mathrm{Re}_o = \frac{V_o(2r_0)}{\upsilon} = \left(\frac{\dot{\forall}}{N_o \pi r_o^2}\right)\left(\frac{2r_o}{\upsilon}\right) = \frac{2\dot{\forall}}{N_o \pi \upsilon r_0} \tag{5.24a}$$

$$C_{D,o} = \left[1 + \frac{5.843}{\log\left(\mathrm{Re}_o^{1.432}\right)}\right]^{-0.5} \tag{5.24b}$$

At this point, experimental data is needed to relate k to swirl injector geometry and operating conditions. The data gathered in this work will be related to k in the next section, but data was not gathered to ascertain the effects of injector geometry and design operating parameters. Thus, the measured data from Doumas and Laster's experiments was digitally tabulated in an Excel sheet. Using a solver routine from Mathcad, Equations (5.19) and (5.22) were solved for the area fullness coefficient and the tangential loss factor for a given geometry and measured discharge coefficient. The results for k and α are plotted versus the geometric constant in Figure 5.3.

Examination of Figure 5.3 shows that while the area fullness coefficient has a definite trend of decreasing with increasing geometric constant, k exhibits much more scatter. The overall trend of k with A' is similar to that of the area fullness coefficient, but the large data scatter implies that not all relevant independent parameters have been captured to best define k. Because k is related to the injector flow losses, additional independent flow parameters were chosen to correlate k against. A' is used to represent the flow losses associated with flow contraction and non-uniformity. Increasing A' increases flow losses and should decrease k. $C_{D,o,}$ a function of Re_o according to Equation (5.24b), is also used since flow losses at the slots contribute to the total flow losses of the injector. Increasing $C_{D,o}$ will decrease slot losses and increase k. Re_o is used independently to represent the flow losses along the injector due to wall friction. Increasing Re_o decreases viscous losses and increases k.

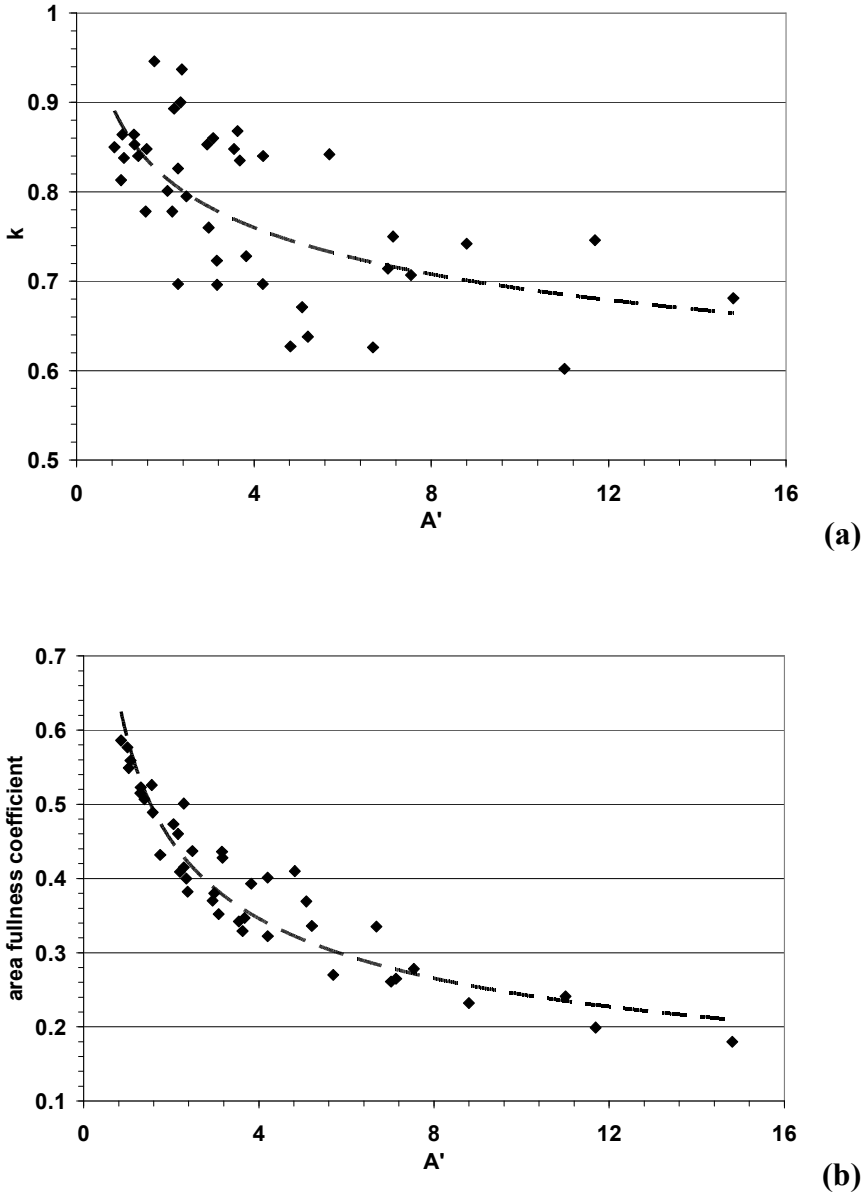

Figure 5.3 (a) Fitted tangential loss factor and (b) area fullness coefficient versus geometric parameter

Figure 5.4 shows *k* versus the combined independent variables. Regression analysis shows that *k* varies with multiple of listed independent variables logarithmically.

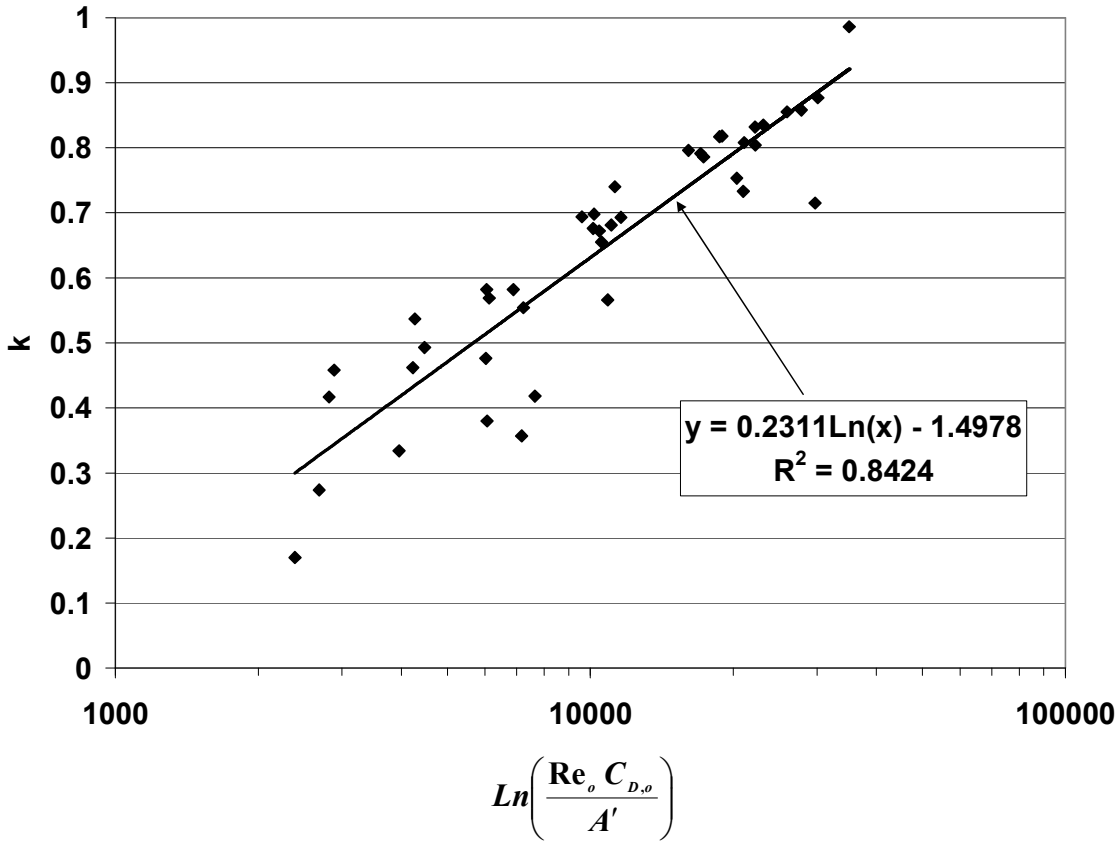

Figure 5.4 Fitted tangential loss factor versus ratio of selected independent variables

Figure 5.4 shows that the use of additional variables aids in collapsing the *k* value data compared to Figure 5.3. Figure 5.4 also shows how the Reynolds number and the geometric constant work to define the *k* value for a given swirl injector. As the Reynolds number is increased via volumetric flow rate, the amount of tangential momentum introduced into the injector is increased. More liquid momentum gives the ability for the swirling flow to overcome friction effects through the swirl body, and still retain a high degree of swirl. Increasing the geometric constant works to increase tangential losses inside the swirl injector, shown by decreasing *k*. Increasing the geometric constant can

occur by either increasing the swirl chamber radius, or by decreasing the slot orifice radius. Increasing the nozzle radius or the swirl chamber radius creates a larger cross-sectional area change that the flow has to move through while swirling down the injector. Even though the injector has a nominal transition angle to aid in the diameter transition, there are still contraction losses associated with moving the flow from a larger swirl chamber radius to a smaller nozzle radius. Losses also occur in the slots where a smaller slot orifice radius can also cause contraction losses of the flow.

Using logarithmic regression analysis, the trend of k was captured to give Equation (5.25).

$$k = 0.2311 \ln\left(\frac{\mathrm{Re}_o C_{D,o}}{A'}\right) - 1.4978 \tag{5.25}$$

Equation (5.25) is plotted in Figure 5.4 to show how the fitted values and the predicted values compare for various inlet Reynolds numbers, slot discharge coefficients, and geometric constants. Over the range of values, the prediction captures the overall data trend well.

One last important variable remains to help close the system: the design spray angle. The general relation between spray angle and features of the flow is through the vector angle of the total liquid velocity exiting the nozzle, defined as Equation (5.26).

$$\tan\left(\frac{\theta}{2}\right) = \frac{V}{U} \tag{5.26}$$

Using Equations (5.5) and (5.10) to replace the velocity components, as well as simplifying the expression using Equation (5.23b), Equation (5.26) becomes Equation (5.27).

$$\tan\left(\frac{\theta}{2}\right) = \frac{A'|_k}{\alpha} \tag{5.27}$$

Equation (5.27) shows that the exiting spray angle into the chamber is not only dependant on the modified geometric constant, but the resulting area fullness coefficient as well. Figure 5.5 shows the measured Doumas and Laster spray angles plotted versus the right hand side of Equation (5.27). It was found that the linear relation defined in Equation (5.27) did not give the best fit; a logarithmic curve fit actually gave the best trend representation.

Equation (5.28) is considered an updated version of Doumas and Laster's empirical definition of the spray angle. The logarithmic relation between the independent variables and the spray angle is counter to the linear definition of Equation (5.27). The spray angle may be linearly related at high values of the modified geometric constant to area fullness coefficient ratio, but Figure 5.5 shows that for low values of this ratio, the spray angle dependence changes.

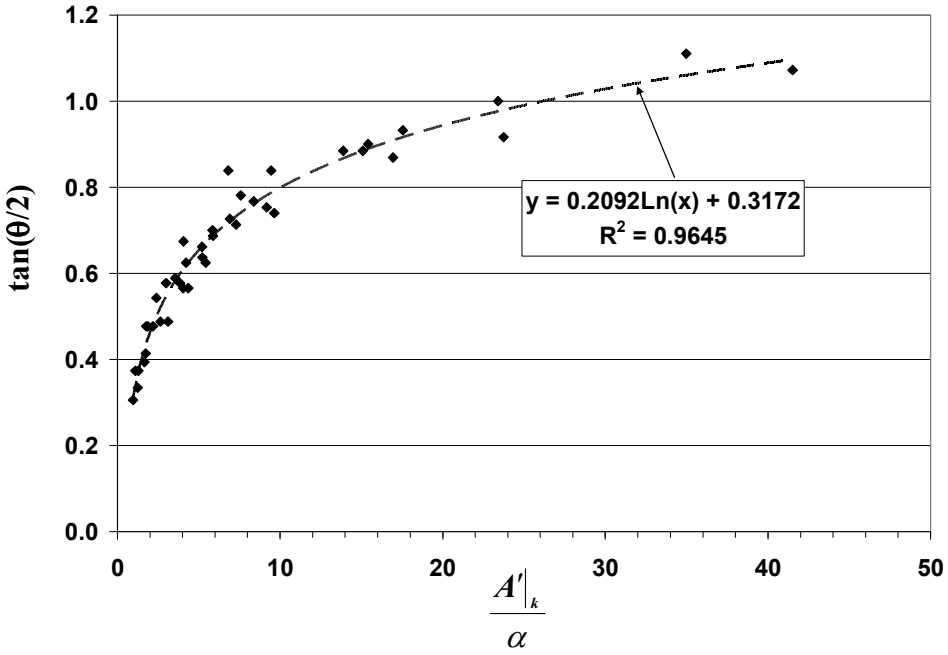

Figure 5.5 Tangent of measured half spray angle versus ratio of Equation (5.23b) and measured area fullness coefficient

$$\tan\left(\frac{\theta}{2}\right) = 0.2092 \ln\left(\frac{A'|_k}{\alpha}\right) + 0.3172 \tag{5.28}$$

With the addition of Equation (5.27), a system of equations has been defined relating all relevant swirl injector design features to each other. Using these equations, the design features of the injector used in this work are defined in Table 5.2. Comparison of the predicted and measured values for the swirl injector design features show that the only parameter showing notably different values from measurement to prediction is the injector pressure drop. The overestimation of the pressure drop is chiefly due to underestimation of the discharge coefficient. Attempts were made to correct this

difference by artificially increasing the inlet slot discharge coefficient, but while the predicted swirl injector discharge coefficient and pressure drop values moved closer to the measured values, the other predicted values of fullness coefficient and the design free spray angle moved away from good agreement with the measured values. It was decided that the best agreement of all of the data points came from the formulas and settings used to define Table 5.2. Namely, it is accepted that the discharge coefficient is slightly underpredicted and the swirl injector pressure drop is somewhat overpredicted.

Table 5.2 Comparison of calculated and measured swirl injector features

Parameter	Measured Value	Equation Used	Predicted Value	Relative Error (%)
R (mm)	2.388			
r_h (mm)	1.041			
r_o (mm)	0.787			
N_o	3			
$\dot{\forall}$ (m^3/s)	$9.076*10^{-5}$			
A’		(5.14)	1.244	
Re_o		(5.24a)	24330	
$C_{D,o}$		(5.24b)	0.72	
k		(5.25)	0.79	
A'_k		(5.23b)	1.528	
α	0.625	(5.22)	0.591	-5.44
θ (deg)	55.42	(5.28)	55.15	-0.49
r_{ac} (mm)	0.668	(5.15)	0.666	-0.30
t (mm)	0.373	$r_h - r_{ac}$	0.375	0.54
C_D	0.380	(5.19)	0.356	-6.32
ΔP (MPa)	2.442	(5.17)	2.796	14.47

5.2 Swirl Injector Operation at Variable Thrust Conditions

The previous section related the film thickness, injector discharge coefficient, and the free cone spray angle to the geometrical and operating parameters of a swirl injector. This section will compare the predictions for these injector parameters to the actual measured results from the previous two chapters in order to assess the difference between predicted operation at design conditions and at varying mass flow rate / chamber pressure conditions.

5.2.1 Film Thickness Profiles

Equation (5.25) was used to find k for each operating condition tested. These values of k, along with calculated orifice discharge coefficients and injector geometric parameters, were used in Equation (5.22) to predict the area fullness coefficient at each operating condition, denoted as α_{pred}. Equation (5.15) was used to find the average fullness coefficient value for each of the film thickness values listed in Figure 3.27. These values, denoted as α_{meas}, were compared by ratio to the predicted values and plotted as Figure 5.6.

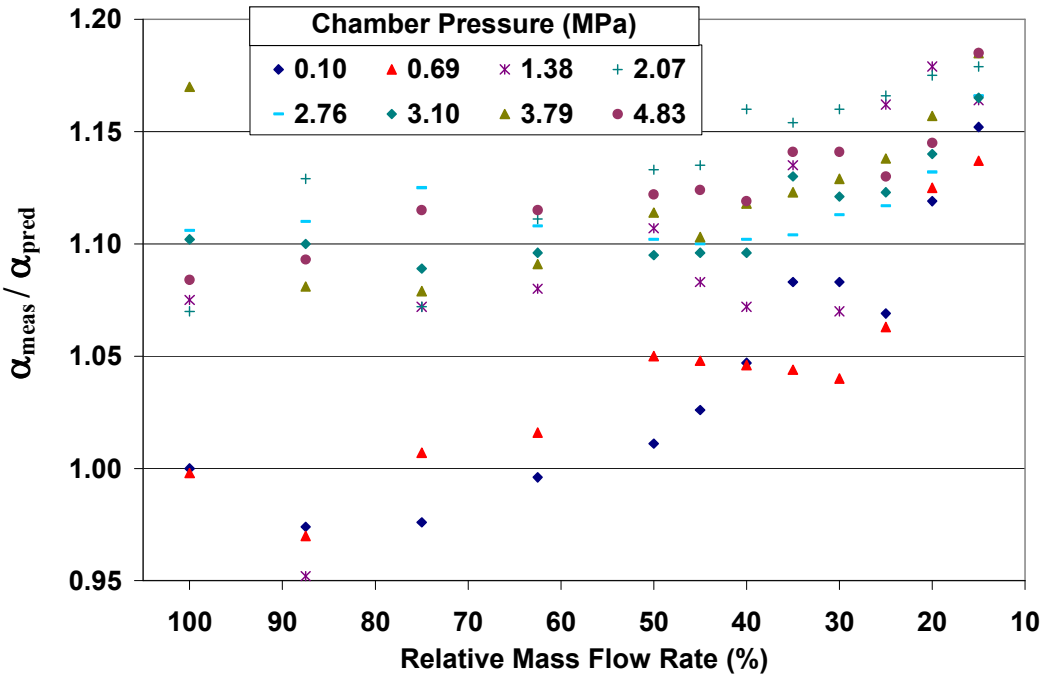

Figure 5.6 Measured to predicted fullness coefficient ratio for tested conditions

Figure 5.6 shows that for both increasing chamber pressure and/or decreasing mass flow rate, the measured fullness coefficient generally increases above the predicted value. Increasing fullness coefficient results from increasing momentum losses through viscosity or decreasing the injected momentum relative to the design value of the injector. The relations derived in this chapter empirically account for the viscous losses in the injector and the tangential orifice pressure drop, but do not have terms explicitly quantifying the momentum loss caused by the vortex breakdown event. The lack of the relations to accommodate for this momentum loss mechanism is considered a primary reason why the predictions are up to 20% lower than the actual measured fullness coefficients. Other reasons include lack of proper implementation of wall friction within

the relations, and the possible change in the axial and tangential velocity profiles after the vortex breakdown.

Increase in film thickness profiles with increasing chamber pressure and decreasing mass flow rate should not be a large concern to the injector designer as long as the injector still meets discharge coefficient and spray angle requirements. However, there is a specific swirl injector design that does benefit from knowing the film thickness profile at elevated chamber pressure and reduced mass flow rate. This injector element design, historically used in several Russian engines, is a mixed jet-swirl injector and has been described by Bazarov [77] and Dranovsky [78].

The jet-swirl design splits part of the liquid propellant flow into swirl screws within the injection element, and the other part into a jet passage within the swirl screw body. The resulting spray is a swirling sheet with a liquid jet aligned along the flow's axial centerline. The liquid jet is present inside the injector element, centered within the swirling flow's vortex chamber. At atmospheric chamber pressure, the jet-swirl injector will perform to design, assuming that the jet diameter is smaller than the gas core of the swirling flow. If the ambient chamber pressure is increased and/or the injected mass flow rate is reduced however, the swirling flow's film thickness can increase and ultimately can touch the centered jet flow. If the jet and swirling flow contact within the element, the subsequent flow will become rough and agglomerated, giving rough atomization and low combustion efficiency.

Dranovsky reported that when the jet-swirl element design was tested at using simulant propellant, the central jet would stay separated from the swirling flow at atmospheric chamber pressure conditions. At elevated chamber pressure operation, the

jet-swirl injector element exhibited a composite flow of the separate jet and swirl liquid components. Given the results from Chapter 3, it is possible that at elevated chamber pressure the internal film thickness profile was higher than predicted and the swirling vortex contacted with the centered jet post. Swirling flow contact with the jet post caused collapse of the swirling flow, yielding a more concentrated agglomerate liquid flow. This liquid agglomeration would disrupt the exiting jet post flow and cause the jet-swirl injector design to perform poorly. Clearly, effects of elevated chamber pressure assessed in cold flow conditions is a positive design impact to this injector type prior to hot fire testing.

5.2.2 Discharge Coefficient

The predicted values of k and α_{pred} were used in Equation (5.18) to predict values of injector discharge coefficient for each operating condition tested. Figure 5.7 shows these predicted values compared to the measured values. Comparison between prediction and measured discharge coefficient values show relatively poor agreement. Inaccurate fullness coefficient predictions affect the accuracy of the predicted discharge coefficient values.

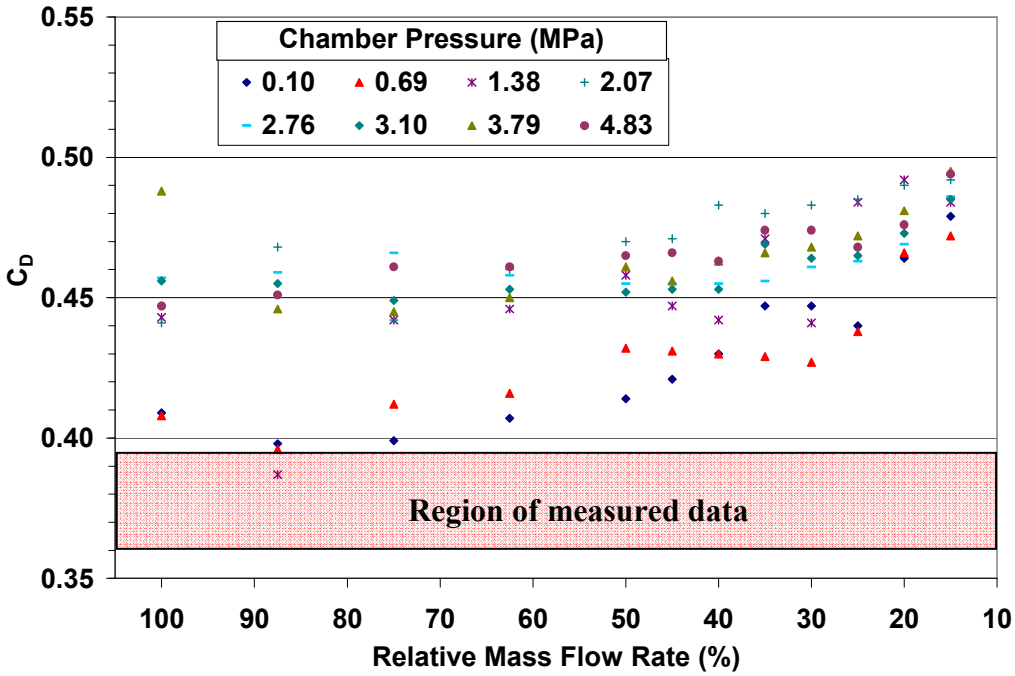

Figure 5.7 Predicted discharge coefficient values

The discharge coefficient measurements reported in Chapter 3 show roughly a maximum of 5% change with respect to the measured value at full mass flow rate and ambient chamber pressure. For an injector designer this change would be considered typically negligible, especially when considering the uncertainty bounds on the data itself. However, the trends of the discharge coefficient shed light on the state of the swirling flow in the injector at the various operating conditions. At low flow rate, the discharge coefficient corresponds to trends noted for assumed orifice flow inside the slots. Also at low chamber pressure, a reduction in slot Reynolds number can potentially drive a hydraulic flip mechanism to occur within the slots. Both effects of low orifice

flow and hydraulic flip can change how the injector discharge coefficient changes with mass flow rate.

Increasing the chamber pressure at a near-design mass flow rate increased the injector discharge coefficient. At a high mass flow rate, increased chamber pressure causes viscous losses due to increased liquid/gas interfacial shear and axial liquid flow recirculation losses. Both loss mechanisms can increase the injector discharge coefficient by raising the liquid flow area through the injector. Equation (5.19) shows that increasing the liquid flow area, represented by the fullness coefficient, will increase the resulting discharge coefficient assuming small changes in the tangential loss factor and slot discharge coefficient.

5.2.3 Spray Angle

The vector tangent of the half spray angle, f_{pred}, was predicted using Equation (5.28) and the values of k and α_{pred}. The measured vector tangent values reported in Figure 4.15, f_{meas}, were compared against the predicted values by ratio, seen below in Figure 5.8. Predictions give good agreement at high relative mass flow rate and atmospheric chamber pressure. Increasing the chamber pressure and/or lowering the relative mass flow rate gives measured values less than the predicted values by 20% and greater.

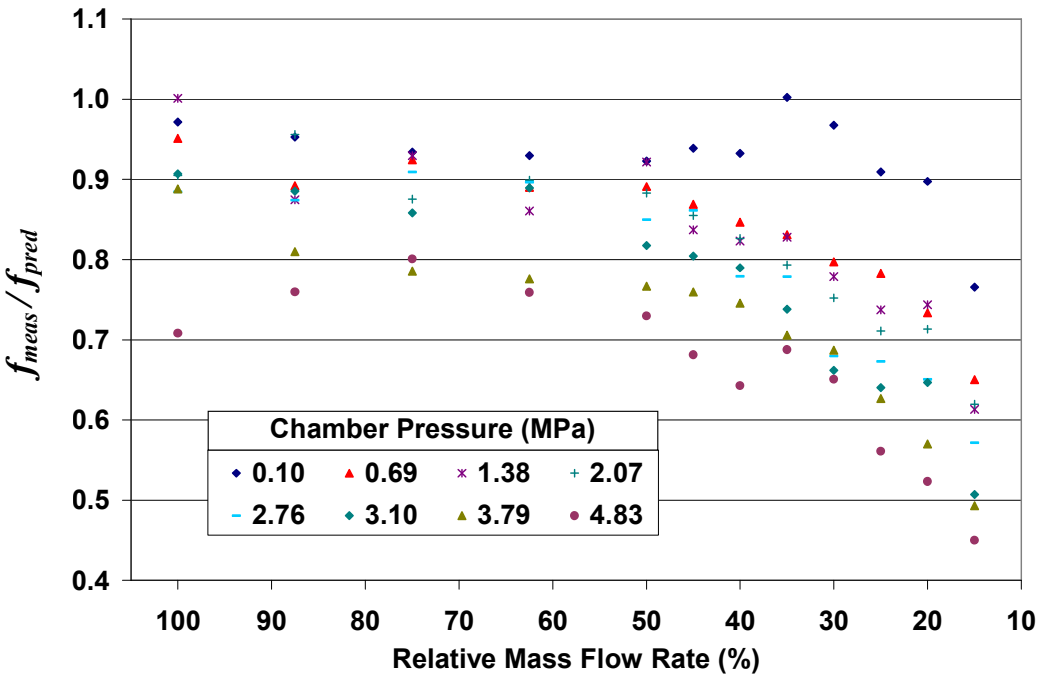

Figure 5.8 Measured to predicted half spray angle values

The free cone spray angle represents the vector angle between the net tangential and axial velocity components exiting the nozzle. Any influence of varying mass flow rate and chamber pressure on these velocity components internal to the injector are related to free cone spray angle values. The free cone spray angle value is the predicted value from the relations derived in the previous section. The effects of lowering mass flow rate and increasing chamber pressure on the swirling liquid sheet downstream of the nozzle exit is related to the measured chamber angle values. Because this work was not able to distinguish whether a measured spray angle is the free cone spray angle or the chamber angle, it is unclear whether the measured spray angle values are best compared

with the predicted values. The relations derived in the section above would have to be extended to model the downstream swirling sheet and the additional effects of downstream gas entrainment on the spray boundary. This extended modeling should be able to comment whether a measured spray angle is truly the free cone spray angle related only to internal injector flow properties, or the chamber angle which is considered the free cone spray angle modified by downstream chamber effects.

CHAPTER 6

CONCLUSIONS AND RECOMMENDATIONS

6.1 Summary and Conclusions

In order to assess the effects of reduced mass flow rate and elevated chamber pressure operation of a liquid swirl injector, a cold flow study was conducted. A tangential slot swirl injector, rated for 0.09 kg/s flow rate and 50 deg free cone spray angle was tested at elevated chamber pressure in a cold flow facility. The injector's delivered flow rate was varied from 100% down to 15% of the design mass flow rate. The injector was also tested at elevated chamber pressure from 0.10 to 4.83 MPa.

The cold flow facility offered optical access into the chamber and a combination backlight and camera system was utilized to image the internal and external flow field of the injector. The swirl injector itself was designed with an acrylic nozzle section to allow visualization of the internal swirling flow at various relative mass flow rate and chamber pressure operating conditions. Both high resolution digital stills and high speed video

captures were used to assess the swirl injector flow field. Images and videos were post-processed using the ImageJ software package.

Three fluid mechanic parameters of the swirl injector design, linked to swirl injector performance, were assessed for effects of reduced mass flow rate and elevated chamber pressure operation. These three parameters are film thickness along the injector nozzle, overall injector discharge coefficient, and downstream spray angle. Each parameter was assessed independently from each other using facility measurements and imaging techniques.

Using backlight illumination, the swirling flow along the swirl injector nozzle was imaged with a high speed video camera and a high resolution camera. High speed video showed that the swirling flow profile displayed a jump in the flow profile at a fixed mass flow rate and moderate levels of elevated chamber pressure. The jump showed fluctuations in time and increased the film thickness locally. For higher chamber pressure, the jump moved further upstream and became spatially stationary in the flow. Swirling flow before the jump displayed film thickness profiles similar to the profiles at atmospheric chamber pressure. After the jump, the swirling flow film thickness profile increased and the liquid/gas interface showed surface undulations.

By comparing the jump structure to previous work performed on swirling flow in tubes, the jump was identified as a strong vortex breakdown occurring with the injector flow. The vortex breakdown phenomenon in swirling flows has already been related to swirl number values below 0.6. Using estimates for the flow parameters, the swirl number for the flow was calculated as being approximately 0.6 at design mass flow rate and atmospheric chamber pressure conditions. This result showed that the internal swirl

injector flow was inherently unsteady and small changes in liquid/gas surface friction or injected mass flow rate could create a vortex breakdown in the flow.

High resolution digital stills were used to capture the flow profile and to quantify the film thickness along the nozzle. Using an edge detection method, the film thickness profiles were determined for each mass flow rate and elevated chamber pressure combination tested. At the design mass flow rate, film thickness profiles at slightly elevated chamber pressure generally matched those at atmospheric chamber pressure. At moderately elevated chamber pressure, the jump in the flow profile notably changed the film thickness profile to give area fullness coefficients of roughly 17 – 20% higher relative to the atmospheric values.

In general, the chamber pressure elevation and/or the injected mass flow rate reduction both affect the swirling flow by increasing flow loss mechanisms. Elevating chamber pressure increased the liquid/gas interfacial friction of the internal swirling flow. This friction component was increased until the swirling flow displayed notable axial recirculation and subsequent vortex breakdown. Upstream of the breakdown, the swirling flow showed the same characteristics as was designed for. Downstream of the breakdown, the flow showed different characteristics, namely, an increased average film thickness profile. A similar observation was seen by reducing injected mass flow rate. By lowering the available liquid momentum, the flow sees an equivalent loss mechanism as was seen with elevating chamber pressure. The internal flow again displayed a breakdown event along the internal flow profile. The only difference was that the flow was much more unsteady at the liquid/gas interface.

The injector discharge coefficient was determined from the measured injector pressure drop and injected mass flow rate for each operating condition tested. At the lowest relative mass flow rate and highest chamber pressure, the value of the discharge coefficient changed approximately 5% relative to the design value. However, the trend of the discharge coefficient change with increasing chamber pressure was sensitive to the injected mass flow rate. In particular, the change of discharge coefficient with chamber pressure was approximately linear, with the slope and intercept of the linear relationship being functions of tangential slot Reynolds number. It was observed that the intercept, representative of the injector discharge coefficient with no chamber pressure influences, showed trend changes with decreasing mass flow rate. One particular trend change at approximately one half of the design mass flow rate was attributed to slot hydraulic flip behavior. The other particular trend change at approximately one quarter of the design mass flow rate was attributed to behavior changes of the orifice flow coefficient below a slot Reynolds number of 4000 or less. The slope generally decreased in value with decreasing mass flow rate relative to the design value.

Multi-image captures of the downstream spray angle were recorded using a high speed video camera. Spray boundary pixel intensities were recorded over multiple frames for each operating condition tested. The spray boundary was determined using a combination of image post-processing techniques and edge detection algorithms. The downstream location of the spray angle was recorded where the spray boundary displayed an inflection point in shape. The subsequent spray angle was then determined by the relative vector angle between the spray boundary inflection point and the injector exit nozzle origin.

Results showed that lowering relative mass flow rate at atmospheric chamber pressure lowered the downstream spray angle of the flow. Elevating the chamber pressure at fixed mass flow rate also lowered the spray angle in a linear fashion. Linear trends of spray angle with mass flow rate and chamber pressure were found to be a function of nozzle-based Reynolds number and Weber number. For increasing Weber number, or increasing liquid sheet relative momentum over surface tension, the downstream spray angle decreased linearly. For decreasing nozzle Reynolds number, or decreasing injected liquid momentum, the effects of increasing Weber number became greater. Increase in the internal film thickness and in the ambient chamber gas density worked to lower the downstream spray angle below predicted spray angle values.

Finally, fundamental relations between the average fullness coefficient, injector discharge coefficient, and free cone spray angle were derived using previously recorded data from Doumas and Laster's work. The relations included the effects of tangential slot pressure drop and of an assumed viscous Rankine vortex structure within the internal swirling flow. The relations showed good agreement with the previously measured data and with the values recorded in this work at design mass flow rate and atmospheric chamber pressure. The relations helped to qualify how reducing mass flow rate and elevating chamber pressure deviated the swirl injector parameters away from the ideal design state.

6.2 Impact to Swirl Design Process

This work represents the first step towards understanding the influences of off-design mass flow rate operation and elevated chamber pressure on swirl injector fluid mechanics. Since typical booster liquid rocket engine operation is on order of 1 – 10 MPa, a swirl injector design based on only atmospheric chamber pressure considerations could be inadequate in describing the actual film thickness profiles, injector discharge coefficient, and downstream spray angle. Specifically, the internal film thickness profile displayed features of axial recirculation and vortex breakdown in the flow. The traditional analytical frameworks of Doumas and Laster and Bazarov do not directly take into account these features, especially at elevated operating chamber pressure. The swirl injector designer should accommodate this change in internal flow behavior to make sure that the downstream film thickness profile, and the related swirl parameters, still satisfies the performance needs of the injector element.

For variable thrust applications where injected mass flow rate is lowered below the design values, the discharge coefficient could show much variability with respect to the rated design value. While the discharge coefficient values in this work only varied on order of 5% with respect to the value at full mass flow rate, the trend of the discharge coefficient changed with operating mass flow rate. That is, the slot Reynolds number was lowered to a point where the flow inside the slots could be transitioning between various types of orifice flow. For this injector, flow Reynolds number changes showed minor differences in the overall injector discharge coefficient. However, other swirl injector designs could be very sensitive to the slot flow regimes of operation. In this

region of operation, the swirl injector designer should take care to note the change in flow regime and adjust the prediction models accordingly.

Finally, the spray angle values measured in this work show large changes with both chamber pressure elevation and mass flow rate reduction when compared to the predicted design spray angle. For effective swirl injector implementation in rocket engines, the injector designer should account for any spray angle changes associated with engine operation. Any subsequent changes in the injection process due to spray angle changes should be captured, and the predicted combustion process should be appropriately updated.

6.3 Recommendations for Future Work

A significant number of results have been generated within the scope of this work. The effect of varying injection mass flow rate and downstream chamber pressure has been observed to change the swirl injector parameters notably from the design values. However, this work raised a number of questions that deserve continued research and development. Several of these questions, as well as suggested research plans, are given below.

What is the swirl injector's internal flow field at various mass flow rate and elevated chamber pressure? In the course of this work, no direct assessment was made of the liquid flow field's axial and tangential velocity components. In Chapter 5, an assumed tangential velocity flow field of modified Rankine flow was used to give a closed system of equations describing the internal injector flow. However, the assumed

relations did not incorporate axial recirculation or vortex breakdown of the flow that the results of Chapter 3 advocated. A useful set of research would consist of measuring the internal flow field of a swirl injector for off-design mass flow rate operation and elevated chamber pressure. PIV techniques such as those employed by Wang [69] could be applied to swirl injector designs to give the details about how the vortex breakdown phenomenon changes with swirl injector operation. Another limitation of this work was that only the nozzle section of the swirl injector was optically accessible. At high enough chamber pressure, the strong vortex breakdown seemed to move further inside the injector into the vortex chamber section. A new swirl injector design with optical access to both the nozzle and vortex chamber could offer a more complete picture of the flow velocity field at elevated chamber pressure.

How does the tangential slot discharge coefficient influence the overall injector discharge coefficient? Observations of the overall injector discharge coefficient measurements within this work imply a strong link between the tangential slot behavior and the measured injector discharge coefficient. For flow in orifices, changing the inlet mass flow rate has often been associated with potential flow detachment and cavitation. A mapping of the flow field within the tangential slots would be very useful in explaining how the slot behavior changes with reduced mass flow rate. Relations derived in Chapter 5 contain a slot discharge coefficient term as a function of inlet Reynolds number, but the Reynolds number was associated with the liquid flowing full in the slot. What is actually needed is a slot discharge coefficient versus inlet mass flow rate inclusive of reducing mass flow rate for fixed slot geometry. This mapping could occur

at atmospheric chamber pressure, and acrylic hardware could be used to note any cavitation that might occur within the slots.

How do the fundamental relations of swirl injector flow change with the inclusion of the vortex breakdown phenomenon? The relations derived in Chapter 5 have no analytical framework to accommodate the axial flow recirculation within the injector. Computational fluid dynamics (CFD) simulations of the swirl injector flow field at reduced mass flow rate and elevated chamber pressure could give insight on how the internal flow structure is defined for various operating conditions. The results from the CFD analysis could be used to make assessments on what important parameters, such as the flow swirl number, should be included within the fundamental design relations to best accommodate the vortex breakdown inception and effects. CFD simulations of the injector of this work would be very useful, since the anchoring data is already available, and the swirl injector element is small enough to model completely.

How do different swirl injector geometries respond to changes in mass flow rate and chamber pressure? Because only one swirl injector geometry was tested in this work, no conclusions were given on how other swirl injector geometries would respond to changing mass flow rate and chamber pressure. For example, the omission of a convergence angle between the vortex chamber and the nozzle may cause the injector's internal flow field to respond differently to increasing chamber pressure. Changing the number and type of tangential slot orifices could cause different injector reactions to hydraulic flip. A series of experiments that subjected different swirl injector configurations to the same scope of test matrix seen in this work would be very interesting and valuable to the swirl injector design engineer.

APPENDICES

APPENDIX A

WNIST FACILITY OPERATING PROCEDURES

Robert J. Kenny
ER32

TEST AND CHECKOUT PROCEDURE FOR THE

WATER/NITROGEN INJECTOR SPRAY TEST

TEST CELL 110/BUILDING 4583

SUBMITTED BY: _____ _____

Robert J. Kenny/ER32 DATE

Test Cell Engineer

APPROVED BY: _____ _____

Kevin W. Pedersen/ET11 DATE

Test Engineer

_____ _____

James Aaron/ET11 DATE

Deputy Branch Chief, Mechanical Branch

_____ _____

Alvin J. Eidson/QS50 DATE

Industrial Safety Dept.

_____ _____

George Schmidt/XD20 DATE

Director, Propulsion Research Center

Robert J. Kenny
ER32

A) PURPOSE

This document describes the procedural steps required for operating the Water/Nitrogen Injector Spray Test (WNIST) located in Test Cell 110 in Building 4583.

B) GENERAL

The TD40 Test Conductor is in charge of test operations conducted for this program and is responsible for ensuring that the appropriate procedures and policies are followed. All activities pertaining to tests that are performed will be coordinated through this Test Conductor.

C) APPLICABLE DOCUMENTS

The latest version of each of the following procedures shall be used at the time the test is performed.

MPG 8715.1	Marshall Safety, Health and Environment(SHE) Procedure
MWI 8715.6	Hazardous Operations
MOU 5.2	Memorandum of Understanding (TD40/TD70): TD40 Use of Test Cells in Building 4583

D) SAFETY

1) Hazards

High pressure gas (GN_2)

- Overpressure of systems is prevented by using properly sized relief valves.
- Pressurized systems will be operated in accordance with pressure certifications.
- Oxygen deficiency detection and alarm systems are functional within Test Cells 109 and 110.
- Hearing protection will be utilized as required

2) Emergency Control Center

Room 113 in Building 4583 will be the emergency control center for TC109/110 if required.

3) Injuries

In the event of an injury at TC110, do not move the injured personnel unless failure to do so may result in further injury.

4) Emergency Telephone Numbers

Safety	4-0046
Ambulance	911
Medical Center	4-2390
Fire	911
Security	4-4357 (4-HELP)
Utilities	4-3919

Teledyne Brown	4-9540
Area Coordinator	4-3080
ET10 Point of Contact	
Kevin Pedersen	4-0532 desk
	518-3542 pager
John Price	4-4645
XD20 Point of Contact	
Noah Rhys	4-2386

E) PRETEST PROCEDURES

1) The Test Conductor will present the test schedule at weekly ET10 scheduling meetings.

a) ( )Coordinate with other Test Cell operations in 4583, with Solar Thermal Test Facility, Test Stand 115, and Test Stand 116.

2) Verify and Implement Safety Controls

Oxygen Deficiciency Detection and Alarm System

a)( )Inspect the Oxygen Deficiency Control Box for indication of a functional oxygen deficiency system. This box is located in Building 4583, Room 114A, on the wall between the windows viewing Test Cells 106 and 107. Card 7, Slot 1 is for Test Cell 110. Verify there is a Green light on this card and the meter reads 21 +/- 1% oxygen. If this is not the case, contact Bobby Collier, EG&G at 544-4016. If temporary replacement equipment is needed or if Mr. Collier is unavailable, contact the medical center at 544-2390. An active oxygen deficiency detection and alarm system

is required before continuing with the execution of this procedure.

Area Control

b)( )NOTE: Barracades and hearing Personal Protection Equipment (PPE) shall be required as described below, unless this requirement is removed after Environmental Health Management personel have taken noise level measurements during vent operations and determined the noise levels are low enough to relax the PPE and barracade requirements.

1( ) Install stanchions and warning signs around vent line on roof of building 4583, above Test Cell 110.

2( ) Install chain barricades across the two stairways providing access to the roof of building 4583.

3( ) Wear hearing PPE whenever outside, near Test Cell 110, during vent operations.

4( ) Contact the Area Coordinator at 4-3080 and ask for the following area announcement:

"High pressure vent operations are about to begin near Test Cell 110, building 4583. All Personnel outside, near Test Cell 110 shall wear proper hearing personal protection equipment."

3) Establish Test Documentation

Facility Record Book

a)( )Verify the Facility Record Book (FRB) does not have any open issues that will prohibit the execution of this procedure.

b)( )Verify the installed Curtain Purge Can and Purge Plate are identified in the FRB. Verify the Curtain Purge Can relief valve, RV-PC-5 is sized properly for this Can and Purge Plate.

c)( )Verify the FRB has documented the current configuration of the fluid system.

d)( )Verify the FRB has a copy of the current version of this test procedure.

e)()Verify the facility configuration has been photographed.

Daily Experiment Profile Sheet

a) ( ) Fill out a Daily Experiment Profile Sheet (DEPS) with the following information, describing the planned experiment:

1) ( ) Injector configuration
2) ( ) Injector and Test Chamber Pressure Profiles
3) ( ) Injector flowrates
4) ( ) Water temperature profiles for GN2 heat exchanger
5) ( ) Curtain Can and Purge Plate configuration

6) ( ) Type of imaging
7) ( ) Computer filename of acquired data
8) ( ) Facility 1st Stage GN2 Pressure
Record this pressure here: _____
Record this pressure in Step E.6.e of this procedure.

b)( )Verify the Curtain Flow Can and Purge Plate will meet the profiles identified in DEPS.

c)( )Verify the FRB does not identify any facility configurations issues that would prevent meeting the objectives identified in the DEPS.

4) Set up/verify Control and Data Acquisition System

a)( )Turn on both 28 volt DC power supplies.

b)( )Start Data Acquistion Display System
Verify transducer measurements are being properly displayed on the Data Acquisition computer screen.

c)( )Start LabView Control System
Verify transducer measurements are being properly displayed on the LabView computer screen. Current interface configuration is pictured in Figures 1(a) and 1(b) at the end of this procedure.

5) Verify Initial Facility Configuration

a) ( )Visually inspect facility fluid systems, verify all systems are fully assembled and that no lock-out/tag-outs are present.

b) ( )Verify injector configuration has been photographed.

c) ( )Visually inspect the Test Chamber windows using a flashlight. If there are any scratches or cracks present, compare these to the pedigree documented in the Facility Record Book. If any new flaws are present, the window must be replaced before the Test Chamber is pressurized. NOTE: Only windows with a pedigree that has been certified for use by the Optics Department may be used in the Test Chamber.

d) ( )Verify the facility system is vented as indicated by 0 psig on the following pressure gauges:

e) ( )PG-N5, 5000 PSIG GN2 Supply

f) ( )PG-N8, 1440 PSIG GN2 Supply

g) ( )PG-I3, Injection GN2

h) ( )PG-W5, Water Tank

i) ( )PG-W9, Injector Water

j) ( )PG-C1, Test Chamber

k) ( )PG-P2, Curtain Flow and Window Purge Pressure Loader

l) ( )Verify initial facility hand valve and hand pressure regulator configuration

m) ( )HOV-C3, Vent Line Drain……..CLOSED

n) ( )HOV-N20, 1440 PSIG GN2 Shutoff……..CLOSED

o) ( )HOV-N12, 2nd Stage GN2 Shutoff……..CLOSED

p) ( )HOV-N4, 5000 PSIG Facility GN2 Shutoff…CLOSED

q) ( )HOV-N9, 1440 PSIG GN2 Vent……OPEN

r)( )HOV-PW4, Window Purge Shutoff……CLOSED

s)( )HOV-PC4, Curtain Flow Shutoff…CLOSED

t)( )HOR-P1, Curtain Flow and Window Purge Pressure Loader……..Fully Vented Position

u)( )Verify Water Tank, T-W4, has adequate water

v)( )Verify Water Tank is vented and reading 0 psig per PG-W6.

w) ( ) HOV-W2, Sight Glass Shutoff…….OPEN

Observe liquid level in SG-W3, Water Tank Sight Glass. Determine if water needs to be added. If so, add water as follows:

1) ( ) HOV-W6, Water Tank Vent……OPEN
2) ( ) HOV-W1, Fill Isolation…….OPEN
3) ( ) Add water to the tank from de-ionized water tank. See appendix for de-ionized water tank refill instructions
4) ( ) HOV-W1, Fill Isolation….CLOSED
5) ( ) HOV-W6, Water Tank Vent……CLOSED

x) ( ) HOV-W2, Sight Glass Shutoff……..CLOSED

6) Set up/verify First Stage Regulator System

a) ( ) HOR-N6, 1440 PSIG GN2 Loader…….Fully Vented Position
b) ( ) Verify PG-N5 and PG-N8 read 0 psig
c) ( ) HOV-N9, 1400 PSIG GN2 Vent……CLOSED
d) ( ) HOV-N4, 5000 PSIG Facility GN2 Shutoff…OPEN

Read PG-N5, GN2 Supply Pressure. Verify GN2 supply pressure is greater than 2000 PSIG.

e) ( ) Load HOR-N6, 1440 PSIG GN2 Loader, to _____.

Read on PG-N8. (NOTE: RV-N10 is set at 1440 PSIG)

7) Set up/verify Second Stage Control Valve Regulator System

a) ( ) HOR-N13, 90 PSIG GN2 Loader…….Fully Vented Position
b) ( ) HOV-N12, 2nd Stage GN2 Shutoff……..OPEN
c) ( ) Load HOR-N13, 90 PSIG GN2 Loader, to 70 psig ± 10

psig. Read on PG-N15. (NOTE: RV-N16 is set at 90 psig)

8) Verify operation of Control Valves and Solenoid Valves

a) ( )Visually verify the following VPVs stroke properly when commanded:
1)( )VPV-I4, Injector Gas Flow Control…100%, 50%, 0%,100%
2)( )VPV-W10, Injector Water Flow Control…100%, 50%, 0%,100%
3)( )VPV-X1, Chamber Main Exhaust Flow Control…100%, 50%, 0%,100%,0%
4)( )VPV-X2, Chamber Small Exhaust Flow Control….100%, 50%, 0%,100%,0%

b) ( )Verify the following SOVs cycle properly when commanded, by feeling (with your hand) the solenoid click open and closed:
1)( )SOV-I1, Injector Gas Shutoff…….OPEN/CLOSED/OPEN
2)( )SOV-N22, Water Tank Vent…OPEN/CLOSED/OPEN/CLOSED
3)() SOV-N21, WaterTank Pressurization…..OPEN/CLOSED/OPEN
4)( )SOV-PW3, Window Purge Shutoff…. OPEN/CLOSED/OPEN
5)( )SOV-PC3, Curtain Flow Shutoff…. OPEN/CLOSED/OPEN

9) Verify Emergency Safe-out Functionality

1)( )Click the Emergency Shutdown Icon on the LabView Screen.
2)( )Verify visually the following VPVs stroke to the identified position:
a)( )VPV-I4, Injector Gas Flow Control…0%

b)( )VPV-W10, Injector Water Flow Control…0%
c)( )VPV-X1, Chamber Main Exhaust Flow Control…100%
d)( )VPV-X2, Chamber Small Exhaust Flow Control….100%

3)( )Verify audibly the following SOVs cycle to the closed position:
a)( )SOV-I1, Injector Gas Shutoff
b)( )SOV-N21, Water Tank Pressurization
c)( )SOV-PW3, Window Purge Shutoff
d)( )SOV-PC3, Curtain Flow Shutoff

4)( )Verify the following SOVs are de-energized by temporarily unplugging the DC power plug with your hand on the SOV and verifying the solenoid does not click. Re-connect the DC power plug when finished. Note this does not need to be done everytime the procedure is executed, only after the LabView software has been modified.
a)( )SOV-I1, Injector Gas Shutoff
b)( )SOV-N21, Water Tank Pressurization
c)( )SOV-N22, Water Tank Vent
d)( )SOV-PW3, Window Purge Shutoff
e)( )SOV-PC3, Curtain Flow Shutoff

10) Start the water Heater

1) ( )Verify the GN2 Heat Exchanger Water tank is full of water by inspecting the sight glass. Add water as required from nearby water hose.
2) ( )Verify the T-HW, GN2 Heat Exchanger Water tank water temperature, and T-HX, GN2 Heater Element are being displayed on the Data

Acquisition Computer and the LabView computer. Determine whether these values are realistic.

3) ( )Verify the Heater's SCR power controller is commanded to 0% power on the LabView Screen.
4) ( )480V Disconnect for the SCR Power Controller……..ON
5) ( )Verify SCR power controller fan is running.
6) ( )Enter the GN2 Heat Exchanger Water temperature value into the LabView screen.
7) ( )Command LabView to automatically control the GN2 Heat Exchanger Water temperature.

11) Open 1440 PSIG Isolation

1) ( )HOV-N20, 1440 PSIG GN2 Shutoff……..OPEN
2) ( )Verify SOV-I1, Injector Gas Shutoff, is closed and not leaking through per PG-I3, Injector GN2 Pressure reading 0 PSIG.
3)( )Verify SOV-N21, Water Tank Pressurization, is closed and not leaking through per PG-W5, Water Tank Pressure is reading 0 PSIG.

12) Set up/verify Third Stage Regulator System

1) ( )Verify IP-P5, Window Purge Loader is commanded to 0 PSIG on the LabView screen
2) ( )Verify IP-P6, Curtain Flow Loader is commanded to 0 PSIG on the LabView screen
3) ( )Load HOR-P1, Curtain Flow and Window Purge Pressure Loader, to 120 +/- 5 PSIG. Read on PG-P2.

13) Setup Remaining Valves

1) ( )HOV-W8, Injector Water Shutoff……OPEN
2) ( )HOV-PW4, Window Purge Shutoff…….OPEN
3) ( )HOV-PC4, Curtain Flow Shutoff……..OPEN
4) ( )SOV-N21, Water Tank Pressurization…..OPEN
   Pressurize the water tank.
5) ( )Verify PG-W5 and PG-W9 match PG-N8
6) ( )Open the valve for the large water flow meter, FM-L, allowing the pressurized water to pass through and flow into the other two lines.
7) ( )Close the valve for the FM-WL flow meter. Open and close the valves for the FM-WM and FM-WS successively.
8) ( )Open the valve for the large gas flow meter, FI-L, allowing the pressurized GN2 to pass through and flow into the other two lines.
7) ( )Close the valve for the FM-IL flow meter. Open and close the valves for the FM-IM and FM-IS successively.

14) Evacuate and Barracade the Test Cell

1) ( )Setup all camera and spray diagnostic systems to be operated remotely from the control room.
2) ( )All personnel shall evacuate Test Cell 110 and Test Cell 109.
3) ( )Install testing notification and warning sign in front of the Test Cell 110 door.

F) TEST OPERATIONS

1) Begin video camera recording if utilized

2) Initiate test flow conditions

(1) ( )Verify Data Acquisition System ready
(2) ( )Verify Illumination System ready
(3) ( )Verify Imaging System ready
(4) ( )Start Recording Data
(5) ( )VPV-X1,Chamber Main Exhaust Flow Control....100% OPEN
(6) ( )SOV-I1, Injector Gas Shutoff…….OPEN
(7) ( )SOV-PW3, Window Purge Shutoff……OPEN
(8) ( )Adjust IP-P5, Window Purge Loader, as required to establish the desired Window Purge. Read pressure on P-PW.
(9) ( )SOV-PC3, Curtain Flow Shutoff……OPEN
(10) ( )Adjust IP-P6, Curtain Flow Loader, as required to establish the desired Curtain Flow. Read pressure on P-PC.
(11) ( )Adjust VPV-I4, Injector Gas Flow Control, as required to establish the desired flowrate per FM-I.
(12) () VPV-X1, Chamber Main Exhaust Flow Control, adjust as required to obtain desired chamber pressure, per P-C.
(13) ( )If flow is too low to control Test Chamber Pressure using VPV-X1, then Adjust VPV-X2, Chamber Small Exhaust Flow Control Valve to obtain desired chamber pressure, per P-C.
(14) ( )Adjust VPV-W10, Injector Water Flow Control, as required to establish the desired flowrate per FM-W.
(15) ( )Verify VPV-X1 or VPV-X2 is holding steady Test

Chamber pressure per P-C.

3) Adjust Flows per Daily Experiment Profile Sheet

(1) ( )Adjust the position of VPV-I4, Injector Gas Flow Control, as required to maintain the desired GN2 flow rate per FM-I

(2) ( )Adjust the position of VPV-W10, Injector Water Flow Control, as required to maintain the desired water flow rate per FM-W

(3) ( )Adjust VPV-X1 and VPV-X2, Chamber Exhaust Flow Control Valves as required to maintain the desired Test Chamber Pressure per P-PC

(4) ( )Adjust IP-P5, Window Purge Loader, as required to maintain the desired Window Purge. Read pressure on P-PW.

(5) ( )Adjust IP-P6, Curtain Flow Loader, as required to maintain the desired Curtain Flow. Read pressure on P-PC.

(6) ( )Signal the camera or image capturing devices to acquire images when desired

4) Terminate test flow conditions

(1) ( )Stop recording data.

(2) ( )VPV-I4, Injector Gas Flow Control……0%

(3) ( )VPV-W10, Injector Water Flow Control……..0%

(4) ( )VPV-X1, Chamber Main Exhaust Flow Control….100%

(5) ( )VPV-X2, Chamber Small Exhause Flow Control…..0%

(6) ( )P-P5, Window Purge Loader……0 PSIG.
Read pressure on P-PW.

(7) ( )IP-P6, Curtain Flow Loader…….0 PSIG.
Read pressure on P-PC.

5) Secure the systems

(1) ( )SOV-I1, Injector Gas Shutoff…….CLOSED
(2) ( )SOV-PW3, Window Purge Shutoff……CLOSED
(3) ( )SOV-PC3, Curtain Flow Shutoff……CLOSED
(4) ( )SOV-N21, Water Tank Pressurization……CLOSED
(5) ( )SOV-N23, Water Tank Vent……OPEN
(6) ()Verify VPV-X1, Chamber Main Exhaust Flow Control…….100% OPEN
(7) ( )Verify Test Chamber Pressure is 0 PSIG per P-C.
(8) ( )Test Cell 110 is now safe to enter. Remove the barricade at the door entrance to Test Cell 110.
(9) ( )If Area Control was implemented in Step E.2.b, then perform the following:

1( ) Contact the Area Coordinator at 4-3080 and ask for the following area announcement:
"High pressure vent operations are complete near Test Cell 110, Building 4583. Area is clear for normal operations."

2( ) Remove the chain barricades across the two stairways providing access to the roof of building 4583.

3( ) Remove the stanchions and warning signs around vent line on roof of building 4583, above Test Cell 110.

(10) ( )HOV-N4, 5000 PSIG Facility GN2 Shutoff…CLOSED
(11) ( )HOV-N9, 1440 PSIG GN2 Vent…..OPEN
Vent the 1440 PSIG GN2 system to 0 PSIG. Read on PG-N8.

(12) ( )HOV-N20,1440 PSIG GN2 Shutoff……..CLOSED
(13) ( )HOV-N12, 2nd Stage GN2 Shutoff……..CLOSED
(14) ( )HOV-W8, Injector Water Shutoff……CLOSED
(15) ( )HOV-PW4, Window Purge Shutoff…….CLOSED
(16) ( )HOV-PC4, Curtain Flow Shutoff……..CLOSED
(17) ( )HOV-C3, Vent Drain……OPEN
Drain water from vent line as required.
(18) ( )HOV-C3, Vent Draing……CLOSED
(19) ( )VPV-X1, Chamber Main Exhaust Flow Control…….0%
(20) ( )Shut Down Water Heater

1( )Command LabView to 0% Power On the SCR Power Controller
2( )480V Disconnect for the SCR Power Controller……..OFF
3( )Verify the SCR power controller fan is OFF.

(21) ( )Terminate video camera recording
(22) ( )Shut down camera system
(23) ( )Verify the facility system is vented as indicated by 0 psig on the following pressure gauges:
(24) ( )PG-N5, 5000 PSIG GN2 Supply
(25) ( )PG-N8, 1440 PSIG GN2 Supply
(26) ( )PG-I3, Injection GN2
(27) ( )PG-W5, Water Tank
(28) ( )PG-W9, Injector Water
(29) ( )PG-C1, Test Chamber

H. EMERGENCY PROCEDURES

1) ( ) Test Chamber Window Cracks, Curtain Flow Can becomes Damaged, or Injector becomes Damaged

a) ( ) Click on the "Automatic Shutdown" icon on the

LabView screen. This will shutdown all flows into the Test Chamber and Open the Test Chamber Exhaust Valve.

b) ( ) Continue with Step F.4 of this procedure.

2) ( ) Oxygen Defiency Alarm Sounds

a) ( ) Click on the "Automatic Shutdown" icon on the LabView screen. This will shutdown all flows into the Test Chamber and Open the Test Chamber Exhaust Valve.

b) ( ) Execute Steps F.4 through F.5.g of this procedure.

c) ( ) HOV-N4, 5000 PSIG Facility GN2 Shutoff…CLOSED

d) ( ) HOV-N9, 1440 PSIG GN2 Vent…..OPEN
Vent the 1440 PSIG GN2 system to 0 PSIG. Read on PG-N8.

e) ( ) Call Security at 4-4357 (4-HELP)and report the Oxygen Deficiency Alarm. Do not remove the barricade to Test Cell 110, nor enter into Test Cell 110 until authorized by the team dispatched by Security.

3) ( ) Loss of 28 VDC Electrical Power

NOTE: 28 VDC systems are not currently on battery backup for Test Cell 110 Systems.

a) ( ) Click on the "Automatic Shutdown" icon on the LabView screen. This will shutdown all flows into the Test Chamber and Open the Test Chamber Exhaust Valve.

b) ( ) Continue with Step F.4 of this procedure.

4) ( ) Loss of 110 VAC Electrical Power

NOTE: 110 VAC systems are not currently on battery backup for Test Cell 110 Systems. Also, 28 VDC is supplied for a power supply using 110 VAC.

a) ( ) Continue with Step F.5.j of this procedure.

I. Figures and Schematics

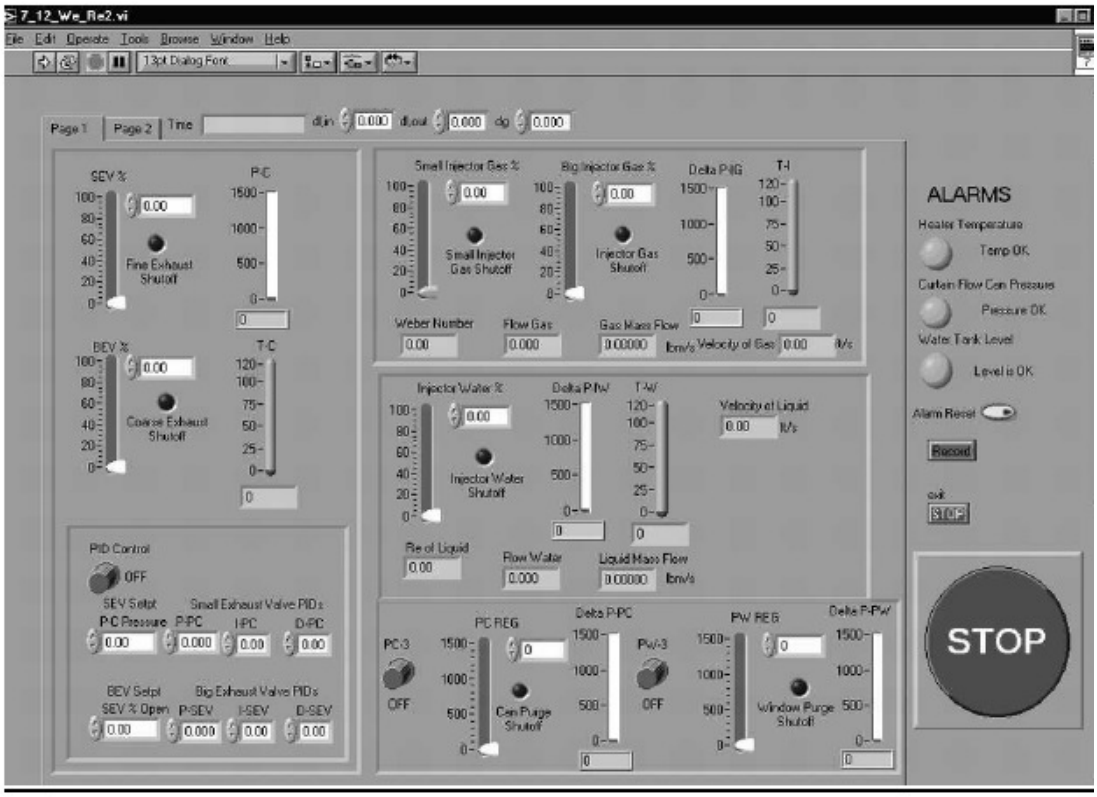

Figure 1(a): Page 1 of the Labview VI control program.

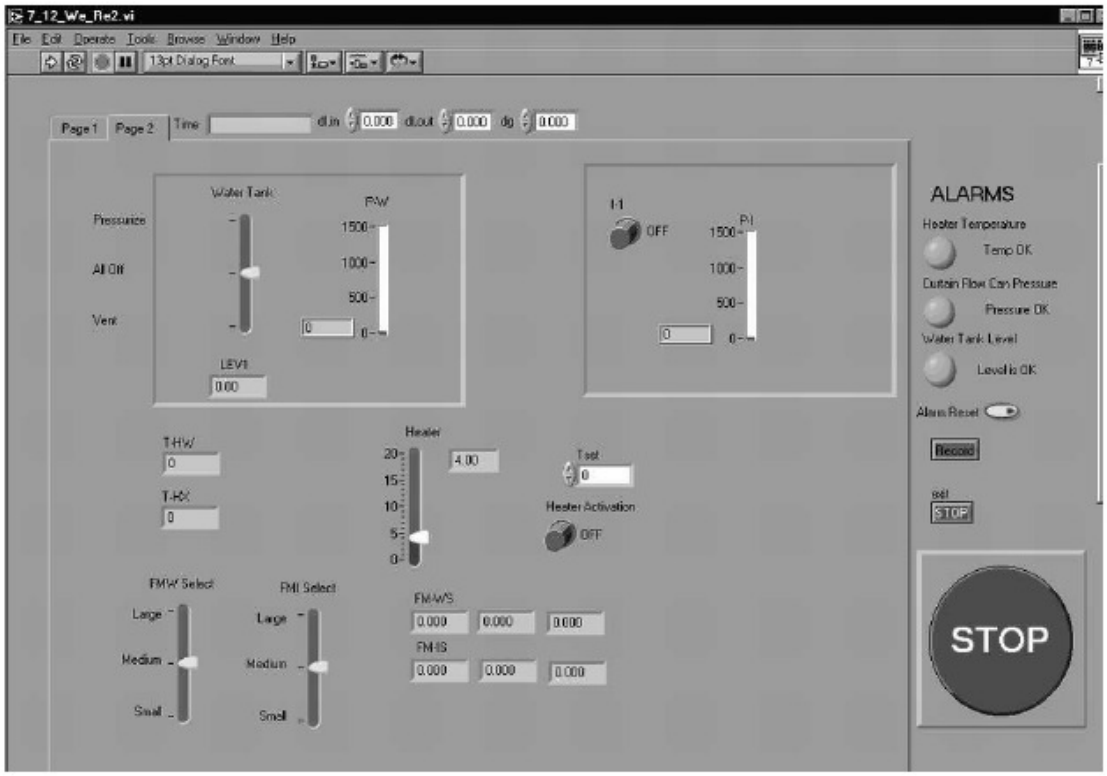

Figure 1(b): Page 2 of the Labview VI control program.

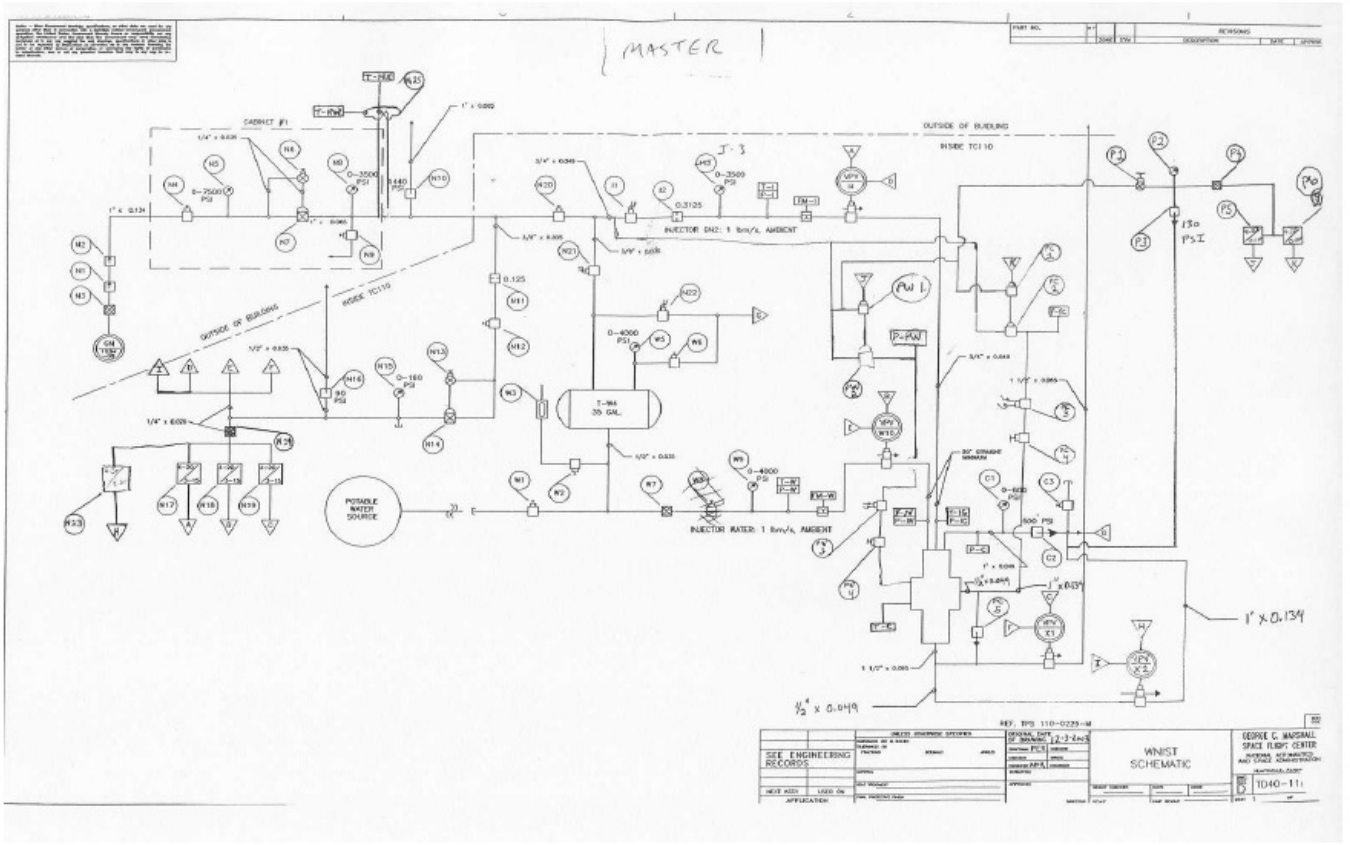

Figure 2. WNIST Facility Schematic. Current as of 11-1-2006.

APPENDIX B

WNIST UNCERTAINTY ANALYSIS

WNIST Facility Uncertainty Program

*Uncertainties given in 95% confidence bands
*Calibration performed at NASA - Marshall Space Flight Center Calibration Lab

Temperature

All temperatures are taken in the facility using Omega Type K thermocouples. The defined systematic uncertainty is given as +/- 0.0075*T (K).

$$B_T(T) := 0.0075T$$

Through inspection of the raw data, the random uncertainty of the thermocouples is determined to be 0.14 K = 2*PT.

$$P_{2T} := 0.14$$

The total uncertainty is the resultant of the systematic and random parts:

$$U_T(T) := \sqrt{B_T(T)^2 + P_{2T}^2}$$

Working Temperature Range

$$T := 4, 5 .. 24$$

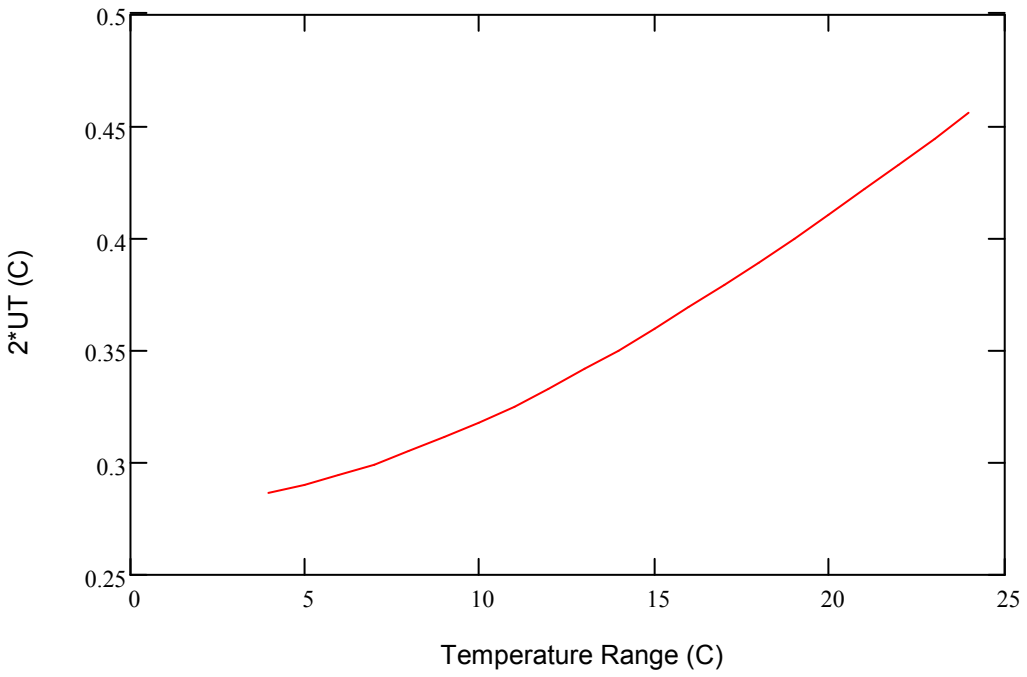

The maximum temperature uncertainty occurs at the maximum temperature seen during testing. After running multiple tests this maximum temperature is approxmately 75 degF, or 24 degC. This corresponds to a total uncertainty of:

$$U_{T\_max} := U_T(24) \qquad 2U_{T\_max} = 0.456 \quad C$$

Gas Pressure

All pressures are measured using Setra Pressure Transducers. The transducers are gage-based with respect to atmospheric conditions; the units calibrated against are in psig. The systematic uncertainties are calibrated down to 0.1% of the reading.

$$B_P(P) := 0.001 \cdot P$$

Measurements of varying transducer pressures give the following values of the standard deviation versus nominal pressure:

StDEV :=

	0	1
0	0	0
1	94.212	0.343
2	141.74	0.269
3	190.852	0.278
4	240.692	0.26
5	290.582	0.398
6	338.384	0.453
7	389.429	0.377
8	439.259	0.591
9	489.096	0.459
10	538.136	0.548
11	586.967	0.541
12	637.126	0.638
13	686.36	0.671
14	735.828	0.633
15	784.624	1.157

$$P0 := StDEV^{\langle 0 \rangle}\ psi \qquad P_{stdev} := StDEV^{\langle 1 \rangle}\ psi$$

$$vs := cspline(P0, P_{stdev})$$

$$P_P(p) := interp(vs, P0, P_{stdev}, p)$$

The data is taken into Mathcad's spline interpolation procedure, and a function relating the random uncertainty to the nominal pressure is created.

The total uncertainty is the vector sum of the systematic and random parts:

$$U_P(P) := \sqrt{B_P(P)^2 + P_P(P)^2}$$

Working Pressure Range

$$P := 0psi, 1psi .. 700psi$$

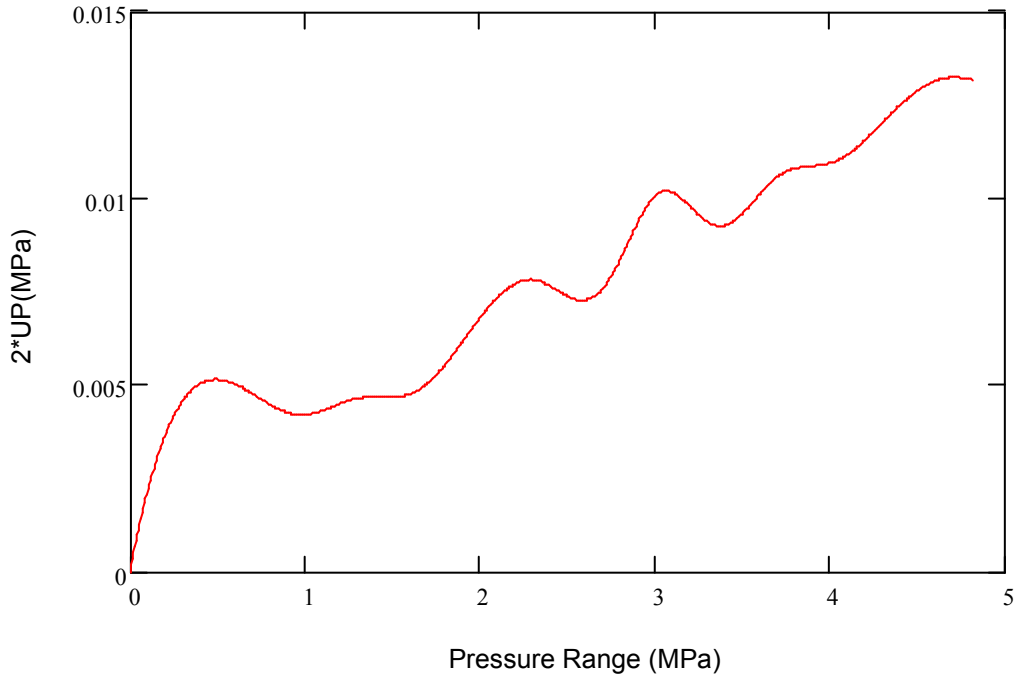

Water Pressure

The systematic uncertainty of the transducer for measuring water pressure is the same as for the gas pressure transducer:

$$B_P(P) := 0.001 \cdot P$$

The random uncertainty of the water gage is taken to be the same as the gas pressure:

The total uncertainty is the vector sum of the systematic and random parts:

$$U_{Pw}(P) := \sqrt{B_P(P)^2 + P_P(P)^2}$$

Working Pressure Range $P := 0psi, 1psi .. 1400psi$

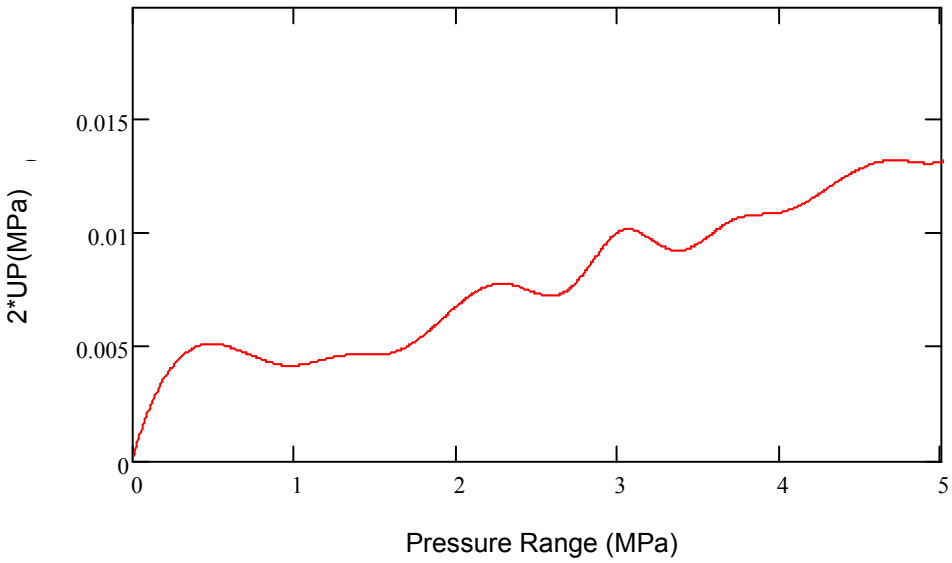

Pressure Differential

Measurements across the injector element consist of the mass flow rate and the pressure drop across the injector element. This pressure drop is the defined as the difference between the upstream static pressure and the downstream chamber pressure. Both pressure measuring devices have the same calibrated bias, and are correlated against the same standard, which is high-quality air. The data reduction equation is:

$$\Delta P = P_{PIW} - P_C$$

The systematic uncertainty is the sum of the water and gas transducer contribiutions:

$$B_{\Delta P}(P_{PIW}, P_C) = \sqrt{(0.001 \cdot P_{PIW})^2 + (0.001 \cdot P_C)^2 - 2 \cdot (0.001 \cdot P_{PIW}) \cdot (0.001 \cdot P_C)}$$

Simplification using the definition of the pressure differential gives:

$$B_{\Delta P}(\Delta P) := 0.001 \cdot \Delta P$$

The random uncertainty can be found similarly as:

$$P_{2\Delta P} = \sqrt{P_{2P}{}^2 + P_{2Pw}{}^2} \qquad P_{\Delta P}(\Delta P, P_C) := \sqrt{P_P(\Delta P)^2 + P_P(P_C)^2}$$

The total uncertainty is:

$$U_{\Delta P}(\Delta P, P_C) := \sqrt{(0.001 \cdot \Delta P)^2 + P_{\Delta P}(\Delta P, P_C)^2}$$

$$\Delta p := 0psi, 1psi .. 1400psi$$

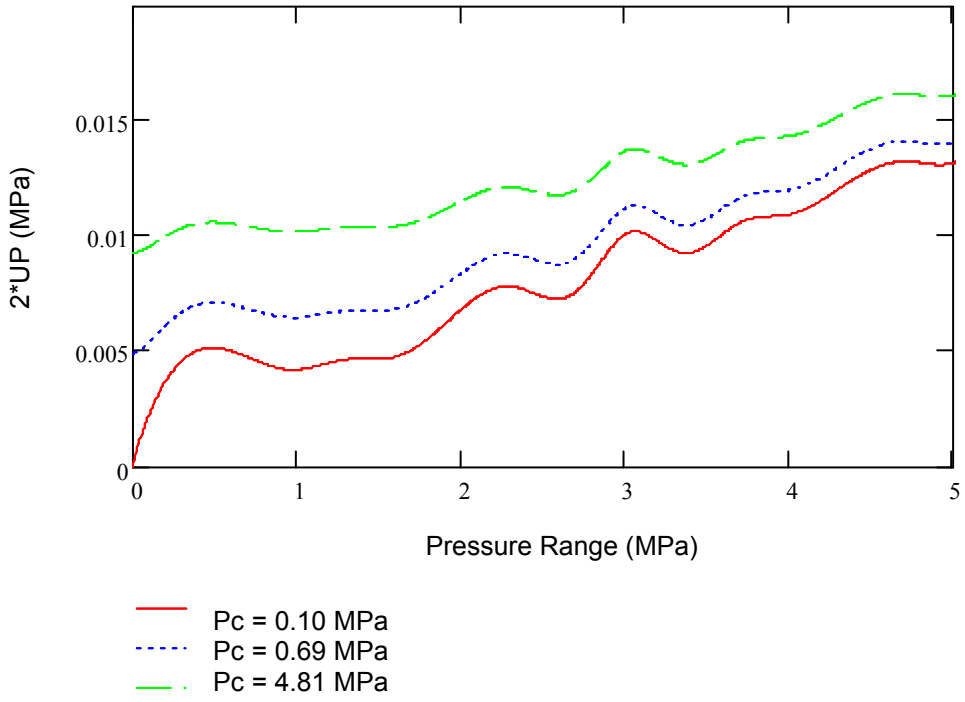

Flow Rate

The two flow meters used all have the same calibration standard of 2% of the reading. The calibration curve is given in gpm, so there is a need to convert to lbm/s. The systematic uncertainty is then:

Liquid density: $\rho := 998 \frac{kg}{m^3}$ $B_m(m) := 0.02 \cdot (m)$

Through inspection of the raw data, the random uncertainty of the flow meter is 0.9% of reading.

$$P_{2mM}(m) := 0.009 \cdot (m)$$

The total uncertainty is the vector sum of the systematic and random parts:

$$U_{mM}(m) := \sqrt{B_m(m)^2 + P_{2mM}(m)^2}$$

Working mass flow rate range:

$$m := 0\frac{lb}{s}, 0.005\frac{lb}{s} .. 0.8\frac{lb}{s}$$

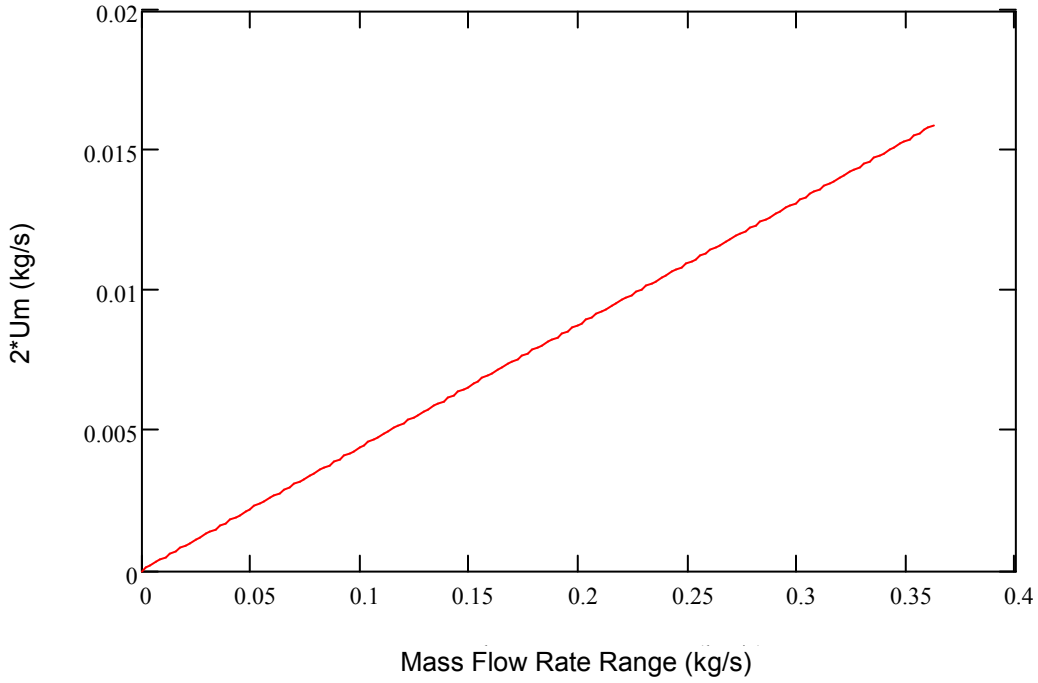

The uncertainties can generalized as linear with respect to the mass flow rate. The total 2*U uncertainties for the flow meter is the respective slope.

Uncertainty for the flow meter:

$$\frac{2\cdot U_{mM}\left(0.091\frac{kg}{s}\right)}{0.091\frac{kg}{s}} = 4.386\%$$

4.4 % of reading

APPENDIX C

SWIRL INJECTOR DESIGN METHODOLOGY

Doumas and Laster Design Methodology (Doumas, 1953)

Nozzle Diameter, Dn $D_n := 2.083\text{mm}$ $\nu := 1.082 \cdot 10^{-5} \frac{\text{ft}^2}{\text{s}}$ $\sigma := 4.988 \cdot 10^{-3} \frac{\text{lbf}}{\text{ft}}$

Nozzle radius, rh $r_h := \frac{D_n}{2}$

Turn Down Ratio, TDR $TDR = \frac{D_s}{D_n}$ $TDR := 2.293$

Swirl Chamber Diameter $D_s := D_n \cdot TDR$ $D_s = 4.776\text{mm}$ $R := \frac{D_s}{2}$

Orifice diameter, Do: $D_o := 1.549\text{mm}$ $r_o := \frac{D_o}{2}$ $r_o = 0.774\text{mm}$

Number of Orifice Inlets, No $N_o := 3$

Cd, inlet $CD_o := 1$ Slot discharge coefficient

Mass Flow Rate $m_L := 0.091 \frac{\text{kg}}{\text{s}}$

Density $\rho := 999.6 \frac{\text{kg}}{\text{m}^3}$

First, find parameter A'

Cross-sectional area of inlet orifice: $A_o := \frac{\pi}{4} \cdot D_o^2$ $A_o = 1.884\text{mm}^2$

Radius from inlets to post centerline: $R' := R - r_o$ $R' = 1.614\text{mm}$

Mean orifice velocity: $V_o(m_L) := \frac{m_L}{N_o \cdot \rho \cdot A_o \cdot CD_o}$ $V_o(m_L) = 16.103 \frac{\text{m}}{\text{s}}$

$A' := \left(\frac{\pi \cdot r_h \cdot R}{N_o \cdot CD_o \cdot A_o} \right) \cdot \sqrt{\frac{r_h}{R'}}$ $A' = 1.11$

Mean Free Cone Spray Half-Angle

$$\theta_m := \frac{43.5}{2}\log(14\cdot A')\cdot deg \qquad \theta_m = 25.918deg$$

$$\alpha' := 0.5$$

Given

$$\frac{A'^2}{2}\cdot\alpha'^3 - \alpha'^2 + 2\cdot\alpha' - 1 = 0$$

$$\alpha' := \text{Find}(\alpha') \qquad \alpha' = 0.618$$

Discharge Coefficient

$$K := \frac{\alpha'\cdot\sqrt{1-\alpha'}}{\sqrt{1-\alpha'+\alpha'^2\cdot A'^2}} \qquad K = 0.414$$

Total pressure drop

$$\Delta P_{tot}(m_L) := \frac{1}{2\rho}\cdot\left(\frac{m_L}{K\cdot\frac{\pi}{4}\cdot D_n^2}\right)^2 \qquad \Delta P_{tot}(m_L) = 2.085MPa$$

Air Core Diameter

$$D_{ac} := D_n\cdot\left(\sqrt{1-\alpha'}\right) \qquad D_{ac} = 1.287mm$$

Exit Film Thickness

$$t_f := r_h - \left(\frac{D_{ac}}{2}\right) \qquad t_f = 0.398mm$$

Nozzle Flow Area Coefficient

$$Ccn := 1 - \left(\frac{D_{ac}}{D_n}\right)^2 \qquad Ccn = 0.618$$

Axial flow velocity

$$V_y = \frac{\frac{mdot}{\rho}}{\pi\cdot\left(r_h^{\,2} - r_{ac}^{\,2}\right)} \qquad V_y(m_L) := \frac{m_L}{\rho\cdot\pi\cdot\left[r_h^{\,2} - \left(\frac{D_{ac}}{2}\right)^2\right]} \qquad V_y(m_L) = 43.208\frac{m}{s}$$

Tangential discharge velocity

$$V_z(m_L) := V_y(m_L)\cdot\tan(\theta_m) \qquad V_z(m_L) = 20.997\frac{m}{s}$$

Total resultant velocity

$$V(m_L) := \sqrt{V_y(m_L)^2 + V_z(m_L)^2} \qquad V(m_L) = 48.039\frac{m}{s}$$

Total dynamic pressure $\quad P_d(m_L) := \frac{1}{2}\cdot\rho\cdot V(m_L)^2 \qquad P_d(m_L) = 1.153\text{MPa}$

Ratio of total dynamic pressure to the total pressure drop $\quad P_{frac}(m_L) := \frac{P_d(m_L)}{\Delta P_{tot}(m_L)} \qquad P_{frac}(m_L) = 0.553$

Measured data

data :=

	0	1
0	7.57	0.029
1	15.26	0.041
2	22.32	0.049
3	32.74	0.06
4	44.28	0.07
5	58.42	0.081
6	72.88	0.091
7	90.33	0.099
8	142.93	0.125
9	203.21	0.151
10	266.81	0.175
11	354.24	0.199

$DP_d := data^{\langle 0\rangle}\cdot psi$

$ml_d := data^{\langle 1\rangle}\cdot\frac{lb}{s}$

$i := 0, 1 .. rows(ml_d) - 1$

Predicted pressure drop $\Delta P_{tot}(ml_d) =$

	0
0	0.044
1	0.086
2	0.125
3	0.187
4	0.256
5	0.337
6	0.425
7	0.505
8	0.809
9	1.183
10	1.587
11	2.056

MPa $\quad \Delta P_i := \Delta P_{tot}(ml_{d_i})$

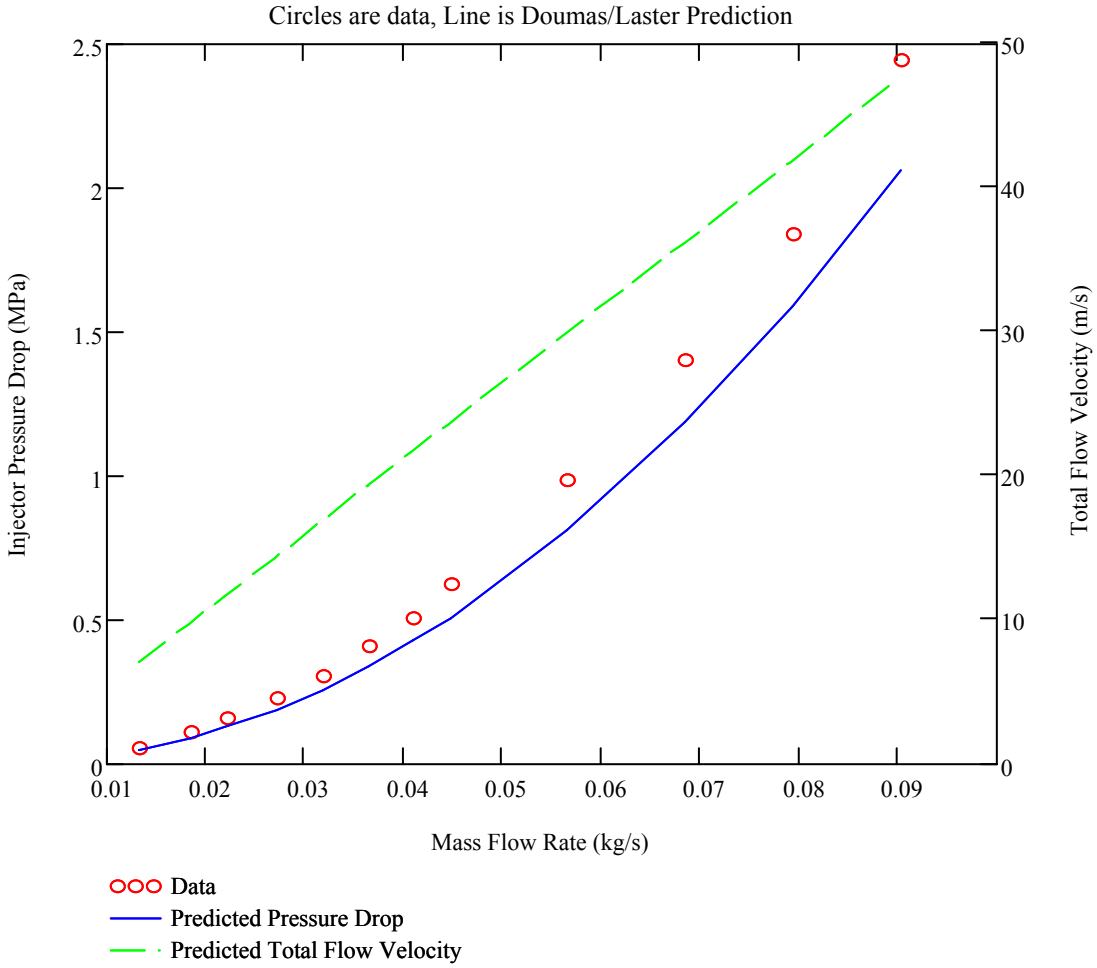

Swirl Atomizer Design Calculations from Bazarov (Bazarov, 2004) ORIGIN:= 1

Half scale mass flow rate $G := 0.091\frac{kg}{s}$

Liquid density $\rho := 999.6\frac{kg}{m^3}$

Set swirler dimensions:

Nozzle diameter: $D_n := 2.083mm$ $R_n := 0.5 \cdot D_n$ $A_n := \pi \cdot R_n^2$

Inlet diameter: $D_{in} := 1.549mm$ $r_{in} := 0.5 \cdot D_{in}$ $A_{in} := \pi \cdot r_{in}^2$

Inlet to centerline radius: $R_{in} := 0.06lin$ Number of slots: $n := 3$

Geometrical parameter: $A := \frac{A_n \cdot R_{in}}{R_n \cdot n \cdot A_{in}}$ $A = 0.897$

From A we can get the fullness coefficient, ϕ: $\phi = \frac{A_l}{A_n} = \left(\frac{D_n - 2 \cdot r_{mn}}{D_n}\right)^2 = \left[1 - \left(1 - \frac{t}{R_n}\right)\right]^2$

$\phi := 0.5$

Given

$$A = \frac{(1-\phi)\cdot\sqrt{2}}{\phi\cdot\sqrt{\phi}}$$

$\phi := Find(\phi)$ $\phi = 0.66$

Interior nozzle spray angle, or helical swirl angle: $\alpha_n := atan\left(\sqrt{2 \cdot \frac{1-\phi}{\phi}}\right)$ $\alpha_n = 45.427deg$

Ideal discharge coefficient: $\mu_i := \sqrt{\frac{\phi^3}{2-\phi}}$ $\mu_i = 0.463$

Value of 'a': $a := (\mu_i \cdot A)^2$ $a = 0.173$

Exit spray angle, or free cone spray angle: $\alpha_e := 2\,atan\left(\sqrt{\frac{a}{1-a}}\right)$ $\alpha_e = 49.085deg$

Film thickness along nozzle: $t_n := R_n \cdot \left(1 - \sqrt{1 - \phi}\right)$ $t_n = 0.4342\text{mm}$

Exit film thickness: $r_{me} := 0.5$

Given

$$\mu_i = r_{me} \cdot \sqrt{r_{me} - \left(\mu_i \cdot A\right)^2} - \left(\mu_i \cdot A\right)^2 \cdot \ln\left[\frac{1 + \sqrt{1 - \left(\mu_i \cdot A\right)^2}}{r_{me} + \sqrt{r_{me} - \left(\mu_i \cdot A\right)^2}}\right]$$

$r_{me}(CD) := \text{Find}\left(r_{me}\right)$ $r_{me}\left(\mu_i\right) = 0.704$ $t_e := R_n \cdot \left(1 - r_{me}\left(\mu_i\right)\right)$ $t_e = 0.309\text{mm}$

Total ideal velocity: $V_{\Sigma i} := \frac{G}{\mu_i \cdot A_n \cdot \rho}$ $V_{\Sigma i} = 57.673\frac{\text{m}}{\text{s}}$

Ideal tangential velocity along nozzle: $V_{un} := V_{\Sigma i} \cdot \sqrt{\frac{2 \cdot (1 - \phi)}{2 - \phi}}$ $V_{un} = 41.084\frac{\text{m}}{\text{s}}$

Ideal axial velocity along nozzle: $V_{an} := \sqrt{V_{\Sigma i}^2 - V_{un}^2}$ $V_{an} = 40.476\frac{\text{m}}{\text{s}}$

Ideal pressure drop: $\Delta P_i := \frac{1}{2} \cdot \rho \cdot V_{\Sigma i}^2$ $\Delta P_i = 1.662\text{MPa}$

Ideal tangential velocity at exit: $V_{ue} := V_{\Sigma i} \cdot \sqrt{a}$ $V_{ue} = 23.956\frac{\text{m}}{\text{s}}$

Ideal axial velocity at exit: $V_{ae} := V_{\Sigma i} \cdot \sqrt{1 - a}$ $V_{ae} = 52.463\frac{\text{m}}{\text{s}}$

Additional swirler dimensions:

Vortex chamber diameter: $D_{vc} := 4.775\text{mm}$

Tangential slot length: $L_{in} := 3.861\text{mm}$

Vortex chamber length: $L_{vc} := 3.912\text{mm}$

Nozzle length: $l_n := 3.124\text{mm}$

Transition angle: $\beta := 118\text{deg}$

Plot of pressure drop versus mass flow rate: $\Delta P(\text{mdot}, \mu_i) := \left(\frac{\text{mdot}}{\mu_i \cdot A_n}\right)^2 \cdot \frac{1}{2 \cdot \rho}$

$$\text{mdot} := 0\frac{\text{lb}}{\text{s}}, 0.01\frac{\text{lb}}{\text{s}} .. 0.2\frac{\text{lb}}{\text{s}}$$

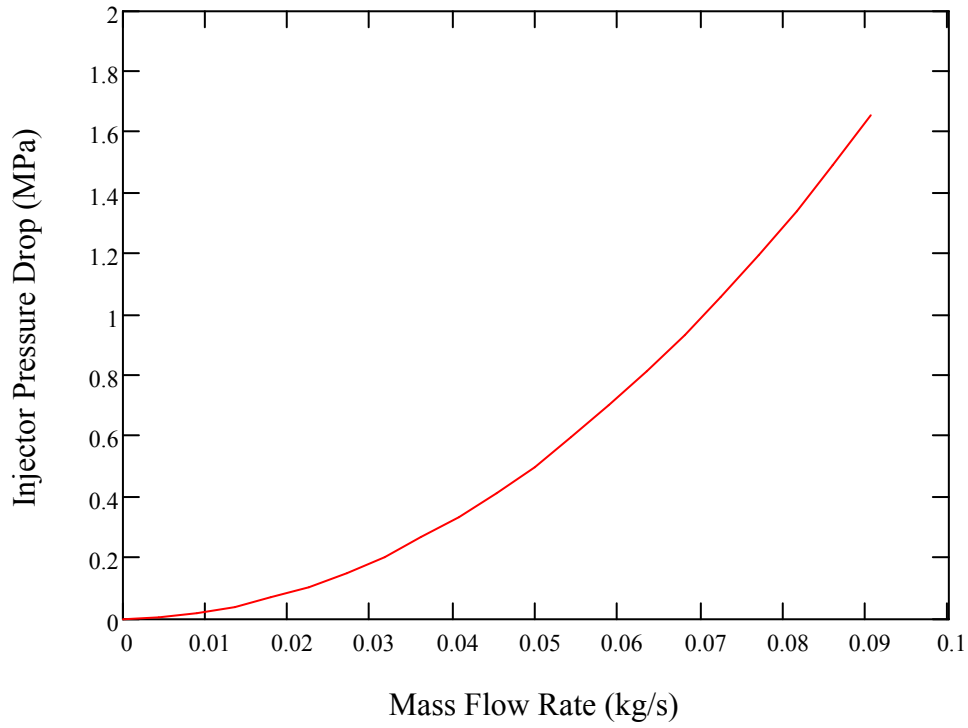

REFERENCES

[1] Sutton, G.P., and Biblarz, O., *Rocket Propulsion Elements*, 7th ed., John Wiley & Sons, Inc., New York, 2001, Chaps. 6 - 9.

[2] Humble, R.W., Henry, G.N., and Larson, W.J. (ed.), *Space Propulsion Analysis and Design*, Space Technology Series, McGraw-Hill, New York, 1995, Chaps. 1, 3, 4, 5.

[3] Ito, J.I., "Propellant Injection Systems and Processes," *Liquid Rocket Thrust Chambers: Aspects of Modeling, Analysis, and Design*, edited by V. Yang, M. Habiballah, J. Hulka, and M. Poppe, Progress in Astronautics and Aeronautics, AIAA, Washington, DC, 2004, pp. 1-18.

[4] Gill, G.S., and Nurick, W.H., "Liquid Rocket Engine Injectors," NASA SP-8089, 1976.

[5] Hulka, J., and Hutt, J. J., "Liquid Oxygen/Hydrogen Instability Phenomena," *Liquid Rocket Engine Combustion Instability*, edited by V. Yang, and W. Anderson, Progress in Astronautics and Aeronautics, AIAA, Washington, DC, 1995, pp. 39-71.

[6] Harrje, D.T., and Reardon, F.H., "Liquid Propellant Rocket Combustion Instability," NASA SP-194, 1972.

[7] Fisher, S.C., Dodd. F.E., and Jensen, R.J., "Scaling Techniques for Liquid Rocket Combustion Stability Testing," *Liquid Rocket Engine Combustion Instability*, edited by V. Yang, and W. Anderson, Progress in Astronautics and Aeronautics, AIAA, Washington, DC, 1995, pp. 545.564.

[8] Dexter, C.E., Fisher, M.F., Hulka, J.R., Denisov, K.P., Shibanov, A.A., and Agarkov, A.F., "Scaling Techniques for Design, Development and Test," *Liquid Rocket Thrust Chambers: Aspects of Modeling, Analysis, and Design*, edited by V. Yang, M. Habiballah, J. Hulka, and M. Poppe, Progress in Astronautics and Aeronautics, AIAA, Washington, DC, 2004, pp. 553.600.

[9] Tomazic, W.A., Conrad, E.W., and Godwin, T.W., "M-1 Injector Development-Philosophy and Implementation," NASA TM-X-52289, 1967.

[10] Corda, S., Moes, T.R., Monagham, R.C., Corpening, G.P., Larson, R.R., and Powers, B.G., "Flight Testing the Linear Aerospike SR-71 Experiment (LASRE)," NASA TM-1998-206567, 1998.

[11] Pauckert, R.P., and Tobin, R.D., "Space Shuttle Orbit Maneuvering Engine Reusable Thrust Chamber Program: Final Summary Report," NASA CR-144441, 1975.

[12] "Space Shuttle Orbital Maneuvering Engine Platelet Injector Program: Final Report," NASA CR-151442, 1977.

[13] "STE Thrust Chamber Technology - Main Injector Technology Program and Nozzle Advanced Development Program (ADP): Final Report," NASA Contract NAS 8-37490, 1994.

[14] Preclik, D., Hagemann, G., and Kretschmer, J., "Technology Efforts Towards Low-cost Thrust Chambers," *AIAA/SAE/ASME 39th Joint Propulsion Conference*, AIAA Paper No. 2003.4616, July 2003.

[15] Preclik, D., Hagemann, G., Knab, O., Brummer, L., Mäding, C., Wiedmann, D., and Vuillermoz, P., "LOX/Hydrocarbon Propellant Trade Considerations for Future Reusable Liquid Booster Engines," *AIAA/SAE/ASME 41st Joint Propulsion Conference*, AIAA Paper No. 2005.3567, July 2005.

[16] Preclik, D., Hagemann, G., Knab, O., Mäding, C., Haesler, D., Haidn, O., Woschnak, A., and DeRosa, M., "LOX/Hydrocarbon Preparatory Thrust Chamber Technology Activities in Germany," *AIAA/SAE/ASME 41st Joint Propulsion Conference*, AIAA Paper No. 2005.4555, July 2005.

[17] Huzel, D.K., and Huang, D.H., *Modern Engineering for Design of Liquid-Propellant Rocket Engines*, Progress in Astronautics and Aeronautics, AIAA, Washington, DC, 1992.

[18] "NASA's Exploration Systems Architecture Study (ESAS): Final Report," NASA TM-2005.214062, 2005.

[19] Chehroudi, B., Talley, D., Mayer, W., Branam, R., Smith, J., Schik, A., and Oschwald, M. "Understanding Injection into High Pressure Supercritical Environments" *5th International Conference on Liquid Rocket Propellant*, Chattanooga, 2003.

[20] Bazarov, V., Yang, V., and Puri, P., "Design and Dynamics of Jet and Swirl Injectors," *Liquid Rocket Thrust Chambers: Aspects of Modeling, Analysis, and Design*, edited by V. Yang, M. Habiballah, J. Hulka, and M. Poppe, Progress in Astronautics and Aeronautics, AIAA, Washington, DC, 2004, pp. 19-103.

[21] Doumas, M., and Laster, R., "Liquid-Film Properties in Centrifugal Spray Nozzles" *Chemical Engineering Progress*, October 1995, pp. 518-526.

[22] Lefebvre, A.H.., *Atomization and Sprays*, 1st ed., Routledge., 1989.

[23] Cox, G.B., "Rocket Engine Injection Element Characterization," *AIAA/SAE/ASME 24th Joint Propulsion Conference*, AIAA Paper No. 1988-3135, July, 1988.

[24] Cohn, R.K., Strakey, P.A., Bates, R.W., Talley, D.G., Muss, J.A., and Johnson, C.W., "Swirl Coaxial Injector Development," *41st Aerospace Sciences Meeting and Exhibit*, AIAA Paper No. 2003-0125, January 2003.

[25] Strakey, P.A., Cohn, R.K., and Talley, D.G., "The Development of a Methodology to Scale between Cold-flow and Hot-fire Evaluation of Gas-centered Swirl Coaxial Injectors," *52nd JANNAF Propulsion Meeting*, 10-14 May 2004.

[26] Kim, D., Jeong, W., Im, J.H., and Yoon, Y., "The Characteristics of Swirl Coaxial Injector Under Varying Geometric and Environmental Conditions," *40th Joint Liquid Propulsion Conference*, AIAA Paper No. 2004.3521, July 2004.

[27] Kalitan, D.M., Salgues, D., Mouis, A.G., Lee, S.Y., Pal, S., and Santoro, R.J., "Experimental Liquid Rocket Swirl Coaxial Injector Study Using Non-intrusive Optical Techniques," *AIAA/SAE/ASME 41st Joint Propulsion Conference*, AIAA Paper No. 2005.4299, July 2005.

[28] Kenny, R.J., Moser, M.D., Hulka, J.R., and Jones, G., "Cold Flow Testing for Liquid Propellant Rocket Injector Scaling and Throttling," 42nd *Joint Liquid Propulsion Conference*, AIAA Paper No. 2006-4705, July 2006.

[29] Mayer, W., and Krülle, G., "Rocket Engine Coaxial Injector Liquid/Gas Interface Flow Phenomena," *Journal of Propulsion and Power*, Vol. 11, No. 3, May-June 1995, pp. 513.518.

[30] Moses, M.P., Heister, S.D., and Farmer, K. O., "Correlating Injector Performance for use as Engineering Design Criteria," 28th *Joint Liquid Propulsion Conference*, AIAA Paper No. 1992.3387, July 1992.

[31] Hutt, J.J., "A Study of Design Details of Rocket Engine Swirl Injection Elements," Ph.D. Dissertation, Dept. of Mechanical Engineering, Pennsylvania State Univ., University Park, PA, 2000.

[32] Rahman, S.A., Pal, S., and Santoro, R.J., "Swirl Coaxial Atomization: Cold-flow and Hot-fire Experiments," *33rd Aerospace Sciences Meeting and Exhibit*, AIAA Paper No. 1995-0381, January 1995.

[33] Hulka, J., and Makel, H., "Liquid Oxygen/Hydrogen Testing of a Single Swirl Coaxial Injector Element in a Windowed Combustion Chamber," *AIAA/SAE/ASME 29th Joint Propulsion Conference*, AIAA Paper No. 1993.1954, June 1993.

[34] Khavkin, Y.I., *Theory and Practice of Swirl Atomizers*, 1st ed., Taylor and Francis, New York, 2004.

[35] Yule, A. J., and Chinn, J. J., "Swirl Atomizer Flow: Classical Inviscid Theory Revisited," *ICLASS-94*, Rouen, France, July 1994.

[36] Bayvel, L., and Orzechowski, Z., *Liquid Atomization*, 1st ed., Taylor and Francis, New York, 1993.

[37] Abramovich, G. N., "The Theory of Swirl Atomizer." In *Industrial Aerodynamics.* Moscow: BNT ZAGI, 1944, pp. 114 – 121.

[38] Cooper, D., and Yule, A. J., "Waves on the Air Core/Liquid Interface of a Pressure Swirl Atomizer," *ILASS - Europe*, September 2001.

[39] Binnie, A. M., "The Theory of Waves Traveling on the Core in a Swirling Liquid," *Proceedings of the Royal Society of London A.,* Vol. 205, 1950, pp. 530 – 540.

[40] Binnie, A. M., and Teare, J. D., "Experiments on the Flow of Swirling Water Through a Pressure Nozzle and an Open Trumpet," *Proceedings of the Royal Society of London A.,* Vol. 235, 1956., pp. 78 – 89.

[41] Binnie, A. M., "Experiments on the Swirling Flow of Water in a Vertical Pipe and a Bend," *Proceedings of the Royal Society of London A.,* Vol. 270, 1962, pp. 462 - 466.

[42] Binnie, A. M., "Annular Hydraulic Jumps," *Proceedings of the Royal Society of London A.,* Vol. 282, 1964., pp. 155 - 165.

[43] Binnie, A. M., and Shaw, A. W., "The Flow of Swirling Water Down a Vertical and an Inclined Tube," *Proceedings of the Royal Society of London A.,* Vol. 304, 1968., pp. 387 – 406.

[44] White, F.M., *Fluid Mechanics*, 4th ed., McGraw-Hill, New York, 1999.

[45] Sarpkaya, T., "On Stationary and Traveling Vortex Breakdowns," *Journal of Fluid Mechanics*, Vol. 45, 1971, pp. 545 – 559.

[46] Shtern, V., and Hussain, F., "Collapse, Symmetry, Breaking, and Hysteresis in Swirling Flows," *Annual Review in Fluid Mechanics*, Vol. 31, 1999, pp. 537 – 566.

[47] Ramamurthi, K., and Tharakan, T.J., "Experimental Study of Liquid Sheets Formed in Coaxial Swirl Injectors," *Journal of Propulsion and Power*, Vol. 11, No. 6, November 1995, pp. 1103.1109.

[48] Ramamurthi, K., and Tharakan, T.J., "Flow Transition in Swirled Liquid Sheets," *AIAA Journal*, Vol. 36, No. 3, March 1998, pp. 420-427.

[49] Ghorbanian, K., Ashjaee, M., Soltanio, M.R., Mesbahi, M.H., and Morad, M.R., "Experimental Flow Visualization of Single Swirl Spray Pattern at Various Pressure Drops," *AIAA/SAE/ASME 39th Joint Propulsion Conference*, AIAA Paper No. 2003.4758, July 2003.

[50] Rahman, S. A., "Primary Atomization Study of a Swirl Coaxial Liquid Propellant Rocket Injector," Ph.D. Dissertation, Dept. of Mechanical Engineering, Pennsylvania State Univ., University Park, PA, 1997.

[51] Simmons, H.C., and Harding, C.F., "Some Effects of Using Water as a Test Fluid in Fuel Nozzle Spray Analysis," ASME Paper 80-GT-90, March 1980.

[52] Rizk, N.K., and Lefebvre, A.H., "Internal Flow Characteristics of Simplex Swirl Atomizers," *Journal of Propulsion and Power*, Vol. 1, no. 3, 1985, pp. 193.199.

[53] Giffen, E., and Muraszew, A., *The Atomization of Liquid Fuels*, Chapman and Hall, New York, 1953.

[54] Suyari, M., and Lefebvre, A.H., "Film Thickness Measurements in a Simplex Swirl Atomizer," *Journal of Propulsion and Power*, Vol. 2, no. 6, 1986, pp. 528-533.

[55] DeCorso, S. M., and Kemeny, G. A., "Effect of Ambient and Fuel Pressure on Nozzle Spray Angle," *ASME Gas Turbine Power Division Conference*, ASME Paper No. 1956-GTP-3, April 1956.

[56] Dodge, L. G., and Biaglow, J. A., "Effect of Elevated Temperature and Pressure on Sprays from Simplex Swirl Atomizers," *Journal of Engineering for Gas Turbines and Power*, Vol. 108, 1986, pp. 209 – 215.

[57] Ortman, J., and Lefebvre, A.H., "Internal Fuel Distributions from Pressure-Swirl Atomizers," *Journal of Propulsion and Power*, Vol. 1, no. 1, 1985, pp. 11-15.

[58] Hautman, D. J., "Spray Characterization of Liquid/Gas Coaxial Injectors with the Center Liquid Swirled," CPIA 498, 25th JANNAF Combustion Meeting, NASA Marshall Space Flight Center, October 1988.

[59] Coleman, H. W., and Steele, W. G., *Experimentation and Uncertainty Analysis for Engineers, 2nd Edition*, John Wiley & Sons, New York, 1999.

[60] E.W. Lemmon, M.O. McLinden and D.G. Friend, "Thermophysical Properties of Fluid Systems" in NIST Chemistry WebBook, NIST Standard Reference Database Number 69, Eds. P.J. Linstrom and W.G. Mallard, June 2005, National Institute of Standards and Technology, Gaithersburg MD, 20899 (http://webbook.nist.gov).

[61] Rahman, S. A., "Primary Atomization Study of a Swirl Coaxial Liquid Propellant Rocket Injector," Ph.D. Dissertation, Dept. of Mechanical Engineering, Pennsylvania State Univ., University Park, PA, 1997.

[62] Ruiz, F., and Chigier, N.A., "Design and Uncertainty Analysis of a Series of Atomization Experiments in Seven Variables," *Journal of Fluids Engineering: Transactions of the ASME*, Vol. 112, March 1990, pp. 96-106.

[63] White, F.M., *Fluid Mechanics*, 4th ed., McGraw-Hill, New York, 1999.

[64] White, F.M., *Viscous Fluid Flow*, 2nd ed., McGraw-Hill, New York, 1991.

[65] Rasband, W.S., Image, J, U.S., National Institutes of Health, Betheseda, MD, USA, http://rsb.info.nih.gov/ij/, 1997-2007.

[66] "Phantom v7.3 Datasheet," Vision Research Inc., October, 2007.

[67] Lucca-Negro, O., and O'Doherty, T., "Vortex Breakdown: A Review," *Progress in Energy and Combustion Science*, Vol. 27, 2001, pp. 431.481.

[68] Gupta, A.K., Lilley, D.G., and Syred, N., *Swirl Flows*, Gordon and Breach Pub., 1984

[69] Wang, D., Ma, Z., and Jeng, S., "Experimental Study on Large-Scale Simplex Nozzle," *AIAA/SAE/ASME 35th Joint Propulsion Conference,* AIAA Paper No. 1999-2401, June 1999.

[70] Hoehn, F. W., Rupe, J. H., and Sotter, J. G., "Liquid Phase Mixing of Bipropellant Doublets," Technical Report JPL-TR-32.1546, 1972.

[71] Ramamurthi, K., and Nandakumar, K., "Characteristics of Flow Through Small Sharp-Edged Cylindrical Orifices," *Flow Measurement and Instrumentation*, Vol. 10 , 1999, pp. 133.143.

[72] Crane Co., "Flow of Fluids through Valves, Fittings, and Pipe," Technical Paper No. 410, Reprinted December 2001.

[73] Dombrowski, N., and Hasson, D., "The Flow Characteristics of Swirl (Centrifugal) Spray Pressure Nozzle with Low Viscosity Liquids," *AIChE Journal*, Vol. 15, n4 July 1969, pp. 604.611.

[74] Babu, K. R., Narasimhan, M. V., and Narayanaswamy, K., "Correlations for Predictions of Discharge Rate, Cone Angle, and Air Core Diameter of Swirl Spray Atomizers," *ICLASS*, 1982.

[75] Ogawa, A., *Vortex Flow*, 1st ed., CRC Press, London, 1993.

[76] Donjat, D., Estivalezes, J., Michau, M., and Lavergne, G., "Phenomenological Study of the Pressure Swirl Atomizer Internal Flow," *ICLASS*, 2003.

[77] Bazarov, V.G., and Yang, V., "Liquid Propellant Rocket Engine Injector Dynamics," *Journal of Propulsion and Power*, Vol. 14, No. 5, September 1998, pp. 797-806.

[78] Dranovsky, M. L., "Uncertainty in Conversion of Propellant to Combustion Products," *Combustion Instabilities in Liquid Rocket Engines: Testing and Development Practices in Russia*, edited by V. Yang, F.E.C. Culick, and D.G. Talley, Progress in Astronautics and Aeronautics, AIAA, Washington, DC, 2007, pp. 23.31.